分类号_____ 密级_____

U D C _____ 编号_____

华中师范大学

博士学位论文

题目：Measurement of D^0 production in Pb-Pb collisions at 5.02 TeV with ALICE

学位申请人姓名: 彭忻烨

申请学位学生类别: 全日制博士

申请学位学科专业: 粒子物理与原子核物理

指导教师姓名: 周代翠 教授

Andrea Dainese 资深研究员

博士学位论文

Measurement of D^0 production in Pb-Pb collisions at 5.02 TeV with ALICE

论文作者：彭忻烨

指导教师：周代翠　　教授

Andrea Dainese 资深研究员

学科专业：粒子物理与原子核物理

研究方向：高能重离子碰撞实验

华中师范大学物理科学与技术学院

2019 年 3 月

博士学位论文
DOCTORAL DISSERTATION

Dissertation

Measurement of D^0 production in Pb-Pb collisions at 5.02 TeV with ALICE

By

Xinye Peng

Supervisors: Pr. Daicui Zhou

Dr. Andrea Dainese

Specialty: Particle Physics and Nuclear Physics

Research Area: Heavy-Ion Collision Experiment

College of Physical Science and Technology

Central China Normal University

Mar 2019

author signature:

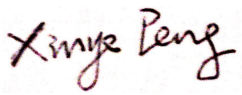

supervisor signature:

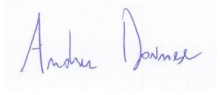

华中师范大学学位论文原创性声明和使用授权说明

原创性声明

本人郑重声明：所呈交的学位论文，是本人在导师指导下，独立进行研究工作所取得的研究成果。除文中已经标明引用的内容外，本论文不包含任何其他个人或集体已经发表或撰写过的研究成果。对本文的研究做出贡献的个人和集体，均已在文中以明确方式标明。本声明的法律结果由本人承担。

作者签名：　　日期：　　年　　月　　日

学位论文版权使用授权书

学位论文作者完全了解华中师范大学有关保留、使用学位论文的规定，即：研究生在校攻读学位期间论文工作的知识产权单位属华中师范大学。学校有权保留并向国家有关部门或机构送交论文的复印件和电子版，允许学位论文被查阅和借阅；学校可以公布学位论文的全部或部分内容，可以允许采用影印、缩印或其它复制手段保存、汇编学位论文。（保密的学位论文在解密后遵守此规定）

保密论文注释：本学位论文属于保密，在 ____ 年解密后适用本授权书。

非保密论文注释：本学位论文不属于保密范围，适用本授权书。

作者签名：　　导师签名：

日期：　　年　　月　　日　　日期：　　年　　月　　日

本人已经认真阅读“CALIS 高校学位论文全文数据库发布章程”，同意将本人的学位论文提交“CALIS 高校学位论文全文数据库”中全文发布，并可按“章程”中的规定享受相关权益。同意论文提交后滞后：□半年；□一年；□二年发布。

作者签名：　　导师签名：

日期：　　年　　月　　日　　日期：　　年　　月　　日

摘要

夸克－胶子－等离子体（QGP）是一种由处于渐进自由的夸克和胶子组成的新物质相，被认为会存在于宇宙大爆炸之后的数微秒。在实验系下，高能重离子碰撞提供了在可控环境下研究这种介质性质的舞台，如美国布鲁克海文国家实验室的相对论重离子对撞机（RHIC）和欧洲核子中心的大型强子对撞机（LHC）。高横动量的部分子与 QGP 的组分碰撞以及介质激发的胶子辐射会导致其损失能量的现象称为喷注淬火，它被公认为 QGP 产生的重要证据。在实验上，此现象可以通过两粒子方位角关联，核修正因子，双喷注能量不均衡以及喷注碎裂函数修正等观测。另一方面，由于重味夸克在硬散射过程中产生早于 QGP 的产生时间，它将经历 QGP 整个系统的演化并与 QGP 的组分发生强相互作用，因此它也是研究 QGP 性质的有效探针。

此论文将介绍基于 LHC 能区 ALICE 实验的高横动量中性π介子作为触发粒子，在质子-质子和中心铅核-铅核碰撞质心能量为 2.76 TeV 中关联的测量结果，直接 D 介子在铅核-铅核碰撞质心能量为 5.02 TeV 中产额的测量结果，以及正在进行的来源于 b 夸克的 D 介子在质子-铅核碰撞质心能量 5.02 TeV 中的分析结果。

两粒子关联的测量手段已经被普遍运用到寻找高横动量部分子的辐射能量剩余以及介质响应之中。通过改变触发和关联粒子的横动量，可以有效地研究软硬过程的相互作用。测量中性π介子强子关联除了可以研究 QGP 性质之外，它也提供了直接光子-强子关联主要背景的参照。在此工作中，选取由电磁量能器（EMCal）上的能量沉积重建双光子衰变道，进而鉴别中性π介子。选取中性 pi 介子作为触发粒子可以有效地避免与关联粒子混合，达到简化计算的目的。关联强子通过内部径迹探测器（ITS）和时间投影室（TPC）重建，相比之前的测量结果，此工作显著地把结果延展到了极低横动量区间（$p_{\mathrm{T}} = 0.5\ \mathrm{GeV}/c$）。在减除包含高阶流的主要背景贡献之后，单位中性π介子触发的强子产额可以在近端和远端提取，进而可以计算此产额在铅核-铅核与质子-质子碰撞中的比值，修正因子$I_{\mathrm{AA}} = Y_{\mathrm{PbPb}}/Y_{\mathrm{pp}}$。分析结果显示：在远端，$I_{\mathrm{AA}}$在$p_{\mathrm{T}} > 3\ \mathrm{GeV}/c$出现～0.6 倍的强压低，随关联强子横动量降低，$I_{\mathrm{AA}}$会逐渐上升，在最低横动量区间到达～5.2。在近端$I_{\mathrm{AA}}$从高横动量到低横动量出现 1.2 到 1.8 倍的增强。此实验数据对全面描述喷注-介质相互作用的模型提供了很好的参照。

直接 D 介子的核修正因子（R_{AA}）可以提供重夸克与 QGP 组分相互作用的重要信息，特别是重夸克能量损失色依赖以及质量依赖的信息。在此测量中，中心快度区的直接 D 介子通过其强子衰变道$\mathrm{D}^0 \rightarrow \mathrm{K}^-\pi^+$重建。在对衰变拓扑学变量限制以及带电粒子鉴别压低组合背景后，D 介子信号可以通过不变质量分析提取。来源于 b 夸克的 D 介子通过基于 FONLL 模型的计算以及对其核修正因子的假设减除。最终得到了直接 D 介子在铅核-铅核碰撞质心能量为 5.02 TeV 中核修正因子的测量结果。相比于质心能量为 2.76 TeV 的结果，新结果显著地拓展了横动量区间和精度。实验数据为基于不同能损机制的理论模型提供了严格的限制。此外，为了研究 b 夸克强子化，本工作还测量了来源于 b 夸克衰变的 D 介子在质子-铅核碰撞质心能量为 5.02 TeV 中的散射截面。此工作运用了基于机器学习的多变量算法（Boosted Decision Trees），首次实现了高纯度来源于 b 夸克衰变的 D 介子的提取，显著地降低了最终结果的统计和系统误差，为在未来铅核-铅核结果的测量作出了重要铺垫，此外，此多变量分析的算法也可被用于到其他低产额信号的提取之中。

本论文的结构如下：在第一章，简单介绍量子色动力学理论和重离子碰撞。第二章致力于凸显重味观测量在研究 QGP 性质中的重要意义。第三章简单介绍 ALICE 装置的结构和性能。第四章与第五章则重点介绍此论文的主要工作，分别为已经发表的中性π介子强子关联以及直接 D 介质核修正因子的测量结果。第六章简要介绍正在进行的来源于 b 夸克衰变的 D 介子的测量。最后给出总结和展望。

关键词：大型强子对撞机（LHC）,大型重离子碰撞实验（ALICE），铅核-铅核碰撞，D 介子测量，重夸克产生，核修正因子，夸克胶子等离子体（QGP）性质，两粒子关联测量

Abstract

The Quark-Gluon Plasma (QGP), a state of strongly-interacting matter in which quarks and gluons are deconfined, is thought to have existed a few micro-seconds after the Big Bang. Ultra-relativistic heavy-ion collisions provide a unique opportunity to study the properties of such deconfined medium. These collisions are realized at the Large Hadron Collider (LHC) and the Relativistic Heavy Ion Collider (RHIC). Jet quenching, the phenomenon in which high transverse momentum partons undergo energy loss by collisions with medium constituents and medium-induced gluon radiation, is widely considered as one of the evidences for QGP formation. Jet quenching can be observed via the measurements of di-hadron angular correlations, the nuclear modification factor ($R_{\rm AA}$), di-jet energy imbalance and via the modification of the jet fragmentation function. Heavy quarks are a powerful probe of the QGP, as they are produced in hard scattering processes on a timescale shorter than the QGP formation time and experience the whole system evolution.

This thesis presents the measurements of jet-like correlations with neutral pion triggers in pp and central Pb–Pb collisions at 2.76 TeV, the measurements of prompt $\rm D^0$ production in Pb–Pb collisions at $\sqrt{s}_{\rm NN} = 5.02$ TeV, and the on-going measurements of non-prompt $\rm D^0$ production in p–Pb collisions at $\sqrt{s_{\rm NN}} = 5.02$ TeV with the ALICE detector at the LHC.

The measurements using two-particle angular correlations between trigger particles and associated particles have been extensively used to search for remnants of the radiated energy and the medium response to the high-$p_{\rm T}$ parton. By varying the transverse momentum for trigger and associated particles one can probe different momentum scales to study the interplay of soft and hard processes. Besides providing access to medium properties, measurements of π^0-hadron correlations determine the most important background contribution of direct photon-hadron correlation measurements. For this analysis, the neutral pions used as triggers are identified in the di-photon decay channel, with energy deposits are reconstructed with the Electromagnetic Calorimeter (EMCal), avoiding admixtures from changing particle composition of the trigger particle, hence should simplify comparisons with calculations. Associated hadrons are reconstructed with the Inner Tracking System (ITS) and Time Projection Chamber (TPC) down to 0.5 GeV/c, and significantly extend the previous measurement that only used charged hadrons above 3 GeV/c. After subtracting the dominant background, including the anisotropic flow harmonics v_2 to v_5, the per-trigger yields are extracted for Near side with $|\Delta\varphi| < 0.7$ and Away side with $|\Delta\varphi - \pi| < 1.1$. The per-trigger yield modification factor, $I_{\rm AA}$, defined as the ratio of per-trigger yields in Pb–Pb to those in pp collisions, is measured on the near and away side for the 0-10% most central Pb–Pb collisions. On the Away side, the $I_{\rm AA}$ is strongly suppressed to around 0.6 for $p_{\rm T} > 3$ GeV/c, and increase as the momenta decrease, reaching about 5.2 at lowest $p_{\rm T}$. On the near side, an enhancement of $I_{\rm AA}$ from 1.2 to 1.8 at lowest $p_{\rm T}$ is observed. The data provides a good constrain to the theoretical models which aim to fully describe jet-medium interactions.

The measurements of prompt $\rm D^0$ nuclear modification factor ($R_{\rm AA}$) can provide

important information about the microscopic interactions of heavy quarks with the medium constituents, in particular on the colour-charge and parton-mass dependence of heavy-quark energy loss. The prompt D^0 are reconstructed at mid-rapidity via the hadronic decay channel $D^0 \rightarrow K^-\pi^+$. Selections on the decay topology and particle identification are applied in order to reduce the combinatorial background. The signal is extracted via an invariant-mass analysis. The feed-down from beauty-hadron decays is subtracted according to expectations based on FONLL calculations and assumptions of feed-down nuclear modification factor. The prompt D^0 nuclear modification factor (R_{AA}) has been measured in Pb–Pb collisions at $\sqrt{s_{NN}} = 5.02$ TeV, in the centrality class 0-10%, 30-50% and 60-80%. The results are compatible with those measured at $\sqrt{s_{NN}} = 2.76$ TeV, with better precision and extended p_T coverage. The data set stringent constraints to theoretical models with different implementations of in-medium energy loss. The cross section of non-prompt D^0 has been measured in p-Pb collisions at $\sqrt{s_{NN}} = 5.02$ TeV, with the goal to further understanding of beauty hadronisation. A multivariate technique (Boosted Decision Trees) is utilised to improve the separation between non-prompt and prompt D^0 by optimally combining discriminating variables related to the D^0 decay topology. This method can significantly improve the statistical precision with which the measurement of non-prompt D^0 can be made in Pb–Pb collisions with ALICE in the future. At the same time, this technique can be utilised for extracting other physics signal with low signal-to-background ratio.

In the first Chapter, the physics of QCD theory and Heavy Ion Collisions will be introduced. The second Chapter describes the role of heavy flavour observables to investigate the QGP. A brief introduction of the ALICE apparatus will be given in Chapter 3. The fourth and fifth Chapters present the main work of the thesis, about π^0-hadron correlations and prompt D^0 R_{AA} measurements. These results have already been published. The sixth chapter describes an on-going work about non-prompt D^0 analysis, which aims to prepare a new measurement in Pb–Pb collisions in the future. Conclusions and Outlook will be drawn in the end.

Keywords: LHC, ALICE experiment, Pb–Pb collisions, ultra-relativistic heavy-ion collisions, D mesons, heavy flavour production, nuclear modification factor, Quark-Gluon Plasma (QGP), two-particle correlations

Contents

List of Figures

List of Tables

Part I

Introduction

Chapter 1

QCD theory and Heavy Ion Collisions

Heavy ion collisions are dedicated to study the properties of deconfined matter constituted by quarks and gluon. After a short introduction about the Standard Model in Sec. 1.1, The Quantum ChromoDynamics theory which describes the strong interaction between quarks and gluons will be discussed in Sec. 1.2. The Lattice QCD approach which predicts the phase transition from hadronic matter to the Quark-Gluon-Plasma (QGP) will be addressed in Sec 1.3. Finally, some examples of possible signatures of QGP existence which has been observed by high energy heavy-ion experiments will be described in Sec. 1.4.

1.1 Standard Model

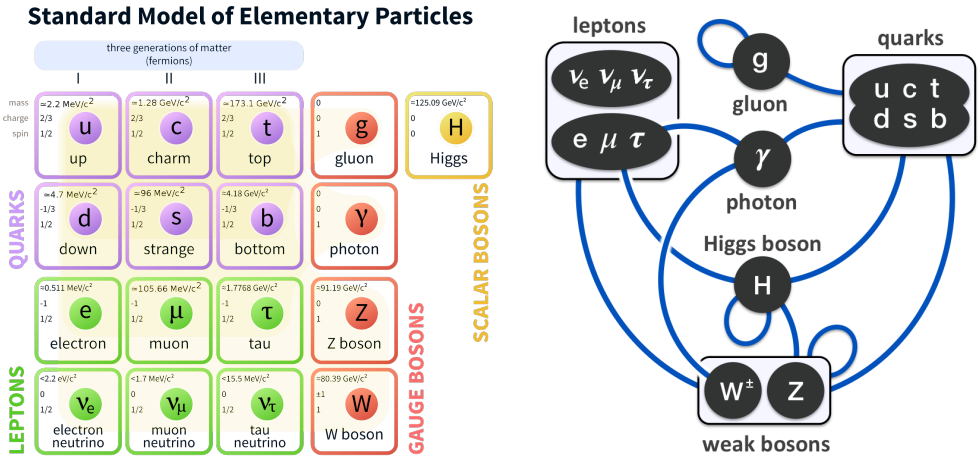

Figure 1.1: Elementary fundamental particles in the Standard Model (left) and the interactions between them (right) [1].

There are four fundamental forces in the current understanding of nature: gravity, strong, weak and electromagnetic forces. The latter three forces can be described by the Standard Model [43, 44] with the gauge symmetry of the group product SU(3)⊗SU(2)⊗U(1). In the Standard Model, fundamental particles can be divided into two groups according to their properties (as shown from Fig. 1.1). In the group

of fermions with spin-1/2, there exist six "quarks" (with colour charge) interacting via the strong interaction (details will be discussed in the next section Sec. 1.2), as well as six "leptons" (without colour charge) interacting via the weak interaction. The other group is called "bosons", which contains "gauge bosons" (spin-1) and "scalar boson" (spin-0). The gauge bosons are recognized as force carriers mediating the strong (the gluon), weak (W and Z bosons) and electromagnetic (the photon) interactions. The Higgs Boson (sole scalar boson), a massive particle endues the masses of the quarks and the leptons by interacting with them and with itself.

1.2 Quantum ChromoDynamics

Quantum ChromoDynamics (QCD) is the non-Albelian gauge theory developed to describe the strong interactions between coloured quarks and gluons. It's the SU(3) component of Standard Model, the Lagrangian can be written as:

$$\mathcal{L} = \sum_q \overline{\psi}_{q,a}(i\gamma^\mu \partial_\mu \delta_{ab} - g_s \gamma^\mu t^C_{ab} \mathcal{A}^C_\mu - m_a \delta_{ab})\psi_{q,b} - \frac{1}{4} F^A_{\mu\nu} F^{A,\mu\nu}. \tag{1.1}$$

Where, γ^μ are the Dirac γ-matrices; $\psi_{q,a}$ are quark field spinors, q and a are the quark flavour and colour indexes, a runs from $a = 1 \to N_c = 3$ (three colours of quarks); the $\mathcal{A}^C_\mu$ refer to the gluon fields with with colour-index C between $C = 1 \to N_c^2 - 1 = 8$ (8 types of gluons); m_q are quark masses generated by the Higgs mechanism and g_s (or $\alpha_s = g_s/4\pi$) is the QCD coupling constant; m_q and g_s (or α_s) are two fundamental parameters in QCD; t^C_{ab} are 8 generators of SU(3) group. The gluon field tensor $F^A_{\mu\nu}$ is expressed as:

$$F^A_{\mu\nu} = \partial_\mu \mathcal{A}^A_\nu - \partial_\nu \mathcal{A}^A_\mu - g_s f_{ABC} \mathcal{A}^B_\mu \mathcal{A}^C_\nu, \tag{1.2}$$

where f_{ABC} are the structure constants of SU(3), the last term $g_s f_{ABC} \mathcal{A}^B_\mu \mathcal{A}^C_\nu$ which is main difference with QED reflects the gluon self-interactions.

QCD reveals two peculiar features of the strong interaction called **colour confinement** and **asymptotic freedom**.

1.2.1 Confinement and Asymptotic Freedom

Due to the quantum fluctuations, the QCD vacuum is not completely empty, but a polarizable vacuum contains virtual particles. Gluons create virtual quark-antiquark ($q\overline{q}$) pairs as "dipoles". Analogous to QED, the virtual antiquark is closer to the real quark, thus this effectively cancels out some of the colour of the real quark, smearing it out and screening it, colour charge decreases with the increase of the distance between two quarks; however, due to the gluon self-interactions, particles with colour charge (quarks and gluons) will be confined inside QCD potential, thus combine into hadrons with zero net colour charge. That's why we can't "see" free quarks in the nature world. Also, the colour charge of gluons will contribute to the effective colour charge of quarks, leading to an anti-screening effect, colour charge

decreases with the distance. The interplay of these screening and anti-screening effects determines how the coupling constant α_s runs with the distance (or energy). Within the frame-work of **perturbative QCD** (**pQCD**) [45], this property can be described in the renormalization group equation:

$$\beta(\alpha_s) = \mu_R^2 \frac{d\alpha_s}{d\mu_R^2} \tag{1.3}$$

Where μ_R is the QCD renormalization scale. The first order of the $\beta - function$ has been calculated as $\beta_1(\alpha_s) = \frac{\alpha_s^2}{\pi} b_0 = \frac{\alpha_s^2}{\pi}(-\frac{11N}{6} + \frac{n_f}{3})$ [46]. With N = 3 (SU(3) gauge theory) and $n_f = 6$ (6 quark flavours), this gives a negative sign, which means that at large energy, anti-screening is greater than screening effect, α_s will go close to zero, this property is call **asymptotic freedom**. Considering only the first term (b_0) , under the assumption $\mu_R^2 \simeq Q^2$, one can write α_s as [47, 48]:

$$\alpha_s(Q^2) = \frac{1}{b_0 \ln(Q^2/\Lambda_{QCD}^2)}, \tag{1.4}$$

where, Λ_{QCD} is the non-perturbative QCD energy scale where pQCD cannot be

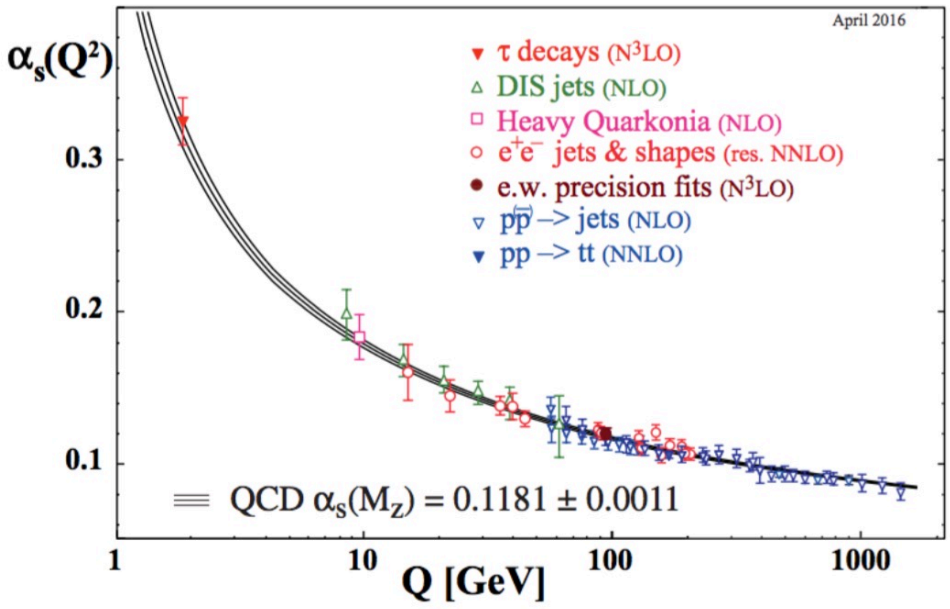

Figure 1.2: The summary of measurements of QCD running coupling α_s as a function of Q. Taken from [1].

used. Q^2 is related to the momentum transfer. Eq. (1.4) has been confirmed experimentally as shown in Fig. 1.2.

In summary, as in nature world, Q^2 is always very small, thus α_s should be very large, quark and gluons are confined in the hadrons. On the other hand, for Q^2 process, α_s becomes close to zero, which will lead "free" quark and gluons exist in the QCD vacuum, this is known as "asymptotic freedom".

1.3 Quark-Gluon Plasma

As discussed in previous Sec. 1.2.1, with the increase of momentum transfer or decrease the distance, which equivalent to heating or compression, strong interactions will be weaker. At extremely high temperatures or energy densities, a phase transition from the normal hadronic matter to a new state of matter with free quarks and gluons is expected, this new state of matter is so-called **Quark-Gluon Plasma** (QGP). It's very curial to understand the properties of the phase transition.

1.3.1 Lattice QCD and QCD Phase diagram

At high Q^2, a perturbative approach of QCD can be used. However the phase transition relates to a process with long distance where pQCD is not valid. Thus **Lattice QCD (lQCD)** was implemented by K. Wilson in 1974 [49], which based on first principles to solve the non-perturbative QCD equations at low energy.

In lattice gauge theory, Euclidean space-time is discrete in a hypercubic lattice with spacing a. The quarks are defined at the lattice sites and gluons connect the sites to exchange the strong force. When the space between the lattice sites reduce to zero, it approaches to the continuum QCD. Field configurations can be extracted by calculating the gauge configurations with the interaction between gauge bosons and gauge-fermion, then use the configurations to get hadronic propagators and correlation functions. Physicals results can be obtained by calculating the limit for lattice space a down to zero.

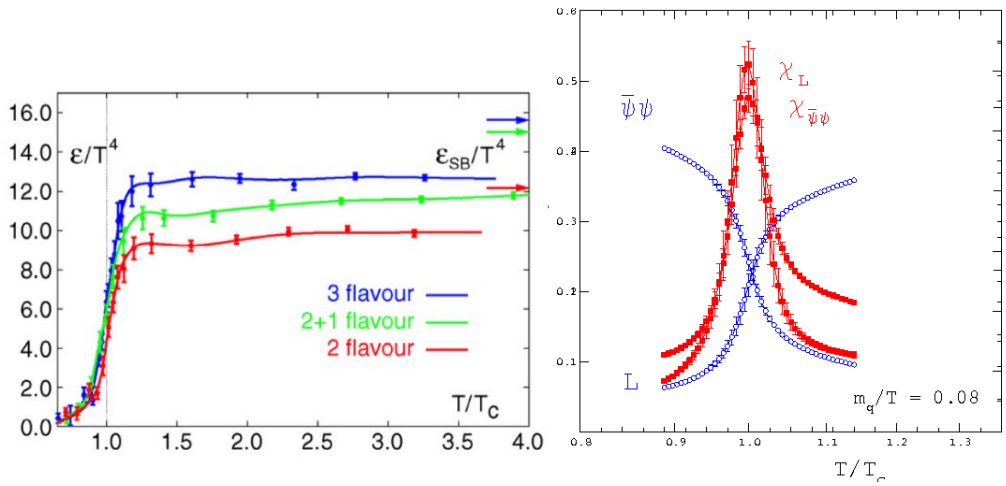

Figure 1.3: Left: energy density ε/T^4, versus temperature T from Lattice QCD [2]. Right: Deconfinement and Chiral Symmetry restoration in 2-flavour QCD [3].

According to the prediction from Lattice QCD, around the critical temperature $T_c = 155$ MeV, the energy density of the system will have a rapid rise in 2-flavour QCD [2], which indicates the liberation of the quark and gluon degrees of the freedom, as shown in Fig. 1.2 (Left). With the increase of T, the density increases

approximately by an order of magnitude near T_c, and becomes almost flat beyond T_c. The flat behavior at high T depends on the degrees of the freedom, and it's believed the phase transition will change from second order to first order if decreasing strange quark mass, so it's hard to describe the order of phase transition as the strange quark mass is unknown.

Another hint of the QCD phase transition [3] can be described by $< L >$, which is the order parameter for deconfinement: $< L >= 0$ for $T < T_c$ indicates the confined phase, while $< L >> 0$ for $T > T_c$ corresponds to the deconfined phase. The sudden change in the long distance behavior can be observed by the Polyakov loop susceptibility χ_L. Also, the chiral condensate $< \overline{\Psi}\Psi >$ is restored at $T = T_c$: $< \overline{\Psi}\Psi >> 0$ for $T < T_c$ corresponds to the symmetry broken phase with large effective quark mass, while $< \overline{\Psi}\Psi >= 0$ for $T > T_c$ corresponds to the phase with small effective quark mass. The results are shown in Fig. 1.2 (right).

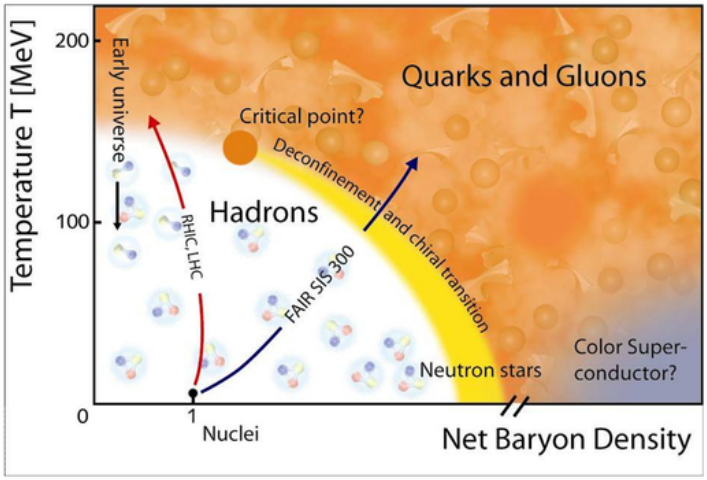

Figure 1.4: A sketch of the QCD Phase Diagram.

Nuclear matter is expected to appear in different states depending on the temperature T and baryo-chemical potential μ_B [50]. Fig. 1.4 shows a sketch of the QCD phase diagram. At low temperatures and small μ_B, nuclear matter is confined as atomic nuclei and hadrons. Increasing of the system energy density, by "heating" (increasing T) or "compression" (increasing μ_B), nuclear matter will reach a hadronic gas phase in which nucleons will interact and form pions, excited states of the protons and neutrons and other hadrons. If the system energy density is further increased, the transition to the Quark Gluon Plasma is predicted: the confined quarks in hadrons will vanish, thus QGP formed. Theses phase transition can be fulfilled with different "paths" as shown in the (μ_B, T) plane. For the process of neutron stars formation, the transition appears at T close to zero and with very high baryonic density caused by the gravitational collapse. In the early universe the transition took place at very high temperatures and vanishing baryo-chemical potential. Also in high energy heavy ion collisions, for the LHC, the transition is

expected at $\mu_B \sim 0$.

1.4 Heavy Ion Collisions

As discussed in the previous Sec. 1.3, a transition to Quark-Gluon Plasma phase happens at extremely high values of temperature and energy density, which is expected to have existed in the primordial Universe few microseconds after the Big Bang [51]. Such extreme conditions can be reached in the laboratory by ultra-relativistic heavy-ion collisions. The experimental research started since1980's, with the fixed target experiments of the Super Proton Synchrotron (SPS) at CERN and the Alternating Gradient Synchrotron (AGS) at Brookhaven National Laboratory (BNL) with maximum centre of mass energy per colliding nucleon pair $\sqrt{s_{\rm NN}} = 17.2$ GeV and 4.6 GeV respectively; then the Relativistic Heavy Ion Collider (RHIC) at BNL has been operated with Au–Au collisions with the centre of mass energy up to $\sqrt{s_{\rm NN}} = 200$ GeV; Currently the Large Hadron Collider (LHC) at CERN with Pb–Pb collisions can reach the highest centre of mass energy up to $\sqrt{s_{\rm NN}} = 5.02$ TeV, and will increase to 5.5 TeV from 2021.

1.4.1 Space-time evolution of relativistic heavy-ion collisons

In ultra-relativistic heavy-ion collisions, as shown in Fig. 1.5, the space-time evolution of the collision system can be summarized as following:

Initial stage : The nuclei approach each other with the velocities close to the velocity of light in the laboratory frame. Due to the Lorentz contraction, they look like two "thin pancakes", as presented in Fig. 1.6. Many nucleon-nucleon collisions happen at the same time, the overall geometry overlap region can be defined by the distance between two colliding nucleus's centers called impact parameter b. The nucleons inside the overlap region which undergo the primary interactions are called *participants*, the total number counted as "$N_{\rm part}$"; while the ones outside the overlap region called *spectators*. The total number of nucleon-nucleon interactions are called "$N_{\rm coll}$". The centrality percentile which depends on the impact parameter b can be calculated by Glauber model [52];

Pre-equilibrium : High energy partons are produced via hard scattering process, they will interact with each other to form the fireball, this stage last the time scale around τ = 0.6-1 fm/c, high transverse momentum particles (such as jets, heavy quarks, photons) are also generated at this stage;

QGP phase : If the temperature exceeds the critical temperature T_c, the system goes to a deconfined phase with partonic and gluonic degrees of freedom, the QGP expands and cools down rapidly;

Hadronisation : The medium's temperature drops below T_c, which will lead to the transition of QGP phase to hadrons gas. During this process, it's expected that a "mixed phase" exist between QGP phase and the hadronic phase.

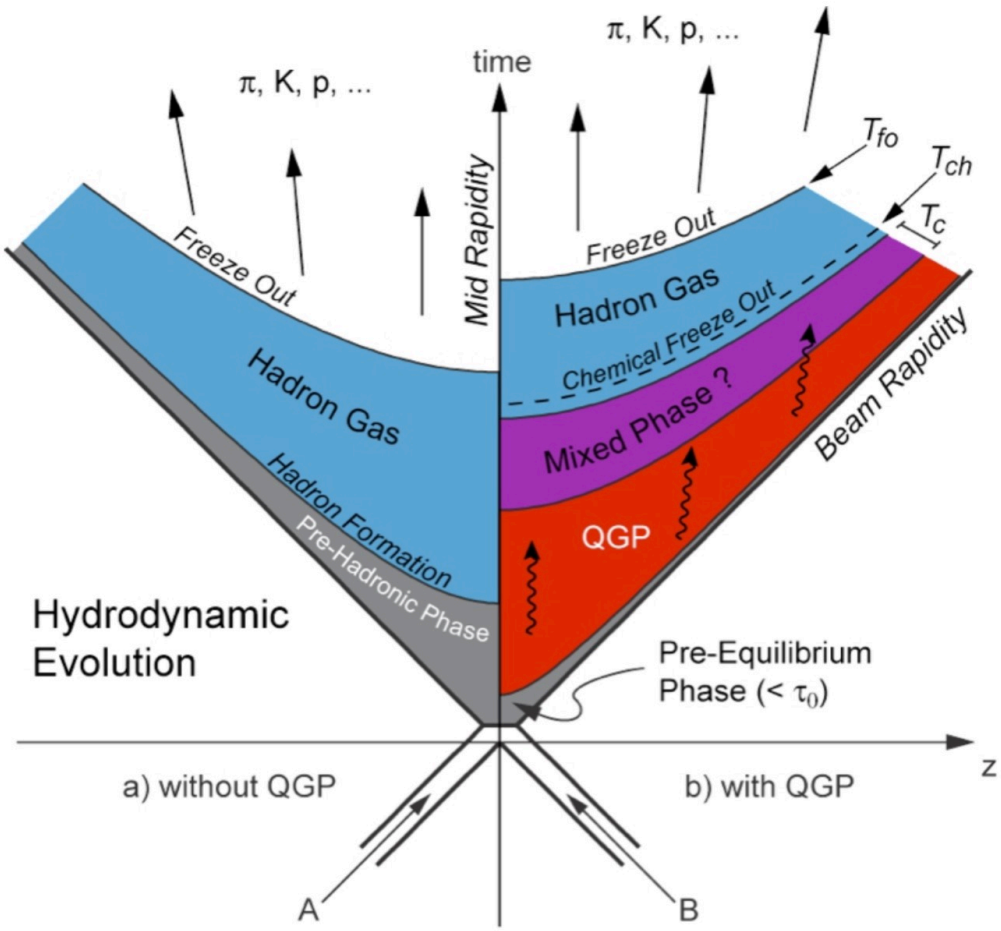

Figure 1.5: A sketch of the space-time evolution in a ultra-relativistic heavy-ion collision system with (right) and without (left) QGP.

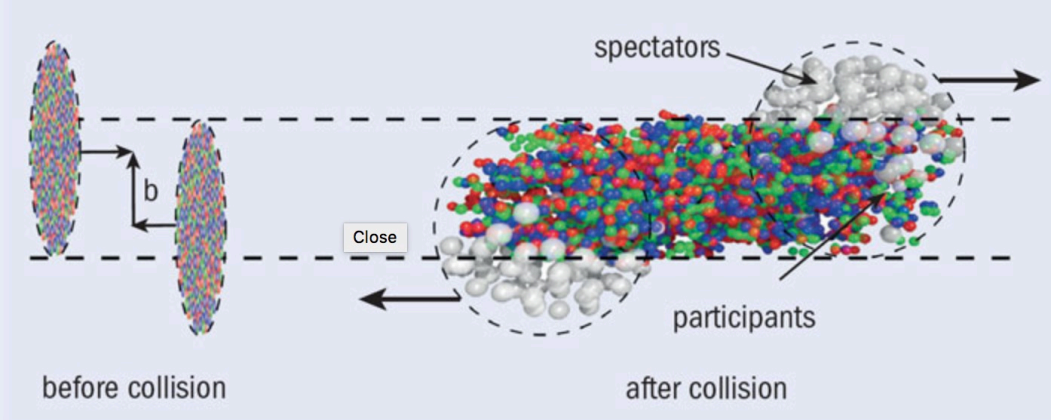

Figure 1.6: Two heavy ions before (left) and after collision with impact parameter b.

Chemical freeze-out : Inelastic processes cease, at this stage, all the hadron species are fixed.

Kinetic freeze-out : Elastic processes stop, the finial momentum of the produced hadrons are determined.

1.4.2 Selected signatures of the QGP

1.4.2.1 Global Event Properties

Multiplicities and energy densities

Multiplicity is the number of particles produced in the collision system, which is related to the collision geometry, as well as the energy density. This property can be presented by measuring primary charged particles per unit of pseudorapidity ($\eta = -\ln(\tan(\theta/2))$) $\mathrm{d}N_{\mathrm{ch}}/\mathrm{d}\eta$. Usually this measurement is scaled by the average number of nucleon pairs participating in the collision $\langle N_{\mathrm{part}} \rangle /2$. Fig. 1.7 [4], shows the charged particle pseudorapidity density per participant pair at mid-rapidity, for proton-proton, proton-nucleus and central nucleus-nucleus collisions, as a function of the centre-of-mass energy per nucleon-nucleon collision in different systems (left). The results in proton-proton and proton-nucleus collisions are found to be consistent and can be fitted by a power law function (as^b), with the parameter b = 0.103±0.002. While data for the central heavy-ion collisions, can be fitted with the parameter b = 0.155±0.004, and raise more rapidly with energy compared with small systems. On the right, the centrality dependence of this measurement in different collisions and energies measured in ALICE indicates a strong dependence on $\langle N_{\mathrm{part}} \rangle$, and a decreasing from most central to peripheral collisions.

The initial energy density can be estimated by the simplified Bjorken model [53] using the measured $\mathrm{d}N_{\mathrm{ch}}/\mathrm{d}\eta$:

$$\varepsilon_{Bj} = \frac{\langle m_T \rangle}{\tau_f A} \frac{\mathrm{d}N_{\mathrm{ch}}}{\mathrm{d}y}, \tag{1.5}$$

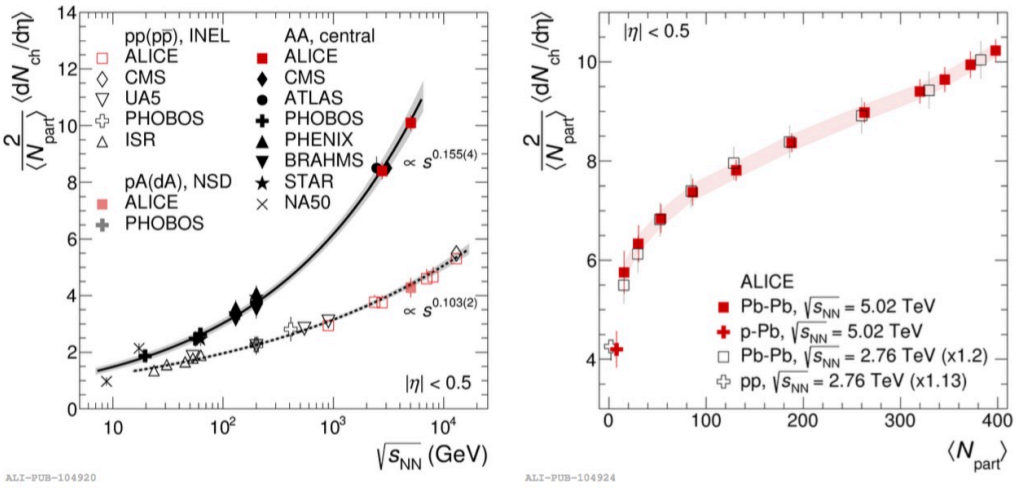

Figure 1.7: Left: the charged particle pseudorapidity density per participant pair at mid-rapidity, for proton-proton, proton-nucleus and central nucleus-nucleus collisions, as a function of the centre-of-mass energy per nucleon-nucleon collision in different systems. Right: centrality dependence of this measurement in different collisions and energies in ALICE [4].

Where $\langle m_T \rangle$ is average transverse mass of produced particles, τ_f is the formation time of the secondary particles, A is the two colliding nuclei overlap region, and y is the rapidity. At RHIC energy (Au+Au 200 GeV), the initial energy density is measured around 5 GeV/fm^3, while for central Pb–Pb collisions at 2.76 TeV LHC energy, it's as high as 12 GeV/fm^3 [54]. Both are obviously above the critical point according to the Lattice QCD prediction for the phase transition to QGP.

Integrated hadron yields

The final hadron productions are fixed after chemical free-out, which is considered to be a approximate thermal and chemical equilibrium process. The integrated light-hadron yields can be determined via a statistical approach (Grand Canonical) [7], depending on the thermal parameters of temperature T, volume V and chemical potentials μ_B. However this doesn't apply to strange particles, which have a deviation from the expected equilibrium abundance. The deviations from (Grand Canonical) equilibrium can be described by introducing parameters for strange, charm or light quarks (γ_s, γ_c and γ_q). The γ_s depends on the strangeness content of the particle, γ_c is needed as charm is so heavy that can only be generated in the initial phase of the collisions, while γ_q is only used for the non-equilibrium model SHARE [8]. As shown in Fig. 1.8, Grand-Canonical thermal fit for identified integrated hadron yields measured with ALICE in 0-10% central Pb–Pb collisions at $\sqrt{s_{\rm NN}}$ = 2.76 TeV [5], with different models [6, 7, 8]. The temperature from the fit is of the order of 155 MeV, while from low energy RHIC data, the fit for the temperature is 160 - 170 MeV. The fit temperature at LHC energy will go up to around 160 MeV (closer to RHIC result) if excluded the proton yield, taking into

account the disagreement between the measurement. A possible explanation for the significant deviation is the large cross section for antibaryon-baryon annihilation in the hadronic phase [55].

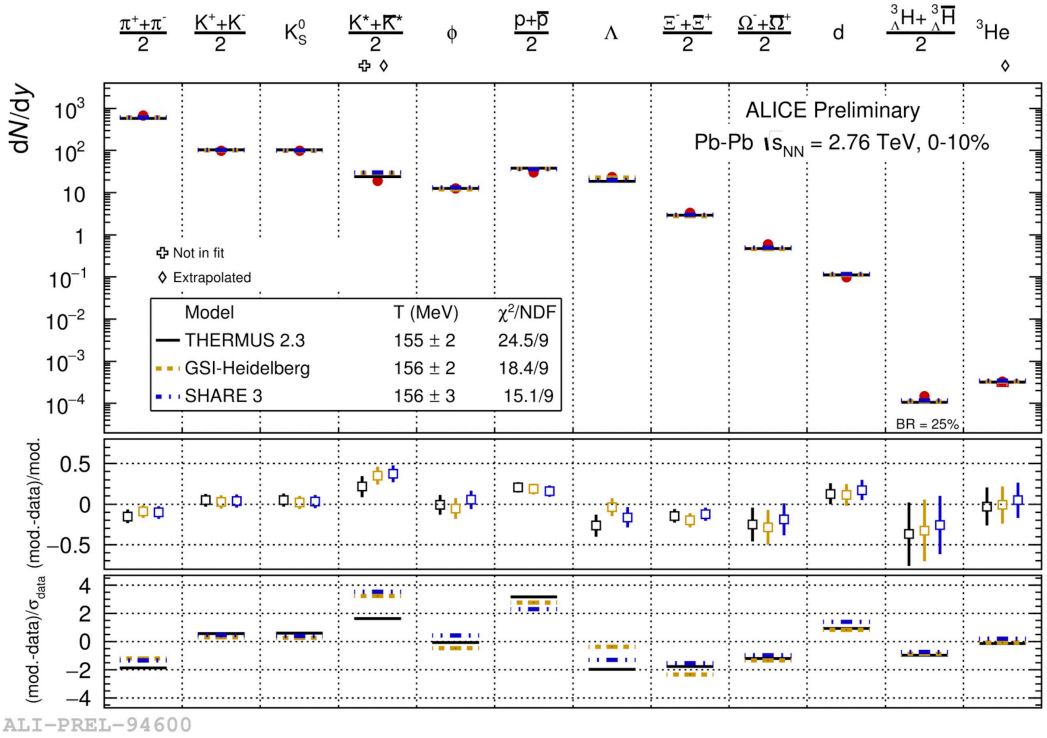

Figure 1.8: Grand canonical thermal fit of 0-10% central Pb-Pb collisions at ALICE [5], with 3 models (THERMUS [6], GSI [7], SHARE [8]). Excluded volume correction implemented in THERMUS and GSI with $\gamma_q = 0.3$ fm μ_B fixed to 0, γ_s fixed to 1, γ_c fixed to 20 (THERMUS and GSI).

1.4.2.2 Collective Flow

The collective flow [56], which is related to the physics for the expansion of the system, gives access to the study of the hydrodynamical properties and the Equation of State (EOS) of the medium. As shown in Fig. 1.9, in non-central heavy-ion collisions, pressure gradient will generate between the overlap and the periphery region, and varies with azimuth, is larger in the reaction plane than the perpendicular direction. Thus the initial geometrical anisotropy is transferred to a finial state momentum-space anisotropy. Experimentally, the azimuthal distributions can be parametrized with a Fourier expansion:

$$E\frac{\mathrm{d}^3\sigma}{\mathrm{d}^3\vec{p}} = \frac{\mathrm{d}^2\sigma}{2\pi p_t \mathrm{d}p_t \mathrm{d}y}[1 + \sum_{n=1}^{\infty} 2v_n \cos n(\phi - \Psi_R)], \tag{1.6}$$

$$v_n = < \cos n(\phi - \Psi_R) >, \tag{1.7}$$

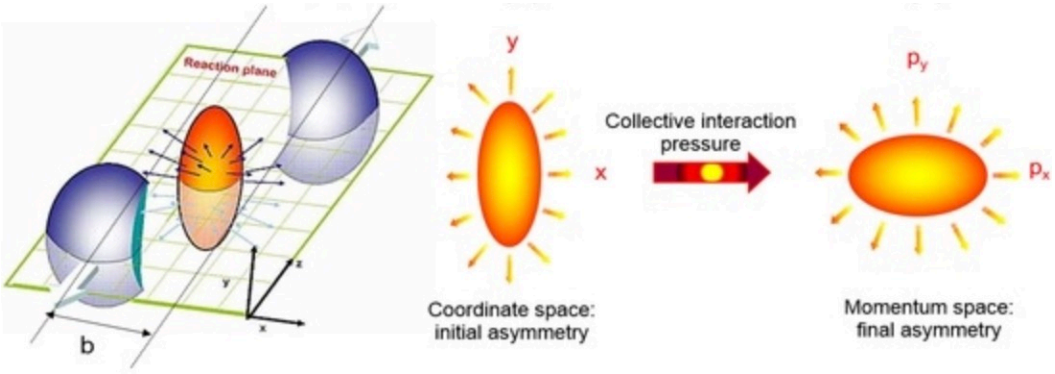

Figure 1.9: The cartoon of a semi-peripheral collision and the pressure gradients in a geometrical anisotropy.

Where $\vec{p}$, is the 3-momentum, p_{t} is transverse momentum, y is rapidity, ϕ is azimuth of the particles. Ψ_{R} is the reaction plane, and v_n are the Fourier coefficients that can be evaluated as shown in Eq. 1.7. The first order of harmonic coefficient, v_1, is the directed flow which is related to the overall shift of the particle distribution in the transverse plane. v_2, is the so-called elliptic flow. The positive value of v_2 indicates the particle re-scattering behavior during the system evolution. Any delays or absence of re-scatterings will lead to a reduced or null elliptic flow signal. The non-zero value of higher harmonic coefficients (n $>$ 2) is caused by the initial fluctuations of the positions of nucleons in the overlap region. Fig. 1.10 shows the p_{T}-differential v_2 of pions, protons, kaons, phi, lambda and k0s mesons for various centrality classes with the scalar product method, measured in Pb-Pb collisions at $\sqrt{s_{\mathrm{NN}}}$ = 5.02 TeV by ALICE [9]. In the low p_{T} region ($p_{\mathrm{T}} < 2$ GeV/c), dominated by the soft process, the mass ordering of v_2 is found for different particle species, which can be described by the hydrodynamics. At middle p_{T} region ($3 < p_{\mathrm{T}} < 8$ GeV/c), the interplay between soft and hard processes, the mass ordering effect is trivial, instead, the meson's v_2 seems to be grouped which is weaker than v_2 of baryon, which is expected under the hypothesis of hadrons produced via quark coalescence [57]. At high p_{T} region ($p_{\mathrm{T}} > 10$ GeV/c), dominated by the hard process, a non-zero v_2 is found and attributed to the path-length energy loss.

The measurement of v_n can also help to extract the information of shear viscosity over entropy η/s [58] of the medium. As shown in Fig. 1.11, the v_n for Pb-Pb collisions at the LHC energy (left panel) and for Au-Au collisions at RICH energy (right panel), compared with viscous hydrodynamics calculations [10]. The value of shear viscosity over entropy displays equal to 0.12 seems to have a good parameterisation of the hydro calculations for Au–Au collisions 200 GeV at RHIC energy, while the value equal to 0.2 is found to have a good description of Pb–Pb collisions at LHC energy. This reflects the fact that the shear viscosity over entropy η/s of the medium depends on the temperature of system.

Collectivity in small system

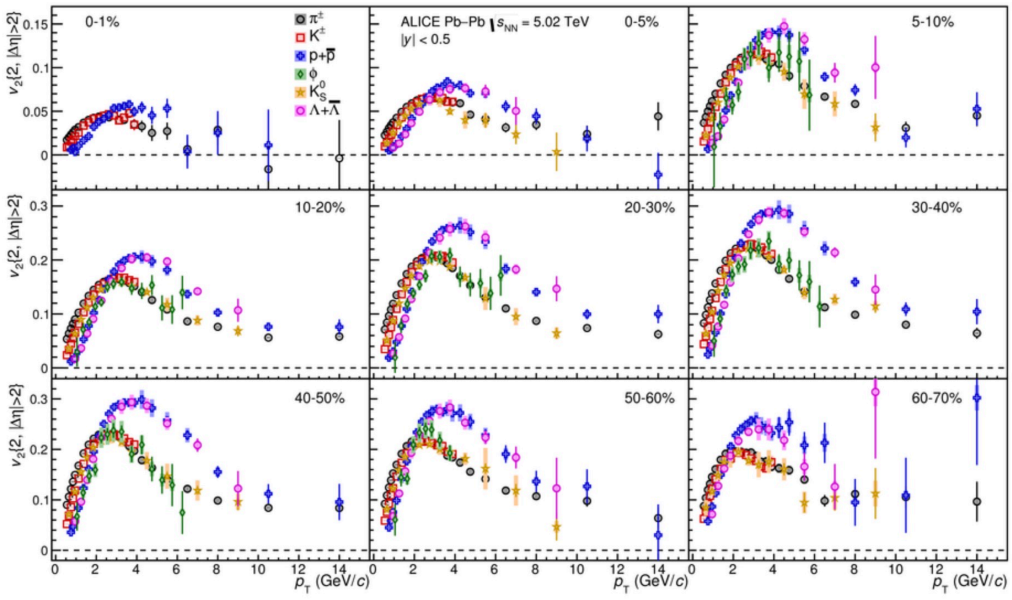

Figure 1.10: The p_T-differential v_2 of pions, protons, kaons, phi, lambda and k0s mesons for various centrality classes, measured with the scalar product method [9].

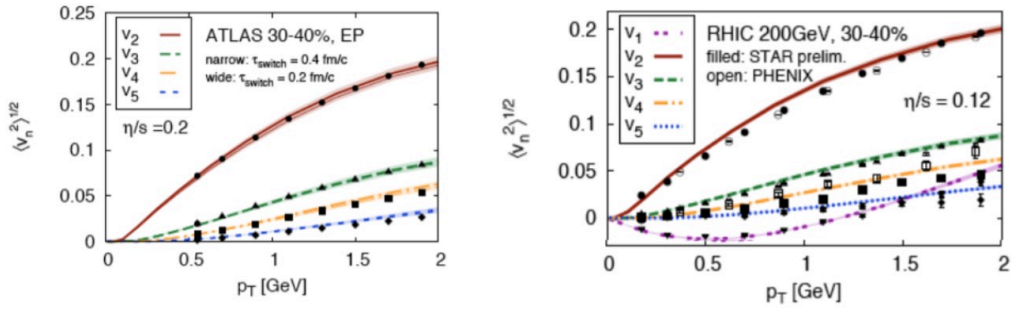

Figure 1.11: the v_n for Pb-Pb collisions at the LHC energy (left panel) and for Au-Au collisions at RICH energy (right panel), compared with viscous hydrodynamics calculations [10].

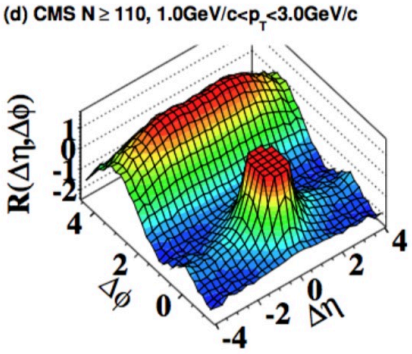

Figure 1.12: 2-D two-particle correlation functions for 7 TeV pp collisions with high multiplicity ($N_{trk}^{offline} > 110$) events with $1 < p_{\mathrm{T}} < 3$ GeV/c [11].

A surprising "ridge" effect – a significantly separated long-range rapidity correlation was discovered by CMS in 2010 with high multiplicity pp collisions at $\sqrt{s}$ = 7 TeV [11], as shown in Fig. 1.12. After subtraction of the jet-like structures, a "double ridge" behavior can be observed on the near and away side [59], thus the anisotropic flow coefficients can be extracted, and are found to have non-zero value. In heavy-ion collisions, such long range ridges is attributed to collective expansion of the medium, however, in small system, it's still not clear whether such a phenomena is due to the hydrodynamics or other mechanisms which gives a similar structure, such as initial state effects (glass condensate) and final-state effects (multiple parton interactions), as described in [60].

1.4.2.3 Strangeness enhancement

As the colliding nuclei doesn't contain strange quarks, the strangeness must be generated in the collisions or in the QGP. At $T < T_c$, strange hadrons have a very small production rate since their effective mass is larger than T_c where chiral symmetry is broken. While in the QGP ($T > T_c$), where chiral symmetry is restorated, strange quarks are easier to produce, at the same time, due to the large gluon density in the QGP, strange quarks can be generated in the gluon-fusion processes $gg \rightarrow s\bar{s}$, in consequence, strangeness enhancement is widely considered to be the signature of QGP formation.This was first measured by the NA57 and WA97 collaborations in fixed-target experiments in the SPS [61].

Recently, ALICE reported the first measurement about strangeness enhancement in high multiplicity in pp collisions [12], as shown in Fig. 1.13. The left panel shows p_{T}-differential yields of K_s^0, $\Lambda + \bar{\Lambda}$, $\Xi^+ + \Xi^-$, $\Omega^+ + \Omega^-$ measured at mid-rapidity in ALICE, for selected event classes, indicated by roman numbers, with decreasing multiplicity. The spectra becomes harder with the increase of the multiplicity, Similar characteristic has already been observed in p–Pb [62] and Pb–Pb collisions, and it can be explained by the hydrodynamical expansion. Simultaneously fitting

all the highest multiplicity class p_{T} spectra with the blast-wave model, one can extract the kinetic freeze-out temperature $T_{fo} = 163 \pm 10$ MeV and the transverse velocity $\langle\beta_{\perp}\rangle = 0.49 \pm 0.02$. On the right, shows those p_{T}-differential yields to pions ratios as a function of $\langle \mathrm{dN_{ch}}/\mathrm{d}\eta \rangle$ in different collision systems, and compared with model predictions. A significant enhancement for strange hadron production with respect to non-strange hadrons is observed, increasing with multiplicity, and a "smooth" connection among different systems is found, while not significant dependence of centre-mass-energy is seen, indicating that the strangeness production is relied more on the properties of the final state instead of the collision system or energy. Unfortunately, the current available models can't reproduce the data, so further understanding about the potential mechanisms of strangeness production in small systems for high multiplicity events is necessary.

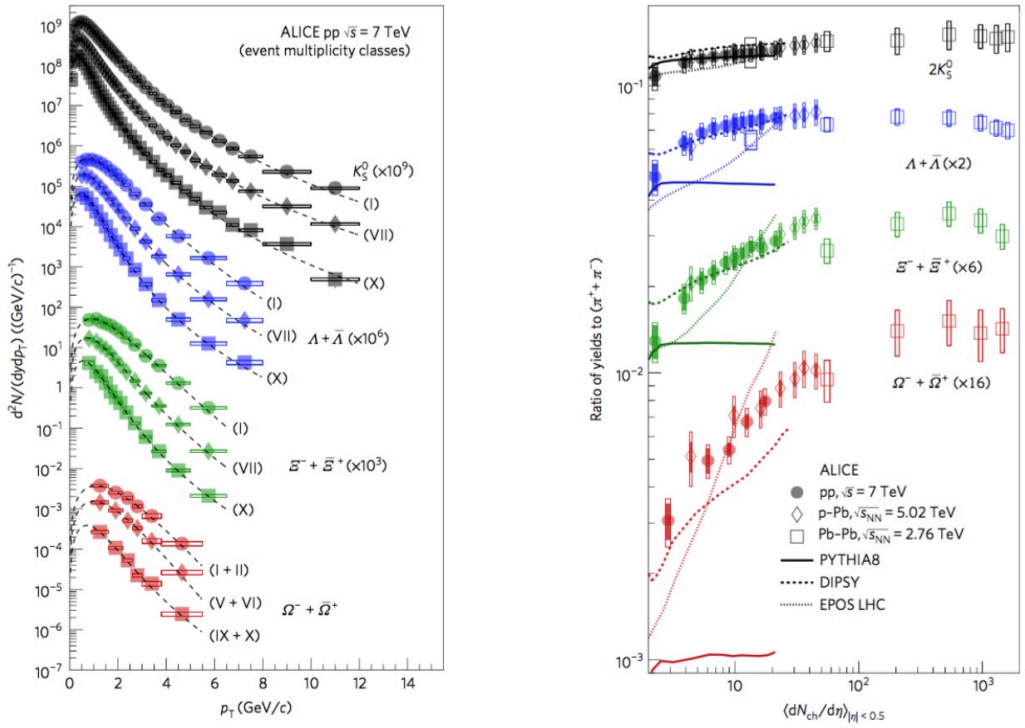

Figure 1.13: Left: p_{T}-differential yields of K^0_s, $\Lambda + \bar{\Lambda}$, $\Xi^+ + \Xi^-$, $\Omega^+ + \Omega^-$ measured at mid-rapidity in ALICE, for selected event classes, indicated by roman numbers, with decreasing multiplicity. Right: those p_{T}-differential yields to pions ratios as a function of $\langle \mathrm{dN_{ch}}/\mathrm{d}\eta \rangle$ in different collision systems, and compared with model predictions [12].

1.4.2.4 Jet quenching

When high transverse momentum (p_{T}) partons propagate inside the medium, they will undergo the energy loss by medium-induced gluon radiation and interac-

tions with the medium constituents. Experimentally, this phenomenon can be studied by the measurements of inclusive high-p_{T} hadron (jet) production, di-hadron azimuthal correlation, and di-jet energy imbalance.

high-p_{T} hadron

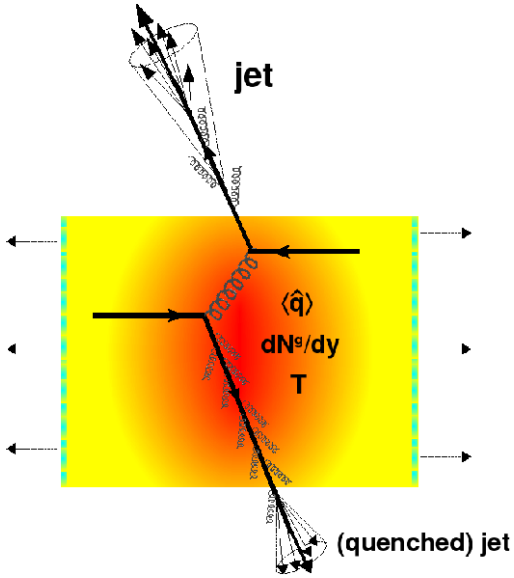

Figure 1.14: Jet Quenching sketch.

As shown in Fig. 1.14, high-p_{T} partons could fragment into two back-to-back hadron jets. When QGP is formed, one can "trigger" on a high transverse momentum jet, which will come from the "surface" of the QGP, and cross the medium with a small path-length, losing a small fraction of its energy. While the other jet will have a long path-length and be quenched strongly. Experimentally, the measurement of nuclear modification factor (R_{AA}) is the most common observable to study this effect, the ratio between yields measured in nucleus-nucleus collisions and binary-scaled nucleon-nucleon collisions defined as:

$$R_{\mathrm{AA}} = \frac{1}{< N_{\mathrm{coll}} >} \frac{\mathrm{d}N_{\mathrm{AA}}/\mathrm{d}p_{\mathrm{T}}}{\mathrm{d}N_{\mathrm{pp}}/\mathrm{d}p_{\mathrm{T}}} = \frac{1}{< T_{\mathrm{AA}} >} \frac{\mathrm{d}N_{\mathrm{AA}}/\mathrm{d}p_{\mathrm{T}}}{\mathrm{d}\sigma_{\mathrm{pp}}^{\mathrm{INEL}}/\mathrm{d}p_{\mathrm{T}}}, \tag{1.8}$$

where $N_{\mathrm{AA/pp}}$ is the p_{T}-differential yield in nucleus-nucleus/pp collisions, $< N_{\mathrm{coll}} >$ is the average number of binary nucleon-nucleon collisions, $< T_{\mathrm{AA}} >$ is the nuclear overlap function. R_{AA} is expected to be consistent with unity if no medium effects existed. Any deviations indicate the modification of the transverse momentum distributions of the hadrons caused by the medium. As shown in Fig. 1.15, ALICE has measured the nuclear modification factor R_{AA} in Pb–Pb collisions at $\sqrt{s_{\mathrm{NN}}} =$ 5.02 TeV for different particle species in different centrality classes [13]. A strong suppression can be found in the most central collisions, and the suppression decrease with the centrality increase, since the medium is hotter and denser in central collisions. At high p_{T} region, no significant particle species dependence can be found,

indicates that jet quenching will not introduce large modification depending on leading particle's species. At low p_{T}, the mass ordering effect can be attributed to the radial flow. While at intermediate p_{T}, not only the interplay between jet quenching and hydrodynamics is necessary, but also additional recombination processes should be taken into account, as already discussed in the previous subsection. Note that, beside the in-medium energy loss effect, several other effects should also take into account for nucleus-nucleus collisions, the PDFs is different between bounded and free nucleons, as well as cold nuclear matter effects such as k_{T} broadening in consequence of multiple scattering in the nucleus. More details about R_{AA} will be given also in the next Chapter.

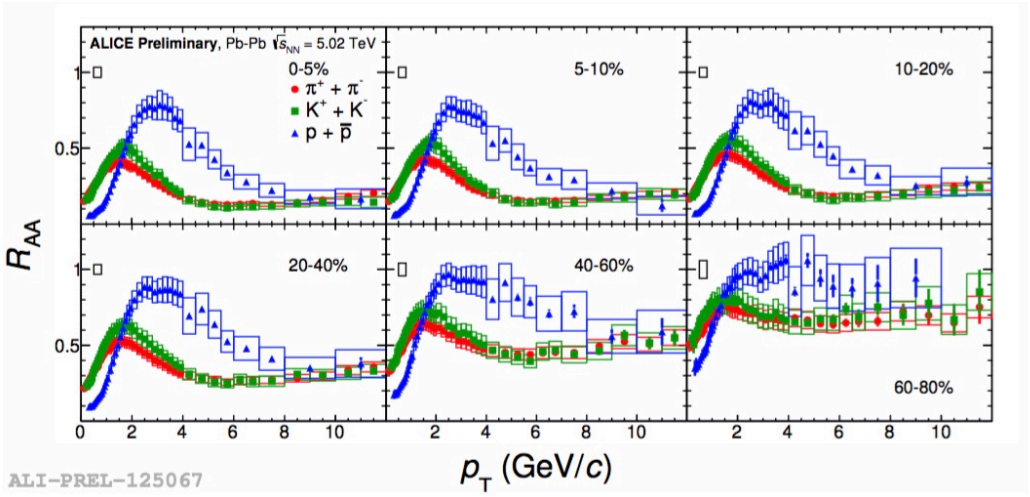

Figure 1.15: The nuclear modification factor R_{AA} measured by ALICE in Pb–Pb collisions at $\sqrt{s_{\mathrm{NN}}} = 5.02$ TeV for different particle species with different centrality classes [13].

di-hadron azimuthal correlation

The technique of two-particle correlations has been extensively used to characterize the properties of jet quenching, as it's sensitive to the remnants of the radiated energy and the medium response to the hard parton. For such an approach, one can select a particle from a certain p_{T} region named "trigger particle", then "associated particles" can be selected in another p_{T} region, often $p_{\mathrm{T}}^{assoc} < p_{\mathrm{T}}^{trig}$. The associated per-trigger yield can be measured as a function of the azimuthal angle difference($\Delta\varphi = \varphi_{\mathrm{trig}} - \varphi_{\mathrm{assoc}}$ or $\Delta\eta = \eta_{\mathrm{trig}} - \eta_{\mathrm{assoc}}$), expressed as below:

$$Y\left(\Delta\varphi, \Delta\eta\right) = \frac{1}{N_{\mathrm{trig}}} \frac{\mathrm{d}N_{\mathrm{assoc}}}{\mathrm{d}\Delta\varphi \mathrm{d}\Delta\eta} \tag{1.9}$$

Varying p_{T} region for trigger and associated particles can help to probe the interplay of soft and hard processes. At RHIC energy, PHENIX measured di-hadron correlation, per-trigger yield as a function of $\Delta\varphi$ various trigger and associated p_{T} in pp and 0-20% Au+Au collisions at $\sqrt{s_{\mathrm{NN}}} = 200$ GeV [14], as shown in Fig. 1.16.

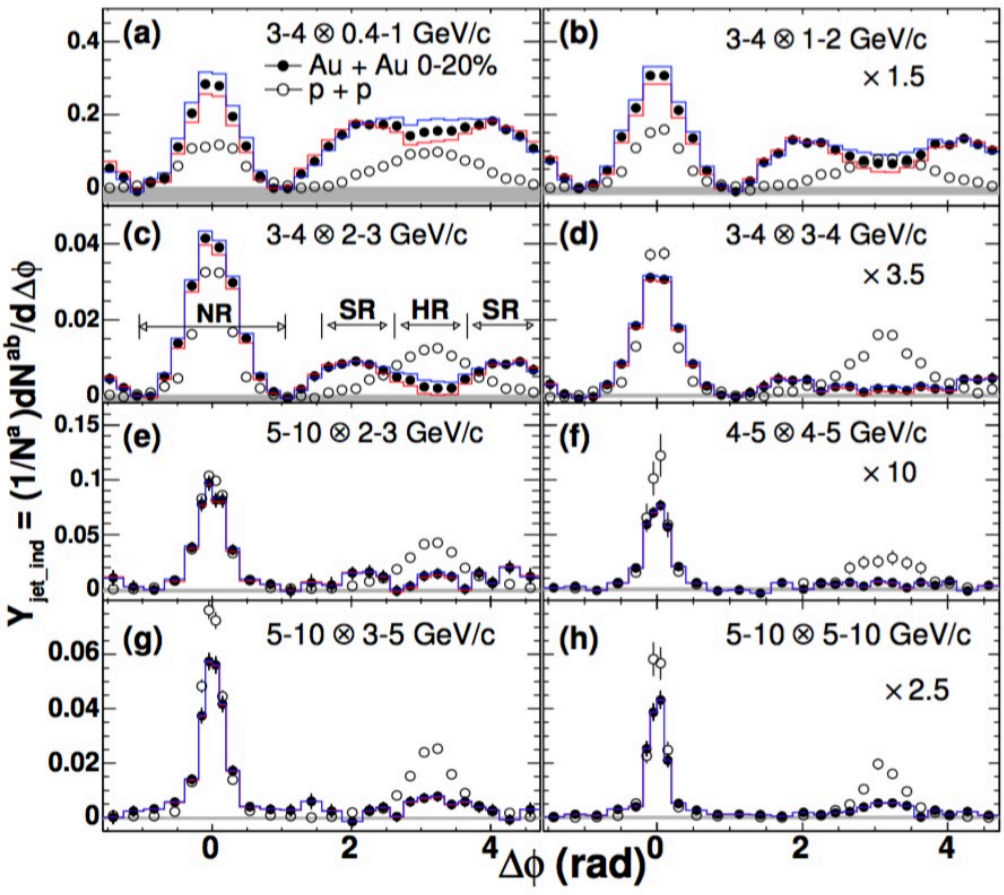

Figure 1.16: Per-trigger yield as a function of $\Delta\varphi$ various trigger and associated p_{T} in pp and 0-20% Au+Au collisions at $\sqrt{s_{\mathrm{NN}}} = 200$ GeV measured by PHENIX [14].

$\Delta\varphi around 0 and \pi$ defined as the near side and away side, respectively. In away side, with $p_{\mathrm{T}}^{assoc} > 2$ GeV/c, strong suppression can be found in Au+Au with respect to pp collisions, can be understood as the parton energy loss, with $p_{\mathrm{T}}^{assoc} < 2$ GeV/c, the distribution becomes broaden, even a double-shoulder structure appeared, which can be explained by different mechanisms such as Mach cone shockwave [63], Cherenkov radiation from the jet [64], large angle gluon radiation [65]. Later, the peak in near side was also found to be enhanced and broaden with low p_{T}^{assoc} and p_{T}^{trig} in Au+Au collision by PHENIX [66], may related to radiated gluons broaden by longitudinal flow [67] or radial flow and trigger bias [68]. With these, modification of the jet-like pair yields I_{AA} can be extracted, defined as the ratio of the integrated yields in AA over pp, expressed as:

$$I_{\mathrm{AA}} = \int_X J_{\mathrm{AA}}(\Delta\varphi)\mathrm{d}\Delta\varphi / \int_X J_{\mathrm{pp}}(\Delta\varphi)\mathrm{d}\Delta\varphi \tag{1.10}$$

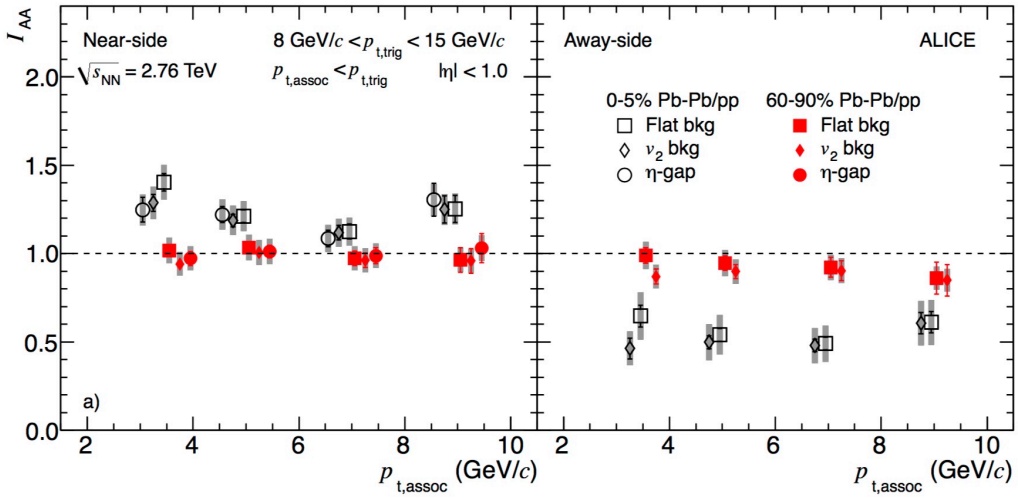

Figure 1.17: I_{AA} as a function of p_{T} measured by ALICE in central Pb–Pb collisions at $\sqrt{s_{\mathrm{NN}}} = 2.76$ TeV, in both near and away side, background subtracted in different scenarios: flat pedestal, v_2 subtraction and η-gap subtraction [15].

Where X is either the near side peak region or the away side peak region. At LHC energy, as shown in Fig. 1.17. I_{AA} as a function of p_{T} was measured by ALICE in central Pb–Pb collisions at $\sqrt{s_{\mathrm{NN}}} = 2.76$ TeV [15], in both near and away side, with background subtracted in different scenarios: flat pedestal, v_2 subtraction and η-gap subtraction. The enhancement in near side gives a hint of medium effects, and the strong suppression in away side is related to the parton energy loss. However, later it was understood that the subtraction of v_2 is not enough as the azimuthal correlations spanning a long-range in pseudorapidity is also affected by higher-order flow harmonics ($v_n, n > 2$), which originates from anisotropic pressure gradients with respect to the initial-state symmetry planes [69]. More details will be discussed in Chapter 4.

di-jet energy imbalance

Another approach to study the strong jet energy loss in the medium is measuring the asymmetry of di-jets in nucleus-nucleus collisions. A simple way is only focus on the balance between the highest p_{T} pair of jets which have the azimuthal angle separation $\Delta\phi = |\phi_1 - \phi_2| > \pi/2$, to avoid multi-jets in the final state. Then the asymmetry A_J of jet energy imbalance can be defined as:

$$A_J = \frac{E_{T1} - E_{T2}}{E_{T1} + E_{T2}} \tag{1.11}$$

Where E_{T1}, E_{T2} are the transverse energy of the back-to-back two jets. ATLAS measured centrality dependence of the asymmetry A_J in Pb–Pb collisions at $\sqrt{s_{\mathrm{NN}}}$ = 2.77 TeV [70], as shown in Fig. 1.18. In peripheral collisions, the di-jet asymmetry in Pb–Pb is similar to that in pp collisions. While towards the central collisions, the distribution in Pb–Pb develops a different shape with respect to pp: the peak from zero shift to a higher asymmetry values, and the asymmetry distribution broadens, which can be attributed to the jet energy loss in the QGP medium.

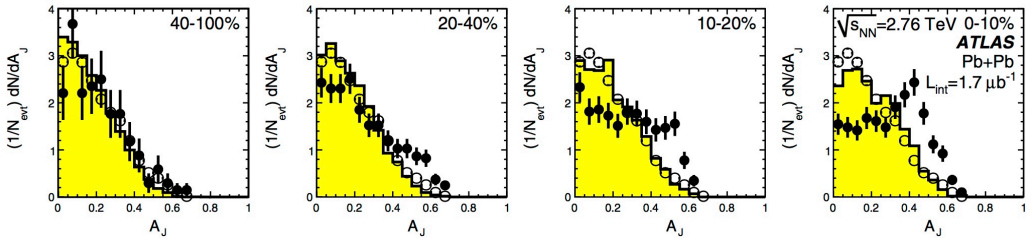

Figure 1.18: Di-jet asymmetry distributions for Pb–Pb collisions at $\sqrt{s_{\mathrm{NN}}}$ = 2.77 TeV (points) and unquenched HIJING with superimposed PYTHIA di-jets (solid yellow histograms), as a function of collision centrality. And proton-proton data shown as open circles 1.18.

1.4.2.5 Quarkonium production

Quarkonium, which refers to the bound state of a $c\bar{c}$ (charmonium) pair or a $b\bar{b}$ (bottomonium) pair, produced at very initial state in hard scatterings, is considered as effective probe of the QGP formation.

Based on the lattice QCD prediction, J/Ψ production will be suppressed due to the Debye screening of the quark-antiquark potential in the deconfined medium, which will become stronger as the QGP temperature increases [71]. This was first measured by NA38, NA50 and NA60 experiments at the SPS [72], as shown in Fig. 1.19. The measured J/Ψ yield is normalized the expected yield based on the ordinary nuclear absorption in different systems, the ratios are presented as a function of energy density ε. When $\varepsilon < 2$ GeV/fm^3, the measured yield is at the similar magnitude than the expected one, while in Pb–Pb collisions, $\varepsilon > 2$ GeV/fm^3, a large deviation can be found between these two, and the J/Ψ have a stronger suppression

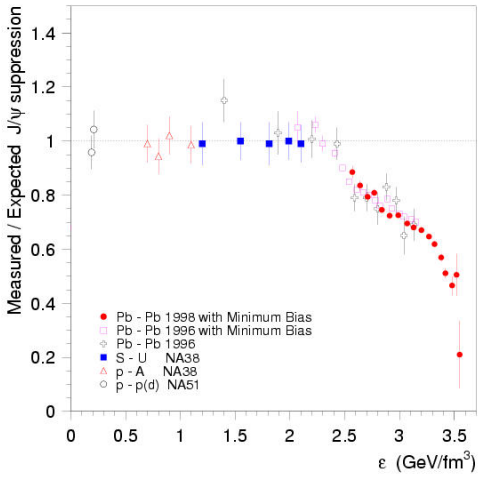

Figure 1.19: Ratio between measured J/Ψ yield and expected yield as a function of energy density ε of the medium.

with the increase of ε. When the collision energies increase to the LHC energy, a reduced suppression was observed by ALICE [16]. Fig. 1.20, shows J/Ψ R_{AA} as a function of centrality (left) and transverse momentum (right) measured in Pb–Pb collisions by ALICE at $\sqrt{s_{\mathrm{NN}}}$ = 2.76 TeV [16], 5.02 TeV [17], compared with the measurements at RHIC energy in Au–Au collisions at $\sqrt{s_{\mathrm{NN}}}$ = 200 GeV [18]. On the left, a smaller suppression is found at higher collision energy, and ALICE results show no significant suppression when $\langle N_{\mathrm{part}} \rangle$ is larger than 70. On the right, ALICE R_{AA} results show a factor of up to four higher compared to the PHENIX one at low p_{T} region. These can be explained by the (re)combination effect which form low p_{T} J/Ψ mesons form deconfined c and $\bar{c}$ quarks.

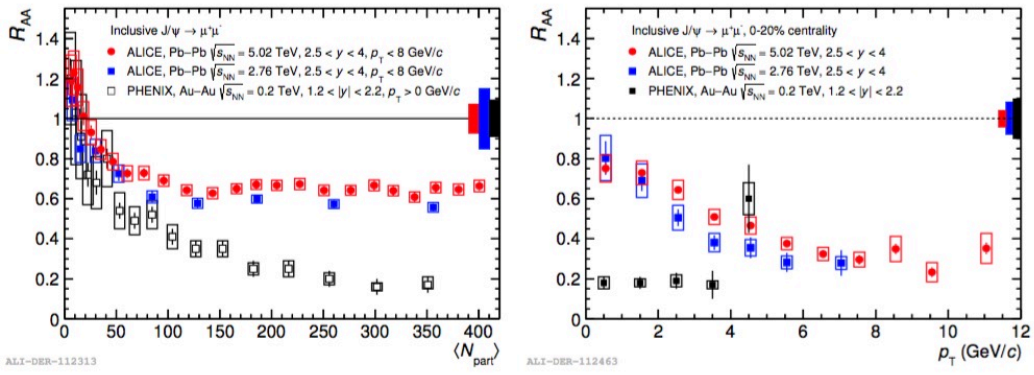

Figure 1.20: J/Ψ R_{AA} as a function of centrality (left) and transverse momentum (right) in nucleus-nucleus collisions measured by ALICE at 2.76 TeV [16], 5.02 TeV [17], compared with the PHENIX result at 200 GeV [18].

Chapter 2

Heavy Flavours

The heavy quarks (charm (c) and beauty (b)) are powerful probes of the Quark-Gluon Plasma (QGP) formed in high-energy heavy-ion collisions. They are produced in hard scattering processes on a timescale (0.1, 0.02 fm/c for charm and beauty) shorter than the QGP formation time (0.3-1.5 fm/c at LHC energy [73]) and the long lifetime allows them to experience the whole system evolution interacting with the medium constituents. What's more, due to their large masses, heavy flavours are also effective tools to test the perturbative QCD predictions. In this Chapter, after a quick description of heavy flavour production in pp collision in Sec. 2.1, cold nuclear effects in p–pb collisions, in-medium energy loss and modification of hadronisation in Pb–Pb collisions will be focused in Sec 2.2. The experimental results and corresponding theoretical calculations will also be discussed in each section.

2.1 Open Heavy Flavour Production in pp collision

In proton-proton collisions (AB $\rightarrow h$), the production cross section of a high-p_{T} hadron can be calculated using the QCD "factorisation theorem" [74]:

$$\sigma^{hard}_{AB\rightarrow h} = f_{a/A}(x_1, Q^2) \otimes f_{b/B}(x_x, Q^2) \otimes \sigma^{hard}_{ab\rightarrow c}(x_1, x_2, Q^2) \otimes D_{c\rightarrow h}(z, Q^2) \quad (2.1)$$

Where $f_{a/A}(x_1, Q^2)$ is the parton distribution function (PDF), which is the non-perturbative dynamic parameter of the proton, represents the possibility of generating a parton which flavour a with a certain momentum fraction x_1(Bjorken x), at a given transfer momentum Q^2. $\sigma^{hard}_{ab\rightarrow c}(x_1, x_2, Q^2)$ is the partonic cross section. $D_{c\rightarrow h}(z, Q^2)$ is the fragmentation function (FF), which respects the probability of the parton c fragments into a hadron h with the fraction z of the initial parton momentum.

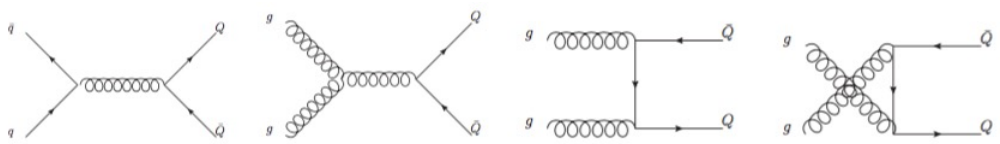

Figure 2.1: Examples of leading-order Feynman diagrams for heavy-quark pair production.

For heavy-quark production, there are two main processes at leading order (LO) based on perturbative theory: $q\bar{q} \rightarrow Q\bar{Q}$ and $gg \rightarrow Q\bar{Q}$, as shown in Fig.2.1. Based on the pQCD calculations, the scale factors, μ_γ introduced for renormalising the strong coupling α_s, and μ_f used for the cross section factorising the long and small distance effects, usually can be assigned as the order of the quark mass. For heavy quarks, the masses ($m_c \simeq 1.5$ GeV/c^2, $m_c \simeq 4.5$ GeV/c^2) are larger than Λ_{QCD}, so pQCD approach is accessible down to low-p_{T}, thus several pQCD approaches have been develop to calculate heavy flavour production, such as GM-VFNS and FONLL.

General-Mass Variable-Flavour-Number Scheme(GM-VFNS) [75] is the scheme, which is applicable in the whole p_{T} region by unifying Fixed Flavour Number (FFN) scheme and Zero-Mass Variable-Flavour-Number Scheme (ZM-VFNS). at low p_{T}, FFN can be used by assuming only light flavour quarks are active in the initial state, while heavy quarks can only appear in the finial state and never act as a parton. While at large p_{T}, under the framework of ZM-VFNS, conventional quarks consider as massless parton, heavy quarks treats as additional sources absorbed into the PDF and FF.

Fixed-Order-Next-to-Leading-Log (FONLL) [76], is another approach, that combines Next-Leading-Order (NLO) calculation for low p_{T} and Next-To-Leading-Log (NLL) method for high p_{T} region, the final cross section can be expressed as:

$$\mathrm{d}\sigma_{\mathrm{FONLL}} = \mathrm{d}\sigma_{\mathrm{FO}} + (\mathrm{d}\sigma_{\mathrm{RS}} - \mathrm{d}\sigma_{\mathrm{FOM0}}) \times \mathrm{G}(\mathrm{m_Q}, \hat{\mathrm{p}}_{\mathrm{t}}) \tag{2.2}$$

Where $\mathrm{d}\sigma_{FO}$ is based on the NLO calculation at low p_{T}, where heavy quarks are massive at fixed-order (FO). $\mathrm{d}\sigma_{RS}$ is calculated by NLL method assuming massless heavy quarks at high p_{T}. and the fixed terms $\mathrm{d}\sigma_{FOM0}$ appearing in FO calculations need to be subtracted from the NLL in the massless limit to avoid double counting, and $G(m_{\mathrm{Q}}, \hat{p}_{\mathrm{t}})$ is a matching function, the limit is

$$\lim_{m_{\mathrm{Q}}/\hat{p}_{\mathrm{t}} \to 0} G(m_{\mathrm{Q}}, \hat{p}_{\mathrm{t}}) = 1 \tag{2.3}$$

Both these two calculations which based on NLO theory can have a good agreement with experimental measurements, as an example shown in Fig. 2.2. p_{T}-differential production cross section of prompt D^0 mesons at mid-rapidity in pp collision at $\sqrt{s} = 7$ TeV by ALICE, compared with theoretical predictions from FONLL (left) [77] and GM-VFNS (right) [78]. the theoretical models are consistent with data within uncertainties at the full p_{T} region, although the data points located at the upper band of FONLL and lower band of GM-VFNS uncertainties. At the same time, models based on NLO theory can also calculate the cross sections for charmed baryon, such as Λ_{c}. Fig. 2.3, shows ALICE measurements [79] about Prompt Λ_{c}^+ baryon p_{T}-differential cross section via different decay modes in pp collisions at $\sqrt{s} = 7$ TeV, compared with GM-VFNS (blue) [78] and POWHEG (orange) [80] predictions. POWHEG is based on the NLO theory and interfaced with PYTHIA for the parton shower simulation and hadronisation. Obviously from the plots, the models underestimate the data, so something is missing when reproduces the charmed baryon results as the NLO theory can give a promising prediction on

charmed meson results. One of the possible reason is that the fragmentation functions used in these calculations were tuning from low energy e^+e^- data, gives the hint that the fragmentation functions may not be universal, which has already been found and discussed for light flavour sectors in [81].

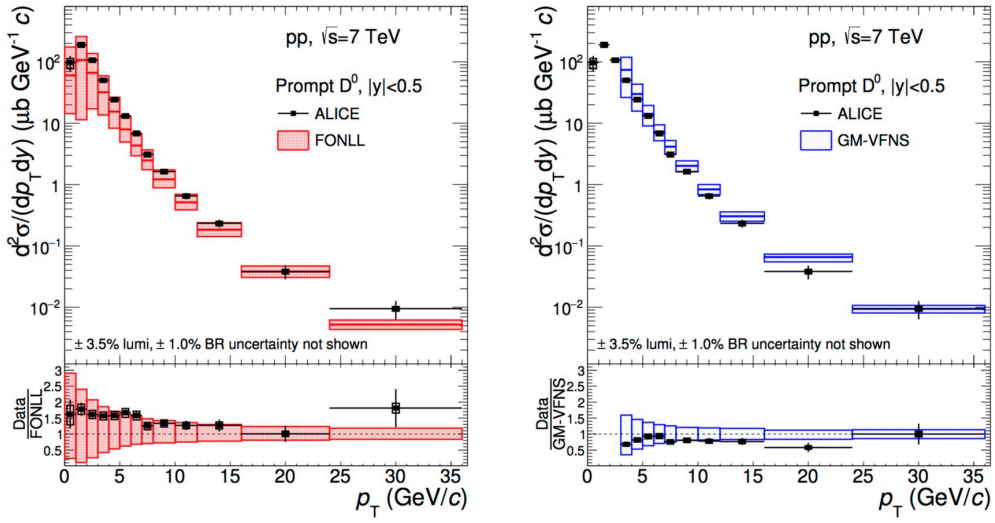

Figure 2.2: p_{T}-differential production cross section of prompt D^0 mesons at mid-rapidity in pp collision at $\sqrt{s} = 7$ TeV by ALICE [19], compared with theoretical predictions from FONLL (left) and GM-VFNS (right).

2.2 Open Heavy Flavour Production in p–Pb and Pb–Pb collisions

Due to the presence of nuclei, related effects should take into account for proton-nucleus and nucleus-nucleus collisions. In nucleus-nucleus collisions, heavy quarks will lost their energy in the medium via elastic collisions and inelastic processes, called hot nuclear matter effects. While other processes such as modification of the nuclear parton distribution function or multiple scatterings of partons, named cold nuclear matter(CNM) effects are not the consequence of interacting with QGP, which are supposed breaking the binary scaling in nucleus-nucleus collisions, participating also in proton-nucleus collisions.

2.2.1 Cold nuclear matter effects

In heavy-ion collisions, nucleons are in the bounded state in which the properties are different from the free ones due to the interactions and correlations among them. The nuclear modification is assumed to be sensitive to the Bjorken-x regions that

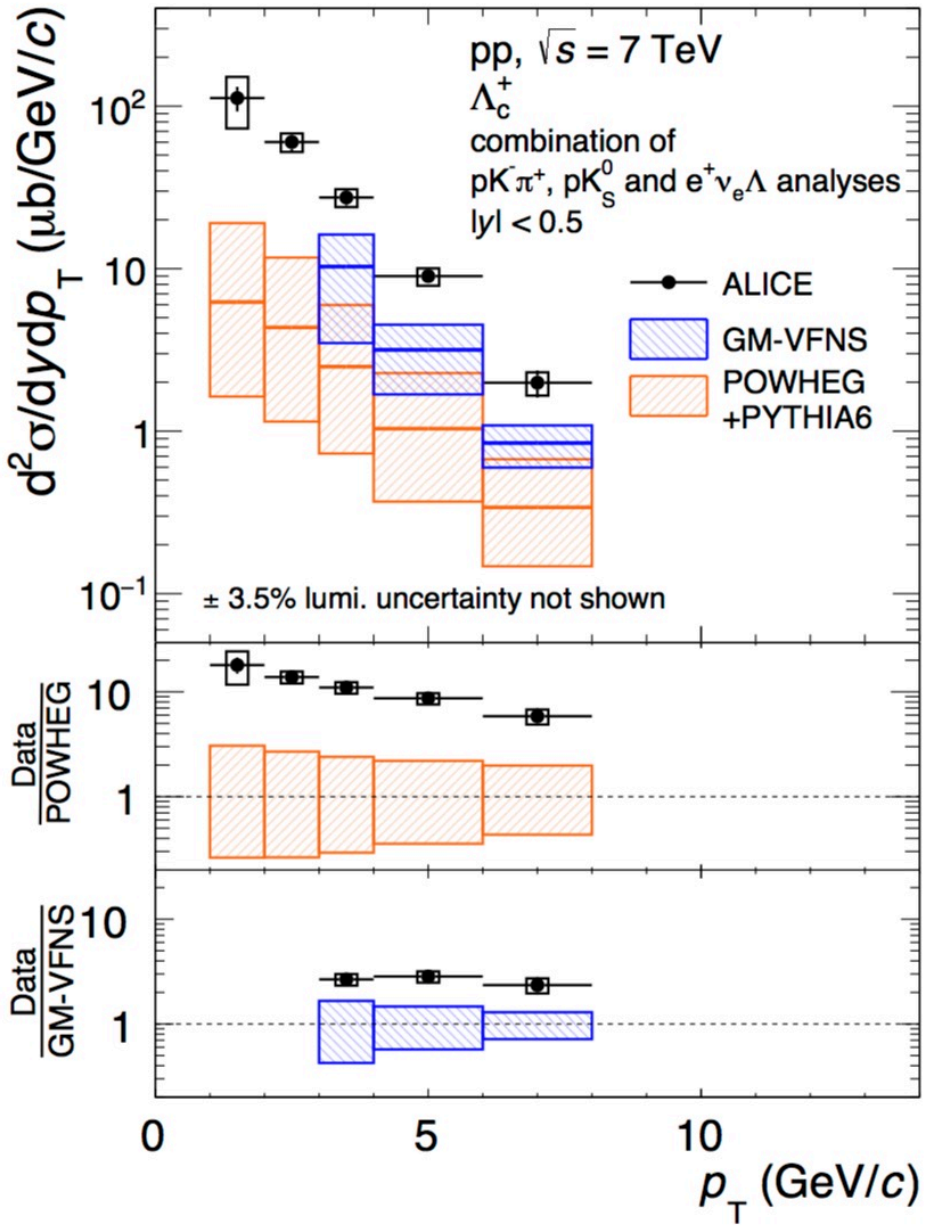

Figure 2.3: Prompt Λ_c^+ baryon p_T-differential cross section via different decay modes in pp collisions at $\sqrt{s} = 7$ TeV by ALICE, compared with GM-VFNS calculations and POWHEG event generator.

can be quantified by the ratio of the PDFs between bounded and free nucleons:

$$R_i^A(x, Q^2) = \frac{f_i^A(x, Q^2)}{f_i^N(x, Q^2)}, \tag{2.4}$$

Where i is the parton specie index (valence, sea quark and gluon), $f_i^A(x, Q^2)$ and

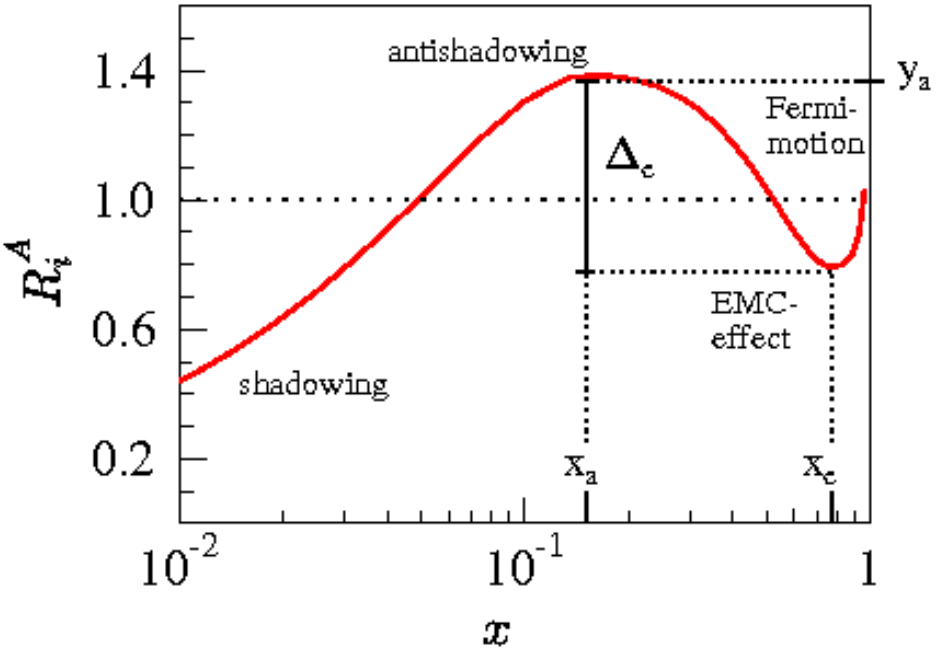

Figure 2.4: a sketch of R_i^{A} as a function of Bjorken-x.

$f_i^{\mathrm{N}}(x, Q^2)$ are the PDFs of nucleons in nucleus and free nucleons respectively. As shown in Fig. 2.4, different cold nuclear effects covers the whole Bjorken-x region: $x \lesssim 0.1$, shadowing effect, $R_i^{\mathrm{A}}(x, Q^2) < 1$. $0.1 \lesssim x \lesssim 0.3$, anti-shadowing effect, $R_i^{\mathrm{A}}(x, Q^2) > 1$. $0.3 \lesssim x \lesssim 0.8$, MC effect, $R_i^{\mathrm{A}}(x, Q^2) < 1$. While when $x \to 1$, Fermi motion effect, $R_i^{\mathrm{A}}(x, Q^2) > 1$. At LHC energy, as reported in [82], charm production corresponds to the Bjorken $x \approx 10^{-4}$, related to the region affected by shadowing effect. That's the reason why the measurements of charm R_{AA} in LHC is less than 1 at low p_{T} region. Usually, nuclear PDFs can be obtained by global fits of several experimental data. Fig. 2.5, shows the comparison of the average valence, sea-quark and gluon nuclear modifications at $Q^2 = 10$ GeV^2 among different global fit models, EPPS16 [83], EPS09 [84], DSSZ [85]. The latest EPPS16 with less biased, not only constrained by deep inelastic lepton-nucleus scattering (DIS), Drell-Yan (DY) di-lepton production and inclusive pion production measured at RHIC, but also including the 2013 data from LHC, especially CMS di-jet data, which have more constraints for the gluons than others.

Another CNM effect is the Cronin Effect, or called k_{T} broadening, which occurs at intermediate p_{T} region (2-5 GeV/c), originates from multi parton scatterings. It can be understood as the partons from the nucleon suffers several elastic scatterings before the hard inelastic scattering, which will lead the partons taking an

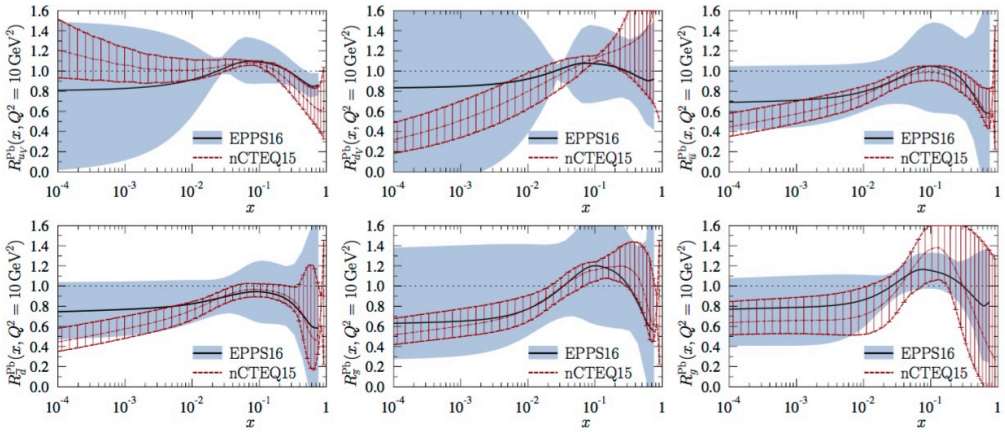

Figure 2.5: the comparison of the average valence, sea-quark and gluon nuclear modifications at $Q^2 = 10$ GeV^2 among different global fit models.

extra momentum along the transverse plane, thus the hadron p_{T} spectra will be broaden. Commonly, the nuclear modification factor is usually measured at a certain pseudorapidity, this broadening will lead the reduction of the measured yield in nucleus–nucleus collisions, that's why we saw the enhancement of R_{AA} at such a p_{T} region.

Experimentally, these CNM effects can be tested by the measurements of nuclear modification factor. The nuclear modification factor of muons from heavy-flavour hadron decays as a function of p_{T} for p–Pb collisions at $\sqrt{s_{\mathrm{NN}}} = 5.02$ TeV measured by ALICE at forward and backward rapidity [86], as shown in Fig. 2.6. Note that, forward rapidity is located at the Bjorken-x from $5 \cdot 10^{-6}$ to 10^{-2}, and backward rapidity correspond to the range from 10^{-3} to 10^{-2}, which are sensitive to the CNM effects at low Bjorken-x. From the plots, at backward rapidity, R_{pPb} is larger than unity with a significance around 2σ at low p_{T} and compatible with unity at high p_{T}. At forward rapidity, it's compatible with unity within uncertainties in the whole p_{T} region. the data can be reproduced by the model predictions within uncertainties either based on pQCD calculations including nPDFs from EPS09 [87], or CNM effects with shadowing, k_{T} broadening and energy loss in cold nuclear matter [88], or the model considering incoherent multiple scattering effects in both initial and finial state [89]. At the same time, the models mentioned before with only CNM effects can also describe well ALICE D meson R_{pPb} result [90] at $\sqrt{s_{\mathrm{NN}}}$ = 5.02 TeV, except the calculation by Kang et al., which is disfavoured by the data at low p_{T}, details can be found in the left panel of Fig. 2.7. In addition, other models with only CNM effects can also reproduce the data: the calculation based on Color Glass Condensate formalism [91] and FONLL calculation [92] with EPPS16 NLO nuclear modification. The results imply that CNM effects are very small and dominated at low p_{T} region, however with current uncertainties of data, it's still hard to discriminate different CNM effects inside the models. Nevertheless, transport

models Duke [93] and POWLANG [94] also have the predictions for the D mesons results, they both assume a "small-size" QGP formed in p–Pb collisions, based on the Langevin approach for the transport of heavy quarks through an expanding deconfined medium described by hydrodynamics. As the interplay of CNM effects and interactions of charm quarks with the radially expanding medium, their results show a structure with a maximum at $p_{\mathrm{T}} \approx 2.5$ GeV/c, and followed by a moderate suppression at higher p_{T} which is disfavoured by the data.

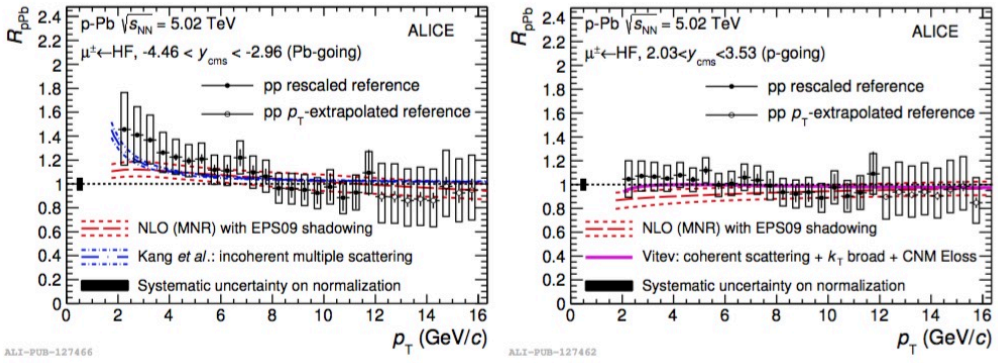

Figure 2.6: The nuclear modification factor of muons from heavy-flavour hadron decays as a function of p_{T} for p–Pb collisions at $\sqrt{s_{\mathrm{NN}}} = 5.02$ TeV measured by ALICE at forward and backward rapidity, and the comparison with different model predictions.

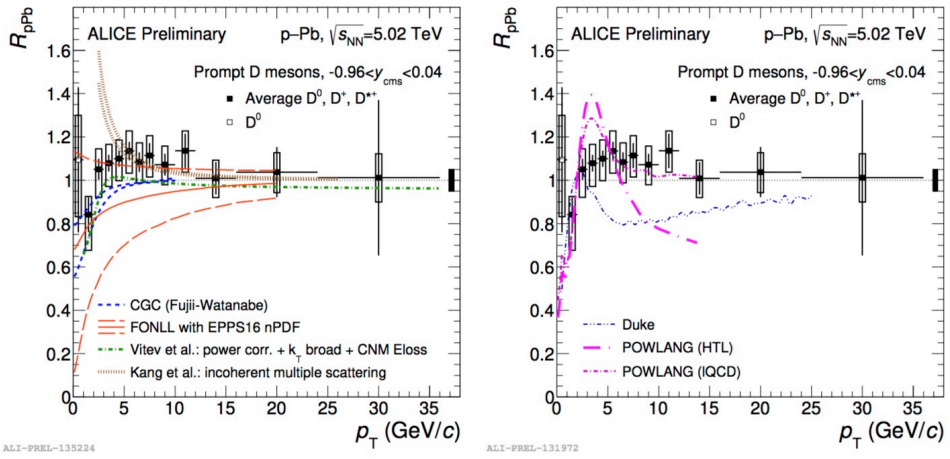

Figure 2.7: The nuclear modification factor of prompt D mesons as a function of p_{T} for p–Pb collisions at $\sqrt{s_{\mathrm{NN}}} = 5.02$ TeV measured by ALIEC, and the comparison with different model predictions either with only CNM effect (left) or transport models (right).

2.2.2 In-medium energy loss

When a high transverse momentum parton goes across the QGP, it will lose its energy via either collisional or radiative processes, collisional energy loss is dominated at low p_{T}, while radiative energy loss is often occurred at high p_{T}. The properties of energy loss depend on the characteristics of the particle (energy E and mass m) and the plasma (temperature T, particle-medium interaction coupling α_s and thickness L).

The energy loss in QCD is different compared with that in QED, as the gluon can interact with each other. In the medium, considering the different coupling of quarks and gluons, the relative strengths of the three QCD vertices($g \to qg$,$g \to gg$, $g \to q\bar{q}$) can be described by the structure (Casimir factors) of the gauge SU(3) group. the Casimir factor $C_R = 3$ for the process $g \to gg$, and $C_R = 4/3$ for $g \to qg$, and $C_R = 1/2$ for $g \to q\bar{q}$.

2.2.2.1 Collisional energy loss

Collisional energy loss is in the $2 \to 2$ process, which is due to the parton elastic scatterings with the medium constituents. The average energy loss in one of such elastic scattering can be expressed as following:

$$\left\langle \Delta E_{coll}^{1scatt} \right\rangle \approx \frac{1}{\sigma T} \int_{m_D^2}^{t_{max}} t \frac{\mathrm{d}\sigma}{\mathrm{dt}} \mathrm{dt}, \tag{2.5}$$

Where T is the temperature of the medium, σ is the integrated cross section of particle-medium interaction, t is the squared momentum transfer and m_D is the Debye mass. If one considers the integral limits from Debye mass squared to the total energy in the scattering $t_{max} = s$ - ET (E is the energy of initial parton), the parton-parton t-different cross section can be written as $\frac{\mathrm{d}\sigma}{\mathrm{dt}} \approx C_R \frac{4\pi\alpha_s^2(t)}{t^2}$. For heavy quark, if $E \gg M^2/T$, the parton collisional energy loss can be calculated as $-\frac{\mathrm{d}E_{coll}}{dl} \mid_Q = -\frac{\mathrm{d}E_{coll}}{dl} \mid_q -\frac{2}{9} C_R \pi T^2 \left[\alpha_s(m_Q^2) \alpha_s(ET)) ln(\frac{ET}{m_Q^2}) \right]$.

What's more, the multiple scatterings of the heavy quarks can be treated as brownian motion and be described by the Langevin equation [95]:

$$\frac{\mathrm{d}\vec{p}}{\mathrm{d}t} = -\eta_D(p)\vec{p} + \vec{\xi}, \tag{2.6}$$

Where $\vec{\xi}$ is the noise term depending on the heavy quark momentum, the diffusion coefficient D_s can be calculated which is related to the momentum space diffusion coefficients via:

$$D_s = \frac{T}{M\eta_D} = \frac{2T^2}{\kappa}, \tag{2.7}$$

It's the only free parameter in the Langevin framework, as $\hat{q} = 2\kappa C_A / C_F$ (C_A and C_F are the colour factors of quarks and gluons), thus the evolution of heavy quarks can be simulated.

2.2.2.2 Radiative energy loss

As described in the BDMPS model [96], when a fast parton goes across the medium along its path length, the gluons in the hard parton wave function will pick up transverse momentum k_{T}, then it will decohere and be emitted. The characteristic of gluon radiated frequency w_c can described as:

$$w_c = \hat{q}L^2/2, \tag{2.8}$$

Where $\hat{q}$ is the transport coefficient of the medium, and L is the path length. For the case when $w \ll w_c$, the distribution of energy w of the radiated gluons can be written as:

$$w\frac{\mathrm{d}I}{\mathrm{d}w}\ \frac{2\alpha_s C_R}{\pi}\sqrt{\frac{w_c}{2w}}, \tag{2.9}$$

Where C_R is the Casimir factor, thus the average energy loss of the patron can be written as

$$\langle \Delta E \rangle = \int_0^{w_c} w\frac{\mathrm{d}I_{rad}}{\mathrm{d}w}\mathrm{d}w \propto \alpha_s C_R w_c \propto \alpha_s C_R \hat{q} L^2, \tag{2.10}$$

From this formula, it implies the the average energy loss doesn't depend on the initial patron but on C_R, which means larger energy loss for gluons than for quarks. Nevertheless, for heavy quarks, the probability of gluon radiation will be suppressed at small angle along the quark direction when the angle $\Theta_0 < m_Q/E$, known as the dead-cone effect [97]. Taking both into account, the hierarchy of the average radiative energy loss is:

$$\langle \Delta E_g \rangle > \langle \Delta E_q \rangle > \langle \Delta E_c \rangle > \langle \Delta E_b \rangle\,, \tag{2.11}$$

Despite smaller energy loss for charm quark than light quark, due to the hard initial distribution of charm quarks, the charm and light quark suppressions are expected to be similar. In this scenario, one can predict prompt D meson R_{AA} should have larger suppression than charged particle's, as prompt D meson are composed of charm quark, light hadrons are composed of both light quarks and gluons. However, ALICE measurements [42] shows similar results for these two at high p_{T} for Pb–Pb collisions at $\sqrt{s_{\mathrm{NN}}} = 2.76$ TeV, which is the well know **Heavy flavour puzzle at LHC**. This can be explained as the charged particle suppression at high p_{T} is dominant by light quark and the harder initial distribution of charm quark, described in [98].

2.2.3 heavy flavour in medium modification of hadronisation

The final hadron yield in heavy ion collision, not only depends on the energy loss mechanisms in the medium mentioned above, but also hadronisation properties. An unique hadronisation mechanism other than fragmentation has been come up, called coalescence or recombination, which describes the phenomena that when quarks are close to each other in position and momentum space, they will coalescence into hadron [99]. This mechanism will have a significant effect at low and intermediate p_{T} region. The measurements of the Λ_{c}^{+} and $\mathrm{D_s}$ are effective probes of this phenomena.

As a strangeness enriched environment will be produced in QGP, the probability of in-medium hadronisation of charm quarks coalescence with light quarks will be increased, thus it's expected an enhanced D_s in Pb–Pb collisions. In this scenario, Λ_c^+ production is also predicted to be enhanced, what's more, if light di-quark bound states exist QGP [100], charm quarks will also recombine with ud, which will lead a further enhancement of Λ_c^+ production. Fig. 2.8, shows spectra of (a) Λ_c and (b) D_0, and (c) the ratio Λ_c/D^0 in midrapidity for central Au+Au collisions at $\sqrt{s_{NN}}$= 200 GeV [101]. Solid lines are for the three-quark model and dashed lines are for the diquark model, compared with results from PYTHIA calculation. The calculation from PYTHIA includes pure thermal model, while in coalescence model, they use thermal initial momentum distributions of light quark and di-quark, and heavy quark in pp collisions at the same energy. In addition, energy loss, resonance and fragmentation processes are also taken into account. The Λ_c/D^0 baryon-to-meson ratio in coalescence models shows a strong enhancement compared with PYTHIA calculation, and the three-quark model calculation(considering three-body collisions, c, u, d, without di-quark state) shows a significant further enhancement compared with di-quark model(two-body collisions with ud di-quark state) at $p_T < 6$ GeV.

Experimentally, as shown in Fig 2.9, on the left panel, STAR has measured the Λ_c/D^0 baryon-to-meson raito in Au+Au collisions at $\sqrt{s_{NN}}$= 200 GeV in 10-60% centrality class for the bin $3 < p_T < 6$ GeV/c [20], the ratio is very high and around 1 within uncertainty. on the right, later, ALICE has also measured this ratio in Pb–Pb collisions at $\sqrt{s_{NN}}$= 5.02 TeV in 0-80% centrality class for a higher p_T interval ($6 < p_T < 12$ GeV/c), the value is similar with STAR's result, and hinting of the enhancement with respect to the measurements in pp and p–Pb collisions. However, when consulting the the models from different system and energy [101, 102, 103, 29], they tend to underestimate the data for the same p_T interval, further understanding is needed for such a process.

Several theoretical model calculations have been developed to describe the mechanisms discussed above. Mainly they can divide into two groups: pQCD-based models which use pQCD-inspired calculations to describe the energy loss, the other is the transport models which including the heavy quarks transports through the medium can heavy quarks are characterized by spatial diffusion coefficient. the main ingredients in these models are energy loss(including radiative and collisional), hadronisation via vacuum fragmentation and/or recombination, hydro-dynamic expansion and and CNM effects.

The examples of pQCD-based models are:

- CUJET3.0 [34]: It's improved model based on CUJET2.0 (pQCD calculation), including some non-perturbative chromodynamical features to describe the QCD confinement cross-over phase transition. In this model, it considers the energy loss mechanism(including radiative and collisional), but not the recombination, hydrodynamic and nPDF.

- Djordjevic [31]: Similar with CUJET3.0, this model also concerns the dynamical energy loss formalism, including the nPDF.

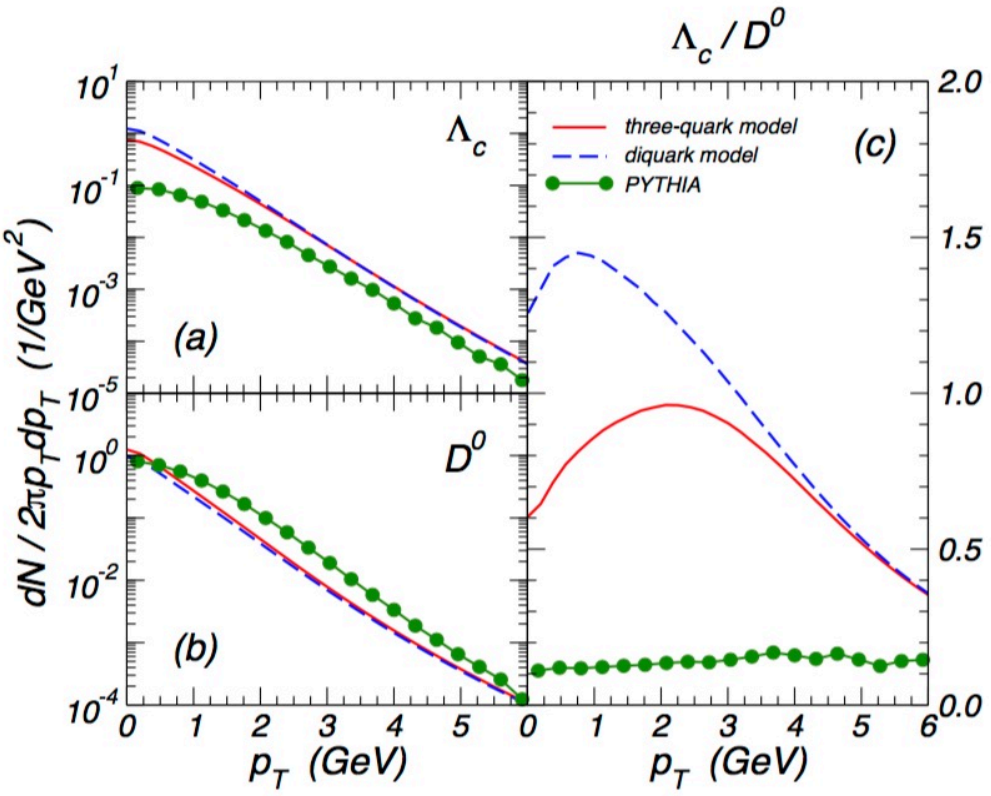

Figure 2.8: Spectra of (a) Λ_c and (b) D^0, and (c) the ratio Λ_c/D^0 in midrapidity for central Au+Au collisions at $\sqrt{s_{\rm NN}}$= 200 GeV. Solid lines are for the three-quark model and dashed lines are for the diquark model, compared with results from PYTHIA calculation.

- SCET [39]: Aiming to describe the interactions of hard probes with the QCD medium by including a Glauber mode that describes the interaction of highly energetic partons with the QCD medium, the medium interactions is described by the effective field theory which means the association and dissociation will happen inside the medium.

- MC@sHQ+EPOS [36]: Using the pQCD to calculate the collisional and radiative energy loss, adding a 3 + 1 d fluid dynamically expanding plasma given from EPOS initial conditions. The evolution of the heavy quarks is sampled by the Boltzmann equation. The hadronization of the heavy quarks via coalescence and fragmentation.

Selected transport models are:

- BAMPS [33]: A partonic transport model based on the Boltzmann approaching. It includes collisional energy loss but lacks radiative energy loss processes with a correction factor applied to the binary cross section. Hadronization is implemented via vacuum fragmentation functions.

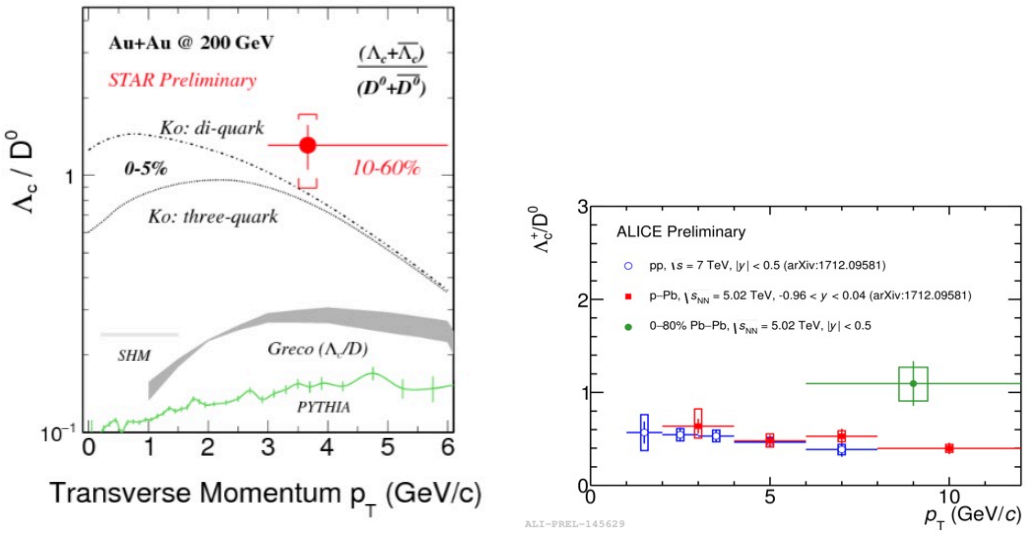

Figure 2.9: Left: Λ_c/D^0 baryon-to-meson raito in Au+Au collisions at $\sqrt{s_{NN}}$= 200 GeV in 10-60% centrality class by STAR [20]. Right: Λ_c/D^0 baryon-to-meson raito in Pb–Pb collisions at $\sqrt{s_{NN}}$= 5.02 TeV in 0-80% centrality class by ALICE, compared with the measurements in pp and p–Pb collisions.

- LBT [35]: It's based on the Langevin equation. In addition to elastic scatterings, the component about radiative energy loss is treated by considering gluon radiation as an additional force term. The space-time evolution of the medium is modeled using a viscous hydrodynamic simulation. the charm recombination process is also included.

- PHSD [37]: The degrees-of-freedom for the QGP phase are massive strongly-interacting quasiparticles. The masses of the dynamical quark and gluon in the QGP are distributed according to spectral functions whose pole positions and widths, respectively, are defined by the real and imaginary parts of their self-energies. The gradient of the potential energy density with respect to the scalar density generates a repulsive force in relativistic heavy-ion collisions and plays an essential role in reproducing experimental flow data and transverse momentum spectra. In the QGP, the charm will interact with off-shell partons and finally are hadronized via fragmentation or coalescence if the energy density is close to the critical energy density for the crossover transition.

- POWLANG [38]: Describes collisional energy loss using the Langevin equation and includes a viscous hydrodynamic expansion of the medium. The transport coefficients are evaluated in a pQCD approach for hard scatterings and with hard-thermal-loop calculations for soft processes. Also in this model, hadronization is implemented via vacuum fragmentation functions without recombinations.

- TAMU [40]: Is based on the Langevin approach, which includes only collisional energy loss and a hydrodynamic medium evolution. The transport coefficients are calculated with a non perturbative T-matrix approach, which includes resonances that transfer momentum from the heavy quark to the medium constituents. the process of charm recombination with light quark in the medium is also implemented.

ALICE preliminary results [21] about non-prompt D mesons at $\sqrt{s_{\rm NN}} = 5.02$ TeV in 0-10% centrality class Pb–Pb collisions are shown in Fig. 2.10, and compared with pQCD-based models (left panel) and transport models (right panel). In general, pQCD-based model can have a good description of the measurements of $R_{\rm AA}$ at high $p_{\rm T}$, as the dominated effect at this region is radiative energy loss, and at low $p_{\rm T}$ region, the transport models can reproduce the data well, which indicate the roles of recombination and elastic scatterings are important, details will also be discussed in latter Chapter.

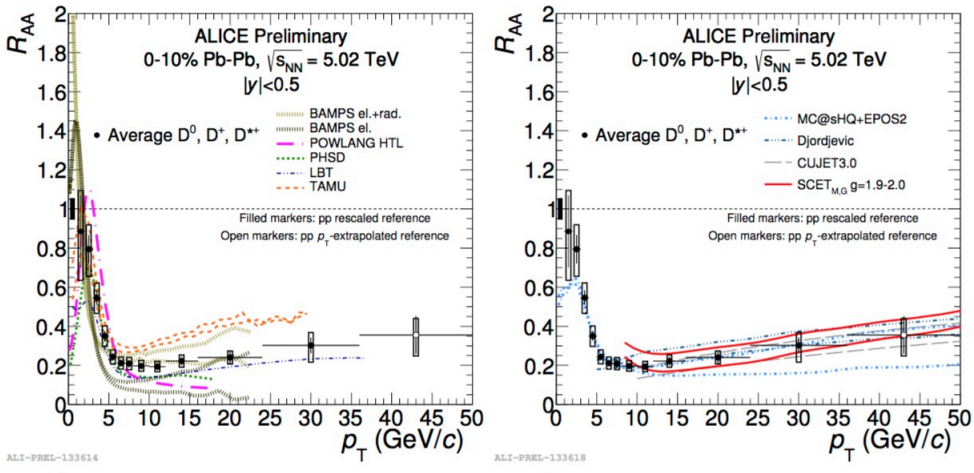

Figure 2.10: ALICE preliminary results [21] about non-prompt D mesons at $\sqrt{s_{\rm NN}}$ = 5.02 TeV in 0-10% centrality class Pb–Pb collisions, compared with pQCD-based models (left panel) and transport models (right panel).

Part II

ALICE Experiment

Chapter 3

The ALICE experiment at the LHC

This Chapter follows the structure: firstly, a short introduction of accelerator complex at CERN will be given in Sec. 3.1, an overview of ALICE setup will be shown in Sec. 3.2 including the description of the detectors which is related to the analysis discussed in this thesis, alice trigger system, and the technical about reconstruction of vertex and tracks.

3.1 The Large Hadron Collider

The Large Hadron Collider (LHC), underground 100 m with a circumference around 27 km, which is the world largest and most powerful particle accelerator, located near Geneva, Switzerland. It was built by the European Organisation for Nuclear Research (CERN) from 1998 to 2008, aiming to discover the Higgs boson and explore its properties, search the physics beyond the Standard Model. The design luminosity is $10^{34} cm^{-2} s^{-1}$ for collide protons and $10^{27} cm^{-2} s^{-1}$ for lead ions, and the design centre-of-mass energies are 14 TeV for pp collision and 5.5 TeV for Pb–Pb collisions [104].

The overview of the CERN's accelerator complex is presented in Fig. 3.1. It's not feasible to reach high beam energy within only one single accelerator, so the accelerate of the particles are in several steps(as accelerator chain described in the figure). There are eight possible interaction points in LHC. The main large experiments are located at four interaction points: ATLAS (A Toroidal LHC Apparatus) and CMS (Compact Muon Solenoid experiment) are designed primarily for pp collisions, in order to search for the Higgs-boson and its properties, in addition, they can also verify Standard Model and search for the physics beyond Standard Model, thus the detectors are designed to detect large momentum particles. The LHCb (LHC beauty) experiment is designed to search for CP-violation through B physics channels, in order to understand the asymmetric behavior of matter and anti-matter in the universe. The ALICE (A Large Ion Collider Experiment) experiment is mainly built to the study the QGP formation and its properties, which concerns more about heavy-ion collisions, details will be discussed in the next section.

In 2009, The LHC delivered first collided proton beams at a centre-of-mass energy of 0.9 TeV, one year delayed as a major operation accident happened which destroyed 1/8 of the magnets. During Run 1 (November 2009 - February 2013), LHC only runs up to the centre-of-mass energy of 8 TeV due to the faulty connections

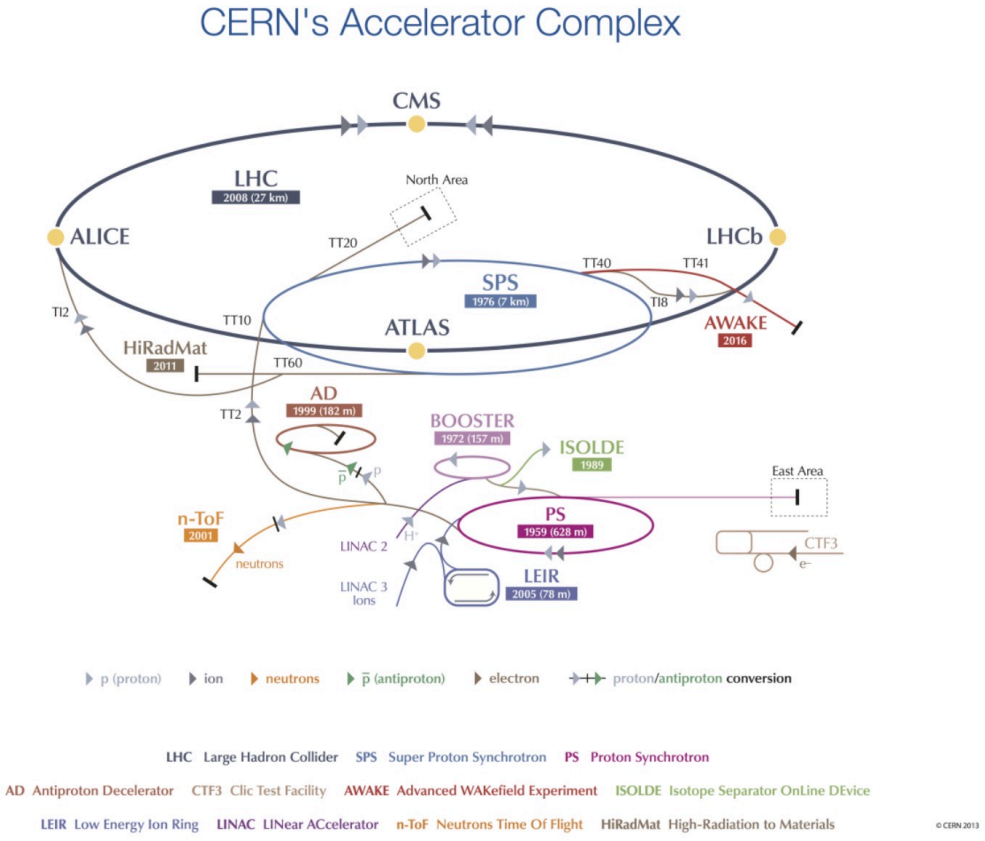

Figure 3.1: The overview of CERN's accelerator complex.

within the magnets. During this period, there were also 3 dedicated heavy-ion programs, collecting Pb–Pb collisions data at $\sqrt{s}_{\rm NN} = 2.76$ TeV in 2010 and 2011, there was a p-Pb run at $\sqrt{s}_{\rm NN} = 5.02$ TeV at the beginning of 2013. After first long shutdown (LS), LHC restarted in April 2015 for Run 2, ramping up to its full energy in pp collisions at $\sqrt{s} = 13$ TeV. The heavy-ion runs data was collected at the end of 2015 in Pb–Pb collisions at $\sqrt{s}_{\rm NN} = 5.02$ TeV at the end of 2015(also including xenon-xenon collisions taken at the mid of 2016, and next Pb–Pb run at $\sqrt{s}_{\rm NN} = 5.02$ TeV taken at the end of 2018), and p–Pb collisions at $\sqrt{s}_{\rm NN}$= 5.02 TeV and $\sqrt{s}_{\rm NN} = 8.16$ TeV at the end of 2016.

3.2 ALICE (A Large Ion Collider Experiment) Apparatus

ALICE [105, 23] is the heavy-ion detector at LHC, designed to the properties of QGP at extreme values of energy density and temperature in nucleus-nucleus collisions. The overall layout of ALICE is sketched in Fig. 3.2, the dimensions is $16 \times 16 \times 26$ m^3 with a total weight around 10000 t. It allows to study of

hadrons, electrons, muons, and photons produced in the heavy-ion collisions down to low momenta and with a wide momentum cover range, handling charged-particle densities up to $\frac{dN}{dy} \approx 8000$ at mid-rapidity. Meanwhile, dedicated proton-nucleus and proton-proton runs are also needed in order to provide the reference and further understanding of the systems.

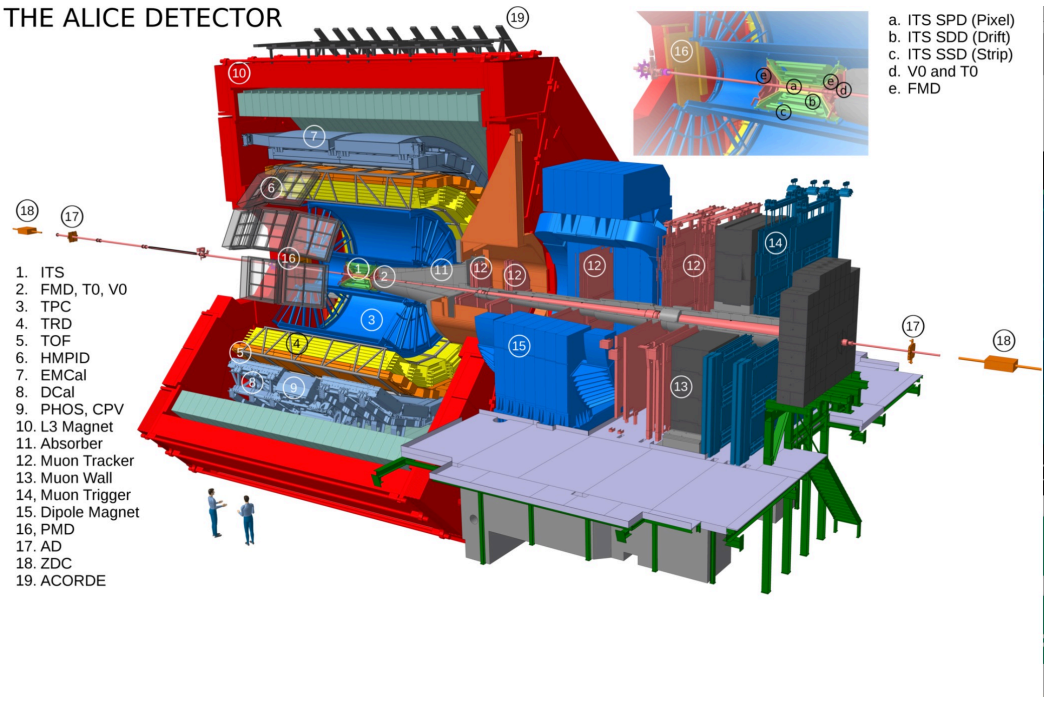

Figure 3.2: The overview of ALICE accelerator complex.

In general, the apparatus can be divided into three parts.

Central Barrel the pseudo-rapidity range $-0.9 < \eta < 0.9$ (polar angles $45^{\circ} < \theta < 135^{\circ}$). It is embedded in the large L3 solenoid magnet providing a moderate solenoidal field of B = 0.5 T for normal running conditions. From the inside out, the Central Barrel contains the Inner Tracking System (**ITS**) made of six planes of high resolution silicon pixel (**SPD**), drift (**SDD**) and strip (**SSD**) detectors, optimized for vertex reconstruction and tracking. The cylindrical Time-Projection Chamber (**TPC**), main detector for tracking and particle identification. The Transition Radiation Detector (**TRD**), for electron identification. The Time-Of-Flight (**TOF**), also used for tracking and particle identification. The High Momentum Particle Identification Detector (**HMPID**). And two electromagnetic calorimeters: the PHOton Spectrometer (**PHOS**) and the ElectroMagnetic CALorimeter (**EMCal**), used to detect neutral particles. All detectors except HMPID, PHOS, and EMCal cover the full azimuth. There is another detector ALICE COsmic Ray DEtector (**ACORDE**), on top of the L3 magnet, used to trigger on cosmic rays.

Global Detectors Several smaller detectors, the Photon Multiplicity Detector (**PMD**), the **Forward Multiplicity Detector** (**FMD**), dedicated to measure photons and charged particles at forward rapidity. The Zero Degree Calorimeter (**ZDC**), as well as the **T0** and **V0** detectors, dedicated to determinate the global characteristics of the events such as centrality , multiplicity, and event plane and triggering.

Muon Spectrometer dedicated to measure muon productions at forward rapidity.

Tab. 3.1 summarizes the acceptance and location information of detector subsystems.

3.2.1 Detector Layout

Below, gives briefly descriptions of important detectors related the analysis discussed in this thesis.

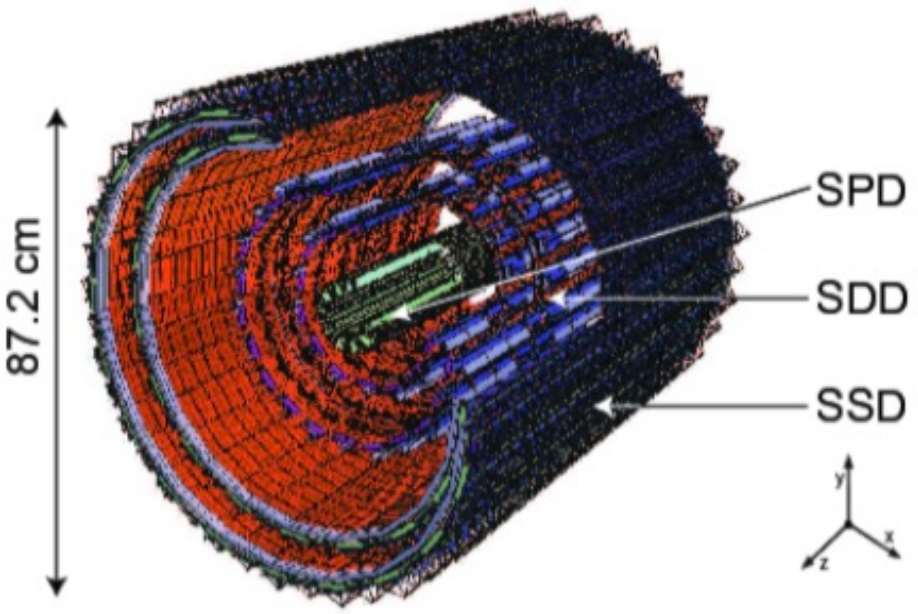

Figure 3.3: View of six silicon layers in ITS.

Inner Tracking System (ITS) The ITS consists of six cylindrical layers of silicon detectors, with a radius between 3.9 cm and 43 cm as shown in Fig. 3.3. It contains three sub-detectors, each contains two layers, from inside to outside are: The Silicon Pixel Detector (SPD), the Silicon Drift Detector (SDD) and the Silicon Strip Detector (SSD). they allow to localize the primary vertex of the interaction, have a very high precision reconstruction of tracking, and also contributed to the particle identification of low-momentum particles. The Silicon Pixel Detector (SPD) is the

Detector	Acceptance (η, ϕ)	Position (m)	Dimension (m^2)	Channels
ITS layer 1,2 (SPD)	± 2, ± 1.4	0.039, 0.076	0.21	9.8 M
ITS layer 3,4 (SDD)	± 0.9, ± 0.9	0.150, 0.239	1.31	133 000
ITS layer 5,6 (SSD)	± 0.97, ± 0.97	0.380, 0.430	5.0	2.6 M
TPC	± 0.9 at $r = 2.8$ m ± 1.5 at $r = 1.4$ m	0.848, 2.466	readout 32.5 m^2 Vol. 90 m^3	557 568
TRD	± 0.84	2.90, 3.68	716	1.2 M
TOF	± 0.9	3.78	141	157 248
HMPID	± 0.9, $1.2^\circ < \phi < 58.8^\circ$	5.0	11	161 280
PHOS	± 0.12, $220^\circ < \phi < 320^\circ$	4.6	8.6	17 920
EMCal	± 0.7, $80^\circ < \phi < 187^\circ$	4.36	44	12 672
ACORDE	± 1.3, $-60^\circ < \phi < 60^\circ$	8.5	43	120
Muon spectrometer				
Tracking station 1	$-2.5 < \eta < -4$	-5.36	4.7	1.08 M
Tracking station 2		-6.86	7.9	
Tracking station 3		-9.83	14.4	
Tracking station 4		-12.92	26.5	
Tracking station 5		-14.22	41.8	
Trigger station 1		-16.12	64.6	21 000
Trigger station 2		-17.12	73.1	
ZDC:ZN	$\lvert\eta\rvert < 8.8$	± 116	2×0.0049	10
ZDC:ZP	$6.5 < \lvert\eta\rvert < 7.5$	± 116	2×0.027	10
ZDC:ZEM	$4.8 < \eta < 5.7$ $-16^\circ < \phi < 16^\circ$ and $164^\circ < \phi < 169^\circ$	7.25	2×0.027	10
PMD	$2.3 < \eta < 3.7$	3.64	2.59	2 221 184
FMD disc 1	$3.62 < \eta < 5.03$	inner: 3.2	0.266	51 200
FMD disc 2	$1.7 < \eta < 3.68$	inner: 3.2		
FMD disc 3	$-3.4 < \eta < -1.7$	outer: 0.752 inner: -0.628 outer: -0.752		
V0A	$2.8 < \eta < 5.1$	3.4	0.548	32
V0C	$-1.7 < \eta < -3.7$	-0.897	0.315	32
T0A	$4.61 < \eta < 4.92$	3.75	0.0038	12
T0C	$-3.28 < \eta < -2.97$	0.727	0.0038	12

Table 3.1: Summary of the ALICE detector subsystems performance information.

innermost 2 layers of the ITS, based on hybrid silicon pixels, it contains 9.8×10^6 pixels with the size $50(r\phi)\times425(z)$ μm^2 allowing for a spatial precision of 12(100) μm along the $r\phi(z)$ direction. The Silicon Drift Detector (SDD) is the two middle layers of the ITS. The intrinsic spatial resolution is 35 μm along the $r\phi$ direction and 25 μm in z direction, it also have the capability of $\mathrm{d}E/\mathrm{d}x$ for particle identification. The Silicon Strip Detector (SSD) makes up the outer two layers of the ITS, consisting of double-sided silicon strip sensor modules. The precision of spatial resolution is 20(830) μm along the $r\phi(z)$ direction and also the $\mathrm{d}E/\mathrm{d}x$ measurement, often it can provide the matching information with TPC for the tracks. The alignment of the ITS sensor modules is crucial to provide precise reconstruction of space points, allows to extract the information of low momentum and impact parameter, which is important for heavy flavour analysis.

Time Projection Chamber (TPC) The TPC is the main tracking detector in the ALICE central barrel. It can provide the measurement of charged particle momentum from 0.1 GeV/c up to $p_{\mathrm{t}} = 100$ GeV/c, good separation of tracks, particle identification and vertex determination in the high multiplicity environment of Pb–Pb collisions. The Time Projection Chamber is made of a cylindrical field cage, filled with 90^3 m^3 of $\mathrm{Ne/CO_2/N_2}$.

The TPC allows to measure charged particles from $p_{\mathrm{T}} = 100$ MeV/c to 100 GeV/c. Particle identification in TPC is performed by simultaneously measuring the specific energy loss ($\mathrm{d}E/\mathrm{d}x$), charge, and momentum of each particle traversing the detector gas. The energy loss can be described by the Bethe-Bloch formula:

$$f(\beta_\gamma) = \frac{P_1}{\beta^{P_4}}(P_2 - \beta^{P_4} - \ln(P_3 + \frac{1}{(\beta\gamma)^{P_5}})) \tag{3.1}$$

Where β is the particle velocity, γ is the Lorentz factor, and P_{1-5} are fit parameters. As presented in Fig. 3.4, TPC can have a clear separation among different particle species. And the $\mathrm{d}E/\mathrm{d}x$ resolution is about 5.2% in pp collisions and 6.5% in 0-5% central Pb–Pb collisions [23].

Time Of Flight (TOF) The TOF is located at a radius from 370 cm to 399 cm with a length of 745 cm, designed for particle identification in the intermediate momentum range, up to 2.5 GeV/c for pions and kaons, 4 GeV/c for protons. In Pb–Pb collisions, the TOF resolution is 80 ps for pions at the momentum around 1 GeV/c in 0-70% centrality class.

V0 Detector The V0 detector is made of two arrays of scintillators , V0A and V0C, located 90 cm (forward side) and 340 cm (backward side) from the interaction point. They cover the pseudo-rapidity ranges $2.8 < \eta < 5.1$ (V0A) and $3.7 < \eta < 1.7$ (V0C). The V0 provides a minimum bias trigger as well as high-multiplicity triggers for the central barrel detectors and can be used to estimate the centrality of the collision based on the energy deposited in the V0 scintillator tiles. What's more, it can be also used for beam-gas background rejection.

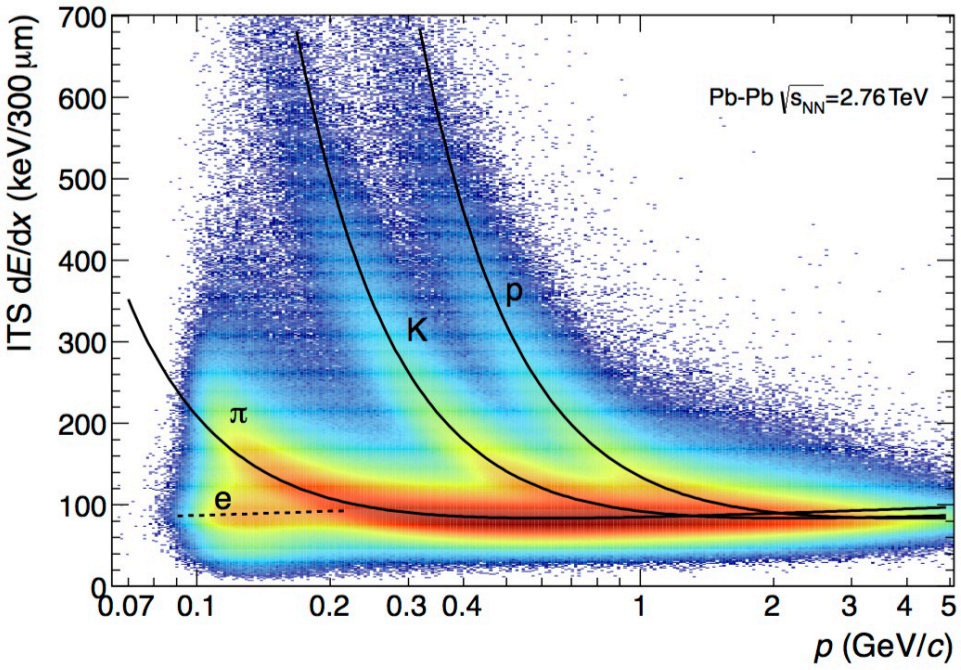

Figure 3.4: Distribution of the energy-loss signal in the ITS as a function of momentum.

For the centrality determination, this can be done by according to measurements of multiplicity (energy) produced in the collision. The distribution can be described by the Glauber model convoluted with a model for particle production based on a negative binomial distribution (NBD) with the formula $P_{\mu,k}(n) \times N_{\text{ancestors}}$, where $N_{\text{ancestors}}$ is independently emitting sources of particles which is related to N_{part} and N_{coll} . $P_{\mu,k}(n)$ gives the probability of measuring n hits per ancestor. One can get the centrality using the NBD-Glauber fit to the sum of V0 amplitudes, as shown in Fig. 3.5. It shows the NBD-Glauber fit result for the ALICE data in Pb–Pb collisions at $\sqrt{s}_{\text{NN}} = 2.76$ TeV [22], the fit parameters can be extracted as f = 0.801, μ = 29.3, k = 1.6. The fit has good agreement with data. The centrality thus can be expressed as a percentage of the total nuclear interaction cross section σ by integrating the V0 amplitude distribution.

ElectroMagnetic Calorimeter (EMCal) [106] The ElectroMagnetic Calorimeter (EMCal) is designed as a layered lead-scintillator sampling calorimeter with a longitudinal wavelength shifting fibers for light collection, covering with the azimuth of107° and pseudo-rapidity $|\eta| < 0.7$. The EMCal detector is positioned to provide partial back-to-back coverage with the PHOS calorimeter. As shown in Fig. 3.6, EMCal contains 10 full size (12×24 modules) and 2 one-third size (4×24 modules) Super Modules. Each physical module is composed by 2×2 cells. The wavelength

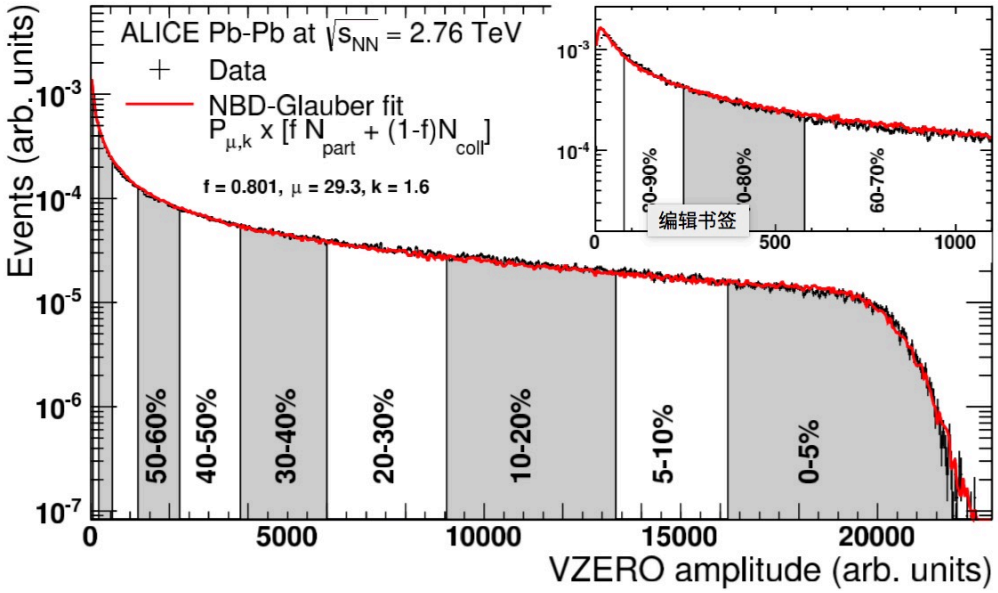

Figure 3.5: Distribution of the sum of amplitudes in the VZERO scintillators [22]. The distribution is fitted with the NBD-Glauber fit shown as a line. The centrality classes used in the analysis are indicated in the figure.

shifting fibers are bundled such that the scintillation light from each cell is read out by an $5 \times 5\ mm^2$ active-area avalanche photodiode.More physical parameters about EMCal module can be found in Fig. 3.7.

The EMCal is focused on the measurement of high p_{T} objects(neutral mesons, electrons and photons), allowing better reconstruction of the neutral components of the jets. The energy resolution of EMCal can be parameterized as:

$$\sigma/E = \sqrt{(\frac{a}{E})^2 + \frac{b}{E} + c^2} \tag{3.2}$$

By fitting 2010 electron test beam, an absolute energy calibration of the test beam data was obtained from the known incident electron energy using an iterative procedure. The energy resolution obtained at the different positions was combined. The simulation data points and a fit to the energy resolution as a function of the incident energy are also where the coefficients of a, b and c are 0.0435, 0.0973 and 0.0163, respectively, shown in Fig. 3.8. One can see that EMCal has a excellent resolution as high p_{T} with $\mathrm{d}\sigma/\mathrm{d}E$ is better than 4% above 10 GeV/c.

3.2.2 Trigger System

ALICE has two different level trigger systems. The low-level one is called Central Trigger Processor (CTP), which is the hardware trigger collecting information from sub-detectors, then decide whether to record this event. The high-level one is

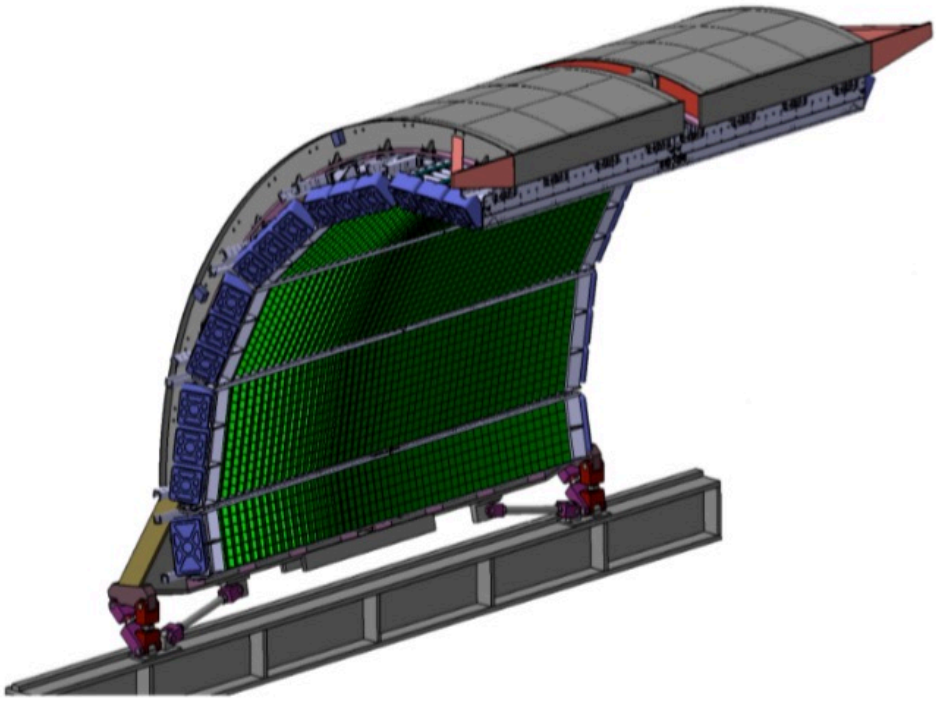

Figure 3.6: Layout of EMCal super module

Parameter	Value
Tower Size (at η=0)	$\sim$6.0 $\times$ $\sim$6.0 $\times$ 24.6 cm^3
Tower Size	$\Delta\phi \times \Delta\eta = 0.0143 \times 0.0143$
Sampling Ratio	1.44 mm Pb / 1.76 mm Scint.
Layers	77
Scintillator	Polystyrene (BASF143E + 1.5%pTP + 0.04%POPOP)
Absorber	natural Lead
Effective RL X_0	12.3 mm
Effective MR R_M	3.20 cm
Effective Density	5.68 g/cm^3
Sampling Fraction	1/10.5
Radiation Length	20.1

Figure 3.7: Physical parameters of EMCal modules.

called High-Level Trigger (HLT), which is the pure software trigger providing further sophisticated logic triggers.

The CTP evaluates the trigger inputs at every machine clock cycle (25 ns). According to different readout time, the trigger inputs can be divided into three levels. The Level 0 trigger decision (L0) at 0.9 μs after the collisions using V0, T0,

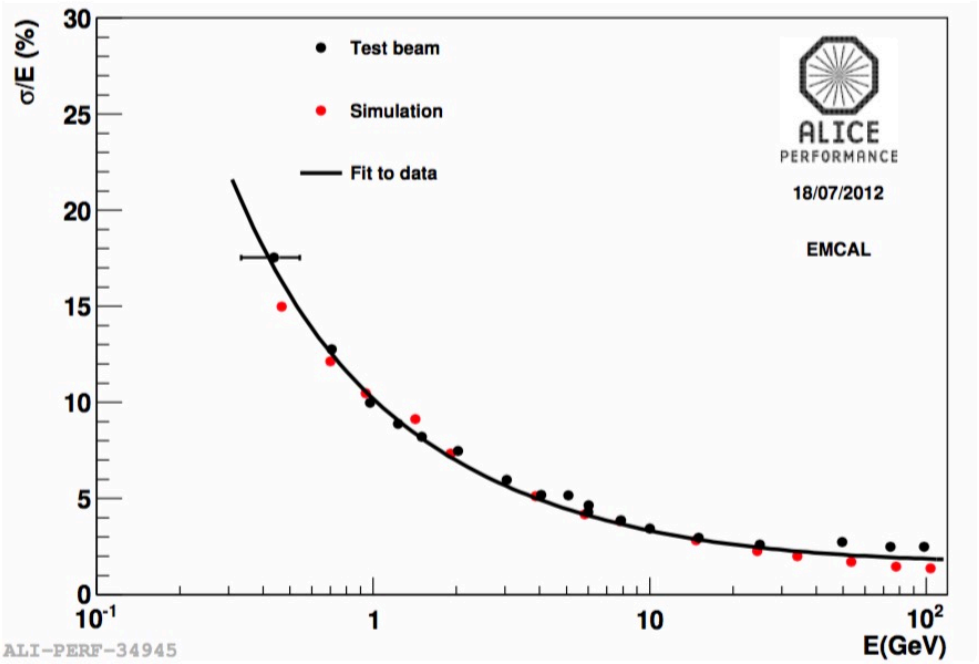

Figure 3.8: EMCal energy resolution as a function of energy, obtained by fitting the 2010 electron test beam data measurements.

EMCal, PHOS, and MTR, then Level 1 trigger (L1) further evaluate the events using ZDC, TRD, EMCal around 6.5 μs due to the propagation and computation time. Considering the TPC drift time, the Level 2 (L2) trigger decision around 100 μs. If the events pass L2 trigger, they will send in parallel to the Data AcQuisition System (DAQ) and HLT, to do detailed analysis filtering, helping to reduce the data volume before storage.

Several different events types can be defined under different trigger conditions. For example, Minimum-bias (MB) events which takes smallest requirements as possible, while avoiding empty events, is the L0 triggered events. In pp collisions, it requires a logical OR between a hit in the SPD and in either of the two hits in V0 (V0A or V0C). More complex triggers which involving various properties of the detected particles can be taken at level 1 such as jet trigger events in the EMCal, even based on rough PID estimation as γ-jet triggers in the EMCal.

3.2.3 Track and Vertex Reconstruction

3.2.3.1 Primary Vertex Determination

The first two innermost of ITS, SPD, provides the first estimation of the primary vertex. The pairs of reconstructed points are selected in these two layers, When the reconstructed points are close in azimuthal in the transverse plane, they're considered as pairs, then z-position of the primary vertex can be estimated using a

linear extrapolation. A similar procedure is repeated in the transverse plane. The resolution in the x and y coordinates is worse than for the z coordinate due to the bending in the magnetic field. However, due to the short distances from the interaction point, these information can be used to improve the estimation of the z-coordinate. The resolution on the position of the primary vertex σ_{vtx} depends on the track multiplicity n_{trklet}, its fluctuation can be expressed as:

$$\sigma_{\mathrm{vtx}} = \frac{\alpha}{\sqrt{n_{\mathrm{trklet}}}} \oplus K. \tag{3.3}$$

In pp collisions ($N_{\mathrm{trklet}} \simeq 6 - 7$) the z-vertex resolution ~ 150 μm, while in Pb–Pb collisions, it can go down to 50 μm with $N_{\mathrm{trklet}} > 60$. After track reconstruction, the precision of the primary vertex can be further reduced by using the global tracks reconstructed in TPC and ITS. Since the readout time of the SPD is 200 ns, so one SPD event could contain several bunch crossings. Especially, for pp collisions, pile-up events are necessary to be removed. In ALICE, the main method used for this removing is called PileupAlgo1 which runs vertexing algorithm N times (usually N = 10) with the SPD tracklets not contributed to the main vertex (the one with largest multiplicity). Then the pile-up candidate can be chosen if there a minimum number if tracklets contributed to it and if the new reconstructed vertex have a z separation (larger than the cut value) with the main vertex.

3.2.3.2 Track Reconstruction

The track reconstruction in ALICE is performed in three steps by finding and fitting using Kalman filtering. Space points chosen from the end of TPC are used as seeds for the Kalman filter. Then the seeds are combined with nearby clusters into tracks inwards to the collision vertex (primary or secondary vertex) until it reaches the innermost pad row of the TPC. A space point will be assigned to a track if it's close to its trajectory, afterwards the covariance matrix is recalculated. When reaches the inner boundary of the TPC, the track are propagated to the ITS layer by layer, using the same procedure as for the TPC. After that, using the combined fit from ITS and TPC, the procedure will be repeated again but start with the primary vertex, in this case, improper points will be removed from the track, and the missed points will be included, when exceed the boundary of TPC, the space points from TRD, TOF, HMPID and the calorimeter towers in the EMCal or PHOS will be assigned to the associate tracks, although they don't have many contributions to the momentum fit. Finally the Kalman filter will be inverted again to calculate the final track parameters assuming the track from primary vertex or secondary vertex. Both final parameters information will be stored. Due to the dead areas of the TPC, some tracks can't be reconstructed in this way, another approaching is developed by removing all the hits which associate to the tracks, using the remaining points in ITS to reconstruct tracks, providing the ITS standalone tracks.

Fig.3.9 shows the TPC tracking efficiency for different collision systems as a function of p_{T}, the efficiency can be defined as the ratio between reconstructed tracks and generated primary particles. The steep dropping at low p_{T} is due to the

energy loss and multiple scattering in the detector material. The fraction is not equal to 1 at high p_{T} caused by the dead zone of readout sectors. The efficiency doesn't depend so much on the collision systems.

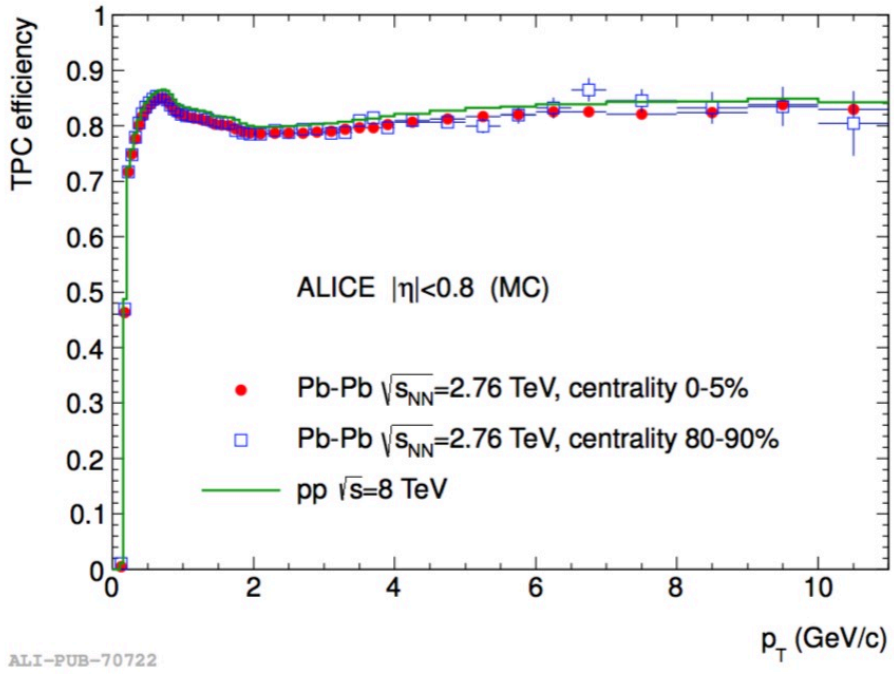

Figure 3.9: Monte Carlo simulations of TPC track finding efficiency for different collision systems [23].

As described above, the reconstruction of the secondary vertex is important especially for the weak-decay particles which contains strange, charm and beauty quark as they will decay after a certain distance away from the primary vertex. Thus some of the track will displace from the primary vertex, such displacement can be estimated by the impact parameter, which is defined as the distance of closest approach of the reconstructed particle trajectory to the primary vertex. The impact parameter resolution can be obtained by fitting the impact parameter distribution in p_{T} intervals, using a Gaussain plus two exponential (Gaussian from primary particles, exponential from the secondary particles from weak decay), the width σ is the resolution. Fig. 3.10 shows the resolution of the $r\varphi$ projection impact parameter for ITS-TPC tracks as a function of p_{T} in different collision systems. The contribution from the vertex resolution is included. The resolution is decrease from pp to Pb–Pb collisions attributed to the improved precision of the primary vertex at higher multiplicity events.

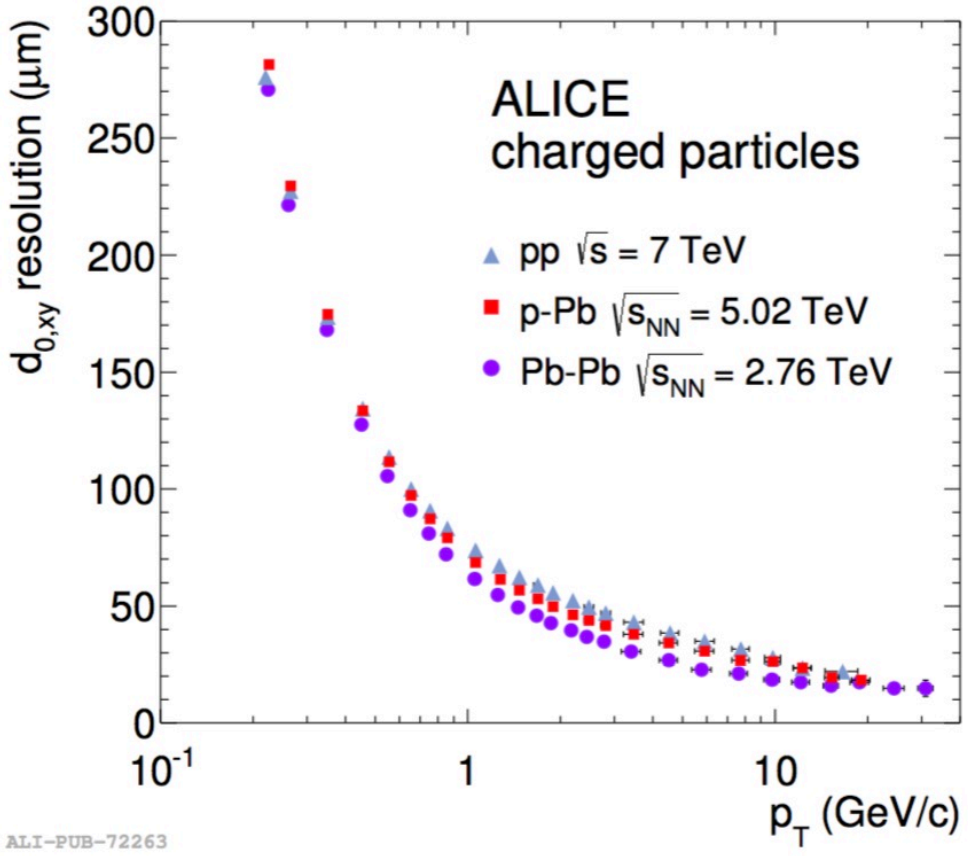

Figure 3.10: Resolution of the $r\varphi$ projection impact parameter for ITS-TPC tracks as a function of p_{T} in different collision systems. The contribution from the vertex resolution is included.

Part III

Analysis Topics

Chapter 4

Neutral pion-hadron correlations

In this Chapter, the analysis of neutral pion-hadron correlations will be performed, which can get the access to the information of the jet-medium interactions in Pb–Pb collisions. What's more, it's also the main background of direct γ-hadron correlations which is the golden probe of the QGP medium as γ will not interact with its constituents when go through it. The chapter organized as following: Sec 4.1 will introduce the data and event selections used for the analysis. After that, an unique technique used to identify high-p_{T} π^0 will be explained in Sec. 4.2. Then the correction procedures and details of systematic uncertainties evaluation will be given in Sec. 4.3 4.4 and 4.5. Finally, the results about azimuthal pion-hadron correlations and the measurement of yield modification factor I_{AA} will be shown in Sec 4.6. The brief summary will be presented in Sec. 4.7.

4.1 Data Sets and Event Selections

This work was performed on the data collected by ALICE detector in 2011 with pp and Pb–Pb collisions at centre-of-mass energy per nucleon-nucleon pair of $\sqrt{s_{\mathrm{NN}}}$ = 2.76 TeV. For pp collisions, the minimum bias (a hit in either V0 or SPD) data was further selected by the EMCal level-0 trigger, which requires a single shower energy larger than 3.0 GeV, the remain number of events are 440k (the integrated luminosity corresponding to 0.5/nb) after all the selections, the dedicated MC was generated using PYTHIA6 jet-jet events with 12 p_{T}-hard bins (named LHC15g1b below). For Pb–Pb collisions, the data was selected by an online trigger in order to central collisions, 5.2M events are kept (corresponding to 0.6/μb), the dedicated MC using HIJING with added signals at 0-10% centrality class (named LHC14a1a below). In addition, only events with a reconstructed primary vertex within $\pm$10 cm from the nominal interaction vertex position along the beam line were used for the analysis. The in-bunch collision pileup is negligible not only for EMCal triggered events in pp collision, but also for Pb–Pb collisions.

4.2 High-p_{T} π^0 Identification and Track Reconstruction

4.2.1 High-p_{T} π^0 Identification

4.2.1.1 Clusterisation

In the EMCal, a calorimeter cluster can be defined as an aggregate of calorimeter towers/cells. The physical information of a cluster is the energy deposited of a

particle either from a single photon, electron or photons from π^0 and η. There are several clusterisation method in EMCal such as V1, V2, N × M, V1 + splitting method. Taking V1 method as an example, it selects a seed cell with energy above a given threshold E_{seed}, adding all cells to the cluster with common side to the seed tower until their energy is below E_{min}. A cell can only belong to one cluster. In general, V1 is used for pp collision, while V2 clusterisation is used for Pb–Pb collisions. Details of each method will not be discussed, but I will focus on the V1+ splitting method as it's effective for high-p_{T} π^0 identification, thus will be used for both pp and Pb–Pb collisions in this work. The reason can be briefly described as below: We use the decay channel $\pi^0 \to \gamma\gamma$ to reconstruct π^0, the invariant mass can be calculated as:

$$M_{\gamma_1\gamma_2} = \sqrt{2E_1E_2(1-\cos\theta_{12})} \tag{4.1}$$

Where E is the two decay photon energy, $\cos\theta_{12}$ is the relative angle between the two photons in the laboratory frame. As shown in Fig. 4.1, according to Lorentz boost, $\cos\theta_{12}$ will become smaller with the increase of the energy. In EMCal, the two photon clusters decayed from π^0 start to merge with the energy larger than 5-6 GeV. In this scenario, a simulation study has been done for single π^0, the phenomena can be found in Fig. 4.2 that above 9 GeV, more than half of the π^0 deposit their energy in a single merged cluster instead of two clusters.

4.2.1.2 Shower Shape of the cluster

The characteristic of cluster is very sensitive to shower surface ellipse [106], which can be defined by the intersection of the cone containing the shower with the front plane of the calorimeter. By building a four terms covariance matrix, which is related to the cluster position in η and ϕ direction in the calorimeter plane, and their logarithmically by the cell energy, the shower surface ellipse axis long λ_0 and short axis λ_1 can be expressed as:

$$\lambda_0^2 = 0.5(\delta_{\varphi\varphi}+\delta_{\eta\eta}) + \sqrt{0.25(\delta\delta_{\varphi\varphi}-\delta_{\eta\eta})^2+\delta_{\varphi\eta}^2} \tag{4.2}$$

$$\lambda_1^2 = 0.5(\delta_{\varphi\varphi}+\delta_{\eta\eta}) - \sqrt{0.25(\delta\delta_{\varphi\varphi}-\delta_{\eta\eta})^2+\delta_{\varphi\eta}^2} \tag{4.3}$$

Where δ are the weighted coefficients by the cell energy. the half long axis square λ_0^2 as a function of cluster energy E in ALICE at $\sqrt{s} = 7$ TeV is presented in Fig. 4.3. Two clear band region can be found in the plots, the bottom one is dominant by the single photon cluster, while the upper band is mainly formed by π^0. In this case, the $\lambda_{0,min}^2$ cut is set to 0.3 in order to remove the contribution from single photon or η contribution. According to this, further study has been done to better discriminate single or merged π^0 band curves, thus a new observable Number of Local Maxima (N_{LM}) need to be defined as the number of cells which have the energy ΔE_{seed} higher than the E_{seed}. In general, below 15 GeV, most merged clusters from π^0 have two local maxima, while with increasing energy the showers further merge, thus the merged clusters from π^0 will mainly have one local maximum above 25 GeV. Finally,

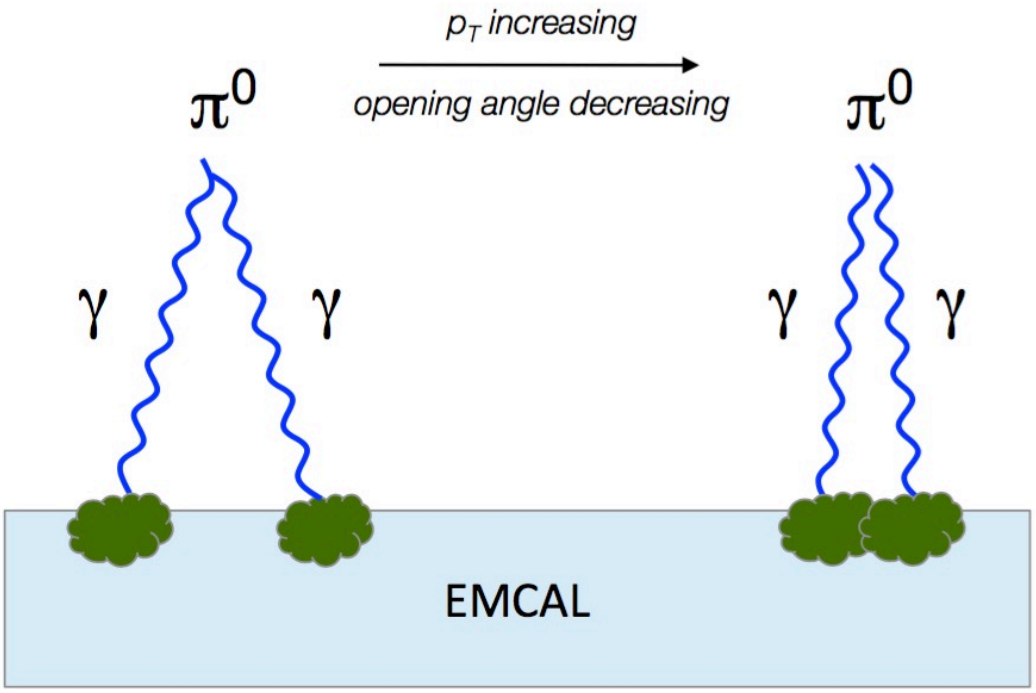

Figure 4.1: The topological cartoon of π^0 decay two photon.

the Band Criterion selection on λ_0^2 can be given by $\lambda_{0,min}^2 < \lambda_0^2 < \lambda_{0,max}^2$, the $\lambda_{0,min}^2$ and $\lambda_{0,min/max}^2$ can be expressed as:

$$\lambda_{0,min/max}^2(E) = e^{a+b\times E} + c + d \times E + e/E \tag{4.4}$$

After the simulation study, for $\lambda_{0,min}^2$, we use a = 2.135, b = -0.245, c = d = e = 0. While for $\lambda_{0,max}^2$, the values depend on the number of local minima, and are a = 0.066, b = -0.020, c=-0.096, d=0.001, and e=9.91 for $N_{\rm LM}$ =1, a=0.353, b=-0.0264, c=-0.524, d = 0.006 and e = 21.9 for $N_{\rm LM}$ = 2. Within $8 < p_{\rm T} < 16$ GeV/c, the range for neutral pions considered in this analysis, more than 80% of the clusters have two local maxima.

4.2.1.3 Cluster Splitting

The merged cluster is subsequently splited into two sub-clusters by grouping neighboring cells into 3×3 clusters centered around the two highest cells (seeds) of the merged cluster. Cells that are neighbor of both seeds are splited based on the fraction of seed to cluster energy, the example can be found in Fig. 4.4, thus the invariant mass can be builded with the two sub-clusters. We use the $M(E)-3\sigma < M_{\gamma\gamma} < M(E)+3\sigma$, 3σ window cut to select π^0 candidate. Concerning the discrepancy of π^0 invariant mass peak and sigma between different $N_{\rm LM}$, the

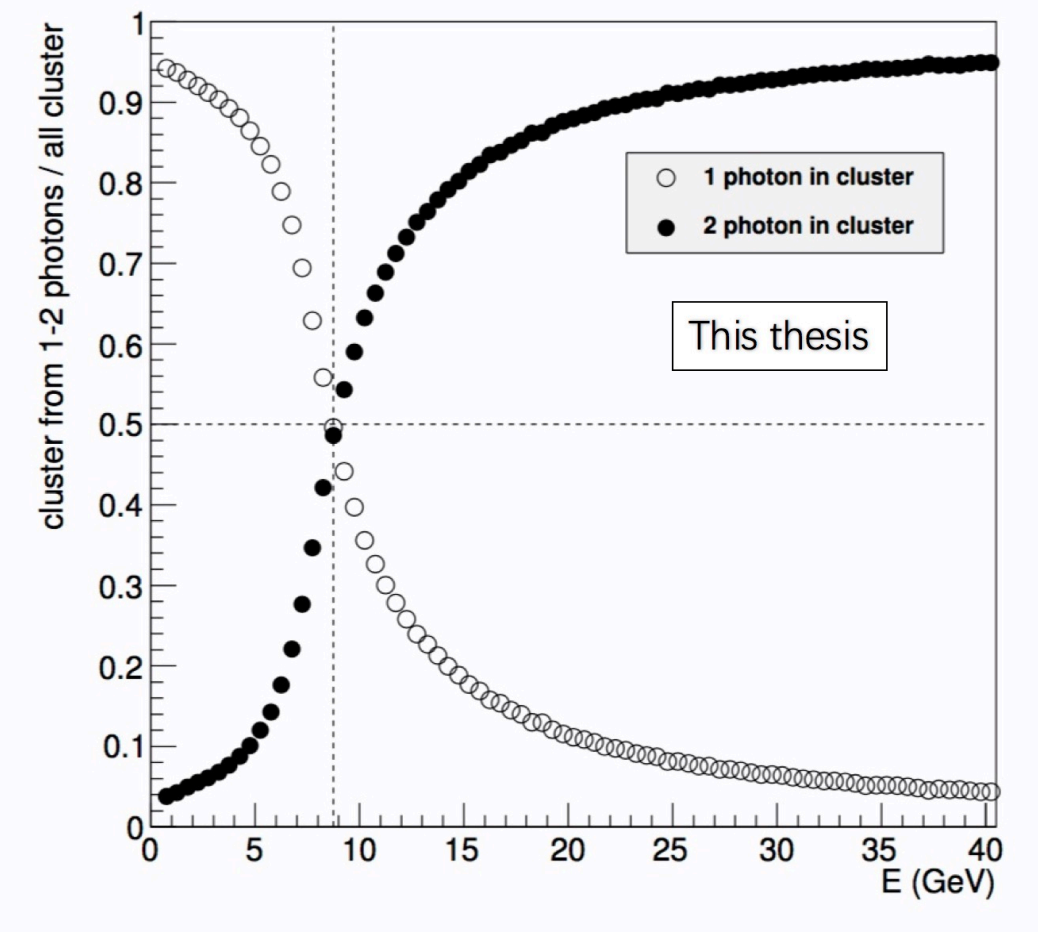

Figure 4.2: The fraction of V1 clusters generated by the electromagnetic shower of two π^0 decay photons (solid points) or a single π^0 decay photon (open points) in a simulation of single π^0 (flat energy distribution from 1 to 50 GeV) over EMCal.

study has been done as shown in Fig. 4.5 and 4.6, the mean mass (upper) and width (lower) of split sub-clusters invariant mass distribution versus cluster energy, for different values of N_{LM} in data and MC in pp and Pb–Pb collisions. MC can reproduce data's result well, for different collision systems and N_{LM}. The selection of π^0 will fail if taking 3σ from expected π^0 mass. In this case, a polynomial fit of the first order can be performance for each scenario expressed as:

$$M(E), \sigma(E) = a + b \times E \tag{4.5}$$

We can extract the information for the analyzed p_{T}, the parameters for $\langle M \rangle$, a = 0.044 and b = 0.005 for $N_{\mathrm{LM}} = 1$, and a = 0.115, b = 0.001 for N_{LM} =2. While for σ they are a = 0.012 and b = 0 for $N_{\mathrm{LM}} = 1$, and a = 0.009, b = 0.001 for $N_{\mathrm{LM}} = 2$. The E_{min} and E_{seed} are set to 50 MeV and 100 MeV for pp collision, 150

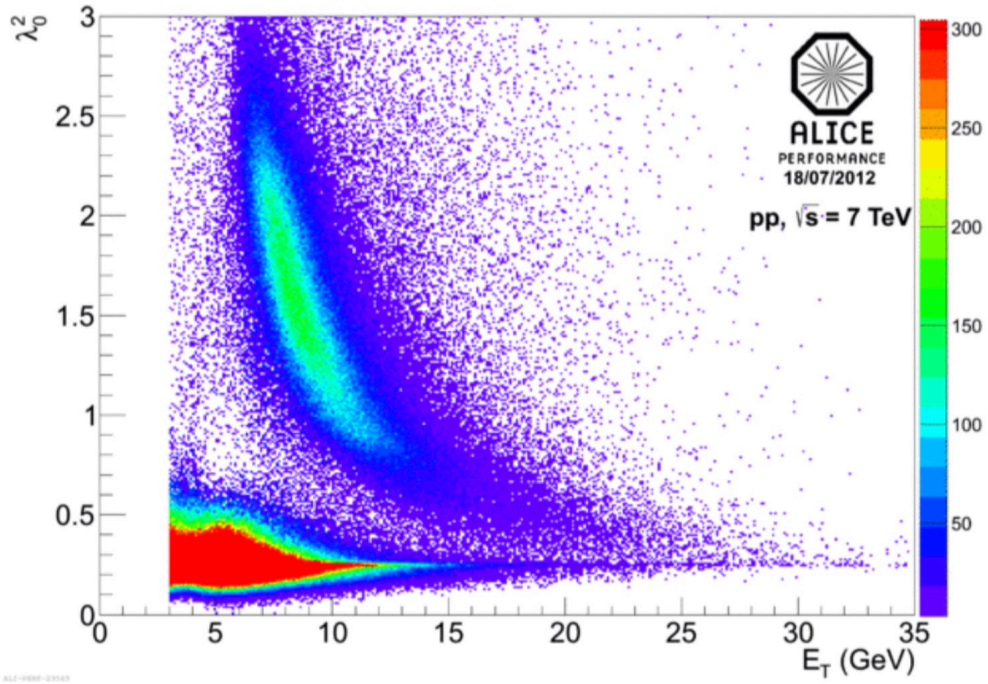

Figure 4.3: The performance study for the half long axis square of a cluster as a function of cluster energy E in ALICE at $\sqrt{s} = 7$ TeV.

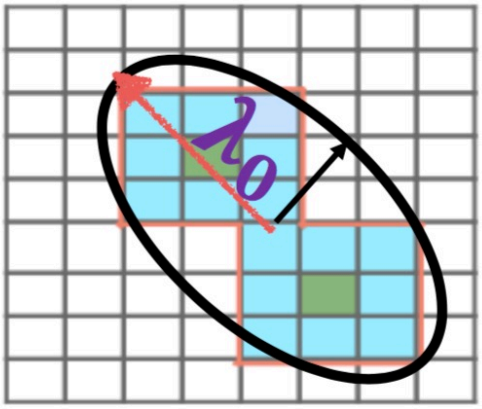

Figure 4.4: An example of the procedure of cluster splitting.

MeV and 300 MeV for Pb–Pb collisions. In order to cross check this π^0 selection method, we performed the MC closure test for the shower shape band criterion and invariant mass showed in Fig. 4.7 for 0-10% central Pb–Pb collisions. For $8 < E$

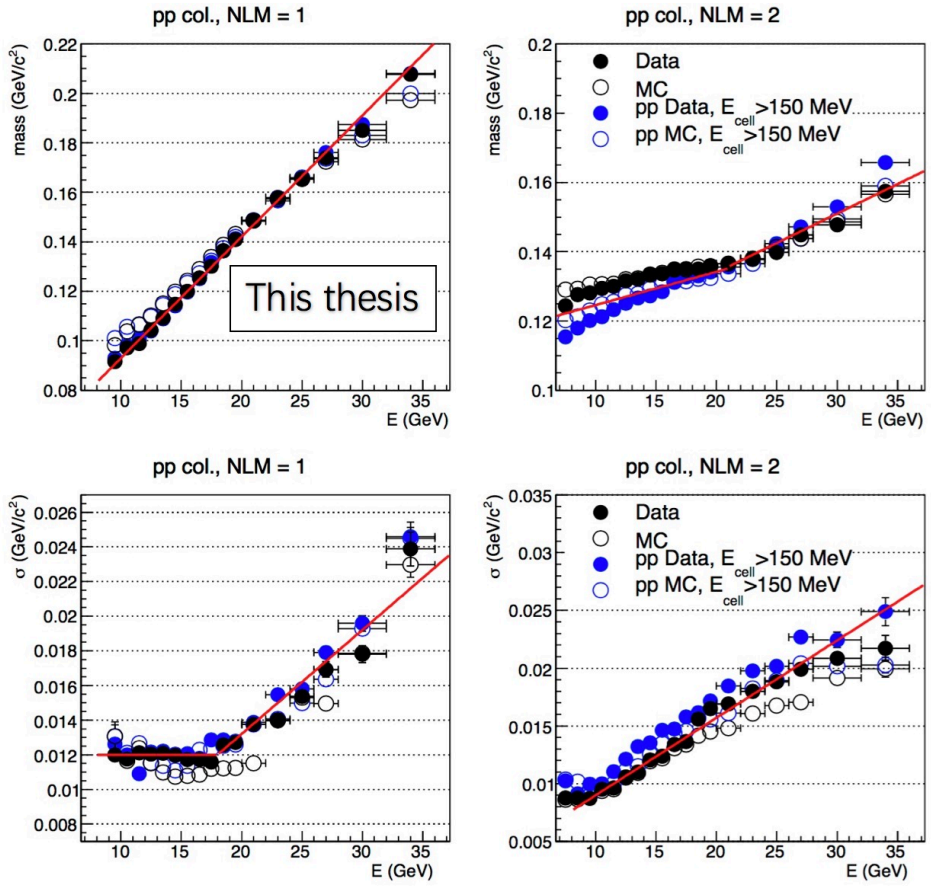

Figure 4.5: Mean mass (upper) and width (lower) of split sub-clusters invariant mass distribution versus cluster energy, for different values of N_{LM} in data and corresponding MC in pp collisions

$<$ 16 GeV and $N_{\mathrm{LM}} = 2$ case, the band criterion selection has a good agreement between data and MC as shown in the left panel. In the right panel, the invariant mass distribution also has a good match between data and MC, and the peak is 0.135 GeV/c^2 at the expected PDG mass of π^0.

4.2.1.4 Other selection of the cluster

Concerning the properties of the EMCal, other selections are also needed for the clusters. The minimum energy of the cluster is requested larger than 0.3 (0.5) GeV in pp (Pb–Pb) collisions. The cell with highest energy in a cluster should be one cell away from the border of the EMCal, and one cluster should contain at least two cells. Taking bad channels in EMCal into account, the cluster should not have bad channels inside, besides, the highest energy cell in cluster should have two cells away from the bad channels. Cluster time is defined the highest energy cell time in a cluster. After the recalibration at the analysis level for the cluster time, one can

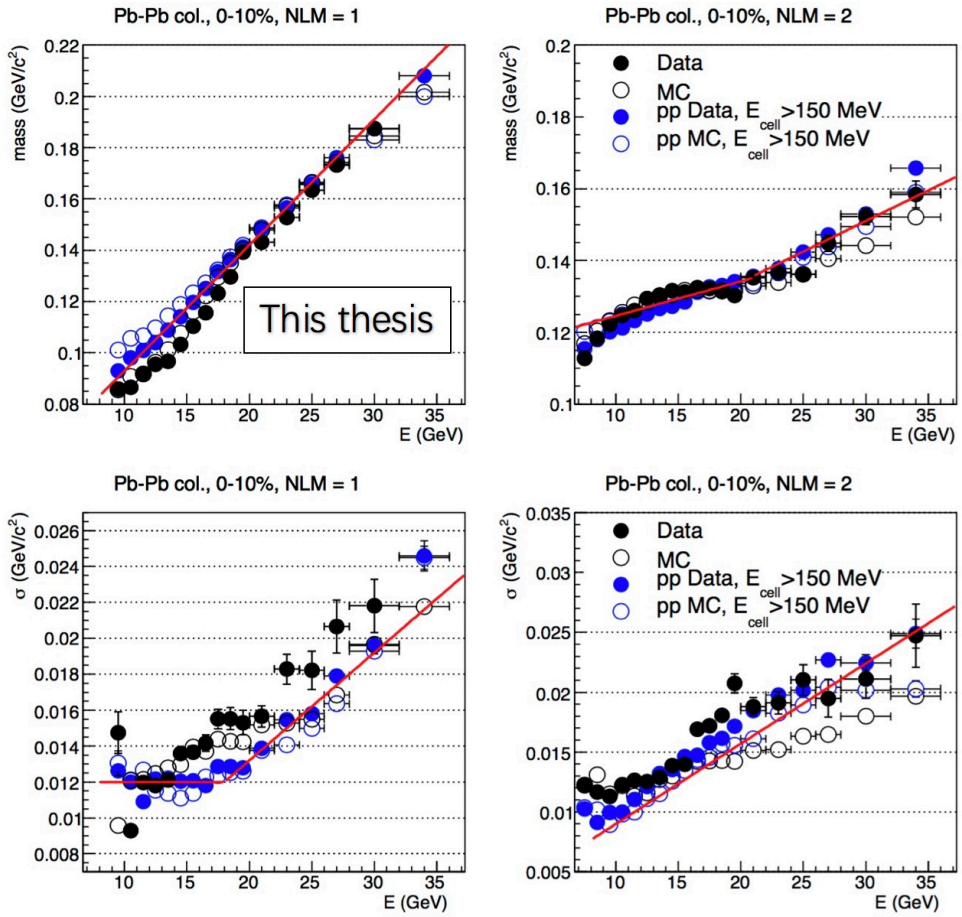

Figure 4.6: Mean mass (upper) and width (lower) of split sub-clusters invariant mass distribution versus cluster energy, for different values of N_{LM} in data and corresponding MC in Pb–Pb collisions.

recenter the time around 0 ns, and gain the time resolution. To further remove the pile up especially for pp collision, the cluster time cut is set to -25 $< t <$ 20 ns.

There are a small fraction of clusters which have large energy but small number of towers, named exotic clusters. These clusters are always generated by slow neutrons (anti-neutrons) interactions with the calorimeter avalanches photo-diodes (APD), specially in EMCal triggered events. However, simulation approach is not available for such process. The rejection is done by identifying these clusters on the quantity:

$$F_{\mathrm{cross}} = 1 - \frac{E_{\mathrm{cross}}}{E_{\mathrm{cell}}^{\mathrm{max}}} \tag{4.6}$$

Where $E_{\mathrm{cell}}^{\mathrm{max}}$ is the energy of the most energetic cell in a cluster. E_{cross} is the summed energies of the three or four cells in the same cluster that share an edge with the $E_{\mathrm{cell}}^{\mathrm{max}}$ cell. If one requires $F_{\mathrm{cross}} > 97\%$, most of such exotic clusters can be removed. In addition, the contributions from the clusters which originated by

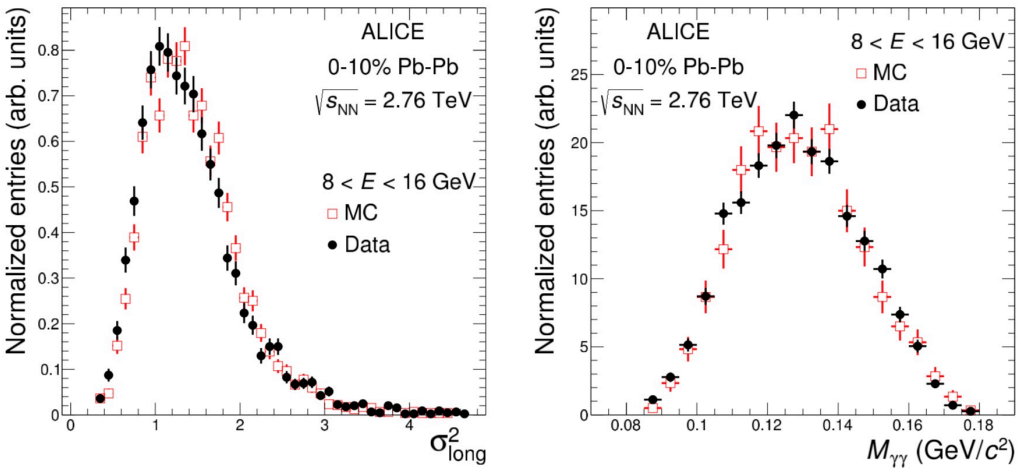

Figure 4.7: Cluster shower shape (left panel) and invariant mass (right panel) distributions for $8 < E < 16$ GeV and $N_{\mathrm{LM}} = 2$ compared between reconstructed π^0 candidates in data and clusters originating from π^0 in HIJING for 0-10% Pb–Pb collisions. The distributions are shown after applying the energy-dependent selections on $\sigma^2_{\mathrm{long}}(\lambda_0^2)$ and $M_{\gamma\gamma}$ [24].

charged hadrons or electrons can be removed by matching the tracks projected to the surface of the EMCal. Due to the tracks interaction with the magnetic field, the η and φ are not exactly the same in the calorimeter, thus the residual requires $\Delta\varphi \leq 0.03$ and $\Delta\eta \leq 0.025$ for pp collision, and $\Delta\varphi \leq 0.035$ and $\Delta\eta \leq 0.03$ for Pb–Pb collisions.

4.2.2 Track selection

The track reconstruction strategy has been described in Sec. 3.2.3.2. The charged hadron reconstruction uses a approach called *hybrid tracks* in order to compensate local inefficiencies in the ITS guaranteeing the uniform distribution in the η and φ direction. It requires tracks containing at least three hits in the ITS, including at least one hit in the SPD, with momentum determined without the primary vertex constraint, and tracks containing less than three hits in the ITS or no hit in the SPD, with the primary vertex included in the momentum determination. The first case contains 90% of the tracks and the latter has 10% of all accepted tracks, independent of p_{T}. Track candidates are further required to have a Distance of Closest Approach (DCA) to the primary vertex less than 2.4 cm in the plane transverse to the beam, and less than 3.0 cm in the beam direction. Accepted tracks are required to be in $|\eta| < 0.8$ and $p_{\mathrm{T}} > 0.5$ GeV/c [24].

4.3 Per-trigger correlated yields

With the identified π^0 as trigger particles and reconstructed tracks as associate particles, one can build the correlation for azimuthal angel and pseudo-rapidity difference $\Delta\varphi = \varphi_{\rm trig} - \varphi_{\rm assoc}$, $\Delta\eta = \eta_{\rm trig} - \eta_{\rm assoc}$. The associated per-trigger yield as a function of these difference can be calculated, details have already been discussed in the first Chapter. In this analysis, we select trigger $p_{\rm T}^{\rm trig}$ range from 8.0 to 16.0 GeV/c, and associate charged hadron in seven $p_{\rm T}^{\rm assoc}$ bin: 0.5-1.0, 1.0-2.0, 2.0-3.0, 3.0-4.0, 4.0-6.0, 6.0-8.0, 8.0-10.0 GeV/c. In principle, the correction and yield extraction should be done for $\Delta\varphi$ and $\Delta\eta$ 2-D map, however, due to the statistic limit(also limited by the EMCal acceptance), the procedures are done only for $\Delta\varphi$ (integrated $\Delta\eta$) to avoid bias from the limited statistics.

4.3.1 Event mixing

The event mixing method is widely used to subtract the combinatorial background (in this analysis, we use another approach instead of it which will be described below. Because mixed events will introduce additional bias if the statistic is not enough). In addition, it's also used for the correlation analysis to correct the detector acceptance and analysis cut effects (the detectors are not perfect, there should exist some missed TPC sectors). The event mixing method by correlating the trigger π^0 with the charged hadron in different events can destroy the correlation when the trigger and associated particles are from the back-to-back jets. However, the mixed events distribution also depends on the transverse momentum, primary vertex position and events multiplicity, it's necessary to build the mixing event pool in the same vertex position and multiplicity class with the one from the same events. Taking also the statistics and memory cost into account, for pp collision, we use 100 events in the pool, z vertex divides into 10 bins from -10 to 10 cm, multiplicity bins are 0-5, 5-10, 10-20, 20-30, 30-40, 40-55, 55-70, >70. For central Pb–Pb collisions, considering the memory cost, the events in the pool reduce to 50, z vertex bins keep the same. multiplicity class uses 2% bin for 0–10% centrality class. What'e more, the mixing event should select the no bias events (using MB trigger instead of other centrality or EMCal trigger events).

As the mixed events are got in the pool, it need to be normalized properly. Commonly, it will be scaled to unity using the value which is the entries of mixed events at $\Delta\varphi = 0$ (why we don't do this correction in $\Delta\varphi - \Delta\eta$ 2-D plane has been explained before). Fig. 4.8 shows same event (black point) and mixed event (red point, after normalization) azimuthal correlations with π^0 trigger transverse momentum of $8.0 < p_{\rm T}^{\rm trig} < 16.0$ GeV/c, associated charged hadrons transverse momentum for $1.0 < p_{\rm T}^{\rm assoc} < 2.0$ GeV/c. the same event uses EMCal L0 trigger, while the mixed event uses the MB trigger. The mixed event distribution is almost flat (our detector is in good performance), the correction for detector acceptance is done by using the same events azimuthal correlations divide the mixed events ones. It's needed to point out that we don't correct the mixed events for high $p_{\rm T}$ associated bins because the statistics of the mixed event are not enough which will

introduce additional bias to the correlation distribution. In order to overcome this difficulty for the statistics, another approach is to use Toy-MC simulation to build the mixed events, which will not be discussed in this thesis.

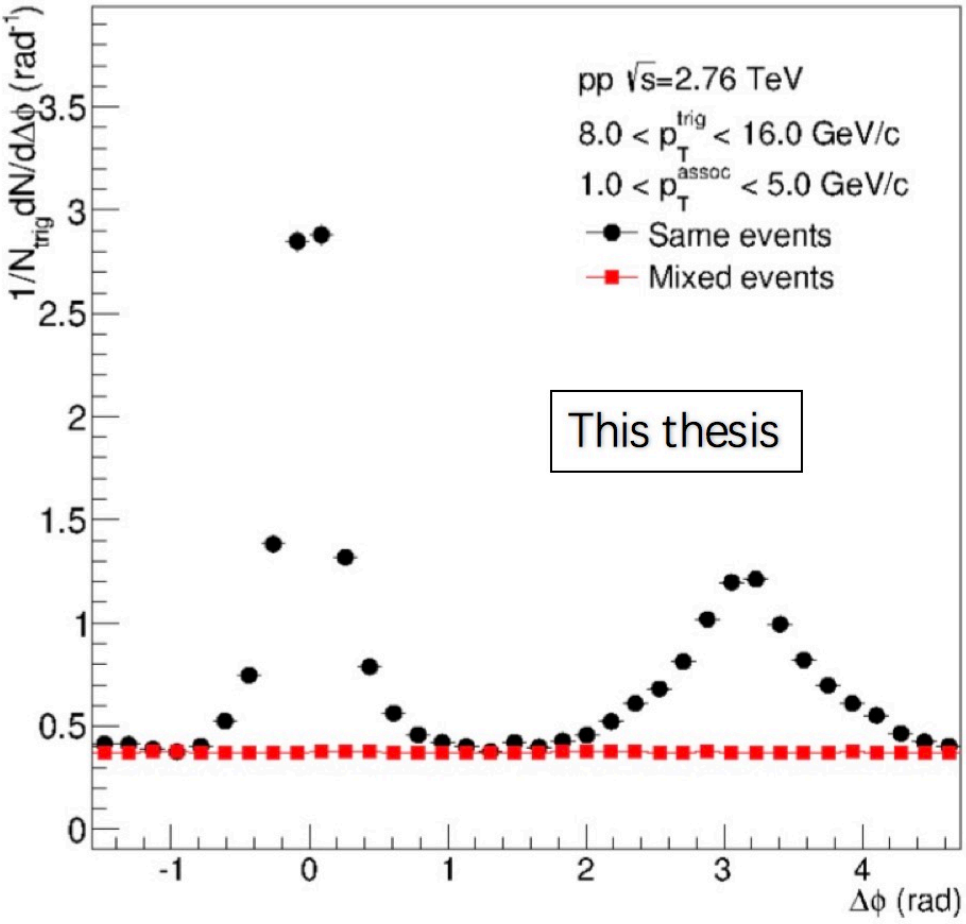

Figure 4.8: Same event (black point) and mixed event (red point, after normalization) azimuthal correlations with π^0 trigger transverse momentum of $8.0 < p_{\mathrm{T}}^{\mathrm{trig}} < 16.0$ GeV/c, associated charged hadrons transverse momentum for $1.0 < p_{\mathrm{T}}^{\mathrm{assoc}} < 2.0$ GeV/c. the same event uses EMCal L0 trigger, while the mixed event uses the MB trigger.

4.3.2 Yield extraction

For the azimuthal correlation distribution, it contains the correlated and un-correlated pairs as shown in Fig. 4.9. Due to not well understand the yield distribution, we don't use the fit method to extract the un-correlated yield. Instead, the counting pairs technique is used in different $\Delta\varphi$ width. Pedestal subtraction extracting correlated yield of charged hadrons uses the technique called Zero Yield At

Minimum (ZYAM) which allows to minimum estimate the background. The yield on the near (away) side is summed over a region of 0 (π) $\pm$ some width. In our analysis, two regions are taken into account to extract the yield.

- Near side $|\Delta\varphi| < 0.7$ *radians*
- Away side $|\Delta\varphi - \pi| < 1.1$ *radians* (considering the broaden of Away side peak in Pb–Pb collisions for low $p_{\mathrm{T}}^{\mathrm{assoc}}$)

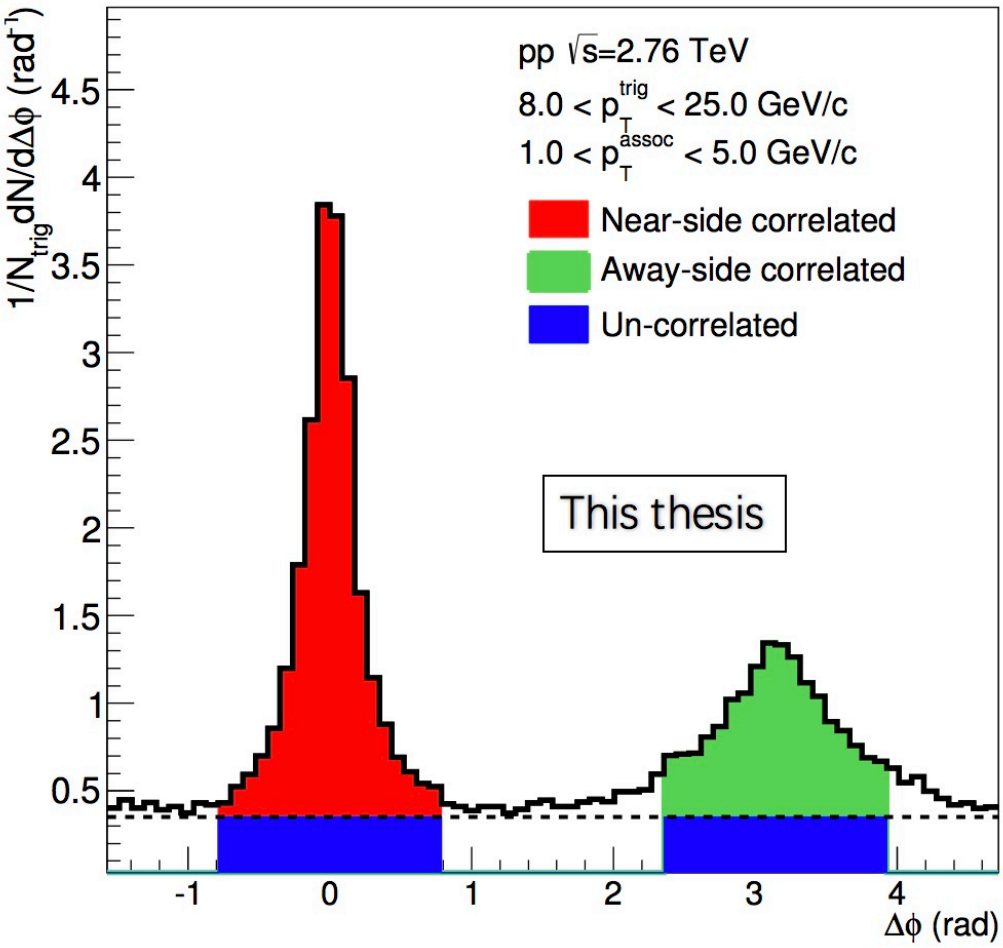

Figure 4.9: The example of π^0 triggered charged particles azimuthal correlations. The red and green regions are the signal correlated pairs in near and away side, and the blue region is the un-correlated paris (underlying event contributions).

Fig. 4.9 shows the example of π^0 triggered charged particles azimuthal correlations. The red and green regions are the signal correlated pairs in near and away side, and the blue region is the un-correlated pairs (underlying event contributions). Considering the near (aways) side jet peak broaden in Pb–Pb collisions, we modify the definition of the regions, details will be discussed later.

4.3.2.1 Pedestal (flat) subtraction

Considering uncorrelated pairs as a flat distribution in $\Delta\varphi$, it's true for the pp collision case. The uncorrelated background is determined by ZYAM method which uses three calculations, and take the average as center value. The three values can also be used to estimate the systematic uncertainties for yield extraction, will be discussed later.

- 1. Two minimum points are taking at $1 < |\Delta\varphi| < \frac{\pi}{2}$ plus two smallest points within 0.2 around the minimum, then the average is decided as the center value.

- 2. Constant fit in $1 < |\Delta\varphi| < \frac{\pi}{2}$. Fig. 4.10 shows the constant fit in $1 < |\Delta\varphi| < \frac{\pi}{2}$ in pp (left) and Pb-Pb (right).

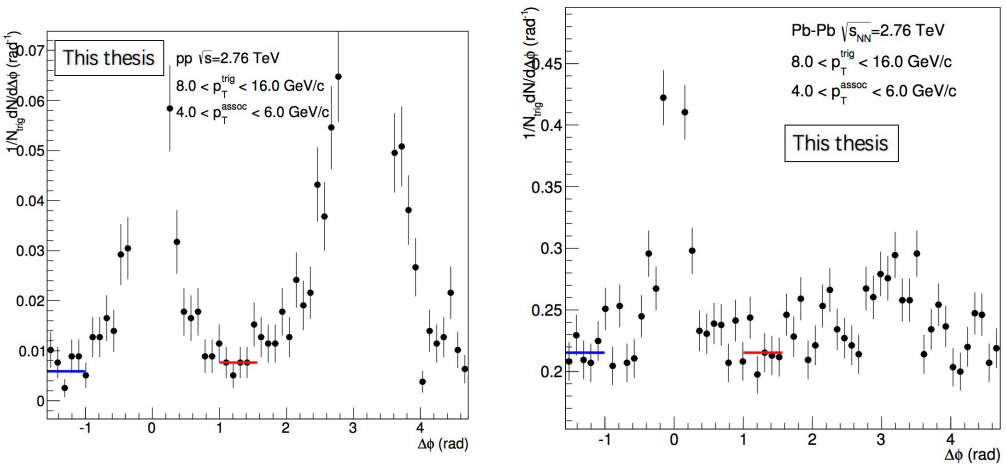

Figure 4.10: The constant fit for the pedestal in $1 < |\Delta\varphi| < \frac{\pi}{2}$ in pp (left) and Pb-Pb (right) according to calculation 2.

- 3. Average value of the eight smallest points in full $|\Delta\varphi|$ range.

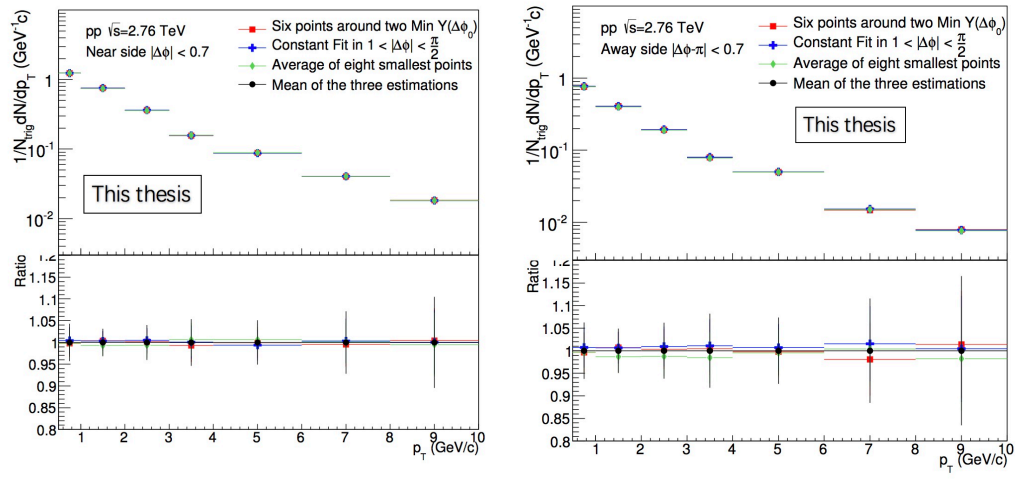

Figure 4.11: The extracted signal using the three different calculations in Near side $|\Delta\varphi| < 0.7$ (left), Away side $|\Delta\varphi - \pi| < 0.7$ (right) in pp at $\sqrt{s} = 2.76$ TeV, respectively. The ratio is each calculation's results with respect to the average among these three.

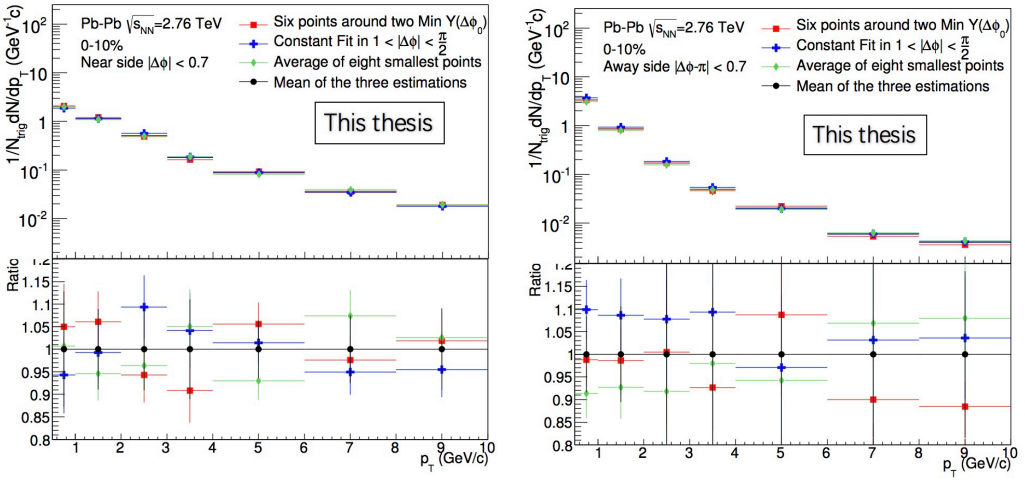

Figure 4.12: The extracted signal using the three different calculations in Near side $|\Delta\varphi| < 0.7$ (left), Away side $|\Delta\varphi - \pi| < 0.7$ (right) in Pb-Pb 0-10% at $\sqrt{s_{\rm NN}} = 2.76$ TeV, respectively. The ratio is each calculation's results with respect to the average among these three.

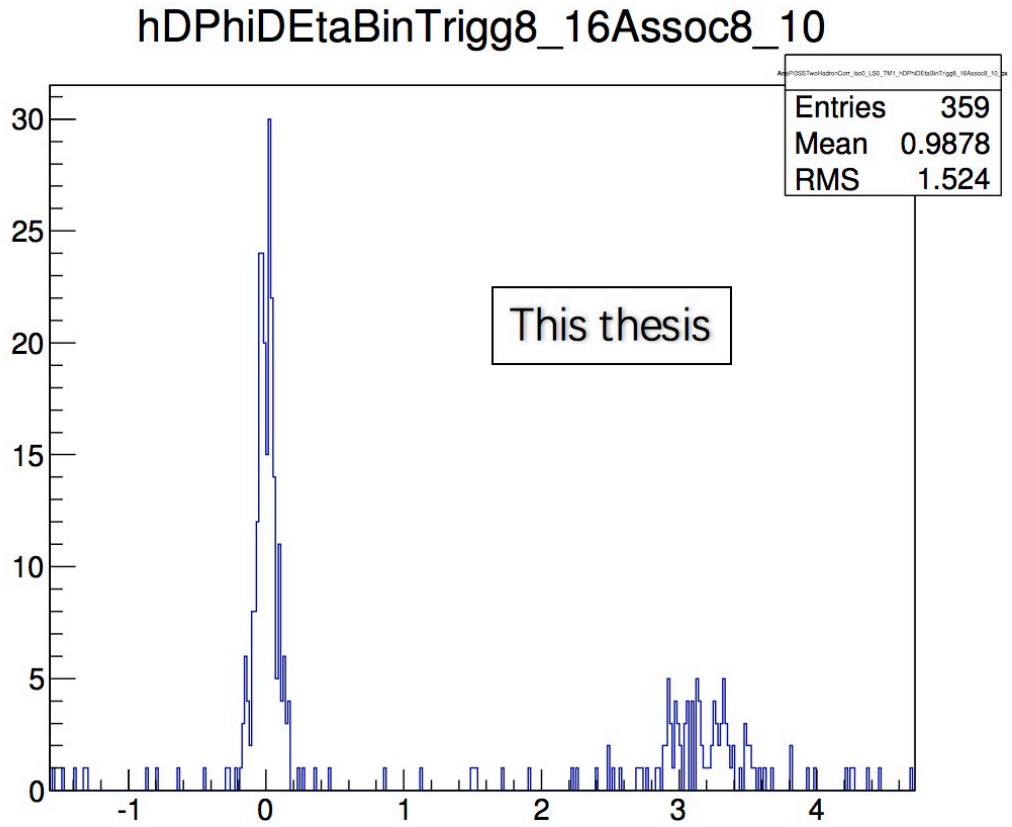

Figure 4.13: The raw azimuthal correlations for trigger p_{T} at $8.0 < p_{\mathrm{T}} < 16.0$ GeV/c and associated hadrons p_{T} at $8.0 < p_{\mathrm{T}} < 10.0$ GeV/c in pp at $\sqrt{s} = 2.76$ TeV.

In addition, Fig. 4.13 shows the raw azimuthal correlations for trigger p_{T} at $8.0 < p_{\mathrm{T}} < 16.0$ GeV/c and associated hadrons p_{T} at $8.0 < p_{\mathrm{T}} < 10.0$ GeV/c in pp at $\sqrt{s} = 2.76$ TeV. A lot of empty bins appear in background region. the standard fit method will underestimate the background. Thus we use Likelihood fit method for high associate p_{T} which is suitable for such low statistics case (fit option is 'LLIE', 'LL' is an improved Log Likelihood fit in case of very low statistics and when bin contents are not integers. 'I' uses integral of function in bin instead of value at bin center. 'E' performs better errors estimation using the Minos technique). Fig. 4.11 and Fig. 4.12 show the results of extracted per-trigger yield of hadrons using the three different methods in Near side $|\Delta\varphi| < 0.7$ and Away side $|\Delta\varphi - \pi| < 0.7$ regions for pp at $\sqrt{s} = 2.76$ TeV and Pb–Pb at $\sqrt{s_{\mathrm{NN}}} = 2.76$ TeV, respectively. Taking the Root Mean Square (RMS) of these three calculations, one can get the yield extraction systematic uncertainties as the blue boxes shown in Fig. 4.14 in pp collision at $\sqrt{s} = 2.76$ TeV and Fig. 4.15 in Pb–Pb collisions at $\sqrt{s_{\mathrm{NN}}} = 2.76$ TeV. In general, the systematic uncertainties are larger in Pb–Pb than pp collisions due to the large background fluctuation in Pb–Pb collisions. and Away side uncertainties

are larger compared with Near side as the signal in Away side is smaller.

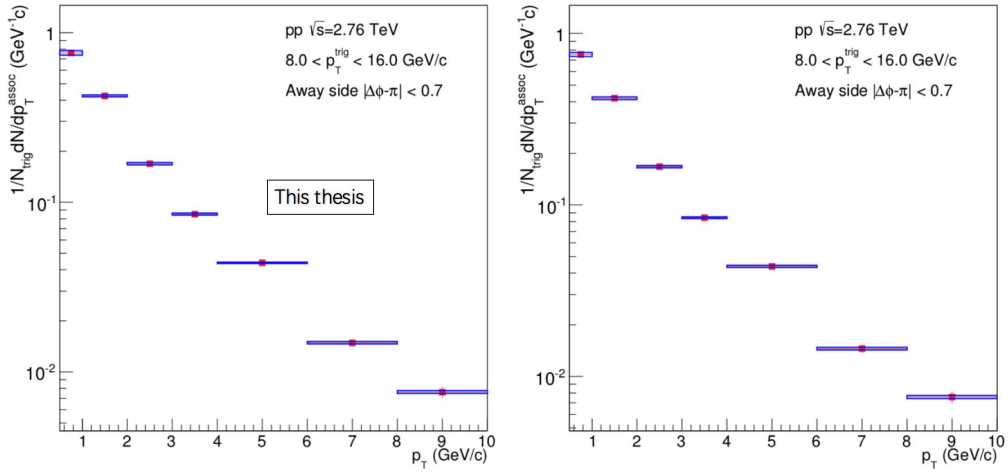

Figure 4.14: The systematic uncertainty for yield extraction (flat background) on Near side $|\Delta\varphi| < 0.7$ (left) and Away side $|\Delta\varphi - \pi| < 0.7$ (right) in pp at $\sqrt{s} = 2.76$ TeV, respectively. The blue boxes are the systematic uncertainties.

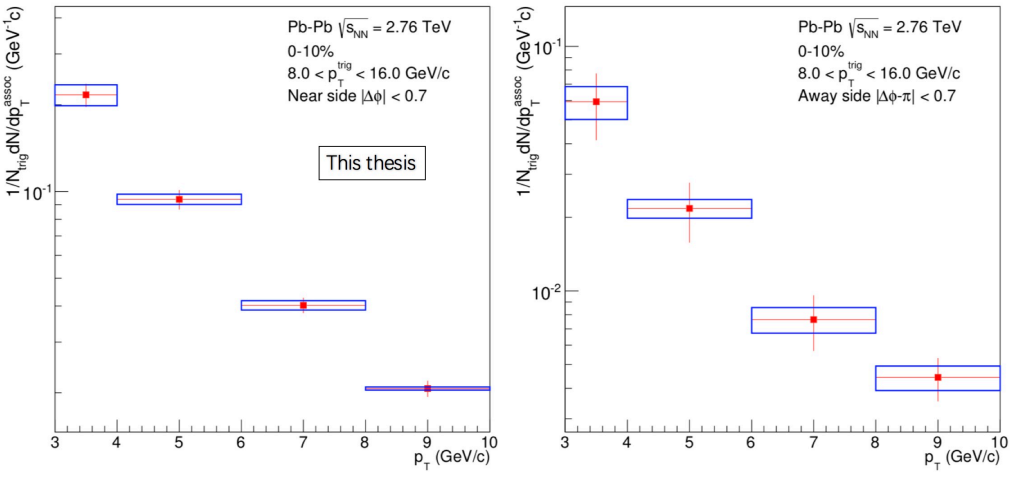

Figure 4.15: The systematic uncertainty for yield extraction (flat background) on Near side $|\Delta\varphi| < 0.7$ (left), Away side $|\Delta\varphi - \pi| < 0.7$ (right) in Pb-Pb 0-10% at $\sqrt{s_{\rm NN}} = 2.76$ TeV, respectively. The blue boxes are the systematic uncertainties.

4.3.2.2 Flow subtraction

In above, we present the subtraction of the background which is considered as a flat distribution. It makes sense only in pp collisions. While for Pb-Pb collisions as discussed in Chapter 1, not only v_2 but also higher-order flow should have no

negligible contributions to the background. Thus in this analysis, we consider v_2–v_5 contributions for the yield extraction in Pb-Pb collisions.

For the v_2 contribution, we extract v_2 from [107]. Since the v_2 of π^0 was not obtained at ALICE, the v_2 of charged pions is used instead of the v_2 of π^0. For v_3–v_5, we take ALICE published charged hadrons result [108] for associate hadrons, and it's also used for π^0 as it's known that π^0 v_n contribution at high p_{T} is similar with that for charged hadron.

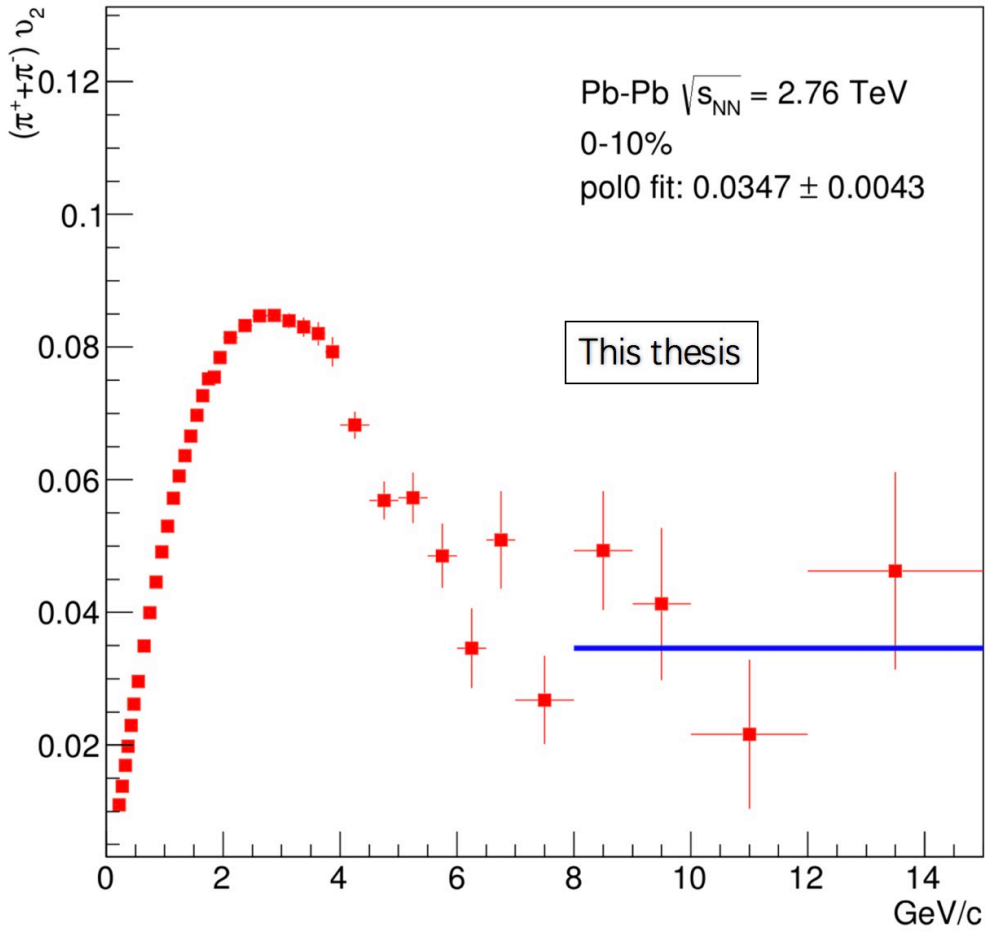

Figure 4.16: v_2 flow of charged pions in Pb-Pb 0-10% at $\sqrt{s}_{\mathrm{NN}}$= 2.76 TeV. The blue line is the polynomial one fit at $8.0 < p_{\mathrm{T}} < 16.0$ GeV/c, the value obtained is0.0347 ± 0.0043. The fit error can be used to estimate the systematic uncertainty.

The v_2 of charged pions is shown in Fig. 4.16. As the flow is almost flat as high transverse momentum, we use polynomial one to fit the region $8.0 < p_{\mathrm{T}} < 16.0$ GeV/c. The fit result is 0.0347 ± 0.0043. The fit error will be used to estimate the systematic uncertainty.

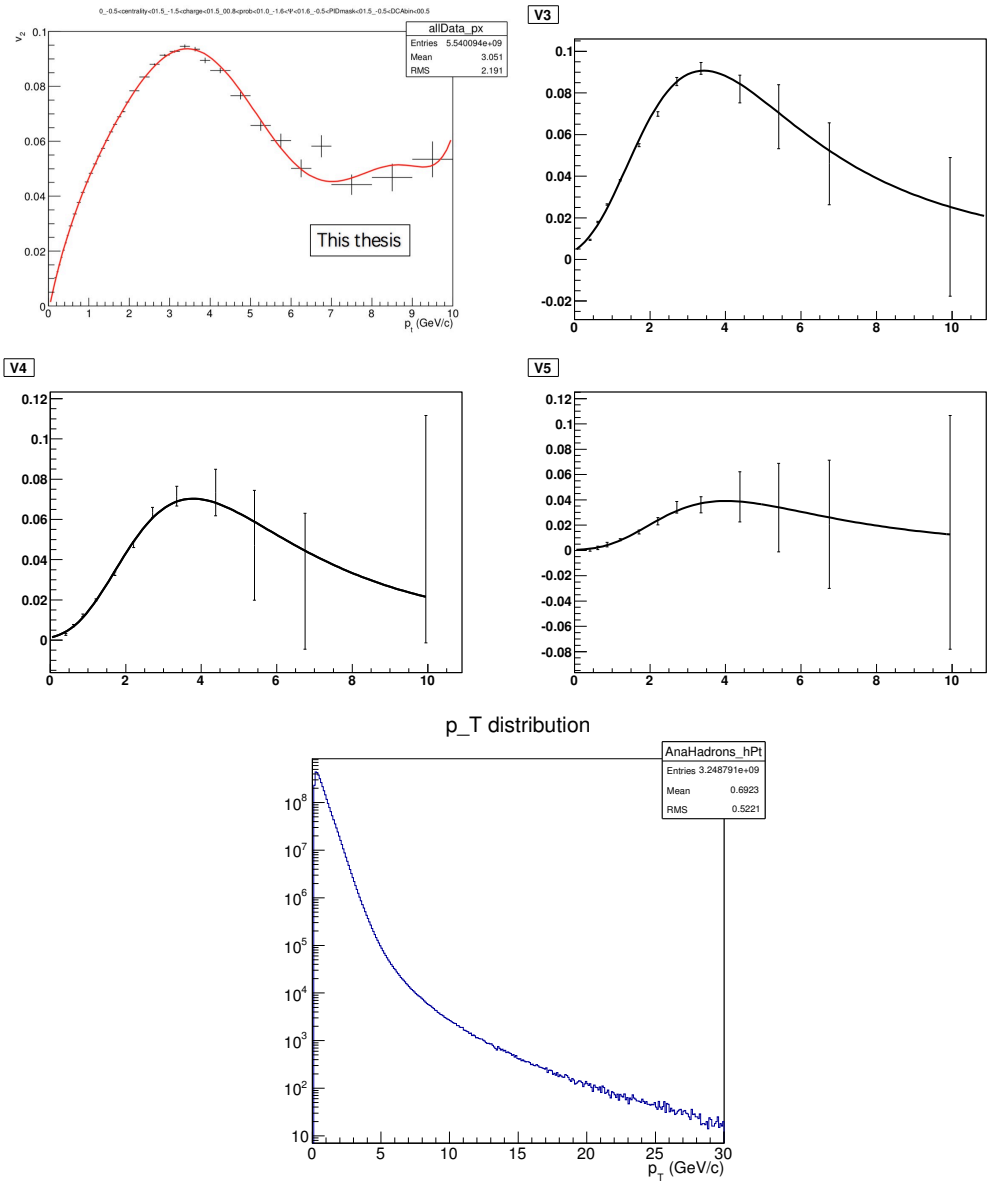

Figure 4.17: v_n and fit function of charged hadrons in Pb–Pb 0-10% at $\sqrt{s_{\rm NN}}$= 2.76 TeV. The last plot is the charged hadrons' raw spectrum from the Pb–Pb data in the analysis.

v_2–v_5 of charged hadron is showed in Fig. 4.3.2.2. Firstly, we use landau distribution or high-order polynomial to fit them and extend to high $p_{\rm T}$ (16 GeV/c), using the integrated fit value for $8.0 < p_{\rm T} < 16.0$ GeV/c as trigger π^0 v_n. For the v_n of associate charged hadron, it's not exactly in the same binning as we used, it's necessary to re-weight them with charged hadron spectrum got in this analysis (the bottom plot is the charged hadrons' raw spectrum from the Pb–Pb data in the analysis), after re-weighting, they can be applied for each $p_{\rm T}$ integral. After calculation, the re-weighted v_n value is less than 4% different from the one before

re-weighting. The fit error is also used to calculate the systematic uncertainties of flow.

Finally, the jet-like correlations can be obtained by

$$J(\Delta\varphi) = C(\Delta\varphi) - b_0(1 + 2\langle v_2^{trig} v_2^{assoc}\rangle \cos(2\Delta\varphi) + 2\langle v_3^{trig} v_3^{assoc}\rangle \cos(3\Delta\varphi) + ...) \tag{4.7}$$

where $J(\Delta\varphi)$ and $C(\Delta\varphi)$ are the jet-like correlations and all correlations. v_n^{trig} and v_n^{assoc} are the flow of trigger particles and associated particles, b_0 is the background scaled factor, which is obtained using ZYAM method of background estimation shown in Sec. 4.3.2.1. The flow contribution is dominant at Near and Away side region, at the background region ($1 < |\Delta\varphi| < \frac{\pi}{2}$), it's very small and can be treated as flat. we estimated two cases: one is treating background region is flat, the other is considering background region with flow contribution (used for the analysis). The extracted b_0 have 0.62% difference between these two.

However, there are also other methods to subtract the flow contribution, such as η-gap method, which getting the azimuthal distribution at large $\Delta\eta$ region where is believed to have no jet contribution (but have flow contribution), then use it as the source to subtract the background in central $\Delta\eta$ region. It was tried for this analysis but due to the lack of statistic, it will introduce large bias thus abandoned for this analysis. At the same time, it's argued whether the background (included flow) is the same between central and large $\Delta\eta$, thus this is the weak point for this method. Recently, an updated method was developed which is actually the combine of η-gap and v_n parameters fit method: by fitting the whole azimuthal distribution with flow contribution at large $\Delta\eta$ region, then applying the extracted fit parameters to the central $\Delta\eta$ region fit. I think this method can be used in the future analysis if we have more statistics, at the same time, v_1 contribution can be taken into account.

4.4 Correction

The correction for the azimuthal correlation should be considered on both trigger π^0 and associated charged hadrons sides, mainly about the reconstruction efficiency, purity (contamination) and p_{T} resolution. Usually these corrections are done both as a function of $\Delta\varphi$ and p_{T} (only selected plots are showed): After got the azimuthal correlations, the N_{trig} should be normalized after the π^0 efficiency correction, other corrections will be applied separately on the azimuthal $\Delta\varphi$ correlation and Near (Away) side yields (after the underlying subtraction), details will be described as below:

4.4.1 π^0 contamination correction

With the cluster splitting method for reconstruction π^0, it will contain the fake contribution of single γ and hadrons. Fig. 4.18 show the MC simulations for the ratio of true π^0 (black), single γ (red) and hadrons (blue) cluster over all the clusters using the cluster splitting reconstruction method for pp collision at $\sqrt{s} = 2.76$ and 7 TeV (left plot), and for Pb–Pb collisions at 0-10% at $\sqrt{s_{\mathrm{NN}}} = 2.76$ TeV (right plot).

As the purity of π^0 is very high with this reconstruction method (90% in pp and 85% in Pb–Pb collisions), instead building fake π^0-hadron correlation to correct for the purity, we can use a simple ratio between reconstructed candidate π^0-hadron correlations and true reconstructed π^0-hadron correlations as the correction factor for π^0 purity, expressed as:

$$P(Gen.p_{\mathrm{T}}, pair) = \frac{\text{reconstructed candidate } \pi^0 - h^{\pm}(Gen.p_T)}{\text{reconstructed true}\pi^0 - h^{\pm}(Gen.p_{\mathrm{T}})} \tag{4.8}$$

The π^0 trigger contamination correction factors are shown in Fig. 4.19, 4.20, 4.21

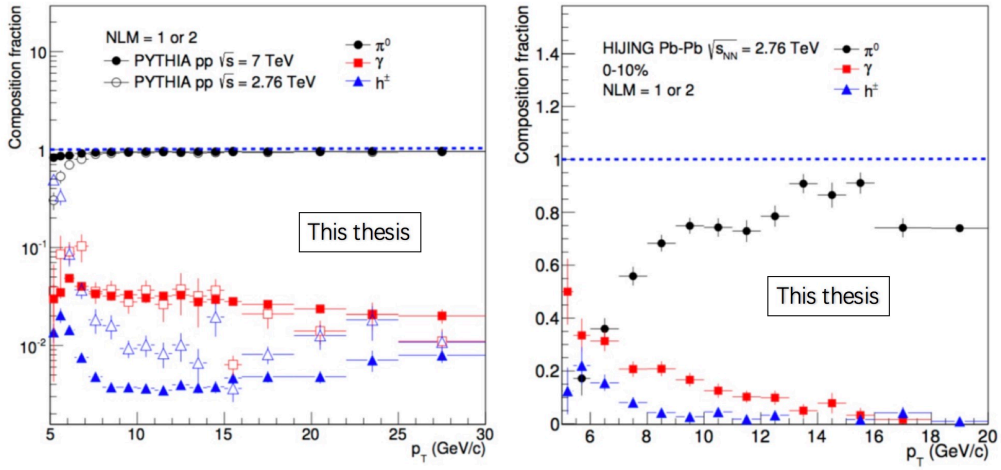

Figure 4.18: The MC simulations for the ratio of true π^0 (black), single γ (red) and hadrons (blue) cluster over all the clusters using the cluster splitting reconstruction method for pp collision at $\sqrt{s} = 2.76$ and 7 TeV (left plot), and for Pb–Pb collisions at 0-10% at $\sqrt{s_{\mathrm{NN}}} = 2.76$ TeV (right plot).

and 4.22. Either as a function $\Delta\varphi$ or p_{T} for Near and Away side in both pp and central Pb–Pb collisions. Different fits are performed in order to calculate the systematic uncertainties, details are described in each caption.

4.4.2 π^0 efficiency correction

Fig. 4.23 shows the π^0 reconstruction efficiency using the cluster splitting method in pp collision at $\sqrt{s} = 2.76$ TeV (left), and 0-10% central Pb–Pb collisions at $\sqrt{s_{\mathrm{NN}}} = 2.76$ TeV (right). The efficiency is around 30% for pp and 20% for Pb–Pb collisions (really higher than the traditional method) considering the limit of EMCal acceptance and reconstruction method. Although, we measure the per-trigger yield, with or without correction of trigger efficiency should not have a effect on the total production, it could have some modification about the Near or Away side correlation jet shape if we use a wide p_{T} integral, besides, the efficiency is not flat as a function of p_{T}, the correction for the trigger efficiency is necessary. A better way to do it is

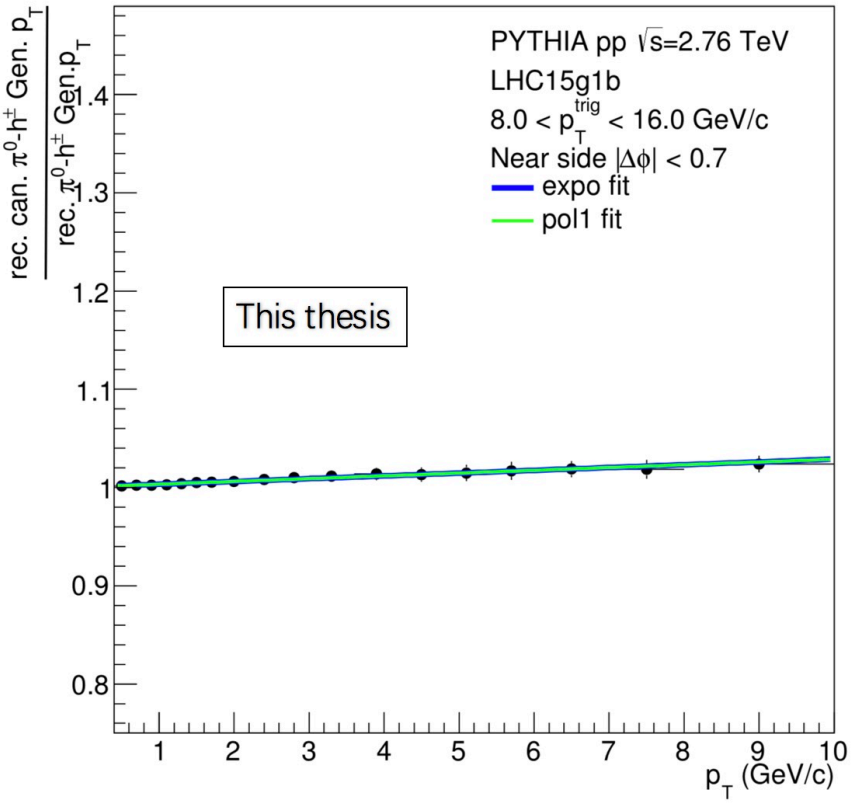

Figure 4.19: The π^0 trigger contamination correction factor as a function of p_{T} from LHC15g1b simulation for pp collisions at $\sqrt{s} = 2.76$ TeV on Near side $|\Delta\varphi| < 0.7$. exponential and polynomial 1 fit results are performed in different colour which will be used for the systematic uncertainty estimation.

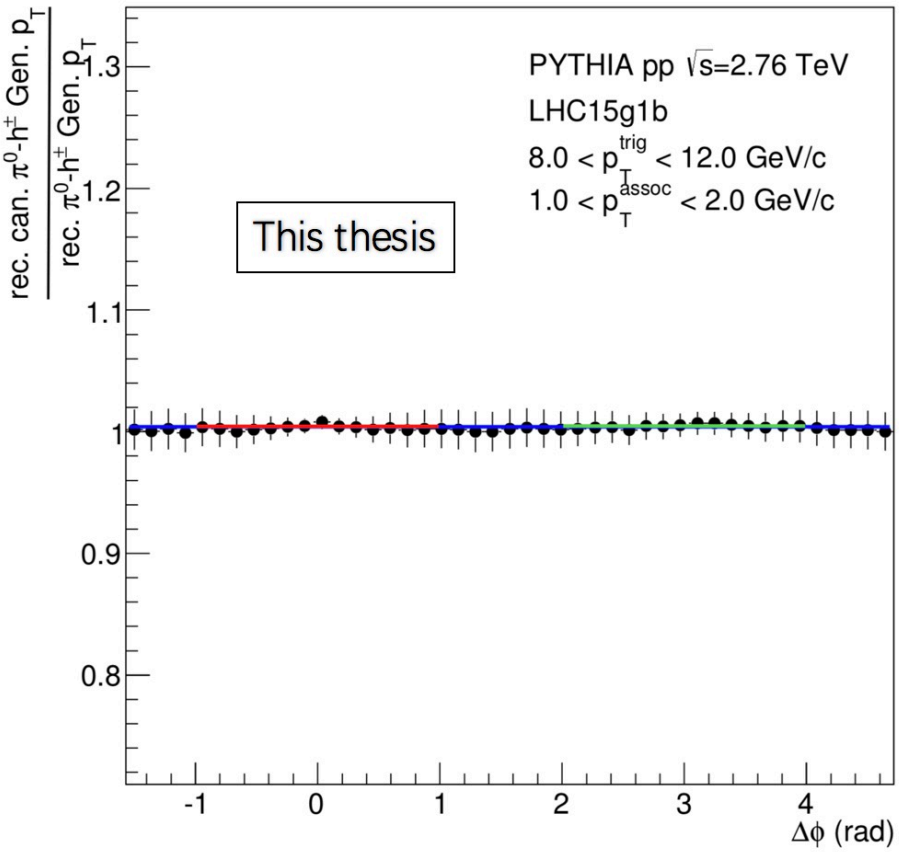

Figure 4.20: The π^0 trigger contamination correction factor as a function of $\Delta\varphi$ with trigger p_{T} region in $8.0 < p_{\mathrm{T}} < 12.0$ GeV/c , associated p_{T} region in $1.0 < p_{\mathrm{T}} < 2.0$ GeV/c, from LHC15g1b simulation for pp collisions at $\sqrt{s} = 2.76$ TeV. A polynomial 1 fit is performed in three different $\Delta\varphi$ ranges, which will be used for the systematic uncertainty estimation.

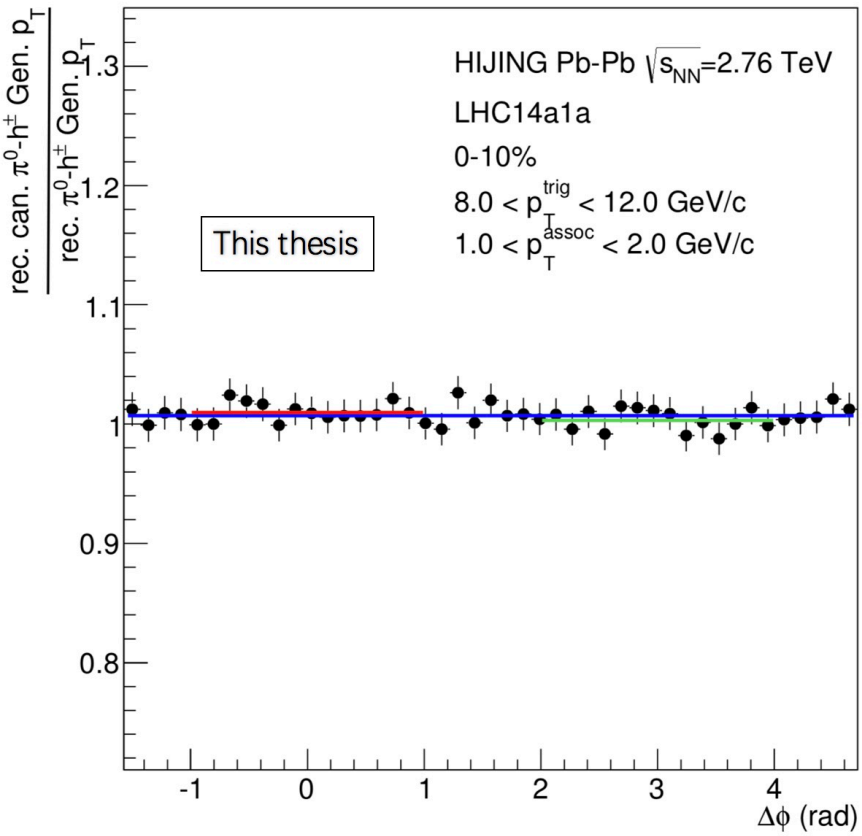

Figure 4.21: The π^0 trigger contamination correction factor as a function of $\Delta\varphi$ with trigger p_{T} region in $8.0 < p_{\mathrm{T}} < 12.0$ GeV/c , associated p_{T} region in $1.0 < p_{\mathrm{T}} < 2.0$ GeV/c, from LHC14k1a simulation for 0-10% Pb–Pb collisions at $\sqrt{s}_{\mathrm{NN}} = 2.76$ TeV. A polynomial 1 fit is performed in three different $\Delta\varphi$ ranges, which will be used for the systematic uncertainty estimation.

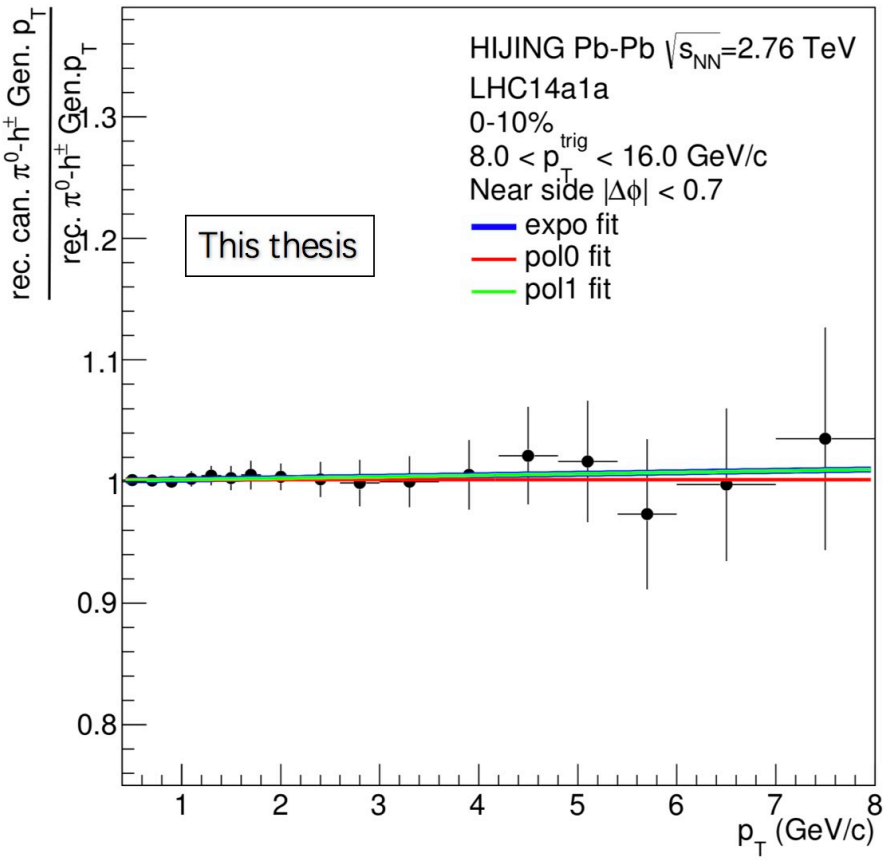

Figure 4.22: The π^0 trigger contamination correction factor as a function of p_{T} from LHC14k1a simulation for 0-10% Pb–Pb collisions at $\sqrt{s_{\mathrm{NN}}} = 2.76$ TeV on Near side $|\Delta\varphi| < 0.7$. exponential and polynomial 1 fit results are performed in different colour which will be used for the systematic uncertainty estimation.

to fit the efficiency, then apply the correction before build the correlation. In this analysis, we first build the correlation in smaller trigger p_{T} then do the bin-by-bin correction (the minimum p_{T} bin is set to Δp_{T}= 1.0 GeV/c) before summed the correlation distribution in bins, which can be expressed as:

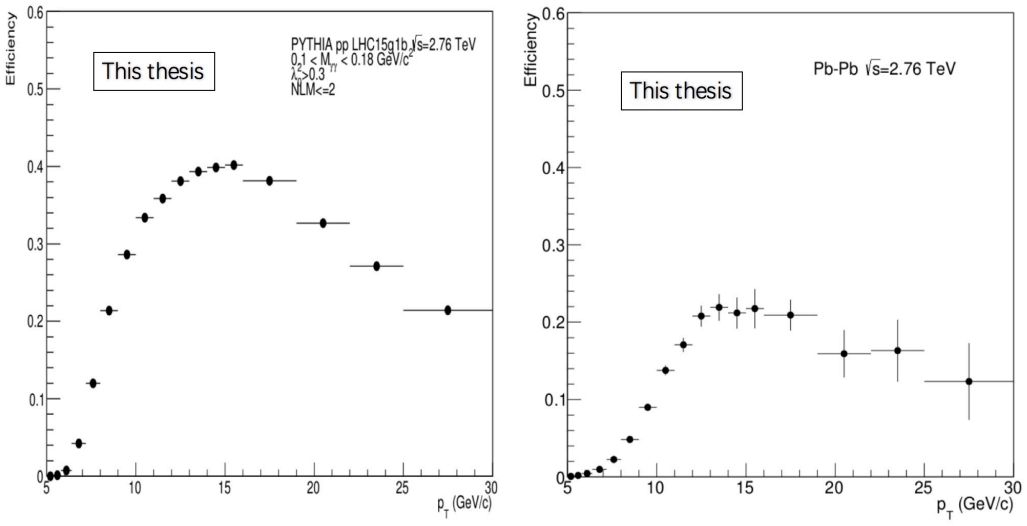

Figure 4.23: π^0 reconstruction efficiency using the cluster splitting method for pp collision at $\sqrt{s}$ = 2.76 TeV (left) , and 0-10% central Pb–Pb collisions at $\sqrt{s}_{\mathrm{NN}}$ = 2.76 TeV (right).

$$\frac{1}{N_{\mathrm{trig}}^{corrected}}\frac{dN_{\mathrm{pair}}^{\mathrm{corrected}}}{d\Delta\varphi} = \frac{1}{\sum_{\Delta p_{\mathrm{T(i)}}}\frac{1}{\varepsilon_i}N_{\mathrm{trig(i)}}(\Delta p_{\mathrm{T}}^{\mathrm{trig}})}\sum_{\Delta p_{\mathrm{T(i)}}}\frac{1}{\varepsilon_i}\frac{dN_{\mathrm{pair(i)}}^{Raw}}{d\Delta\varphi}(\Delta p_{\mathrm{T}}^{\mathrm{trig}}) \quad (4.9)$$

Fig. 4.24 shows the comparison of azimuthal correlations with (red) and without (blue) π^0 trigger efficiency correction and ratio in pp (top plots) and 0-10% Pb–Pb (bottom plots) collisions for two different trigger p_{T} region with associated p_{T} region in $1.0 < p_{\mathrm{T}} < 2.0$ GeV/c. One can find that this correction has some modification about the $\Delta\varphi$ shape, and within 2% effects at this specific p_{T} integral region.

4.4.3 π^0 and track pairs p_{T} resolution correction

Similar with what we did for trigger π^0 purity correction, the correction for p_{T} resolution of trigger π^0 and associated charged hadron are done at the same time at the level of correlation pairs. Thus the correction factor can be expressed as:

$$R(Rec.p_{\mathrm{t}}, Gen.p_{\mathrm{t}}, pair) = \frac{\text{reconstructed true } \pi^0 - h^{\pm}(Rec.p_T)}{\text{reconstructed true } \pi^0 - h^{\pm}(Gen.p_T)} \quad (4.10)$$

Which is the ratio between reconstruction and generated p_{T} of the π^0-hadron correlations. Fig. 4.25 and 4.26 show the simulations of the correction factors as a

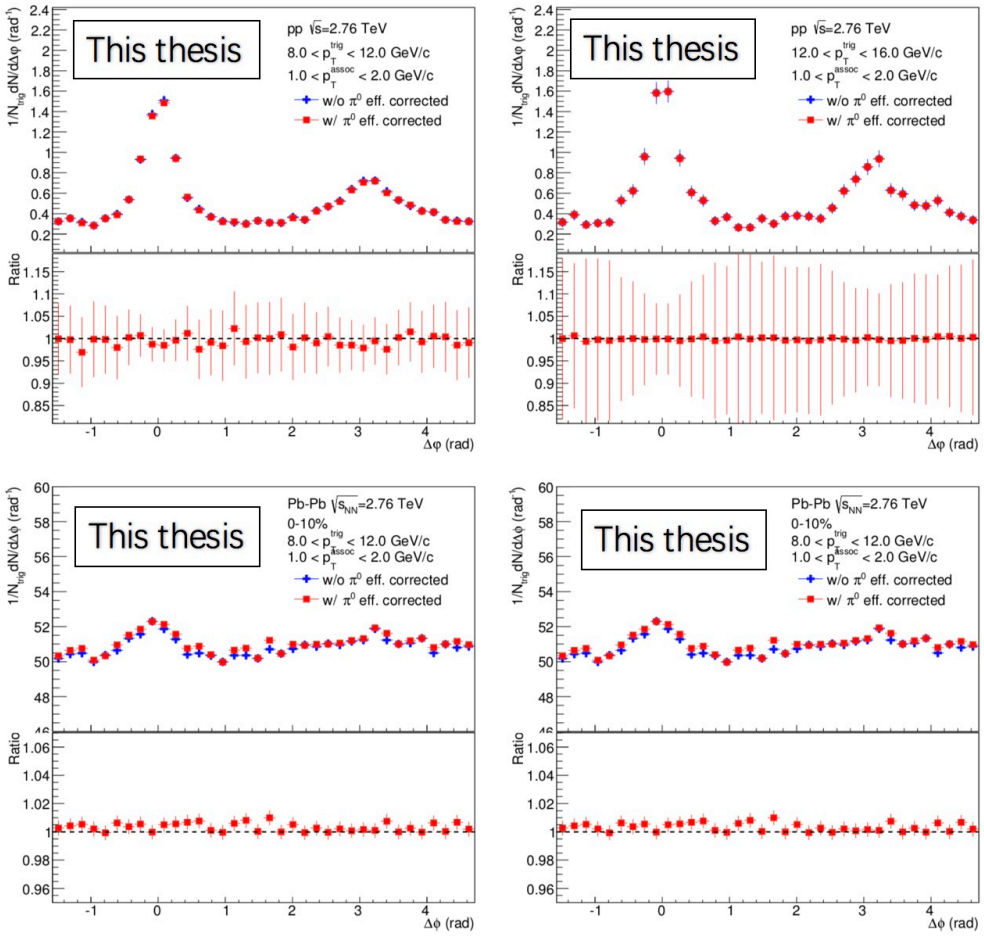

Figure 4.24: The comparison of azimuthal correlations with (red) and without (blue) π^0 trigger efficiency correction and ratio in pp (top two) and 0-10% Pb–Pb (bottom two) collisions for two different trigger p_{T} region with associated p_{T} region in $1.0 < p_{\mathrm{T}} < 2.0$ GeV/c.

function of $\Delta\varphi$ and p_{T} on Near side $|\Delta\varphi| < 0.7$ from LHC15g1b for pp collision and LHC14a1a for 0-10% Pb–Pb collisions at 2.76 TeV, different fits are performed in order to calculate the central correction factor and systematic uncertainty, details are explained in each caption.

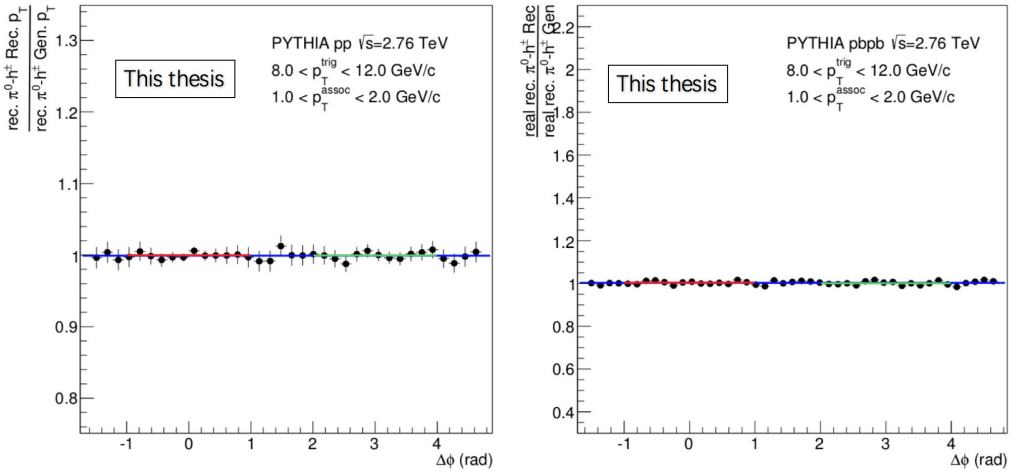

Figure 4.25: The MC simulation of π^0-hadron correlations p_{T} resolution correction factor as a function of $\Delta\varphi$ from LHC15g1b for pp collision (left) and LHC14a1a for 0-10% Pb–Pb collisions (right) at 2.76 TeV with trigger p_{T} region in $8.0 < p_{\mathrm{T}} < 12.0$ GeV/c , and associated charged hadron region in $1.0 < p_{\mathrm{T}} < 2.0$ GeV/c. Polynomial 0 fits are performed in different $\Delta\varphi$ region in order to calculate the central correction factor and systematic uncertainty.

4.4.4 Track purity and efficiency corrections

The track efficiency need to be corrected considering the ITS+TPC acceptance (we choose $|\eta| < 0.8$) and the hybrid track reconstruction method, it can be got from the ratio between reconstruction and generated level number of primary tracks. For the track purity, what we need for the physical analysis is the charged tracks (charged pions, kaons and protons) which from the primary decay, so that the ones from secondary decay should be removed. the track efficiency (red line) and purity (blue line) are around 85% and 95% estimated with PYTHIA generator (LHC15g1b) simulation in pp collisions at $\sqrt{s} = 2.76$ TeV as shown in Fig. 4.27. For 0-10% central Pb–Pb collisions at $\sqrt{s_{\mathrm{NN}}} = 2.76$ TeV, Fig. 4.28 indicates the track purity (black points) is 98% and efficiency (red points) is 78% by HIJING generator (LHC14a1a).

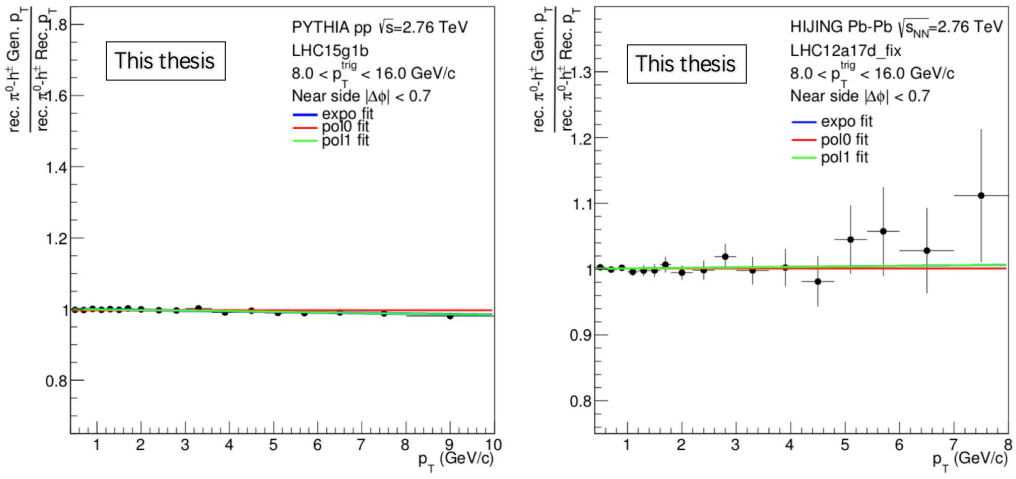

Figure 4.26: The MC simulation of π^0-hadron correlations p_{T} resolution correction factor as a function of p_{T} on Near side $|\Delta\varphi| < 0.7$ from LHC15g1b for pp collision (left) and LHC14a1a for 0-10% Pb–Pb collisions (right) at 2.76 TeV with trigger p_{T} region in $8.0 < p_{\mathrm{T}} < 16.0$ GeV/c , and associated charged hadron region in $1.0 < p_{\mathrm{T}} < 2.0$ GeV/c. Polynomial 0, 1 and exponential fits are performed in order to calculate the central correction factor and systematic uncertainty.

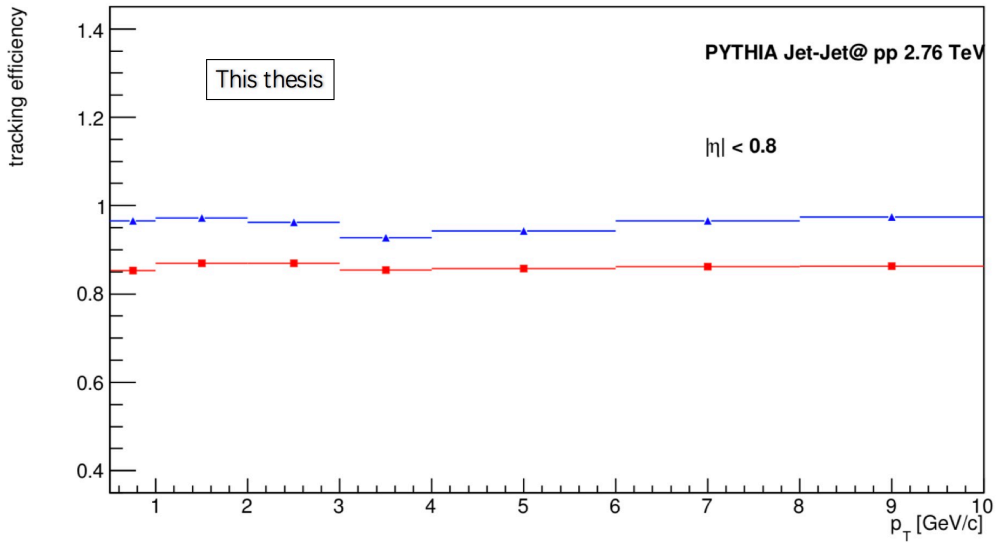

Figure 4.27: Hybrid track purity (blue line) and efficiency (red line) estimated with PYTHIA generator (LHC15g1b) simulation in pp collisions at $\sqrt{s} = 2.76$ TeV.

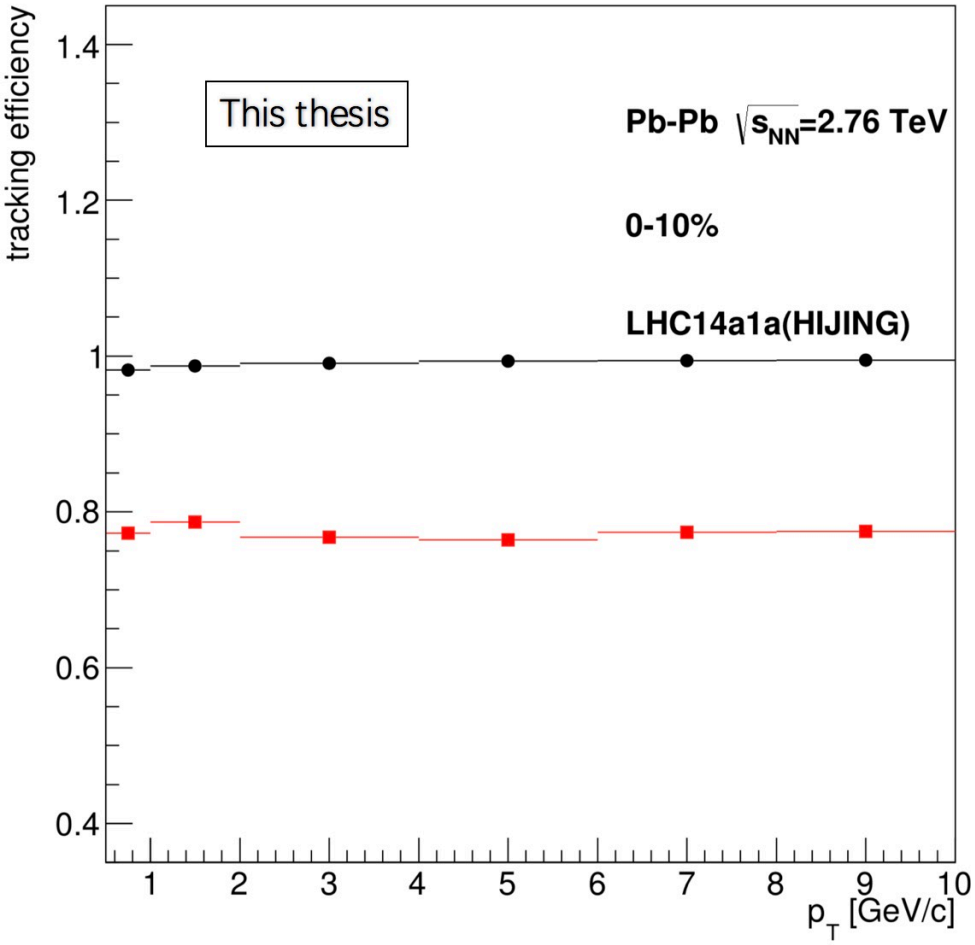

Figure 4.28: Hybrid track purity (black points) and efficiency (red points) simulated by HIJING generator (LHC14a1a) for 0-10% central Pb–Pb collisions at $\sqrt{s}_{\mathrm{NN}}$ = 2.76 TeV.

4.5 Systematic uncertainty

In this section, the systematic uncertainty sources will be discussed. As we know, for the data analysis, we should use as looser cuts, less steps of correction procedures as we can to avoid bias the data. However, due to the limited statistics, we have to apply some tighter cuts optimized the selections of the observables. For this analysis, the systematic uncertainty sources mainly come from the selections of trigger π^0 and associated charged tracks, at the same times, the uncertainties to obtain the correction factors. The systematic about the correction factors are calculated using different fit (either using different fit function or different fit regions $-\frac{\pi}{2} < \Delta\varphi < \frac{3\pi}{2}$, $1.0 < \Delta\varphi < 1.0$ and $2.0 < \Delta\varphi < 4.0$, according to the RMS), and the flat or flow background subtraction system uncertainties are also described in Sec. 4.4. Below, details about each systematic sources will be given.

4.5.1 MC closure test

Before MC closure test, a useful check has been done before correlation on π^0 and charged hadron which makes sure the identification of the trigger and associated particle is in good quality. Fig. 4.29 shows the charged hadron spectrum use for this analysis (black points) compared with ALICE published result (red points) in pp [109] and Pb–Pb [110] collisions at 2.76 TeV. Note that, in order to get the same physical results, the correction procedures are followed exactly the same with in the papers, in addition, we rerun the pp data with MB trigger events (in this analysis, we use EMCal-level 0 trigger) using the same framework. these results match well within uncertainties. Due to the lack of sources for the publications about π^0 spectrum, we only compare the result of π^0 at raw spectrum level with the one got from spectrum analyzer in ALICE for pp collision at $\sqrt{s} = 2.76$ TeV, the results are also consistent with each other within uncertainties as shown in Fig. 4.30. The correction factors are obtained from MC simulation, it's necessary

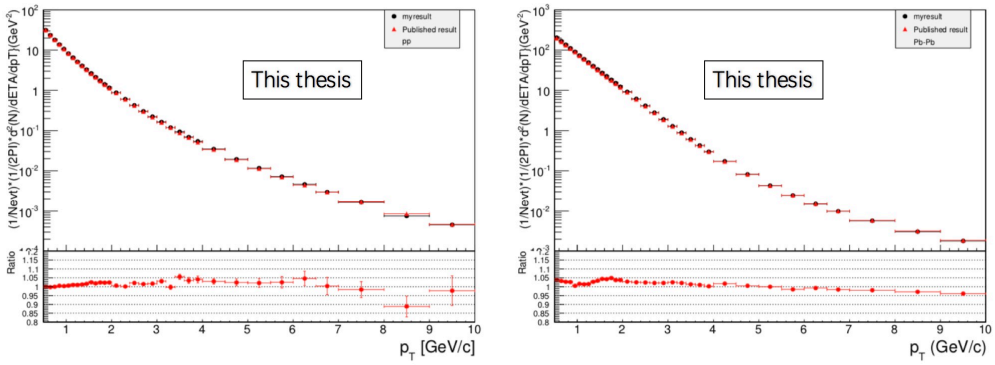

Figure 4.29: The comparison of our charged hadron spectrum with the ALICE published results in pp (left) and Pb–Pb (right), and the ratio of them.

to guarantee the MC can reproduce the data. Fig. 4.31 shows azimuthal correction

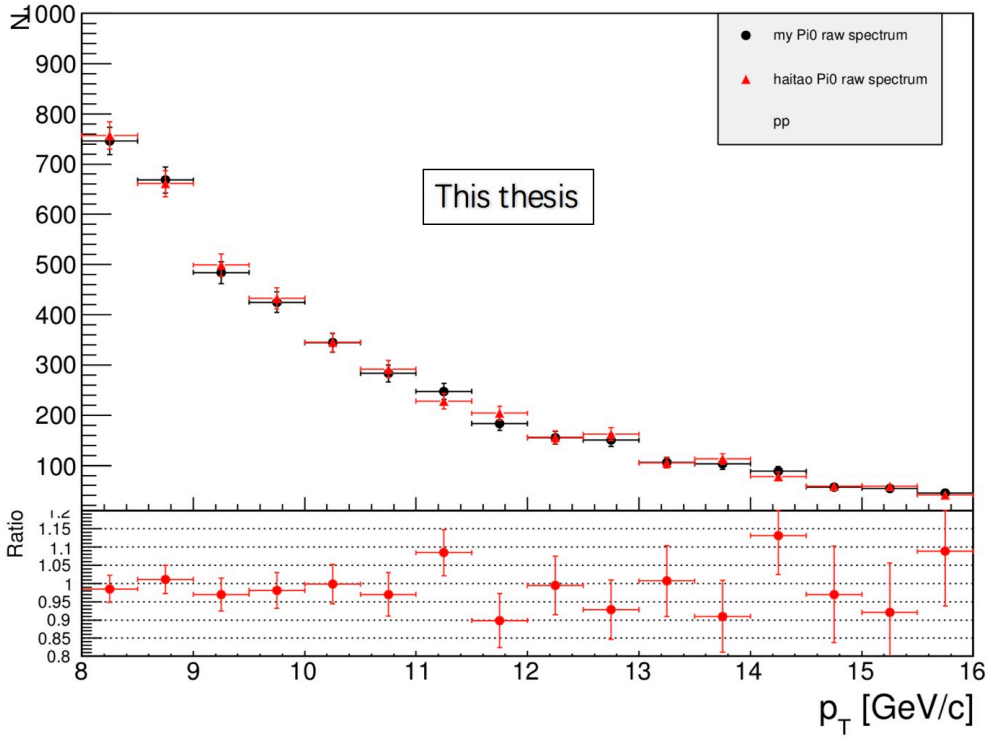

Figure 4.30: The comparison of π^0 raw spectrum with the one got from spectrum analyzer in ALICE for pp collision at $\sqrt{s} = 2.76$ TeV.

of π^0-hadron in different cases for pp (left) and Pb–Pb (right) collisions at 2.76 TeV, the correction procedure applied to MC reconstruction level (black points), it has good agreements with MC generated level (blue points), the ratio is fluctuation around unity (from the below of the plots). At the same time, the MC simulation matches the corrected data spectrum well for the pp collisions (left), and lower than that in Pb–Pb collisions as it's known that HIJING generator can't describe the background well. Thus less than 2% systematic uncertainties are assigned to it.

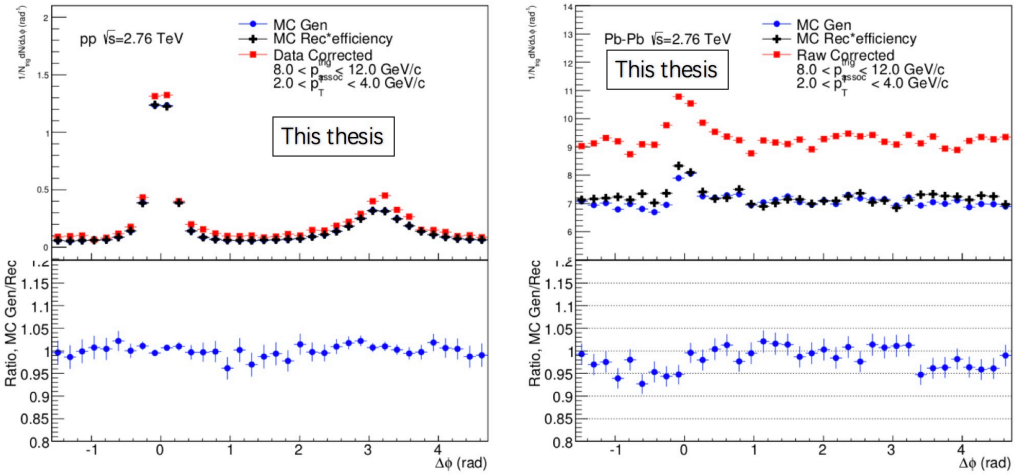

Figure 4.31: The correction procedure applied to MC simulations as a closure test for pp LHC15g1b (left) and Pb–Pb LHC14a1a (right), details explained in the text.

4.5.2 Centrality check

The online trigger for high centrality collisions selects events based on the sum of amplitudes measured in the forward V0 detectors above some fixed threshold. However online we can access the signal only in 25ns (1 LHC clock cycle), offline we can sum over several clock cycles, in central collisions up to 6-7 clock cycles are needed. So offline the threshold that was approximately set to 0-10% is smeared and the trigger efficiency is smaller than 1. The centrality dependence of events for the Pb–Pb data taken in 2011 is showed in Fig. 4.32 (left panel), the efficiency is almost 100% for 0-8% centrality class, while around 80% for 8-10%. In order to check the effect of the not fully efficient for the centrality. We use polynomial 0 to fit the centrality region 0-8%, then flatten the centrality by scaling the region 8-10% to the fit value: add about 10% events for centrality class 8-9% and 43% events for centrality class 9-10% obtained by rerunning the analysis in the centrality classes for 8-9% and 9-10%). Finally, we compare the azimuthal correlation with flatten centrality and without flatten centrality (right panel), the difference is less than 1% (even less after the background subtraction), so it should have negligible effect on our final results.

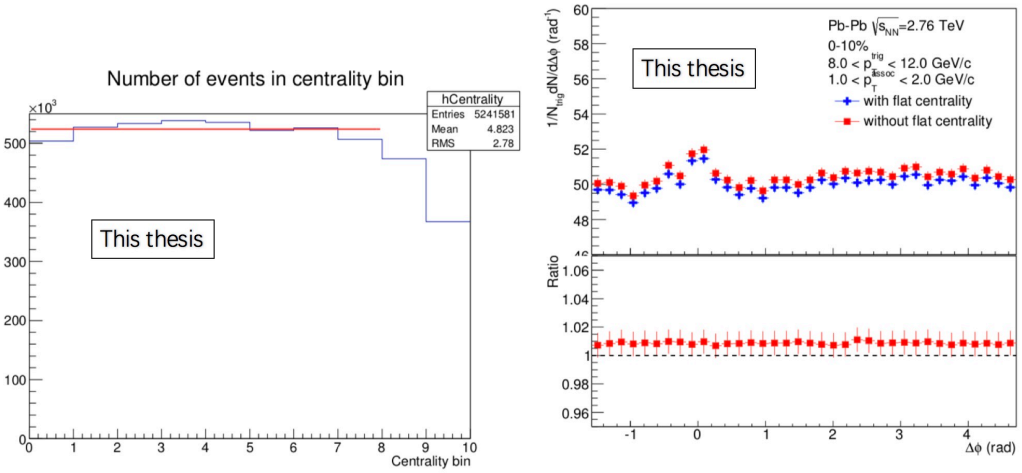

Figure 4.32: The centrality dependence of events and polynomial 0 fit for centrality class 0-8% (left), right plot shows the comparison of azimuthal correlation with flatten centrality (blue points) and without flatten centrality (red points), and the ratio of them.

4.5.3 systematics on the cuts

4.5.3.1 cuts on trigger π^0

As described before, the shower shape cuts are used to select trigger π^0, in order to cross check it, another rough cut is applied which requests $0.3 < \lambda_0^2 < 5$. Fig. 4.33 shows the comparison of per-trigger yield as a function of $\Delta\varphi$ (left) and p_{T} in Near side (right) obtained using shower shape cuts (red points) and $0.3 < \lambda_0^2 < 5$ cut (blue points) in pp collisions at $\sqrt{s} = 2.76$ TeV, and Fig. 4.33 shows the results for Pb–Pb collisions. In general, the discrepancy for the $\Delta\varphi$ distribution between these two selections are very small, while for the p_{T} distribution, it's around 2-3%.
The invariant mass window cuts are also checked. We change from the default cut $M(E) - 3\sigma < M_{\gamma\gamma} < M(E) + 3\sigma$ to the 2.5σ cut. Fig. 4.35 shows the comparison of per-trigger yield as a function of $\Delta\varphi$ (left) and p_{T} in Near side (right) obtained using standard invariant mass 3σ cut (red points) and 2.5σ cut (blue points) in pp collision at $\sqrt{s} = 2.76$ TeV, and Fig. 4.36 gives the comparison in Pb–Pb collisions at $\sqrt{s_{\mathrm{NN}}} = 2.76$ TeV. The uncertainties are less than 3%.

4.5.3.2 cuts on associated charged hadron

In this analysis, we use hybrid tracks for the charged hadrons selections, another selection which reconstruct tracks only based on the information from TPC called TPC-Only track are used to estimate the cut systematic uncertainties. Fig. 4.37 shows the comparison of per-trigger yield as a function of $\Delta\varphi$ (left) and p_{T} in Near side (right) obtained using standard Hybrid track cut (red points) and TPC-Only track cut (blue points) in pp collision at $\sqrt{s} = 2.76$ TeV, and the check for Pb–Pb

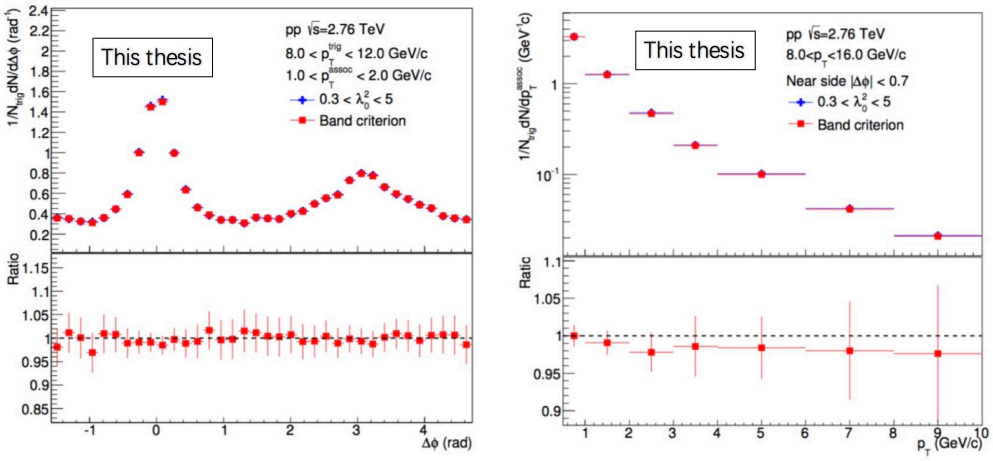

Figure 4.33: The comparison of per-trigger yield as a function of $\Delta\varphi$ (left) and p_{T} in Near side (right) obtained using shower shape cuts (red points) and $0.3 < \lambda_0^2 < 5$ cut (blue points) in pp collision at $\sqrt{s} = 2.76$ TeV.

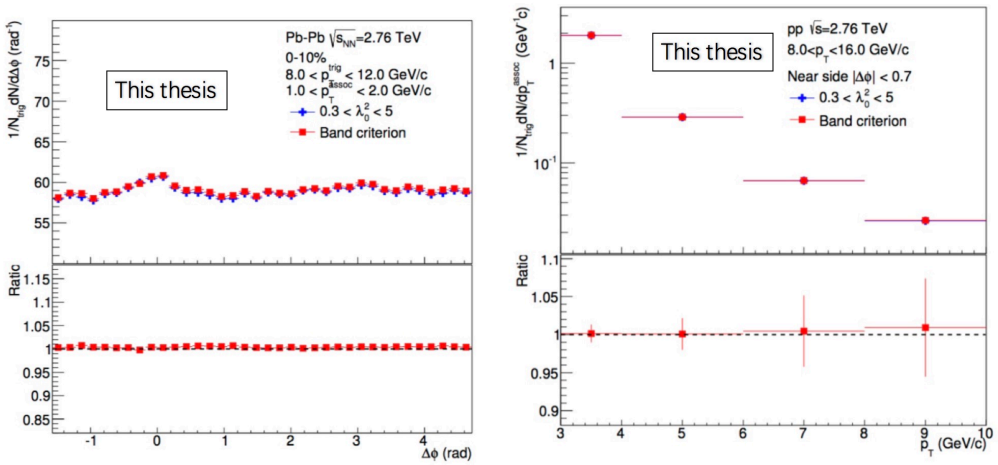

Figure 4.34: The comparison of per-trigger yield as a function of $\Delta\varphi$ (left) and p_{T} in Near side (right) obtained using shower shape cuts (red points) and $0.3 < \lambda_0^2 < 5$ cut (blue points) in Pb–Pb collisions at $\sqrt{s_{\mathrm{NN}}} = 2.76$ TeV.

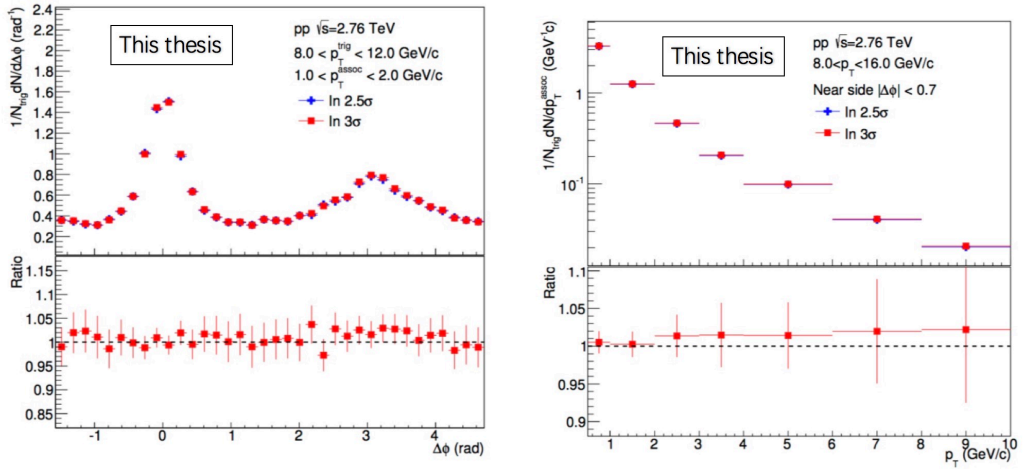

Figure 4.35: The comparison of per-trigger yield as a function of $\Delta\varphi$ (left) and p_{T} in Near side (right) obtained using standard invariant mass 3σ cut (red points) and 2.5σ cut (blue points) in pp collision at $\sqrt{s} = 2.76$ TeV.

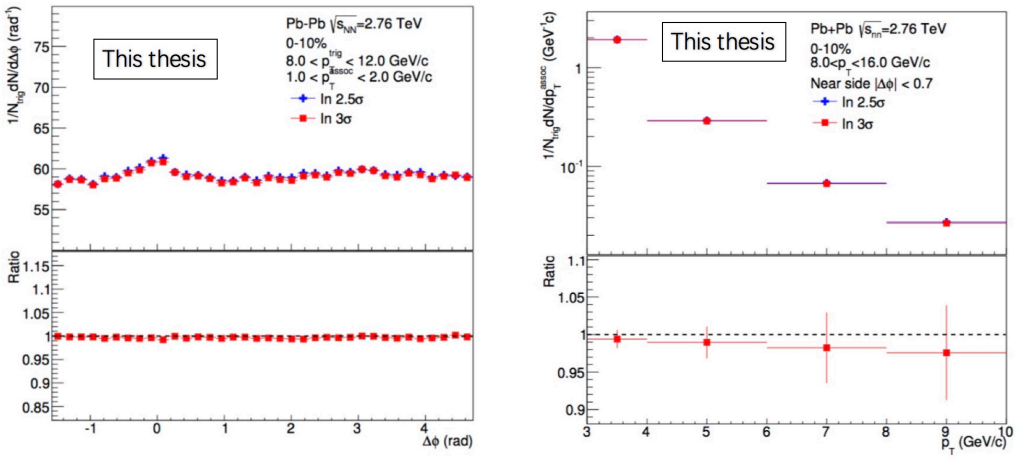

Figure 4.36: The comparison of per-trigger yield as a function of $\Delta\varphi$ (left) and p_{T} in Near side (right) obtained using standard invariant mass 3σ cut (red points) and 2.5σ cut (blue points) in Pb–Pb collisions at $\sqrt{s}_{\mathrm{NN}} = 2.76$ TeV.

collisions is presented in Fig. 4.38.

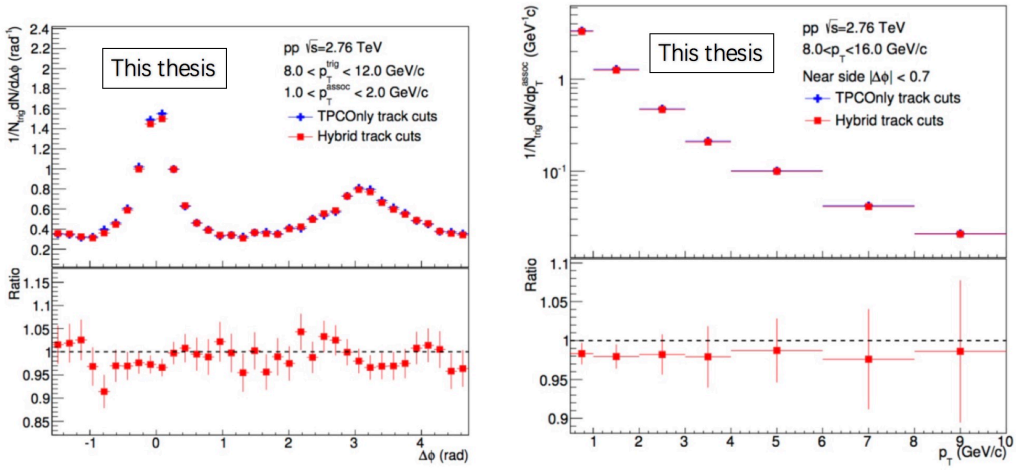

Figure 4.37: The comparison of per-trigger yield as a function of $\Delta\varphi$ (left) and p_{T} in Near side (right) obtained using standard Hybrid track cut (red points) and TPC-Only track cut (blue points) in pp collision at $\sqrt{s} = 2.76$ TeV.

4.5.4 systematics on track efficiency and purity

For the track purity and efficiency systematics, we tried to tighter and looser the hybrid track selections on TPC clusters, the chi2 of the cluster, the distance close approach, the crossed rows and crossed rows/findable clusters, the details are should in Fig. 4.39 for pp collision and 4.40 for Pb–Pb collisions. Thus the track efficiency (left) and contamination (right) can be got with different settings, the comparison with the default hybrid track setting are shown in Fig. 4.41 for pp collision and 4.42 for Pb–Pb collisions. the efficiency changes less than 5%, while the purity affected only less than 1% related to this.

4.5.5 The summary of systematic uncertainties

All the systematic sources are treated as uncorrelated to each other except uncertainties on tracking efficiency and MC closure, which are considered as correlated in $\Delta\varphi$, the total systematic can be computed by sum in quadrature of each individual source. Fig. 4.43 and Fig. 4.44 show each source and total systematic uncertainties for per-trigger yield as a function of p_{T} in Near (left panel) and Away (right panel) side in pp and Pb–Pb collisions at 2.76 TeV, respectively. And the systematic uncertainties in pp and Pb–Pb collisions are also considered independent with each other, depending on p_{T}. The maximum values of per-trigger yield in pp and Pb–Pb collisions and I_{AA} are summarized in Tab. 4.1. In pp collision, the largest uncertainty comes from the tracking efficiency estimation, while in Pb–Pb collisions, due to the

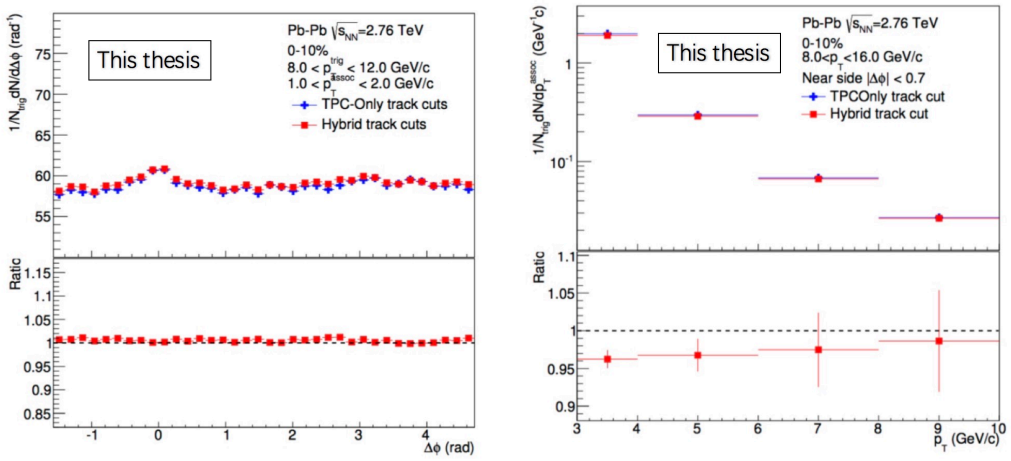

Figure 4.38: The comparison of per-trigger yield as a function of $\Delta\varphi$ (left) and p_{T} in Near side (right) obtained using standard Hybrid track cut (red points) and TPC-Only track cut (blue points) in Pb–Pb collisions at $\sqrt{s_{\mathrm{NN}}} = 2.76$ TeV.

cut	a)	b)	c)	d)
Number of clusters	70	80	60	–
Chi2/cluster	4	3	5	–
d_{xy} (cm)	2.4	1.9	2.9	2.4
d_z (cm)	3.2	2.7	3.7	3.2
Crossed rows	–	–	–	70
Crossed rows/findable clusters				0.8

Figure 4.39: The summary of the hybrid track cut modifications for pp collision at $\sqrt{s} = 2.76$ TeV.

cut	a)	b)	c)	d)	e)	f)
Number of clusters	50	60	40	–	–	–
d_{xy} (cm)	2.4	1.9	2.9	2.4	2.9	1.7
d_z (cm)	3.2	2.7	3.7	3.2	3.7	2.7
Chi2perClusterTPC	4	3	5	4	5	3
Chi2perClusterITS	36	25	49	36	49	25
Chi2TPCConstrainedGlobal	36	25	49	36	49	25
FractionSharedTPCClusters	0.4	0.2	1	0.4	1	0.2
Crossed rows	–	–	–	70	60	80
Crossed rows/findable clusters	–	–	–	0.8	0.7	0.9

Figure 4.40: The summary of the hybrid track cut modifications for Pb–Pb collisions at $\sqrt{s}_{\mathrm{NN}} = 2.76$ TeV.

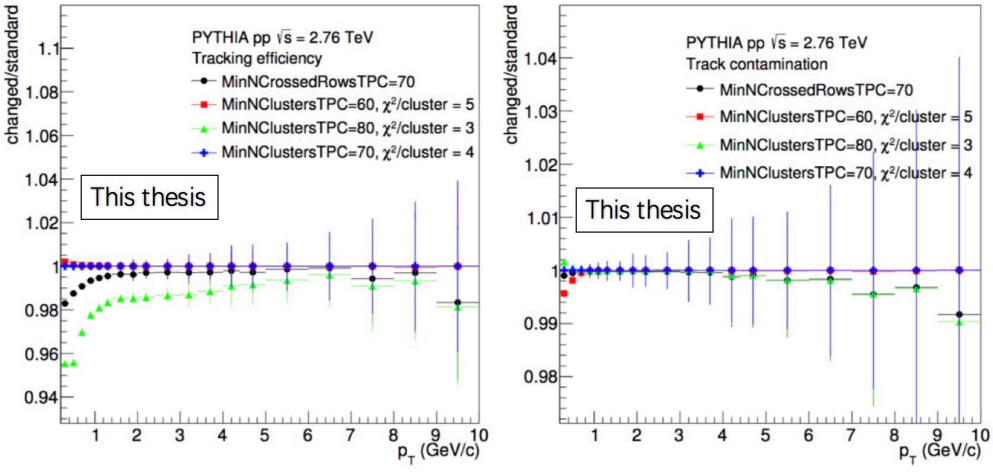

Figure 4.41: The different settings of hybrid track compared with the default one for the track efficiency (left) and track contamination as a function of p_{T} simulated in pp collision at $\sqrt{s} = 2.76$ TeV.

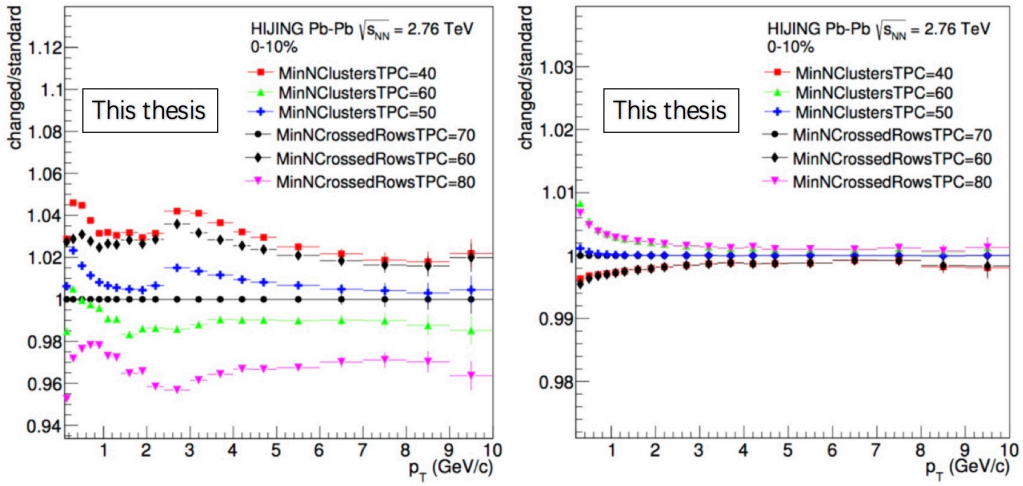

Figure 4.42: The different settings of hybrid track compared with the default one for the track efficiency (left) and track contamination as a function of p_{T} simulated in Pb–Pb collisions at $\sqrt{s_{\mathrm{NN}}} = 2.76$ TeV.

Source	$Y(\Delta\varphi)$ pp	$Y(\Delta\varphi)$ Pb–Pb	I_{AA} (NS)	I_{AA} (AS)
Tracking efficiency	5.4%	6.5%	8.5%	8.5%
MC closure	1.0%	2.0%	1.2%	1.2%
TPC-only tracks	1.0%	3.5%	4.3%	3.8%
Track contamination	1.0%	0.9%	1.1%	1.1%
Shower shape	1.2%	0.7%	3.4%	2.6%
Invariant mass window	1.3%	1.0%	3.5%	3.3%
Neutral pion purity	0.3%	1.1%	0.6%	0.5%
Pair p_{t} resolution	1.0%	1.1%	0.3%	0.3%
Pedestal determination	–	–	9.4%	11.7%
Uncertainty on v_n	–	–	7.1%	5.1%
Total	6.7%	7.4%	12.6%	15.0%

Table 4.1: Summary of sources and assigned systematic uncertainties for the per-trigger yield in pp, and 0–10% Pb–Pb collisions, as well as I_{AA}. For each source of systematic uncertainty and the total uncertainty listed, the maximum values of all p_{T} intervals are given. Uncertainties on tracking efficiency and MC closure are correlated in $\Delta\varphi$. For I_{AA}, pp and Pb–Pb yield uncertainties are assumed to be independent.

large background fluctuation, the main sources are attributed to the pedestal determination and flow values uncertainties which is dominated in low associated charged hadron p_{T} bin (for high p_{T} associated charged hadron, the pedestal is very small, and flow contribution is negligible at that region, so the systematic uncertainties are smaller.)

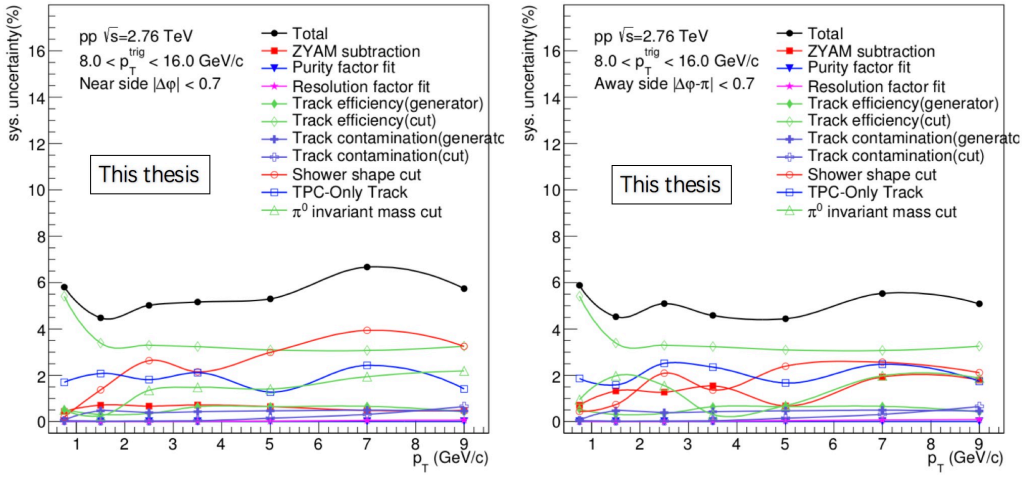

Figure 4.43: The systematic uncertainties for the per-trigger yield as a function of p_{T} on the near side (left) and away side (right) in pp collision at $\sqrt{s} = 2.76$ TeV.

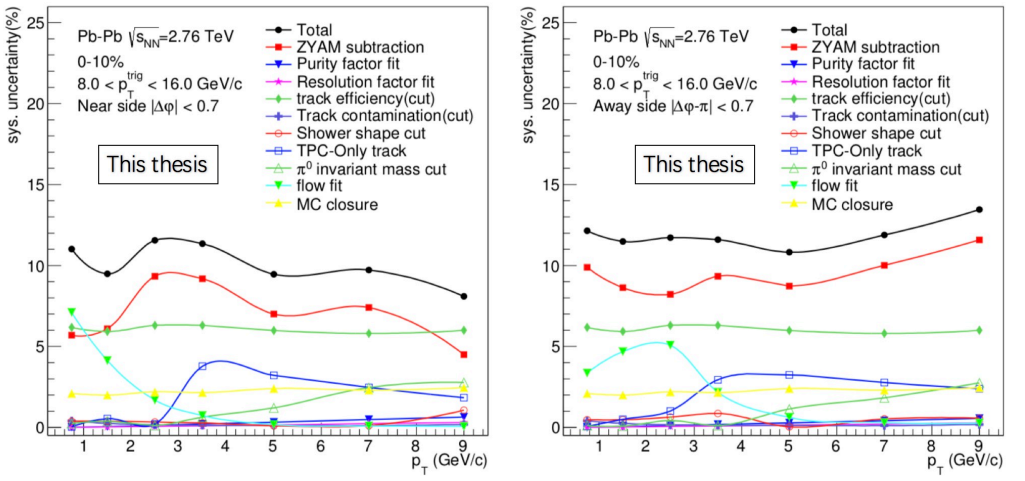

Figure 4.44: The systematic uncertainties for the per-trigger yield as a function of p_{T} on the near side (left), away side (right) in 0-10% Pb–Pb collisions at $\sqrt{s_{\mathrm{NN}}} = 2.76$ TeV.

4.6 Results

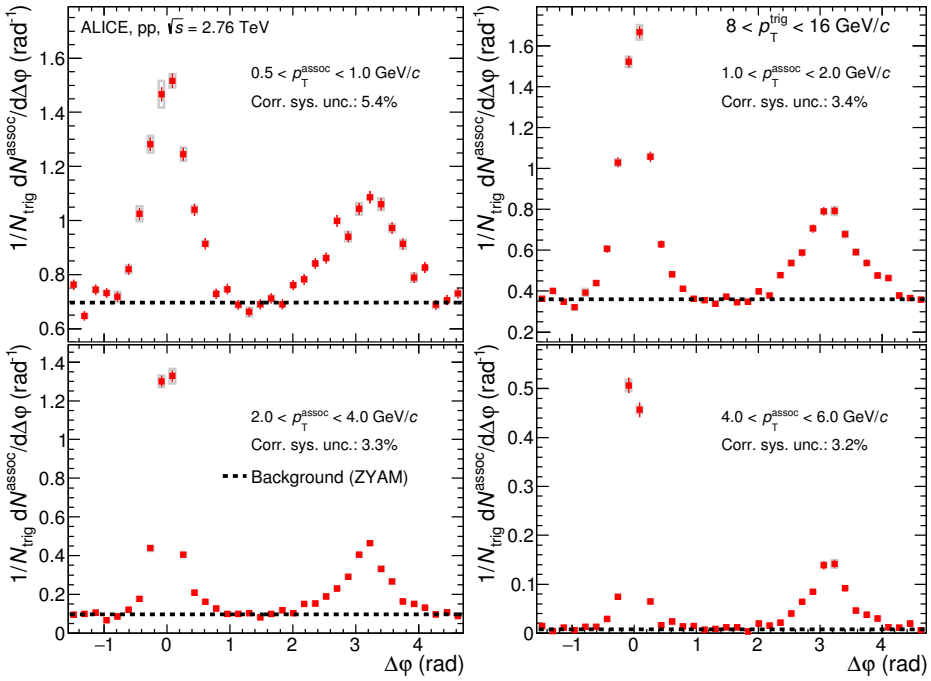

Figure 4.45: The per-trigger yields as a function of $\Delta\varphi$ with different associate p_{T} intervals in pp collision at $\sqrt{s} = 2.76$ TeV [24], details are described in the text.

The results about per-trigger yields of azimuthal correlation (without background subtraction) with π^0 trigger region in $8 < p_{\mathrm{T}}^{\mathrm{trig}} < 16$ GeV/c and associated charged hadrons with p_{T} intervals $0.5 < p_{\mathrm{T}}^{\mathrm{assoc}} < 1$, $1 < p_{\mathrm{T}}^{\mathrm{assoc}} < 2$, $2 < p_{\mathrm{T}}^{\mathrm{assoc}} < 4$ and $4 < p_{\mathrm{T}}^{\mathrm{assoc}} < 6$ GeV/c are shown for pp in Fig. 4.45 and 0–10% central Pb–Pb collisions in Fig. 4.46. The bars are the statistical uncertainties and the grey boxes are the uncorrelated systematic uncertainties, while the correlated ones are presented in the corresponding legends. In addition, the background which is described by the dash lines estimated using the ZYAM method considered as flat in pp collision, and included v_n contribution in Pb–Pb collisions, already explained in the previous sections. It can be found that the background for Pb–Pb collisions with $4 < p_{\mathrm{T}}^{\mathrm{assoc}} < 6$ GeV/c is nearly flat, due to the flow contribution is really small at high trigger and associate p_{T}. In general, double peaks can be found in Near and Away side for the azimuthal correlation which indicate the di-jet behavior. And the Near side peak gets broader for low $p_{\mathrm{T}}^{\mathrm{assoc}}$ in Pb–Pb collisions which should relate to the jet-medium interaction.

The integrated yield can be extracted in Near side with $|\Delta\varphi| < 0.7$ and Away side with $|\Delta\varphi - \pi| < 1.1$ after background subtraction. the modification of the per-trigger yield, I_{AA}, can be calculated as the ratio of the corresponding yields in Pb–Pb over pp, which have already explained in Eq. 1.10. Fig. 4.47 shows the I_{AA} of π^0-hadron correlation (red points) as a function of p_{T} in Near side (left

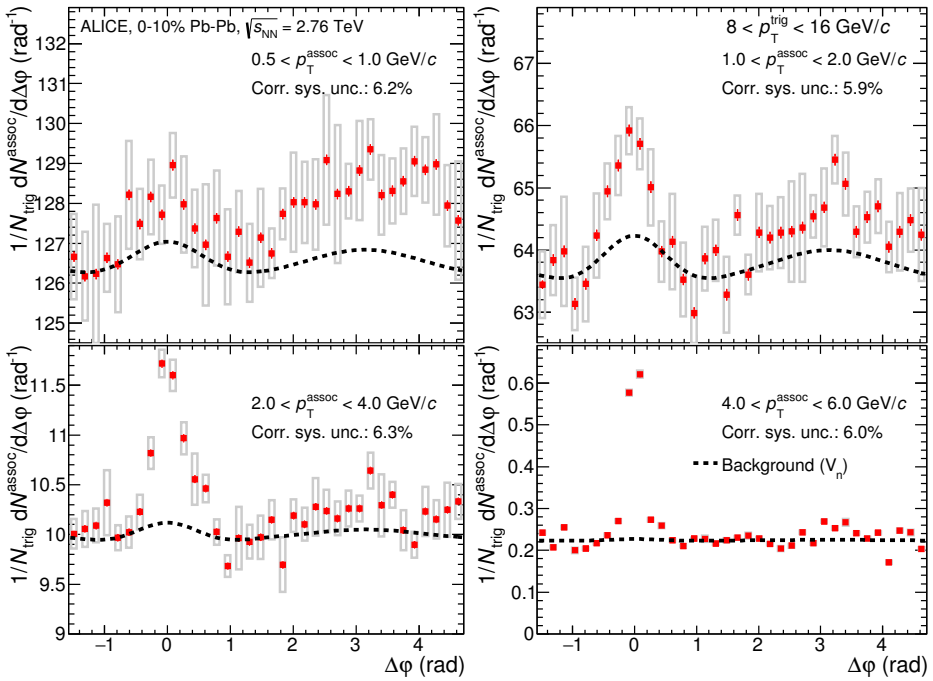

Figure 4.46: The per-trigger yields as a function of $\Delta\varphi$ with different associate p_{T} intervals in Pb–Pb collisions at $\sqrt{s}_{\mathrm{NN}} = 2.76$ TeV [24], details are described in the text.

panel) and Away side (right panel) with trigger π^0 region in $8 < p_{\mathrm{T}}^{\mathrm{trig}} < 16$ GeV/c for 0-10% Pb–Pb collisions at $\sqrt{s}_{\mathrm{NN}} = 2.76$ TeV, and the bars are the statistical uncertainties, boxes represent the systematic uncertainties, and the measurements are compared with di-hadron correlation measurement (showed as the black points, sightly displaced to improve the visibility) by ALICE at $\sqrt{s}_{\mathrm{NN}} = 2.76$ TeV [15], neglecting the higher order harmonics (v_n, n > 2) contributions in the background. On the near side, it can be found that from the high to low $p_{\mathrm{T}}^{\mathrm{assoc}}$, I_{AA} increase from 1.2 to around 1.8, which is consistent with the di-hadron measurement above 3 GeV/c, the slightly enhancement from unity, could leaded by hot medium effects in Pb–Pb collisions which may change the fragmentation function or the quark-to-gluon jet ratio has already discussed in [15], the trend of further enhancement below 3 GeV/c was first observed. For the I_{AA} in Away side, at high p_{T}, it's almost flat and strong suppressed (≈0.6), which is also consistent with di-hadron result within uncertainties (the difference for the bin $3 < p_{\mathrm{T}}^{\mathrm{assoc}} < 4$ GeV/c should relate to the contribution from v_3 which is no negligible and negative at this region), it's dominant by the parton energy loss [111, 112, 113, 114, 115]. While at low p_{T}, strong enhancement can be observed which reaches around 5 for the lowest $p_{\mathrm{T}}^{\mathrm{assoc}}$. The interpretation of the enhancement is not straight forward, it acts as the interplay of such as cronin effect [116], medium excitation [26] and large angle gluon radiation [117]. What's more, if compared with the results at RHIC energy [66], the away side enhancement at low p_{T} is similar which reaches 2-3 at lowest p_{T} with

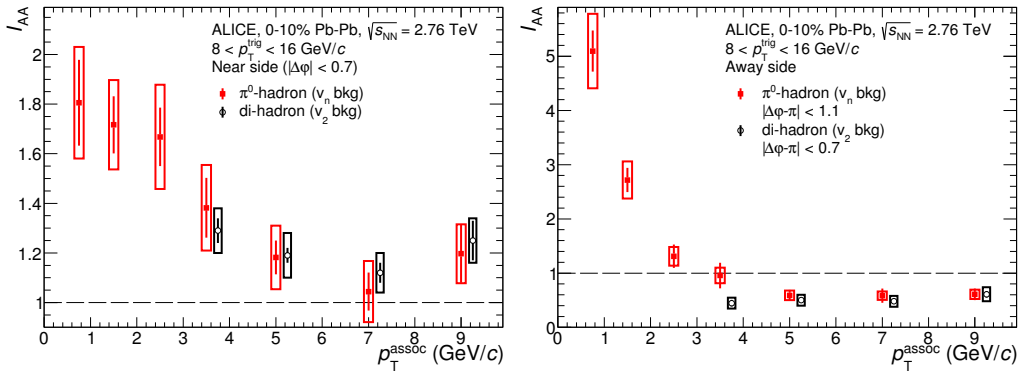

Figure 4.47: Per-trigger yield modification, I_{AA}, on the near side (left) and away side (right) for 0–10% Pb–Pb collisions at $\sqrt{s_{\mathrm{NN}}} = 2.76$ TeV [24], details described in the text.

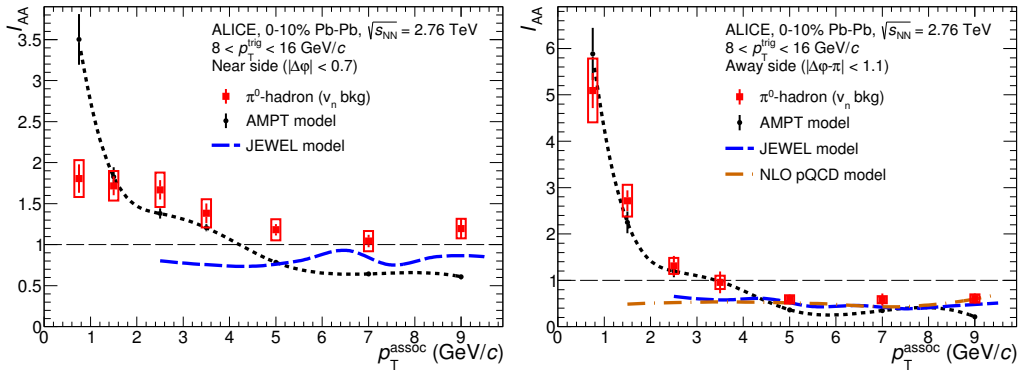

Figure 4.48: The I_{AA}, on the near side (left) and away side (right) [24] compared with theoretical model predictions [25, 26, 27] as explained in the text.

v_2 background subtraction, however, the Near side yield is consistent with unity, no significant enhancement can be observed. Nevertheless, the $I_{\mathrm{AA}} > 1$ at low p_{T} is consistent with the enhancement of charged jet fragmentation function in Pb–Pb with respect to pp collisions at LHC [118, 119].

The I_{AA} are compared with theoretical calculations in Fig. 4.48 including JEWEL (blue line) [25] and AMPT (black line) [26] event generators, as well as pQCD calculation (brown line) [27]. JEWEL [25] is based on pQCD calculations, which use the transport coefficient $\hat{q}$ to describe the parton-medium interaction. Hard scatters are generated according to Glauber collision geometry including the effects of soft scatterings by continuing the pQCD matrix elements into the infra-red region. Partons suffer from elastic and radiative energy loss in the medium, including a Monte Carlo implementation of LPM interference effects. However, in the default JEWEL model, the total p_{T} is not conserved in the event and some soft particle production is missing. Thus the so called 'recoil hadrons' are included which produced by fragmenting medium partons that interacted with the propagating hard parton. Note that the JEWEL model used here is without mixed events correction, which should

affect the yields, but will have negligible effect on the $I_{\rm AA}$. Another pQCD calculation [27] is performed within the next-to-leading order perturbative QCD parton model with modified jet fragmentation functions due to jet quenching. It uses nuclear parton distribution functions for initial-state cold nuclear matter effects, and a phenomenological model for medium-modified fragmentation functions calculated in leading-order (LO) at twist-4 in the high-twist approach of jet quenching. The evolution of bulk medium for parton propagation is done with a 3+1 dimensional ideal hydrodynamic model, and the value $\hat{q}$ is from JET collaboration, which was extracted using experimental data [120]. AMPT [121] is a transport model which uses a standard HIJING triggered jet technique, followed by parton and hadron cascades with elastic scatterings for final-state interaction. String melting with a parton interaction cross section of 1.5 mb and parton recombination for hadronization is used with parameters from [122], which was shown to well describe collective flow in heavy-ion collisions at RHIC and LHC, the flow background determined following the same strategy in [26].

All the models can qualitatively the $I_{\rm AA}$ strong suppression at high $p_{\rm T}$ for Away side, which is attributed to the radiative energy loss in the QGP medium. JEWEL can't give reasonable predictions for low $p_{\rm T}$ as 'recoil hadrons' will produce unreliable soft contributions, also shows unexpected behavior of $I_{\rm AA} < 1$ for Near side, probably related to transverse jet profile in JEWEL is more strongly modified than in data and that the fragmentation in JEWEL gets a bit harder at high $p_{\rm T}$. And pQCD calculation shows suppression at low $p_{\rm T}$ which is caused by jet quenching. However, this suppression is not reliable since the low $p_{\rm T}$ region are affected by many other processes such as the initial $k_{\rm T}$ broadening and the medium excitation by jets will enhance the final yield at low $p_{\rm T}$ region in AA collisions compared to that in pp collisions. In fact, NLO pQCD parton model calculations are still valid in the collinear factorized form. Strictly speaking, the collinear model doesn't work at low $p_{\rm T}$ region. Inclusion of transverse momentum and broadening will influence the low $p_{\rm T}$ $I_{\rm AA}$. While AMPT can quantitatively describes the enhancement at both the Near (except at lowest $p_{\rm T}$) and Away side, which is attributed to the excitation of soft particles by jet. However, AMPT shows a strong suppression of $I_{\rm AA}$(around 0.6) on Near side, and more suppression on Away side the with $p_{\rm T} > 5$ GeV/c, which is disfavored by the data. It's also found that AMPT overestimates the single-particle suppression in central Pb–Pb collisions [123], indicating the AMPT model is still not complete.

4.7 Summary

In this chapter, we measured two-particle correlations with trigger π^0 neutral pions region in $8 < p_{\rm T}^{\rm trig} < 16$ GeV/c and associated charged hadrons region in $0.5 < p_{\rm T}^{\rm assoc} < 10$ GeV/c, the azimuthal correlations $\Delta\varphi$ at midrapidity are presented in pp and central Pb–Pb collisions at $\sqrt{s}_{\rm NN} = 2.76$ TeV. After subtracting the flat (v_n) background in pp (Pb–Pb) collision, the per-trigger yields can be extracted in Near side with $|\Delta\varphi| < 0.7$ and Away side with $|\Delta\varphi - \pi| < 1.1$. The $I_{\rm AA}$ mea-

sured as the ratio of per-trigger yields in Pb–Pb to that in pp collisions. On the Away side, the I_{AA} is strongly suppressed to around 0.6 with $p_{\mathrm{T}} > 3$ GeV/c, and increase as the momenta decrease, reaching about 5.2 at lowest p_{T}. On the near side, an enhancement of I_{AA} from 1.2 to 1.8 at lowest p_{T} is observed. Consulting the model predictions with the JEWEL and AMPT event generators, as well as a pQCD calculation.All the models can qualitatively describe the strong suppression on Away side at high p_{T}. Only AMPT can qualitatively predict the enhancement at low p_{T} on both Near and Away side. However, it's disfavored by data above 5 GeV/c, especially on the Near side. The data itself not only gives the main background source of γ-hadron correlations, but also provides a important constrain to the model calculations which aim to fully describe jet-medium interactions.

Chapter 5

D^0 production in Pb–Pb collisions

This chapter is dedicated to describe the D^0 analysis in Pb–Pb collisions. The analysis goal is to measure the D^0 production yield and nuclear modification factor in Pb–Pb collisions. In Sec. 5.1, the Pb–Pb data sample will be described. The D^0 reconstruction and selection strategy will be presented in Sec. 5.2. After giving the description of the correction procedures in Sec. 5.3, the systematic uncertainties estimation will be discussed in Sec. 5.4. Finally, the results about D^0 production yield, different D-meson ratios and nuclear modification factors will be presented in Sec. 5.5, and a brief summary will be given in Sec. 5.6.

5.1 Data Sets and Event Selections

This work was based on the LHC run 2 data acquired by ALICE detector in 2015 with Pb–Pb collisions at centre-of-mass energy per nucleon-nucleon pair of $\sqrt{s_{\rm NN}} = 5.02$ TeV, using the minimum-bias trigger according to the information of the define $V_{0\rm AND}$ VZERO detector, the number of events used for the analysis after reconstructed primary vertex cut ($\pm$ 10 cm) are 10.4M for 0-10% (central), 20.8M for 30-50% (semi-central) and 60-80% (peripheral). The corresponding integrated luminosity is $L_{\rm int} \approx 13\mu b^{-1}$. The dedicated MC was generated using the HIJING generator, with addition of D-meson signal decaying by the hadronic channel from PYTHIA6 requesting the $c\bar{c}$ pairs in 50% of the events and the $b\bar{b}$ pairs in the remaining half. The in-bunch collision pileup was negligible for Pb–Pb collisions.

5.2 D^0 Reconstruction

The D^0 mesons and their charge conjugates can be reconstructed via their hadronic decay channel at mid-rapidity in ALICE. In this analysis, we use the channel $D^0 \to K^-\pi^+$ with the branch ratio $(3.88 \pm 0.05)\%$ [44]. There is another decay channel $D^0 \to K^-\pi^+\pi^0$, with branching ratio more than three times larger than the previous channel. The reconstruction of a three prongs channel is more challenging than the two prongs one, but this channel can be tried in the future using the technical of cluster splitting to identify π^0 which mentioned in Chapter. 4 and with EMCal triggered events, can significantly improve the statistics at high-$p_{\rm T}$.

5.2.1 Secondary Vertex Reconstruction and Single Track Selection

D^0 mesons decay through weak decay processes few hundred microns ($c\tau \approx$ 123 μm) away from the primary vertex, as shown in Fig. 5.1. The secondary vertex

can be reconstructed at the point of closest approach (PCA) between the pair of opposite-sign tracks. The PCA is calculated using the minimum distance segment between the two helices, based on the different spatial precision of the track trajectories, which can be estimated by the track covariance matrix. High momentum tracks can be better reconstructed as the multiple scattering is small, thus the PCA is closer to the track with higher momentum. The resolution of secondary vertex is related to the impact parameter resolution, at low p_{T}, the resolution is bad due to the multiple scattering, while at high p_{T}, it is limited by the small the angle between decay tracks.

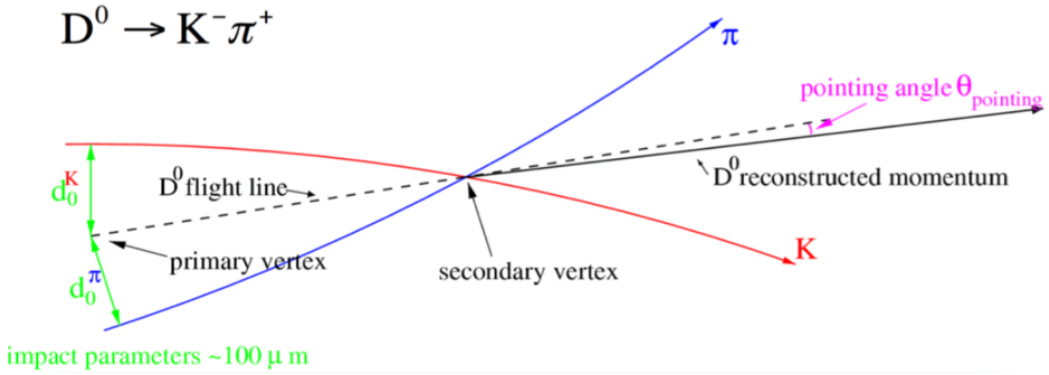

Figure 5.1: Schematic view of the decay channel $\mathrm{D}^0 \to \mathrm{K}^-\pi^+$.

Secondary vertices of D^0 meson candidates were constructed using tracks having $|\eta| < 0.8$, $p_{\mathrm{T}} > 0.5$ GeV/c obtained with Kalman filter fit in TPC and ITS. Moreover, a minimum number of 70 crossed rows in the TPC together with a crossed rows over findable clusters ratio of 0.8 was required. A cut on the transverse impact parameter d_0 was applied for tracks with $p_{\mathrm{T}} < 2$ GeV/c, requiring $d_0 > 50$ μm. These selections were meant to limit the CPU time needed to perform the track combinatorics when creating the AODs with the D meson candidates. Furthermore, all tracks were selected requiring at least 70 (out of a maximum of 159) associated space points and $\chi^2/ndf < 2$ in the TPC, and at least one associated hit in either of the two pixel layers (SPD) to remove the contributions from the secondary tracks and increase the secondary vertex resolution.

5.2.2 Topological Selections

The D^0 can be selected based on the secondary vertices which are computed from the charge opposite K, π tracks. However, most of them are combinatorial association. In order to improve the signal-to-background ratio and have a better statistical significance of the signal and at the same time, reduce the fraction of candidates which originated from beauty hadron decay, selections are optimized according to the typical kinematical and geometrical properties of the secondary vertex. The variables used are described below: prefernoiaccy

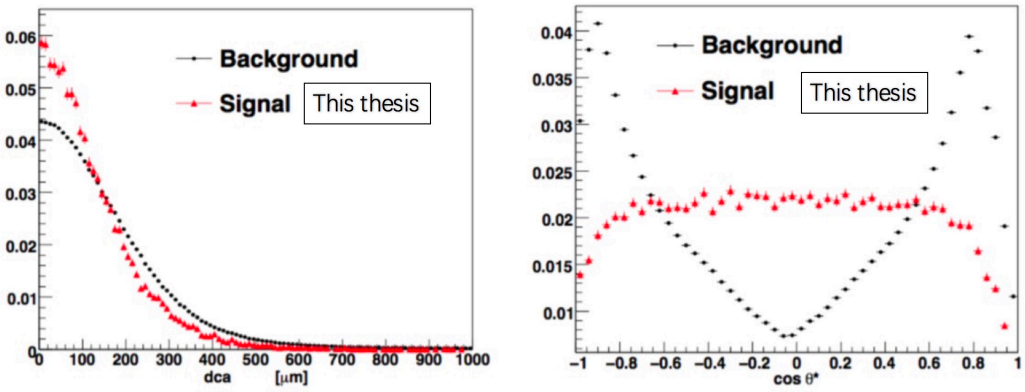

Figure 5.2: The pp simulation for DCA (left) and $cos(\theta^*)$ (right) distributions, the red points are the signal D^0 candidates, while the black points are the background candidates.

DCA(distance of closest approach) This variable is defined as the minimum distance between the two track trajectories. In ideal case, the distance is equal to zero if they have a common secondary vertex, however, they could have some distance away from each other depending on the resolution of the track positions. The simulation of signal and background distributions can be found in the left panel of Fig. 5.2.

$cos(\theta^*)$ The angle between D^0 flight line and the pion momentum direction is named as θ^*. If the pion origins from D^0, the $cos(\theta^*)$ distribution is almost flat as the pions are emitted isotropic. On the contrast, the background candidates have the $cos(\theta^*) = \pm 1$, thus the background can be significantly removed with the cut of $|\cos(\theta^*)| < 0.8$, the details can be found in the right panel of Fig. 5.2.

$d_{0,K} \times d_{0,\pi}$ d_0, the distance of closest approach of the reconstructed particle trajectory to the primary vertex, the kaon and pion from D^0 decay will more probably have d_0 in opposite sign, while the background one will have symmetric $d_{0,K} \times d_{0,\pi}$ distribution with respect to zero, as shown on the left panel of Fig. 5.3. So one can select the cut $d_{0,K} \times d_{0,\pi} < 10000\ um^2$ to suppress the background.

$cos(\theta_{point})$ the θ_{point} is defined as the angle between the direction of one reconstructed D^0 momentum and the line connecting secondary and primary vertex (D^0 flight line). For the signal, it's almost located at the $cos(\theta_{point}) = 1$, as shown in the right panel of Fig. 5.3. A similar variable $\theta_{pointXY}$ is the θ_{point} projected in the (x,y) plane.

Norm L_{XY} L_{XY} is the decay length of D^0 (the distance between primary vertex and secondary vertex) projected on the transverse plane. L_{XY} normalized by

its uncertainty, was used with the cut > 2.

$|d_0 - d_0^{exp}|^{prong}(n\sigma)$ It is defined as the difference between the expected impact parameter value $d_{0,t,\phi}^{exp} \approx L_{XY} \cdot \sin(\theta_{XY})$ where L_{XY} is the decay length on XY plane and θ_{XY} is the angle between the reconstructed D meson and the charged particle on xy plane, and the reconstructed one d_0^{reco} , then normalized by the square root of their respective uncertainties summed in quadrature. A selection based on this variable can reduce the feed-down D-meson efficiency while keeping higher that of prompt D mesons. The cut < 2 significantly removes the contributions from feed-down D^0 and the background.

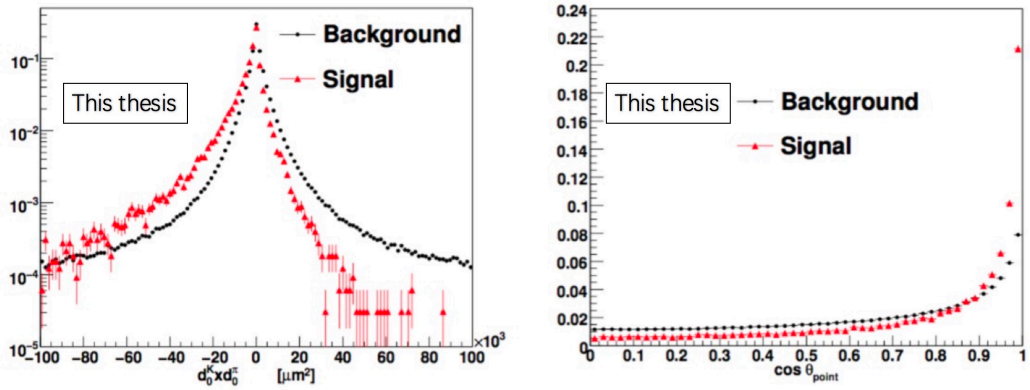

Figure 5.3: The pp simulation for $d_{0,K} \times d_{0,\pi}$ (left) and $cos(\theta_{point})$ (right) distributions, the red points are the signal D^0 candidates, while the black points are the background candidates.

Finally we applied the cuts depending on p_T interval and centrality classes as listed in Table. 5.1 5.2 5.3.

Table 5.1: List of the main topological selections applied for the D^0 analysis in 0-10% centrality class.

p_t (GeV/c)/variable	[1,2]	[2,3]	[3,4]	[4,5]	[5,6]	[6,7]	[7,8]	[8,10]	[10,12]	[12,16]	[16,24]	[24,36]	[36,50]
ΔM_{D^0} (GeV)	< 0.040	< 0.040	< 0.040	< 0.040	< 0.040	< 0.040	< 0.040	< 0.040	< 0.040	< 0.040	< 0.040	< 0.040	< 0.040
DCA (cm)	< 0.040	< 0.030	< 0.030	< 0.030	< 0.030	< 0.030	< 0.030	< 0.030	< 0.030	< 0.040	< 0.040	< 0.040	< 0.040
$Cos(\theta^*)$	< 0.8	< 0.8	< 0.8	< 0.8	< 0.8	< 0.8	< 0.8	< 0.8	< 0.8	< 1.0	< 1.0	< 1.0	< 1.0
$p_t(K)$(GeV/c)	> 0.5	> 0.6	> 0.6	> 0.6	> 0.7	> 0.7	> 0.7	> 0.7	> 0.7	> 0.7	> 0.7	> 0.7	> 0.7
$p_t(\pi)$(GeV/c)	> 0.5	> 0.6	> 0.6	> 0.6	> 0.7	> 0.7	> 0.7	> 0.7	> 0.7	> 0.7	> 0.7	> 0.7	> 0.7
$d_{0,K}$ (cm)	< 0.1	< 0.1	< 0.1	< 0.1	< 0.1	< 0.1	< 0.1	< 0.1	< 0.1	< 0.1	< 0.1	< 0.1	< 0.1
$d_{0,\pi}$ (cm)	< 0.1	< 0.1	< 0.1	< 0.1	< 0.1	< 0.1	< 0.1	< 0.1	< 0.1	< 0.1	< 0.1	< 0.1	< 0.1
$d_{0,K} \times d_{0,\pi}$ ($\times 10^{-3}$) (cm^2)	< -0.30	< -0.36	< -0.36	< -0.36	< -0.23	< -0.23	< -0.23	< -0.10	< -0.10	< -0.10	< -0.10	< -0.10	< -0.10
$Cos(\theta_{point})$	> 0.90	> 0.92	> 0.92	> 0.92	> 0.90	> 0.90	> 0.90	> 0.90	> 0.90	> 0.90	> 0.90	> 0.90	> 0.90
$Cos(\theta_{point})XY$	< 0.991	< 0.997	< 0.997	< 0.997	< 0.998	< 0.998	< 0.998	< 0.998	< 0.998	< 0.998	< 0.995	< 0.995	< 0.995
L_{XY}	> 5	> 7	> 7	> 7	> 6	> 6	> 6	> 5	> 5	> 5	> 5	> 5	> 5
$\|d_0 - d_0^{exp}\|^{prong}(n\sigma)$	< 1	< 1	< 1	< 1.5	< 1.5	< 1.5	< 1.5	< 1.5	< 1.5	< 2	< 2	< 2	$< 2§$

Table 5.2: List of the main topological selections applied for the D^0 analysis in 30-50% centrality class.

p_t (GeV/c)/variable	[1,2]	[2,3]	[3,4]	[4,5]	[5,6]	[6,7]	[7,8]	[8,10]	[10,12]	[12,16]	[16,24]	[24,36]
ΔM_{D^0} (GeV)	< 0.040	< 0.040	< 0.040	< 0.040	< 0.040	< 0.040	< 0.040	< 0.040	< 0.040	< 0.040	< 0.040	< 0.040
DCA (cm)	< 0.030	< 0.025	< 0.025	< 0.025	< 0.025	< 0.025	< 0.027	< 0.030	< 0.030	< 0.035	< 0.040	< 0.040
$Cos(\theta^*)$	< 0.8	< 0.8	< 0.8	< 0.8	< 0.8	< 0.8	< 0.8	< 0.8	< 0.8	< 1.0	< 1.0	< 1.0
$p_t(K)$(GeV/c)	> 0.4	> 0.5	> 0.7	> 0.7	> 0.7	> 0.7	> 0.7	> 0.7	> 0.7	> 0.7	> 0.7	> 0.7
$p_t(\pi)$(GeV/c)	> 0.4	> 0.5	> 0.7	> 0.7	> 0.7	> 0.7	> 0.7	> 0.7	> 0.7	> 0.7	> 0.7	> 0.7
$d_{0,K}$ (cm)	< 0.1	< 0.1	< 0.1	< 0.1	< 0.1	< 0.1	< 0.1	< 0.1	< 0.1	< 0.1	< 0.1	< 0.1
$d_{0,\pi}$ (cm)	< 0.1	< 0.1	< 0.1	< 0.1	< 0.1	< 0.1	< 0.1	< 0.1	< 0.1	< 0.1	< 0.1	< 0.1
$d_{0,K} \times d_{0,\pi}$ ($\times 10^{-3}$) (cm^2)	< -0.43	< -0.40	< -0.36	< -0.27	< -0.21	< -0.14	< -0.14	< -0.05	< -0.05	< 0	< 0	< 0
$Cos(\theta_{point})$	> 0.92	> 0.95	> 0.95	> 0.95	> 0.92	> 0.88	> 0.88	> 0.85	> 0.85	> 0.83	> 0.83	> 0.8
$Cos(\theta_{point})XY$	< 0.993	< 0.991	< 0.993	< 0.995	< 0.995	< 0.995	< 0.995	< 0.995	< 0.995	< 0.995	< 0.995	< 0.995
L_{XY}	> 6	> 6	> 6	> 5	> 5	> 5	> 5	> 5	> 6	> 6	> 6	> 6
$\lvert d_0 - d_0^{exp}\rvert^{prong}(n\sigma)$	< 1	< 1.5	< 1.5	< 1.5	< 1.5	< 2	< 2	< 2	< 1.5	< 1	< 1	< 1§

Table 5.3: List of the main topological selections applied for the D^0 analysis in 60-80% centrality class.

p_t (GeV/c)/variable	[1,2]	[2,3]	[3,4]	[4,5]	[5,6]	[6,7]	[7,8]	[8,10]	[10,12]	[12,16]	[16,24]	[24,36]
ΔM_{D^0} (GeV)	< 0.040	< 0.040	< 0.040	< 0.040	< 0.040	< 0.040	< 0.040	< 0.040	< 0.040	< 0.040	< 0.040	< 0.040
DCA (cm)	< 0.030	< 0.025	< 0.025	< 0.025	< 0.025	< 0.025	< 0.027	< 0.030	< 0.030	< 0.035	< 0.040	< 0.040
$Cos(\theta^*)$	< 0.8	< 0.8	< 0.8	< 0.8	< 0.8	< 0.8	< 0.8	< 0.8	< 0.8	< 1.0	< 1.0	< 1.0
$p_t(K)$(GeV/c)	> 0.4	> 0.5	> 0.7	> 0.7	> 0.7	> 0.7	> 0.7	> 0.7	> 0.7	> 0.7	> 0.7	> 0.7
$p_t(\pi)$(GeV/c)	> 0.4	> 0.5	> 0.7	> 0.7	> 0.7	> 0.7	> 0.7	> 0.7	> 0.7	> 0.7	> 0.7	> 0.7
$d_{0,K}$ (cm)	< 0.1	< 0.1	< 0.1	< 0.1	< 0.1	< 0.1	< 0.1	< 0.1	< 0.1	< 0.1	< 0.1	< 0.1
$d_{0,\pi}$ (cm)	< 0.1	< 0.1	< 0.1	< 0.1	< 0.1	< 0.1	< 0.1	< 0.1	< 0.1	< 0.1	< 0.1	< 0.1
$d_{0,K} \times d_{0,\pi}$ ($\times 10^{-3}$) (cm^2)	< -0.30	< -0.36	< -0.36	< -0.27	< -0.21	< -0.14	< -0.14	< -0.05	< -0.05	< 0	< 0	< 0
$Cos(\theta_{point})$	> 0.80	> 0.94	> 0.92	> 0.92	> 0.92	> 0.90	> 0.90	> 0.85	> 0.85	> 0.83	> 0.83	> 0.8
$Cos(\theta_{point})XY$	> 0.993	> 0.995	> 0.995	> 0.995	> 0.995	> 0.995	> 0.995	> 0.995	> 0.995	> 0.994	> 0.994	> 0.994
L_{XY}	> 5	> 6	> 6	> 6	> 6	> 6	> 6	> 5	> 5	> 5	> 5	> 5
$\lvert d_0 - d_0^{exp}\rvert^{prong}(n\sigma)$	< 1	< 1	< 1	< 1.5	< 1.5	< 1.5	< 1.5	< 1.5	< 1.5	< 2	< 2	< 2§

5.2.3 Particle IDentification

Identification of the charged tracks in the TPC and TOF detectors provides additional background rejection in the low momentum region.Cuts are applied to the difference in the expected and measured signals, which are the specific energy deposited in the TPC, and the particle flight-time for the TOF. A 3σ compatibility cut was applied to the D^0 candidate's daughters. When tracks were without TOF signal, only the TPC particle identification was used. Tracks with contradicting particle identification were considered to be non-identified and retained for further analysis.

5.2.4 "Reflected" signal

The invariant mass distributions contain both $D^0 \to K^-\pi^+$ and $\bar{D^0} \to K^+\pi^-$. However the candidates are also kept if they match both decay channels. Some of the true D^0 will be counted twice, one of them, of course, enters the wrong mass hypothesis assignment, which is called "reflection". PID can significantly reduce the probability of the wrong assignment, but the residual reflection contributions still exist due to the conservative PID cuts.

In order to subtract the contribution of reflection from the real D^0 signal, a template fit of the reflection and the true D^0 signal can be obtained by MC sim-

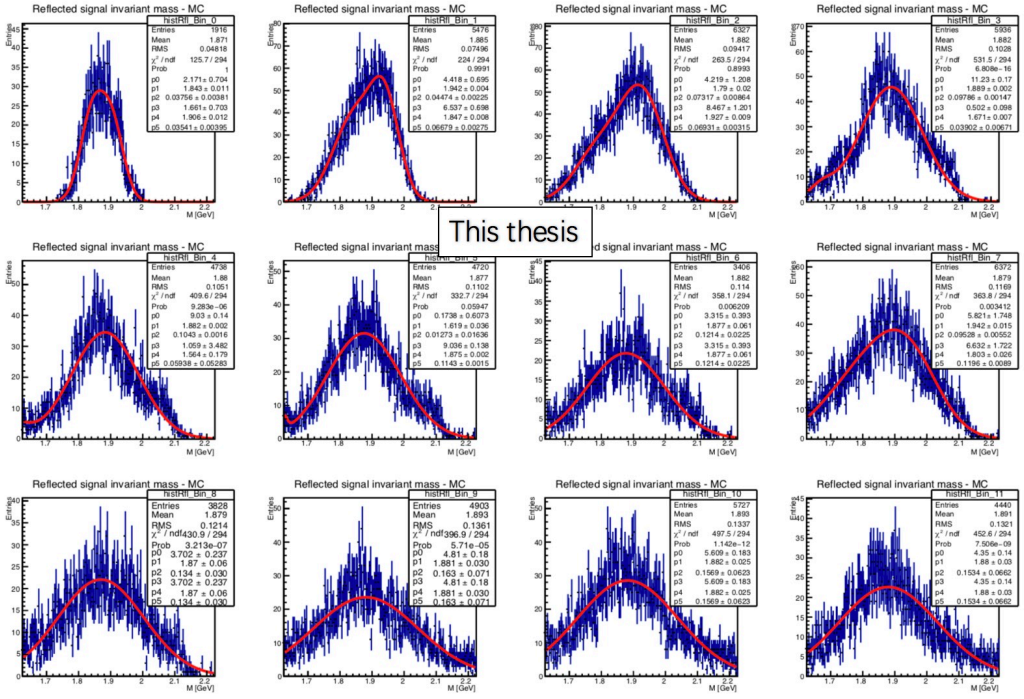

Figure 5.4: D^0 reflections distributions, estimated from the Monte Carlo.

ulation for each p_T interval. Fig. 5.4 shows D^0 reflection distributions, estimated from the Monte Carlo simulation for 30-50% Pb–Pb collisions at $\sqrt{s_{NN}} = 5.02$ TeV. The fit function is a double Gaussian. Thus the parameter of the template fit and the fraction between true D^0 signal and reflections will be kept and used for the D^0 yield extraction, which will be discussed in the next subsection.

5.2.5 Yield Extraction

The D^0 raw yield can be extracted using the invariant mass analysis. In general, the signal can be fitted by a Gaussian function, while the combinatorial background can be described by an exponential function. The total fit can be expressed as:

$$f(M) = \frac{P_1(P_0 - P_2)}{\exp(-P_1 M_{min}) - \exp(-P_1 M_{max})} \exp(-P_1 M) + \frac{P_2}{\sqrt{2\pi} P_4} \exp\left[-\frac{(M - P_3)^2}{2P_4^2}\right] \tag{5.1}$$

In Eq. 5.1, M_{min} and M_{max} are the minimum and maximum value of the fit region, normally it's 1.72 and 2.05 GeV/c^2, with the upper limit changed to 2.15 at high p_T considering the large mass width. P_0 is integral of the total contents in the whole range. P_1 is the background fit function, sets to exponential as default. At low p_T, a background shape was observed which can be better described by a polynomial function. Thus, for 1-2, 2-3 GeV/c, a second-order polynomial function is used (a fourth-order polynomial is used for 0-10% centrality class). P_2, P_3, P_4 are integral,

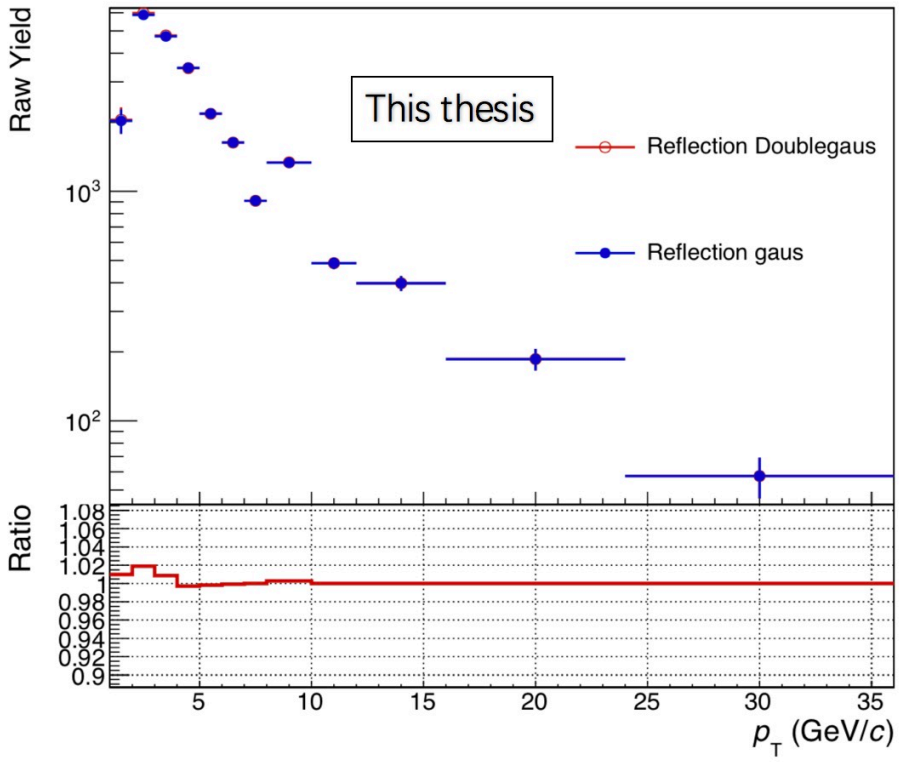

Figure 5.5: The raw yields comparison between Gaussian and double Gaussian fit reflections template.

central value and sigma of the signal peak. The signal is fitted by Gaussian function, the central and sigma of the peak is left free except 1-2 GeV/c for 0-10%(For this bin, the sigma is fixed to the value obtained from simulation as the significance of the signal is poor and sigma is found that has a large discrepancy between data and MC). First, an exponential fit is applied to the side-bands region of the distribution, to obtain the parameter of P_1. Then with P_1, and including the template of the reflection according to the ratio of the total reflection and Gaussian fit of the signal obtained from simulation, an new fit is applied to the whole region to determine the final value of P_1, P_2, P_3 and P_4.

Fig. 5.6, 5.7, 5.8 show the invariant mass fit in different p_{T} intervals for Pb–Pb collisions at $\sqrt{s_{\mathrm{NN}}}$ = 5.02 TeV in the centrality classes, 0-10%, 30-50% and 60-80% respectively. The information for number of signal S, number of background B, signal over background ratio S/B and significance can be found in each panel. In general, a good quality of fit can be obtained in each p_{T} interval with the significance range from 3 to 29 depending on p_{T}. For the bin 1-2 GeV/c at 0-10%, the signal peak is not visible by "eye" due to the big amount of combinatorial background, the residual of the signal peak after background subtraction can be found in Fig. 5.9. The comparison of the Gaussian mean and widths between Data and Monte-Carlo is

shown in Fig. 5.10, 5.11, 5.12. The width is found to have a good agreement between data and MC, while a significant deviation of the data's peak position with respect to MC can be found, which could be caused by the residual tracking systematic biases in data. a summary of the signal raw yield and S/B ratio in different centrality classes is reported in Tab. 5.4.

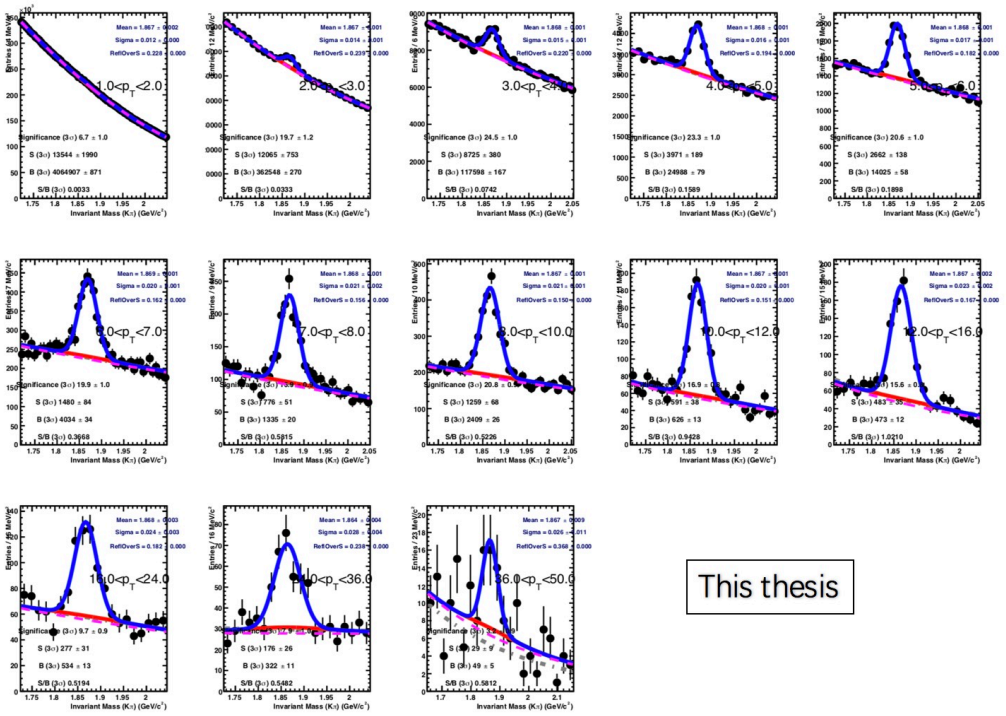

Figure 5.6: The invariant mass fit of D^0 signal with reflection in 13 p_T bins in the range, $1 < p_T < 50$ GeV/c for the 0-10% centrality class in Pb–Pb collisions at $\sqrt{s_{NN}} = 5.02$ TeV.

5.3 Corrections

In order to obtain the p_T-differential yield of prompt D^0 mesons, several correction factors need to be applied to the raw yield. The equation can be expressed as following:

$$\left.\frac{dN^{D^0}}{dp_T}\right|_{|y|<0.5} = \frac{1}{2}\frac{1}{\Delta y\,\Delta p_T}\frac{f_{\rm prompt}(p_T)\cdot N^{D^0\ \rm raw}(p_T)\Big|_{|y|<y_{\rm fid}}}{(\rm Acc\times\varepsilon)_{\rm prompt}(p_T)\cdot \rm BR\cdot N_{evt}}. \quad (5.2)$$

Where f_{prompt} is the prompt D^0 meson fraction in a given p_T bin. The D meson yields were measured in a rapidity range varying from $|y| < 0.5$ at low p_T to

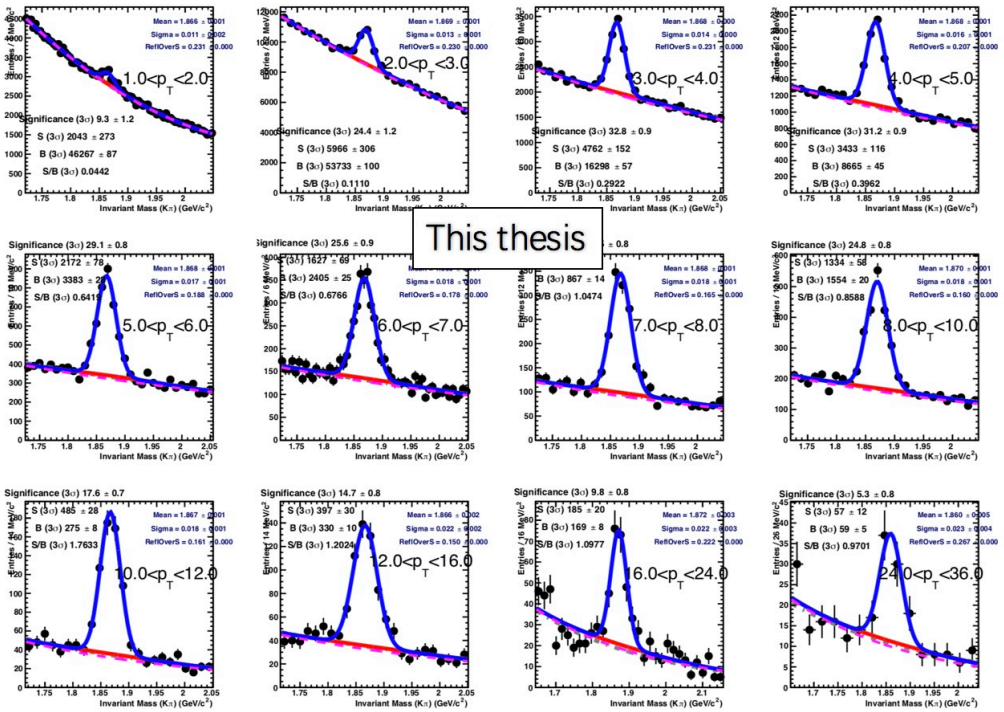

Figure 5.7: The invariant mass fit of D^0 signal with reflection in 12 p_T bins in the range, $1 < p_T < 36$ GeV/c for the 30-50% centrality class in Pb–Pb collisions at $\sqrt{s_{NN}} = 5.02$ TeV.

Table 5.4: D^0 raw yields and signal over background per p_T bin.

Centrality Class (%)	0-10		30-50		60-80	
p_T bin (GeV/c)	D^0 raw yield	S/B	D^0 raw yield	S/B	D^0 raw yield	S/B
[1,2]	13544 ±1990	0.0033	2043±273	0.0442	330 ±53	0.1747
[2,3]	12065±753	0.0333	5966± 306	0.1110	448± 32	0.8814
[3,4]	8725±380	0.0742	4762± 152	0.2922	425±25	1.9827
[4,5]	3971 ±189	0.1589	3433±116	0.3962	273 ± 20	2.3040
[5,6]	2662 ±138	0.1898	2172± 78	0.6419	217±19	1.8040
[6,7]	1480±84	0.3668	1627± 69	0.6766	224±18	2.2823
[7,8]	776±51	0.5815	908± 45	1.0474	139±15	2.31
[8,10]	1259±68	0.5226	1334± 58	0.8588	167 ± 17	1.8803
[10,12]	591±38	0.9428	485± 28	1.7633	81 ±11	2.5683
[12,16]	483±35	1.0210	397± 30	1.2024	83±13	1.3209
[16,24]	277± 31	0.5194	185± 20	1.0977	31±7	1.5502
[24,36]	176 ± 26	0.5482	57± 12	0.9701	19±6	1.6447
[36,50]	29 ±9	0.5812	57± 12	0.9701	-	-

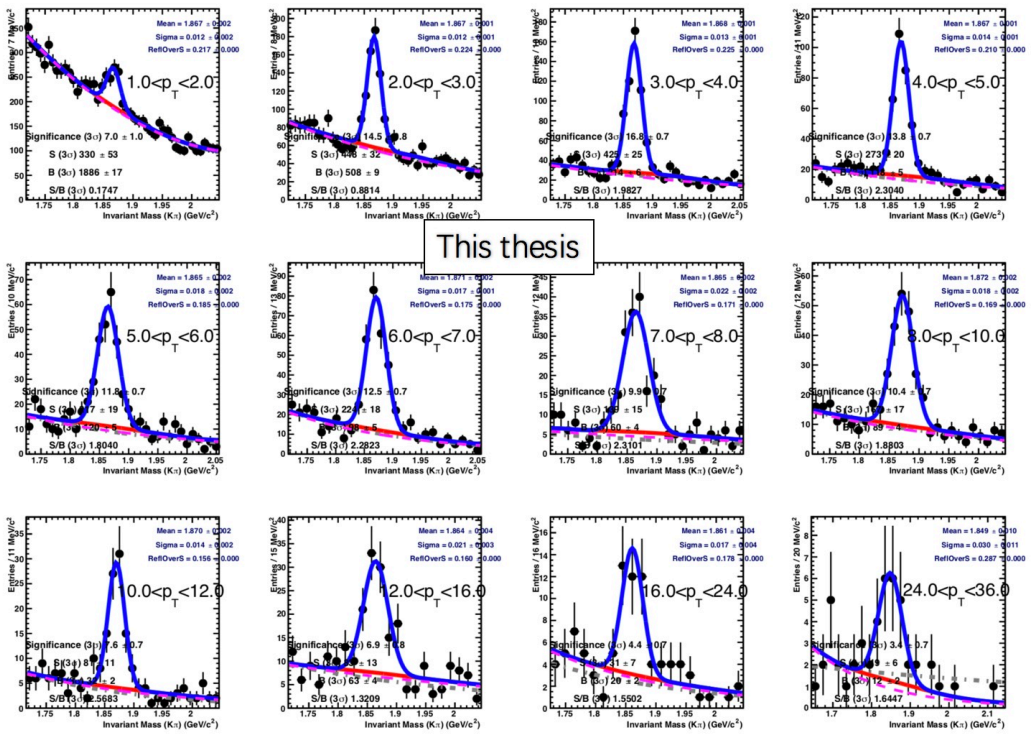

Figure 5.8: The invariant mass fit of D^0 signal with reflection in 12 p_T bins in the range, $1 < p_T < 36$ GeV/c for the 60-80% centrality class in Pb–Pb collisions at $\sqrt{s_{NN}} = 5.02$ TeV.

$|y| < 0.8$ at high p_T. The rapidity acceptance correction factor $\Delta y = 2\, y_{fid}$ assumes an uniform rapidity distribution for D mesons in the measured y range. This assumption was verified with PYTHIA. The raw yield is scaled with 1/2 as it also contains charged conjugates. N_{evt} is the number of analyzed events, and "BR" is the branching ratio of the $D^0 \to K^-\pi^+$ hadronic decay channel. This assumption was verified to the 1% level with PYTHIA [124] proton–proton simulations with the Perugia-0 [125] tuning. The acceptance times efficiency corrections Acc $\times\, \varepsilon$ were obtained using Monte Carlo simulations. As already shortly described before, minimum-bias Pb–Pb collisions at $\sqrt{s_{NN}}$ =5.02 TeV were produced with the HIJING v1.36 [126] event generator . Prompt and feed-down (B decays) D meson signals were added using pp events from the PYTHIA v6.4.21 event generator with the Perugia-0 tuning. Each injected pp event was required to contain a $c\bar{c}$ or $b\bar{b}$ pair and D mesons were forced to decay in the hadronic channels of interest for the analysis. Only particle coming from the heavy quark hadronisation and decays were injected in the HIJING event. The number of pp events added to each Pb–Pb event was adjusted according to the Pb–Pb collision centrality. The simulations used the GEANT3 particle transport package together with a detailed description of the geometry of the apparatus and of the detector response. The simulation was

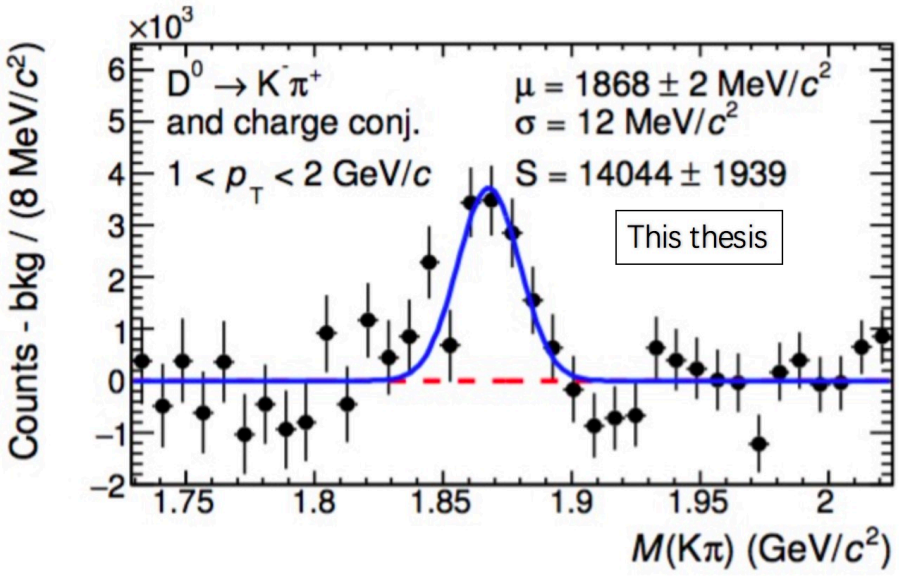

Figure 5.9: The residual of the signal peak after background subtraction for 1-2 GeV/c at 0-10% centrality class.

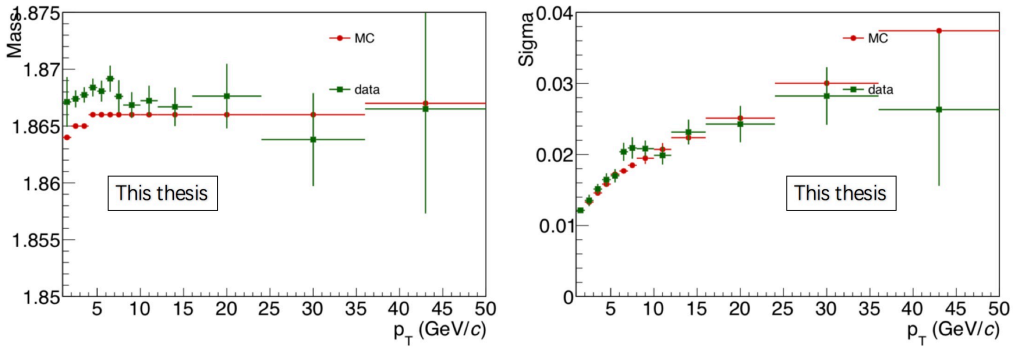

Figure 5.10: The comparison of data (green points) and MC (red points) for the D^0 signal peak mean (left) and width (right) at 0-10%.

configured to reproduce the conditions of the luminous region and of all the ALICE subsystems, in terms of active electronic channels, calibration level, and their time evolution within the Pb–Pb data taking period.

As mentioned before, the impact parameter resolution in MC is better than that in data. The top panel of Fig. 5.13 shows the impacter parameter resolution (left) and mean value (right) comparison between 2015 Pb–Pb data (solid points) and MC (open points). For the low interaction rate runs (collisional frequency $<$ 2kHz), the impact parameter resolution in data is not fully reproduced in MC, and a clear shift

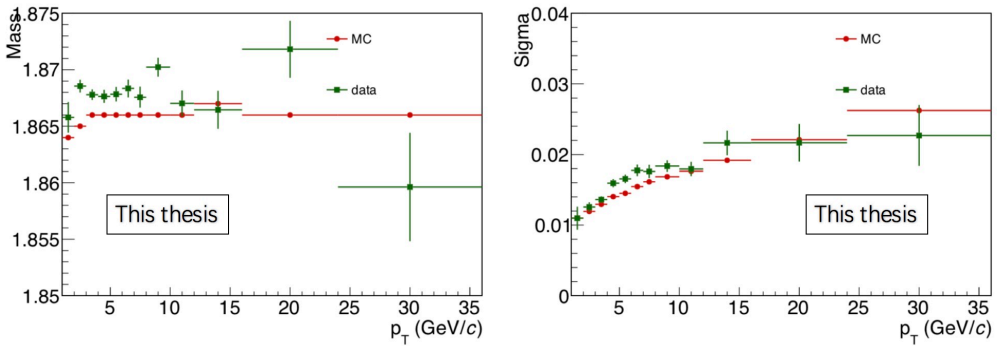

Figure 5.11: The comparison of data (green points) and MC (red points) for the D^0 signal peak mean (left) and width (right) at 30-50%.

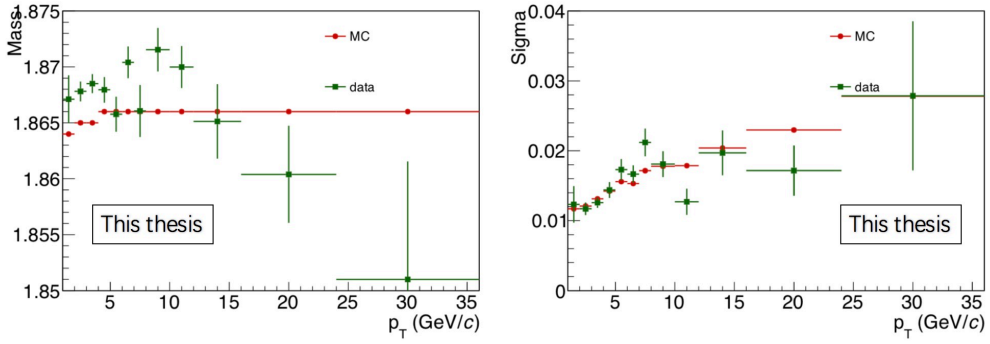

Figure 5.12: The comparison of data (green points) and MC (red points) for the D^0 signal peak mean (left) and width (right) at 60-80%.

can be observed for the impacter parameter mean value, which has a dependence on p_{T} (top left panel of Fig. 5.13) and azimuthal angle (bottom panel of Fig. 5.13). This discrepancy origins from the bias of residual alignment and three SPD modules which were not included in the detector alignment for data. In order to reduce the potential bias caused by this discrepancy, a tuning procedure is applied to MC by applying the tracks in simulation a scaling of the residuals $d_0^{\mathrm{true}} - d_0^{\mathrm{rec}}$ according to the impact parameter resolution ratio of data-to-MC, and using the same shift of d_0^{rec} observed in data. In addition, both the covariance matrix of single tracks and secondary vertex are updated after these corrections to avoid a bias for cuts on the standardized topological variables such as the normalized decay length.

In addition, considering that the D^0 p_{T} shape in the Monte Carlo are generated using PYTHIA which could bias the efficiency, the MC shape is matched to data by applying a weight function to the D^0 shape in MC. In the left panel of Fig. 5.14, the comparison of the cross section in data for the 0-10% centrality class (green points)

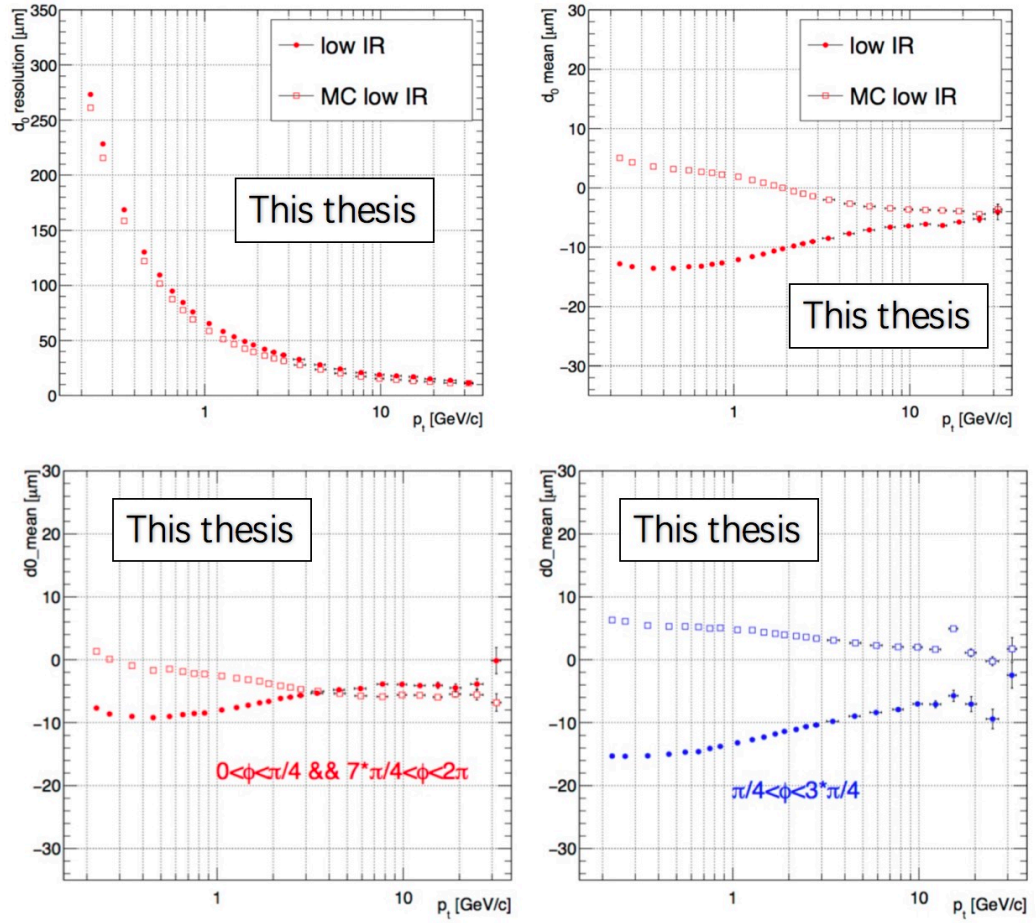

Figure 5.13: Top: the impacter parameter resolution (left) and mean value (right) comparison as a function of p_{T} between 2015 Pb–Pb data (solid points) and MC (open points). Bottom: the comparison of impacter parameter mean value in data and MC as a function of phi.

and the MC production at the acceptance level (red points) are presented, both are scaled with the integral of the entries. A big discrepancy can be found for these two distributions. Then one can fit the ratio of these two distributions to obtain the weight. Fits are applied with Landau, polynomial 5 and exponential functions for the p_{T} region 1-1.5, 1.5-14 and 14-50 GeV/c, respectively. The right panel of Fig. 5.14 shows that the MC with a proper scale can have a good agreement with the corrected yield from data after applying the weight. For the 30-50% centrality class, the weight is calculated using the FONLL calculation [76, 77] multiplied by the R_{AA} predicted by the BAMPS model which implements both elastic and radiative processes [127, 128, 129]. For the 60-80% centrality class, only the FONLL calculations are used as the R_{AA} is nearly flat in the measured p_{T} interval.

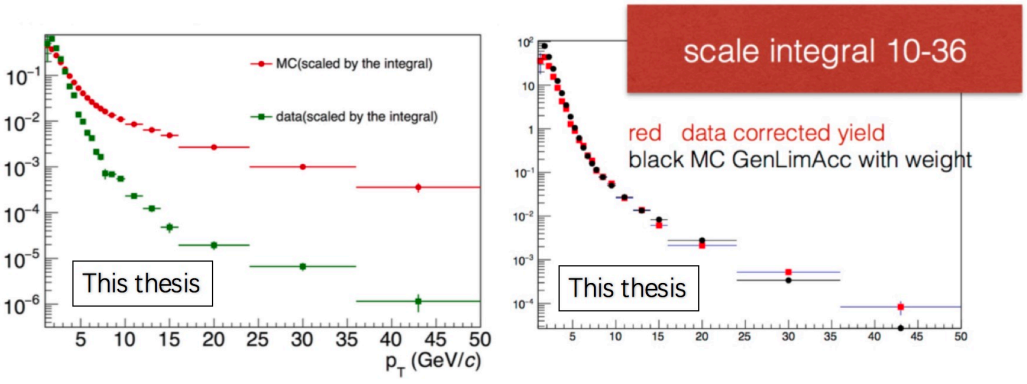

Figure 5.14: Left: the comparison of the cross section in data (green points) and the MC production at the generated limited acceptance level (red points). Right: the comparison of data corrected yield and MC production at the generated limited acceptance level times weight with the same scale.

5.3.1 Efficiency Correction

The raw yield extracted from the invariant mass only contains a fraction of total D^0 production in the collisions, because of the detector limited acceptance, detector dead zone, vertex and track reconstruction, decay topological selections. The raw yield was to be corrected for the reconstruction and selection efficiency in order to get the total yield.

Fig. 5.15 shows the Acc $\times$ ε for the prompt (red points) and feed-down (green points) D^0 mesons in Pb–Pb collisions with the rapidity $|y| < y_{\rm fid}$ at 0-10% (top panel), 30-50% (middle panel) and 60-80% (bottom panel) centrality classes respectively. It rises from few per thousand in the lowest transverse momentum bins included in the analysis and reaching around 20–25% at high $p_{\rm T}$, and the Acc $\times$ ε is higher for more peripheral collisions, since less stringent selections need to be applied because of the less combinatorial background. Feed-down D^0 efficiency is usually higher than the prompt D^0 one, because some of the topological selections, such as decay length, will reject less feed-down contribution (large B-meson lifetime $c\tau \approx 500\ \mu m$ [44]). At high $p_{\rm T}$, thanks to the $|d_0 - d_0^{exp}|^{prong}(n\sigma)$ selection, the contributions of feed-down D^0 meson can be efficiently removed.

5.3.2 Correction for feed-down from B decays

As described in [42], the prompt D^0 meson production yields $\mathrm{d}N/\mathrm{d}p_{\rm T}$ in Pb–Pb collisions are obtained by subtracting the contribution of D mesons from B decays with the same procedure used for the measurement of the production cross sections in pp collisions [130]. In detail, the feed-down contribution was estimated using the beauty production cross section from the FONLL calculation, the B$\rightarrow$D decay kinematics from the EvtGen package, and the Monte Carlo efficiencies for feed-down D mesons. For Pb–Pb collisions, the FONLL feed-down cross section in pp

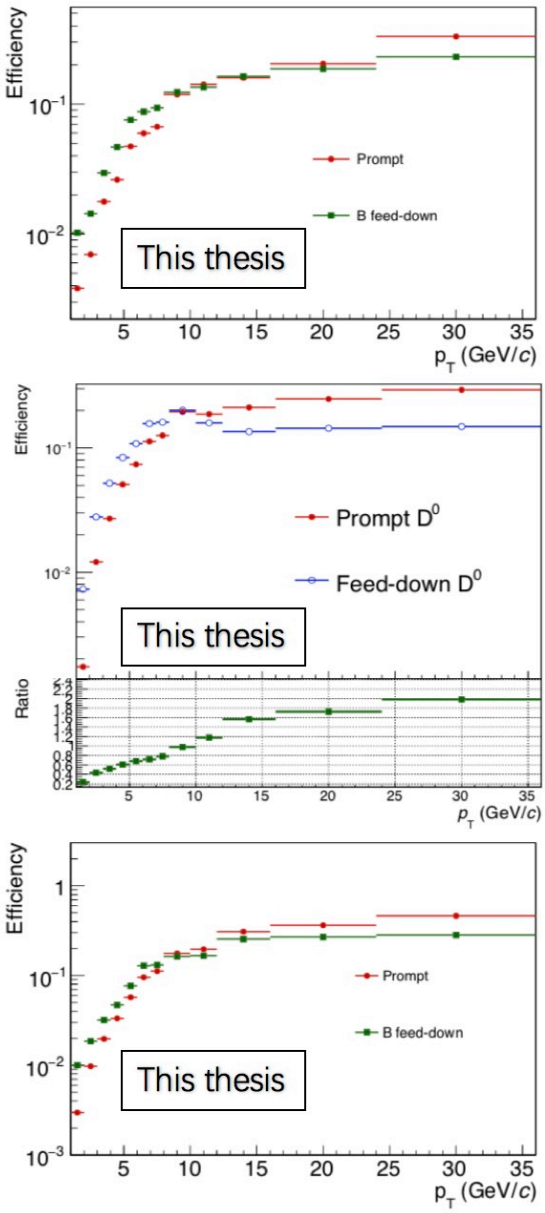

Figure 5.15: The Acc $\times \varepsilon$ for the prompt (red points) and feed-down (green points) D^0 mesons in Pb–Pb collisions at 0-10% (top panel), 30-50% (middlepanel) and 60-80% (bottom panel) centrality classes respectively.

at $\sqrt{s}$ =5.02 TeV was scaled by the average nuclear overlap function $\langle T_{\rm AA} \rangle$ in each centrality class. Thus, omitting for brevity the symbol of the $p_{\rm T}$-dependence ($p_{\rm T}$),

the fraction of prompt D mesons reads:

$$f_{\rm prompt} = 1 - (N^{\rm D^0\ feed-down\ raw}/N^{\rm D^0\ raw}) = \\ = 1 - \langle T_{\rm AA}\rangle \cdot \left(\frac{{\rm d}^2\sigma}{{\rm d}y\,{\rm d}p_{\rm T}}\right)^{\rm FONLL}_{\rm feed-down} \cdot \frac{({\rm Acc}\times\varepsilon)_{\rm feed-down}\cdot\Delta y\,\Delta p_{\rm T}\cdot{\rm BR}\cdot N_{\rm evt}}{N^{\rm D^0\ raw}/2}, \tag{5.3}$$

where $({\rm Acc}\times\varepsilon)_{\rm feed-down}$ is the acceptance-times-efficiency for feed-down D mesons and the factor 2 at the denominator comes for counting both particle and antiparticle are combined while in FONLL not. The nuclear modification factor of the feed-down D mesons, $R_{\rm AA}^{\rm feed-down}$, is related to the nuclear modification of beauty production in Pb–Pb collisions, which is currently unknown. The comparison of the $R_{\rm AA}$ of prompt D mesons ($R_{\rm AA}^{\rm prompt}$) at $\sqrt{s_{\rm NN}} = 2.76$ TeV [131] with that of J/ψ from B-meson decays [132] at the same energy measured by the CMS Collaboration indicates that prompt charmed hadrons are more suppressed than non-prompt charmed hadrons. The $R_{\rm AA}$ values differ by a factor of about two in central collisions at a transverse momentum of about 10 GeV/c [131] and this difference is described by model calculations with parton-mass-dependent energy loss. Therefore, for the centrality classes 0–10% and 30–50%, the value $R_{\rm AA}^{\rm feed\text{-}down} = 2\cdot R_{\rm AA}^{\rm prompt}$ was used to compute the correction for $\rm D^0$ mesons with $3 < p_{\rm T} < 24$ GeV/c. This hypothesis was varied in the range $1 < R_{\rm AA}^{\rm feed\text{-}down}/R_{\rm AA}^{\rm prompt} < 3$ considering the data uncertainties and model variations to estimate a systematic uncertainty. For $1 < p_{\rm T} < 3$ GeV/c and $24 < p_{\rm T} < 50$ GeV/c, where model calculations predict a reduced difference between the $R_{\rm AA}$ values of prompt and non-prompt charm hadrons [31, 40], the hypothesis $R_{\rm AA}^{\rm feed\text{-}down} = 1.5\cdot R_{\rm AA}^{\rm prompt}$ was used, with a variation in $1 < R_{\rm AA}^{\rm feed\text{-}down}/R_{\rm AA}^{\rm prompt} < 2$ for the systematic uncertainty. For the peripheral class 60–80%, in which the medium effects are milder, also the difference between charm and beauty mesons is assumed to be reduced: the value $R_{\rm AA}^{\rm feed\text{-}down} = 1.5\cdot R_{\rm AA}^{\rm prompt}$, varied in the range $1 < R_{\rm AA}^{\rm feed\text{-}down}/R_{\rm AA}^{\rm prompt} < 2$, was used. The resulting $f_{\rm prompt}$ values, for the central hypotheses on $R_{\rm AA}^{\rm feed\text{-}down}/R_{\rm AA}^{\rm prompt}$, range from about 0.80 to 0.85, depending on the centrality class and $p_{\rm T}$ interval, an example of the prompt fraction of $\rm D^0$ yield in the 0-10% centrality class as a function of $p_{\rm T}$ can be found in Fig. 5.16. The systematic uncertainties obtained from the variation of the hypotheses are discussed in Section 5.4.

5.4 Systematic Uncertainties

Systematic uncertainties on the D-meson yield in Pb–Pb collisions were estimated considering the following sources: (i) extraction of the raw yield from the invariant-mass distributions; (ii) track reconstruction efficiency; (iii) D-meson selection efficiency; (iv) PID efficiency; (v) generated $\rm D^0$-meson $p_{\rm T}$ shape in the simulation; (vi) subtraction of the feed-down from beauty-hadron decays. In addition, the uncertainties on the branching ratios [133] were considered. A procedure similar to that described in [134, 42, 131, 135] and outlined in what follows was used to estimate the uncertainties as a function of $p_{\rm T}$ and centrality.

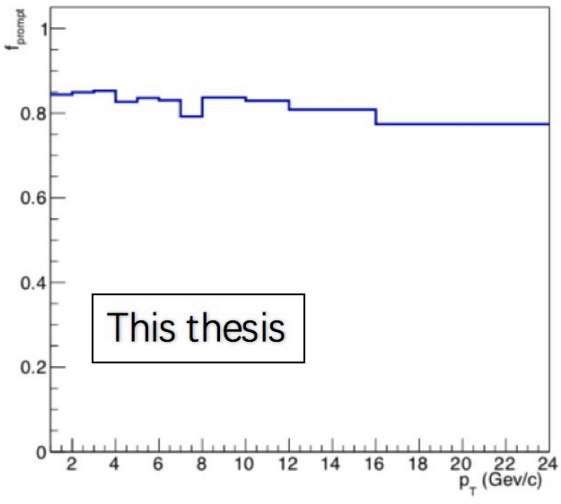

Figure 5.16: The prompt fraction of D^0 yield in the 0-10% centrality class as a function of p_T based on the FONLL calculation and $R_{AA}^{\text{feed-down}}$ hypothesis.

5.4.1 Raw yield extraction

The systematic error on the yield extraction is determined by repeating the fitting procedure described in Sec. 5.2.5 with a different mass range, different histogram bin widths and/or different fitting functions, and using a method based on bin counting after the subtraction of the background estimated from the fit of the side bands. The variations listed above are obtained considering the yields once the reflection contribution has been subtracted.

The systematic uncertainty on the raw yield extraction is evaluated in each p_T interval using a multiple trial approach. The fits to the invariant mass distributions are repeated several times varying i) lower limit of the fit (6 steps in the range 1.65-1.75 GeV/c), ii) upper limit of the fit (6 steps in the range 1.95-2.05 GeV/c), and iii) background fit function (3 cases: exponential, linear and second order polynomial). In addition, all the fits are repeated with the sigma of the Gaussian function fixed to the values obtained from the MC simulation and the mean of the Gaussian function to the PDG value of the D^0 mass. The fits which did not converge or had $\chi^2/ndf >$ 2.0 are rejected and not considered in the evaluation of the systematic uncertainty. In addition, the results obtained with the fitting technique are compared to those obtained by counting the entries within 3.5 σ of the peak in the invariant mass histogram after subtracting the background counts calculated from the background fit function. Also for this check, a multiple trial approach is used. An example of the result for $7 < p_T < 8$ GeV/c with the 30-50% centrality class is shown in Fig. 5.17, the top left, middle and right panels show the Gaussian σ, mean and χ^2/ndf in different trails, respectively. The bottom left and middle panel show the raw yield

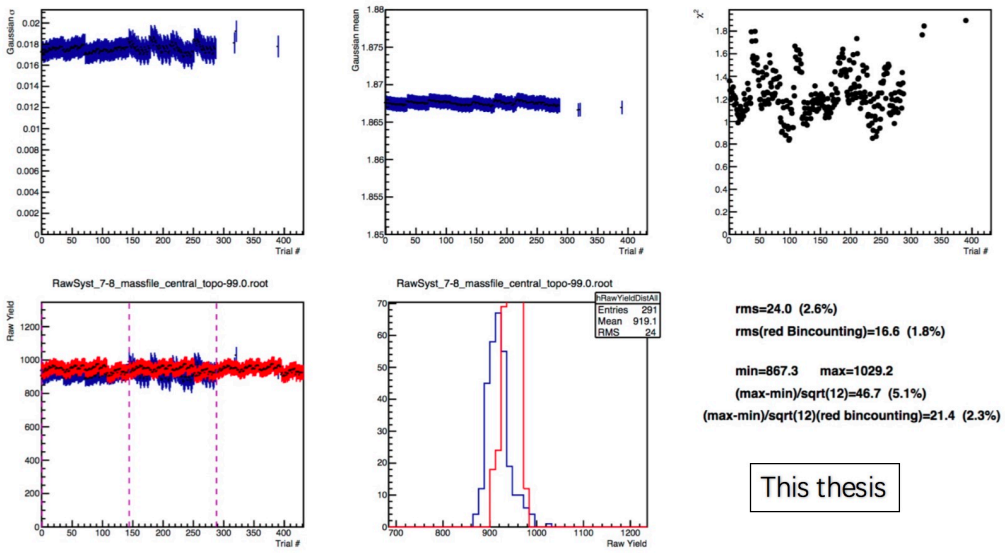

Figure 5.17: D^0 yield extraction systematic uncertainties checks with a multiple trail approach for the bin $7 < p_T < 8$ GeV/c with the 30-50% centrality class.

in different trails and raw yield distributions after sum of all the trials for fitting (blue lines) and bin-counting (red lines) methods. The systematic uncertainty is defined looking at the following statistical parameters:

- difference between the mean and the median of the distribution.
- difference between the mean of the fitting and bin-counting approaches.
- r.m.s. of the distribution.
- full spread of the distribution (i.e. maximum-minimum) divided by $\sqrt{12}$.

For some of the p_T intervals, a difference is observed between free and fixed sigma cases. This suggests that the invariant-mass resolution in these p_T bins is not exactly reproduced in the MC simulation. Therefore, the spread induced by fixing the sigma in the Gaussian function is not considered for the systematic uncertainty evaluation, not to introduce a bias given by the possible not perfect description of the invariant-mass resolution in the MC simulation. At high p_T, a discrepancy between the fitting and the bin counting method is also observed, However, in these ranges, the poor statistics plays a significant role in the raw-yield extraction with the bin counting method, since statistical fluctuations aside the peak could artificially enlarge the signal. Therefore the final systematic uncertainty in these bins is tested with the barlow criterion [136].

The amount of reflected singal also affects the yield extraction, which can be evaluated by varying the reflection shape and reflection/signal ratio, as shown in

Fig. 5.18 for the 0-10% centrality class. The reflection shape is fitted by additional Gaussian, third and sixth order of exponential function, and reflection ratio is changed from half to two times of the standard value. The raw yields obtained with different options are compared with each other. One can found 2% difference from 1-24 GeV/c and 4% for 24-50 GeV/c by varying the reflection shape (left panel), 2% at low p_{T} and up to 5% at high p_{T} by varying the reflection/signal ratio (right panel). This systematic contribution is combined with the one on yield extraction.

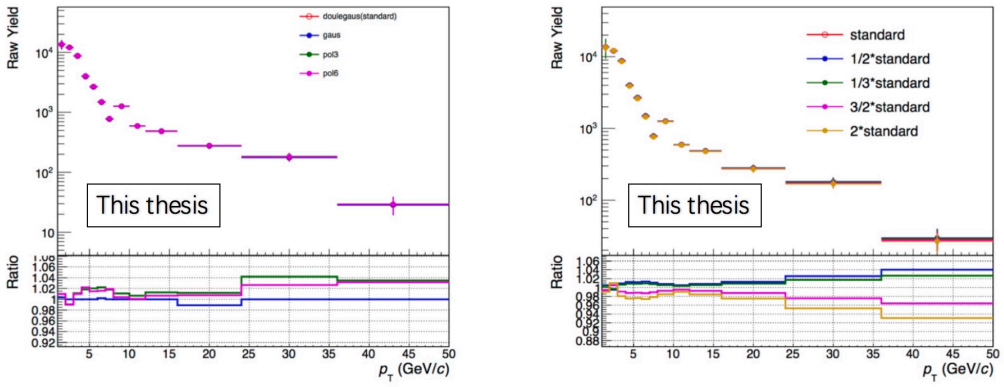

Figure 5.18: The raw yield comparison in the 0-10% centrality class obtained with different reflection shape (left panel) and reflection/signal ratio (right panel).

The total systematic uncertainty for yield extraction is summarized in Tab. 5.5. At both low and high p_{T}, the systematic uncertainty is higher than the one at middle p_{T} region (around 3%), because the huge combinatorial background and lack of signal statistics affect the quality of fitting at low and high p_{T}, respectively.

5.4.2 Interaction rate and rapidity dependence

The final result is checked with the charged K,π requested only from either positive rapidity region or the negative one, the comparison of these two cases is shown in Fig. 5.19: all the cases are compatible with each other within statistical uncertainty, which reflects no systematic bias originates from it.

Another check has been done for the interaction rate effects by separating the sample into high or low interaction rate subsamples. the prompt efficiency for these two cases is different from the mixed sample, which is presented on the left panel of Fig. 5.20 for the 30-50% centrality class. Then the final R_{AA} results are showed on the right panel for these three case, the low or high interaction rate results fluctuate around the mixed one within uncertainties, thus no systematic bias can be found within the current uncertainty for this source.

Table 5.5: Systematic on yield extraction for D^0 in the centrality classes 0-10%, 30-50% and 60-80%.

p_T bin (GeV/c)	0-10%	30-50%	60-80%
[1,2]	14.5	13	10
[2,3]	4.5	9.5	5
[3,4]	2.5	3	2.5
[4,5]	3.5	2	3.5
[5,6]	3.5	2	4
[6,7]	3.5	2.5	4
[7,8]	4.5	3	4
[8,10]	4.5	3	4
[10,12]	4.5	3	4
[12,16]	6	4	4
[16,24]	9.5	4	10
[24,36]	9.5	9.5	10
[36,50]	9.5	–	–

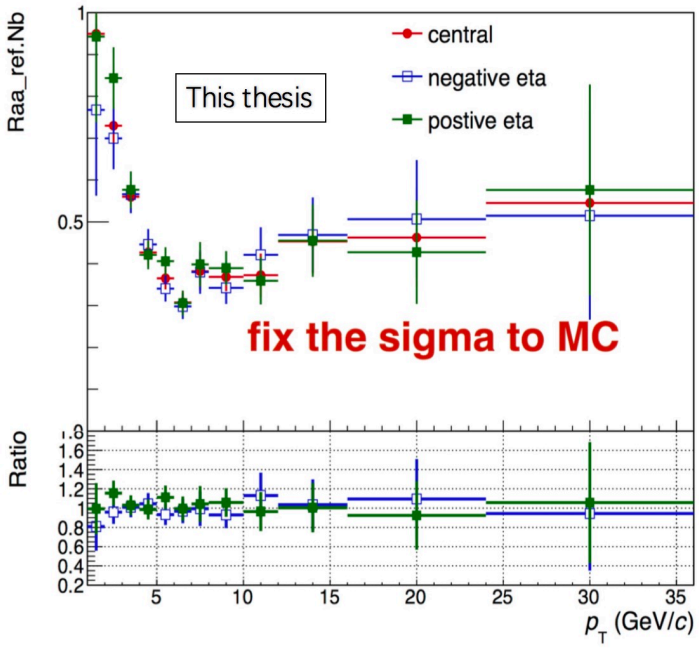

Figure 5.19: The variation of prompt efficiency (left panel) and the final R_{AA} (right panel) with different selections for the 30-50% centrality class.

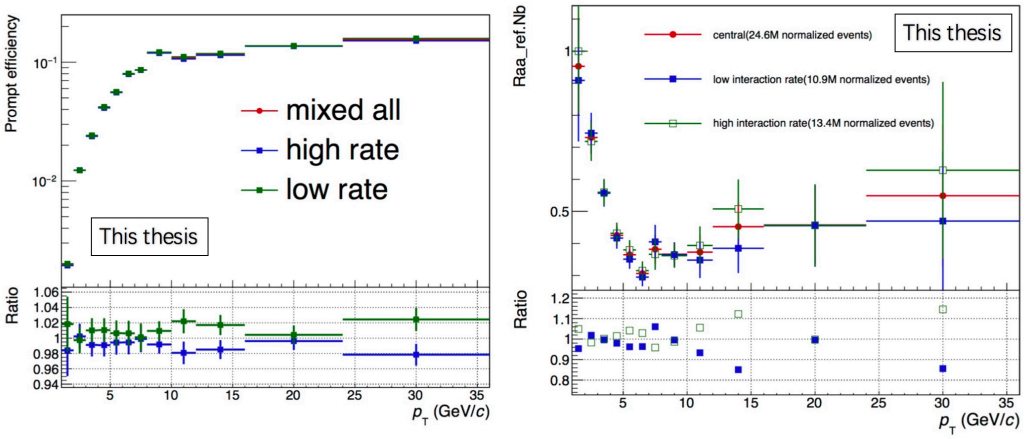

Figure 5.20: The variation of prompt efficiency (left panel) with different interaction rate samples and the final R_{AA} (right panel) of these three cases for the 30-50% centrality class.

5.4.3 Selection efficiency

A further systematic uncertainty can arise due to differences in cut variables shape in data and Monte Carlo and due to residual misalignment. These sources where checked by repeating the analysis varying the main selection cuts by around 30% up and down from the standard set of cuts. Moving the main cuts all left or all right may introduce a bias due to the fact that all the cuts goes in the same direction. Due to this concern, different sets of cuts, alternative to the standard one were tested. An example of the results of the cut variation procedure is shown in Fig. 5.21 for the 30-50% centrality class, two looser and two tighter selections with respect to the standard one have been applied. The selections have been applied for all variables in the same direction, one at a time, in order to search for possible trends or biases. The left panel shows that the prompt efficiency varies by more than 15% with respect to the standard selection. After that, the variation of the R_{AA} is obtained as shown in the right panel. For the bin 1-2 GeV/c, the variation is within $\pm$10%, while for the higher p_{T} region, the variation is within $\pm$5%. All the numerical values assigned as a systematic uncertainty for the selection efficiency are reported in Tab 5.6.

5.4.4 Generated p_{T} shape for efficiencies

Another source of systematic uncertainty investigated is the one arising from the D meson p_{T} shape assumed in the Monte Carlo used for corrections, which has been mentioned in Sec. 5.3. In order to check the stability of our efficiencies against the change in p_{T} shape and to define a systematic uncertainty, several set of weights were used. For 0-10%, the efficiency obtained using the FONLL times LBT [35] weights are considered as the alternative shape, for 30-50%, FONLL shape is used,

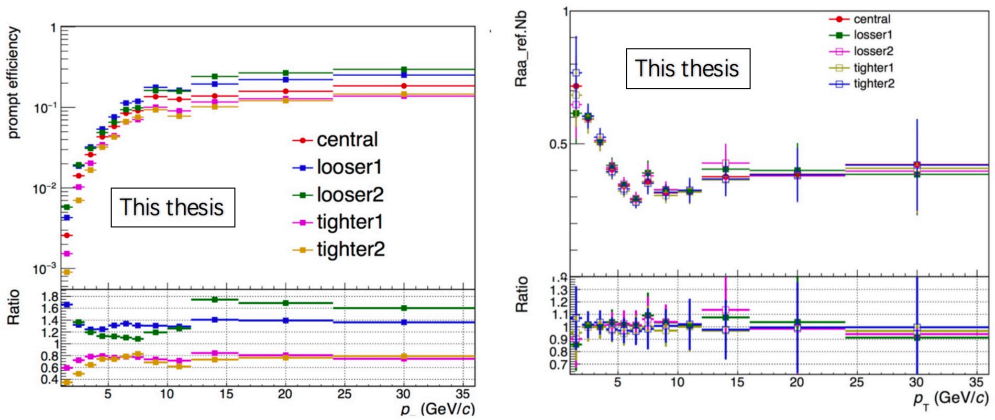

Figure 5.21: The variation of prompt efficiency (left panel) and the final $R_{\rm AA}$ (right panel) with different selections for the 30-50% centrality class.

Table 5.6: Systematic uncertainties on selection efficiency for $\rm D^0$ in the centrality classes 0-10%, 30-50% and 60-80%.

$p_{\rm T}$ bin (GeV/c)	0-10%	30-50%	60-80%
[1,2]	10	10	10
[2,3]	5	5	5
[3,4]	5	5	5
[4,5]	5	5	5
[5,6]	5	5	5
[6,7]	5	5	5
[7,8]	5	5	5
[8,10]	5	5	5
[10,12]	5	5	5
[12,16]	5	5	5
[16,24]	5	5	5
[24,36]	5	5	5
[36,50]	5.5	–	–

while for 60-80%, the additional weights are FONLL times BAMPS [127]. Fig. 5.22 shows the relative change for efficiencies by using LBT and FONLL (blue) or data-driven (red) weights (default) in the left panel for the 0-10% centrality class, and relative change for efficiencies by using FONLL (green) or FONLL times BAMPS (red) weight in the right plots for the 60-80% centrality class.

The analysis is stable against the variation of the MC $p_{\rm T}$ shape above 4 GeV/c, while in the transverse momenta range $2 < p_{\rm T} < 3$ GeV/c a systematic effect of

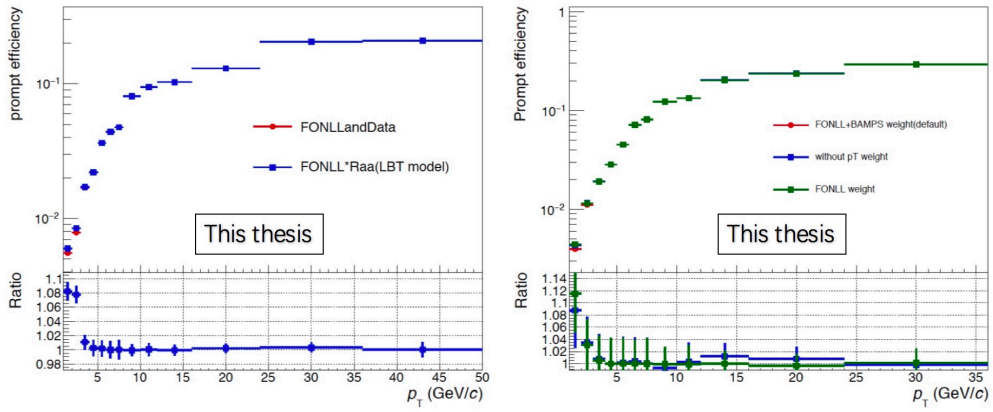

Figure 5.22: Relative change for efficiencies by using LBT and FONLL (blue) or data-driven (red) weights (default) in the left panel for the 0-10% centrality class, and relative change for efficiencies by using FONLL (green) or FONLL times BAMPS (red) weight in the right plots for the 60-80% centrality class.

about 3% is visible and around 8–14% for the bin $1 < p_{\mathrm{T}} < 2$ GeV/c. For the 0-10% centrality class, the LBT weight increases the systematic uncertainties to 7% for the bin 2-3 GeV/c, because the model predicts the maximum value of the R_{AA} to be at 3 GeV/c, unlike the other models. The values of the MC generated p_{T} shape systematic uncertainty are reported in Tab 5.7.

Table 5.7: Systematic uncertainties on generated p_{T} shape for D^0 in the centrality classes 0-10%, 30-50% and 60-80%.

p_{T} bin (GeV/c)	0-10%	30-50%	60-80%
[1,2]	8	14	12
[2,3]	7	3	3
[3,4]	1	1	1
[4,5]	0	0	0
[5,6]	0	0	0
[6,7]	0	0	0
[7,8]	0	0	0
[8,10]	0	0	0
[10,12]	0	0	0
[12,16]	0	0	0
[16,24]	0	0	0
[24,36]	0	0	0
[36,50]	0	–	–

5.4.5 PID efficiency

In the analysis, a PID selection at 3σ level on TPC and TOF signals was applied. The systematic effect due to the PID selection is studied by repeating the analysis without PID selection and comparing the resulting cross section with the one obtained with PID. In the case of the analysis without PID the width of the Gaussian function in the invariant-mass fits is kept fixed to the value obtained with PID. The ratio of raw yield with and without PID is compared with the PID efficiency from MC. In the left panel of Fig. 5.23 for the 0-10% centrality class. The ratios are compatible with unity for most p_{T} bins, the last bin is affected by the difficult signal extraction and is dominated by fluctuations. For the bin 1-2 GeV/c, a large discrepancy can be found for the PID efficiency obtained by data. The residual of the invariant mass after background subtraction for the no PID case is shown in the right panel of Fig. 5.23: It's clear that the fit quality is insufficient, therefore no systematic uncertainty is assigned for the PID efficiency source.

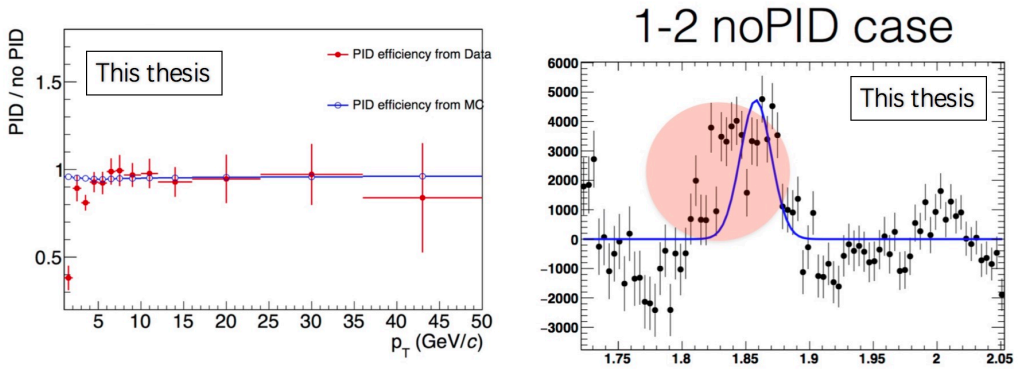

Figure 5.23: The PID efficiency comparison between data and MC at 0-10% is presented in the left panel. The residual of raw yield obtained for the bin 1-2 GeV/c with no PID case showed on the right panel.

5.4.6 Track reconstruction efficiency

The systematic uncertainty related to the tracking efficiency includes the effects arising from track finding in the TPC, from track propagation from the TPC to the ITS, and from track quality selections. It was estimated with the following tests:

- comparison of the cross sections obtained with different track selection cuts;
- comparison of the TPC-ITS track matching efficiency in data and simulations.

These checks are discussed in detail in the following subsections.

5.4.6.1 Variation of track selections

The D-meson raw yields, efficiency and corrected yields are evaluated with different sets of track selection cuts. Only one cut at a time is changed with respect to the standard values reported in Sec. 5.2.5. The following four cut variations are tested:

1. additional cut on number TPC crossed rows $> 120 - (5/p_{\mathrm{T}})$;
2. number of TPC clusters $> 0.65\times$ number of TPC crossed rows;
3. additional cut on number of clusters with TPC dE/dx signal $> 0.5\times$ number of TPC crossed rows;
4. ratio of crossed rows over findable clusters in the TPC > 0.9.

An example of the result for the 30-50% centrality class is reported in Fig. 5.24, which shows the R_{AA} results obtained with various track-cut selections compared with the default one. One can see that a systematic deviation of, on average, about 2% is observed for the two-body decay channel to obtain D^0. So one could account for a 1% systematic uncertainty per track.

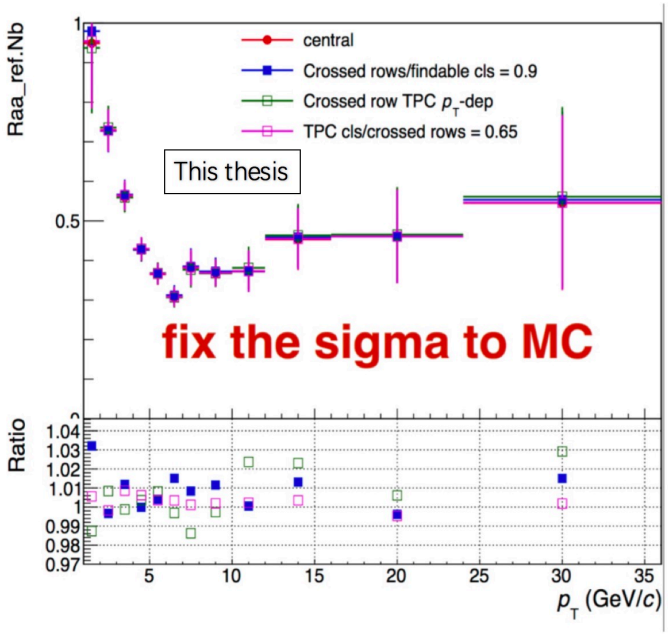

Figure 5.24: The R_{AA} comparison from track selection variations for the 30-50% centrality class.

5.4.6.2 Matching efficiency

Matching efficiency is defined as the fraction of tracks with clusters in both ITS and TPC over the total number of tracks with clusters in TPC. Systematic uncertainty on its determination arises from discrepancies in efficiency between data and Monte Carlo. Matching efficiency for primary tracks is expected to be higher than for secondary tracks (originating from strangeness decay, thus with secondary vertices likely to be out of SPD) or tracks arising from interaction with material. If the fractions of primary and secondary tracks are different in data and in Monte Carlo, this could lead to a wrong estimation of systematic uncertainty in the matching. Hence, the idea here is to evaluate the real fraction of track types in data, and to use them to re-weight respective MC efficiencies to obtain a corrected inclusive MC efficiency. The latter will be compared with efficiency on data to extract the systematic uncertainty.
The ingredients are:

- Matching efficiencies for different particle types: $\mathrm{Eff}^{\mathrm{MC}}_{\mathrm{primaries}}$, $\mathrm{Eff}^{\mathrm{MC}}_{\mathrm{secondaries}}$, $\mathrm{Eff}^{\mathrm{Data}}_{\mathrm{inclusive}}$
- Fraction of primary tracks in data: $\mathrm{f'}_{\mathrm{primaries}}$
- Corrected MC-inclusive efficiency: $\mathrm{Eff}^{\mathrm{MC}}_{\mathrm{inclusive}} = \mathrm{f'}_{\mathrm{primaries}} \times \mathrm{Eff}^{\mathrm{MC}}_{\mathrm{primaries}} + (1\text{-}\mathrm{f'}_{\mathrm{primaries}}) \times \mathrm{Eff}^{\mathrm{MC}}_{\mathrm{secondaries}}$
- Systematic uncertainty: $(\mathrm{Eff}^{\mathrm{Data}}_{\mathrm{inclusive}} - \mathrm{Eff}^{\mathrm{MC}}_{\mathrm{inclusive}})/\mathrm{Eff}^{\mathrm{Data}}_{\mathrm{inclusive}}$

The Charm-enriched productions were not used in this study as not advisable for fitting the DCA distribution at the level of the primary fraction extraction, since the peak shape of the DCA is slightly modified by the heavy flavour enrichment. Efficiency was studied as a function of p_{T}, in 7 bins from 0.5 to 15 GeV/c.

We explain below in detail the steps needed to calculate the systematic uncertainty.

1. **ITS-TPC matching efficiency:** calculated separately for primary and secondary tracks in MC, inclusively on data. For the denominator of the efficiency, i.e. tracks with TPC clusters, the selection was made requiring a TPC refit on the tracks, with no further requests on SPD clusters neither other ITS selections or refit. As for the numerator of the efficiency, the tracks were required to pass the "kAny" selection on SPD clusters, i.e. to have a cluster on at least one of the SPD layers. Tracks were selected requiring a cut on |DCAxy| <2.4 cm and on |DCAz| <3.2 cm.

   In Fig. 5.25, matching efficiency for primary (blue) and secondary (green) tracks in different p_{T} intervals from 0.5 to 20 GeV/c is shown for the MC sample.In Fig. 5.26 the comparison among matching efficiency, both in data and MC, for the three samples analyzed. What one can notice from this plot, is that matching efficiency in data is influenced by pile-up contribution that makes the efficiency lower for samples with higher interaction rate (IR). Moreover, there are effects also on MC efficiencies at high p_{T} coming from

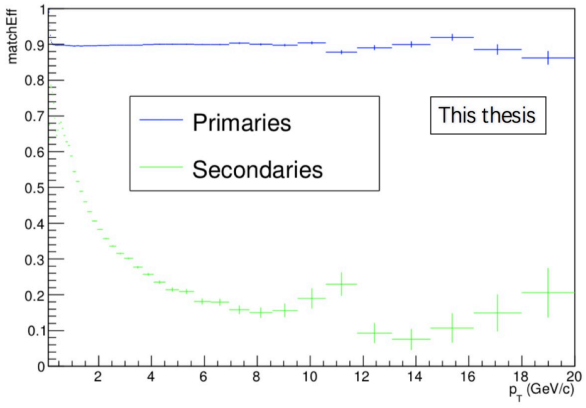

Figure 5.25: Matching efficiency for primaries (blue) and secondaries (green) tracks in the full p_{T} intervals from 0.5 to 20 GeV/c.

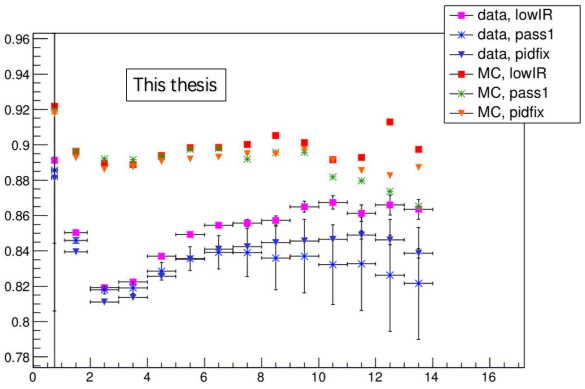

Figure 5.26: Matching efficiency, both in data and MC, for the three sample analyzed versus p_{T}.

residual track distortion effects which are not fully corrected. For this reason, the matching efficiency of the low IR period was used for the systematic uncertaintiy evaluation.

2. **Fractions of primary tracks:** extracted from a fit to the impact parameter distribution on data using MC templates for primary and secondary contributions. The ROOT TFractionFitter package was used to perform the fit. The fit could be resolved using three templates describing primary particles, secondaries from strangeness and secondaries from material. A selection on tracks requiring SPD kAny was used, to assure enough resolution and distinguish pri-

mary from secondary DCA distributions. Fit was performed on the DCAxy distributions of charged particles in the range [-1,1] cm, in different intervals of p_{T} and constraining the 3 fractions within reasonable minimum and maximum values. The fractions were then calculated integrating the histograms resulting from the fit in the range |DCAxy| < 2.4 cm, for consistency with the matching efficiency calculation. In Fig. 5.27 the distributions of DCAxy in data and in MC for the different contributions are shown in different colours, in p_{T} intervals from 0.5 to 15 GeV/c. Finally, in Fig. 5.28, the primary and secondary fractions extracted from fit on data are shown and compared to the ones obtained from MC truth (empty markers). As a closure test, it was verified that the latter MC fractions did not change when extracting them from a fit using TFractionFitter on MC inclusive distribution itself, with the three usual MC templates. The fraction of secondaries in the figure already includes the contribution from material. The fraction of secondaries is underestimated in MC.

3. **Correction to the primary fraction:** since the fraction of primary particles was calculated on tracks passing the selection SPD kAny, we need to rescale the primary fraction to the total number of tracks in TPC. The correction factor is based on MC information and obtained as the ratio of the fraction of primary tracks in TPC with the fraction of primary tracks with match TPC-ITS. The final fraction of primary tracks is hence $\mathrm{f'_{primaries}} = \mathrm{f_{primaries}}$ x correction factor, where $\mathrm{f_{primaries}}$ is the fraction obtained at step 2. Typical values of correction factor are around $\sim$ 0.95-0.98.

4. **ITS-TPC corrected matching efficiency:** calculated as $\mathrm{Eff^{MC}_{inclusive}} = \mathrm{f'_{primaries}}$ x $\mathrm{Eff^{MC}_{primaries}}$ + (1- $\mathrm{f'_{primaries}}$) x $\mathrm{Eff^{MC}_{secondaries}}$. The corrected matching efficiency is shown in Fig. 5.29 as a function of p_{T}, for kaons and pions only (using particle identification, requiring a 3-sigma cut). Finally, the ratios of the latter inclusive MC-corrected efficiencies with data are shown in Fig. 5.29. It is evident how the re-weighting of MC with the real fractions of track types is useful in quoting a truthful and reduced systematic uncertainty.
   Error bars were assigned to matching efficiency to account for statistical fluctuations. A systematic uncertainty of 2% for particles with p_{T} <2 GeV/c and 3 < p_{T} <9 GeV/c, of 3% for 2 < p_{T} <3 GeV/c and of 3.5% for p_{T} > 9 GeV/c per track was assigned. This per-track uncertainty needs to be summed in quadrature with the 1% uncertainty coming from systematic on track selection.
   Finally, a MC simulation was used to propagate the uncertainty at the track level to the D meson level, accounting for the daughter's kinematic in the D-meson p_{T} range of our analysis. In the MC simulation the same topological and PID cuts used on data were applied, to account also for possible influence of topological selection on daughter's kinematics. In the left column of Fig. 5.30, one can see the scatter plot of D-meson p_{T} versus daughter's p_{T}. The right column shows instead the final systematic on matching efficiency for

2-prong D mesons as a function of p_{T}.

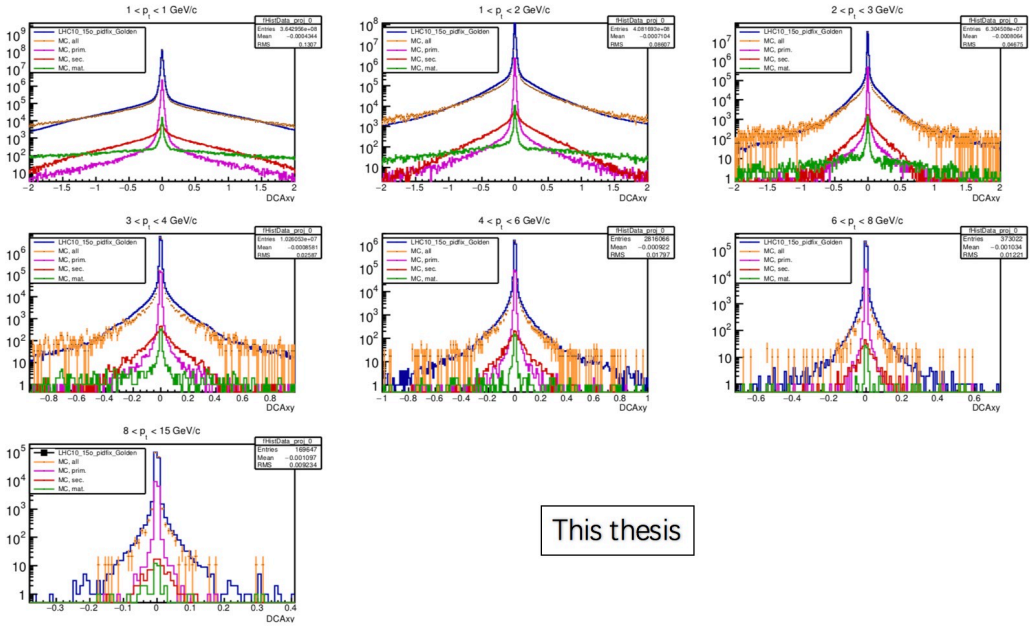

Figure 5.27: DCAxy distributions in data and in MC for primary and secondary tracks in different colours, in p_{T} intervals from 0.5 to 15 GeV/c.

5.4.7 B feed-down subtraction

In order to estimate the systematic uncertainty from the B feed-down subtraction, the perturbative uncertainty on the FONLL beauty production cross section was considered, by varying the b quark mass and the factorization and renormalization scales as suggested in [130]. Another contribution is estimated by varying the range of $R_{\mathrm{AA}}^{\text{feed-down}}/R_{\mathrm{AA}}^{\text{prompt}}$ which has been discussed in Sec. 5.3.2. An example of the relative variation of prompt D^0 yields is presented as a function of the hypothesis on $R_{\mathrm{AA}}^{\text{feed-down}}/R_{\mathrm{AA}}^{\text{prompt}}$ is showed in Fig. 5.31 for 30-50% centrality class. It ranges between 5% to 12% from low p_{T} to high p_{T} region.

5.4.8 Summary of systematic uncertainties

After obtaining the p_{T}-differential yield described by Eq. 5.2, the measurement of R_{AA} can be calculated using Eq. 1.8. The systematic uncertainties on the R_{AA} measurement include those on the D-meson corrected yields described above, those on the proton–proton reference cross section, and the uncertainties on the average nuclear overlap function.

In the calculation of the nuclear modification factor, the systematic uncertainty on the feed-down subtraction deriving from the variation of the parameters of the

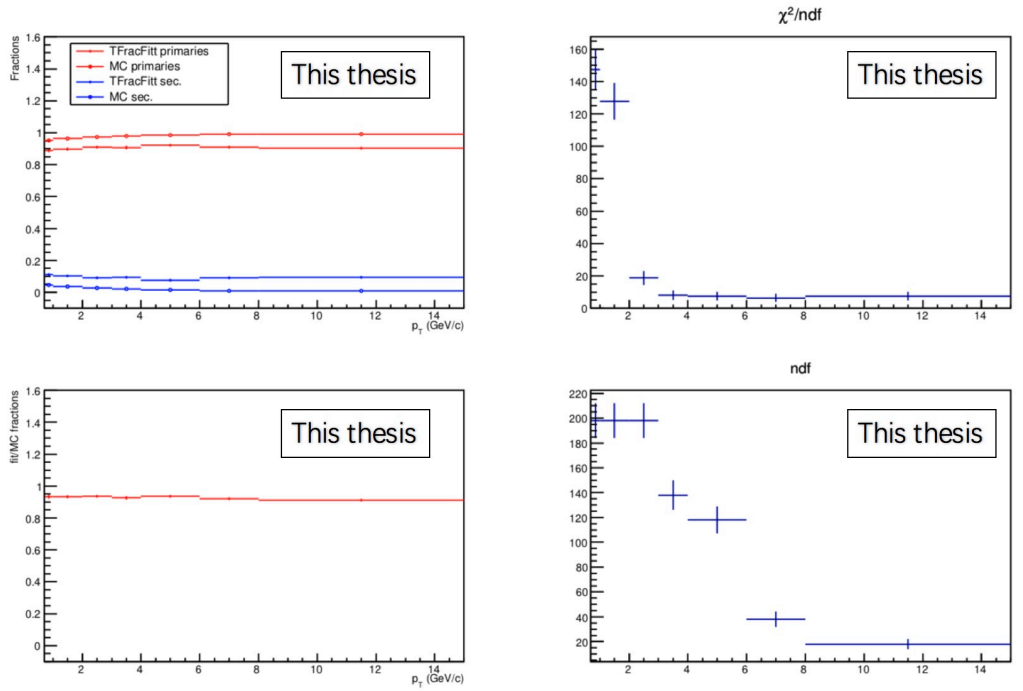

Figure 5.28: Example of fractions of primary (red) and secondary (blue) tracks in data (no marker) and MC (marker) as a function of p_{T}, together with reduced χ^2 values of the fits, involved n.d.f and ratio of fractions from data and MC.

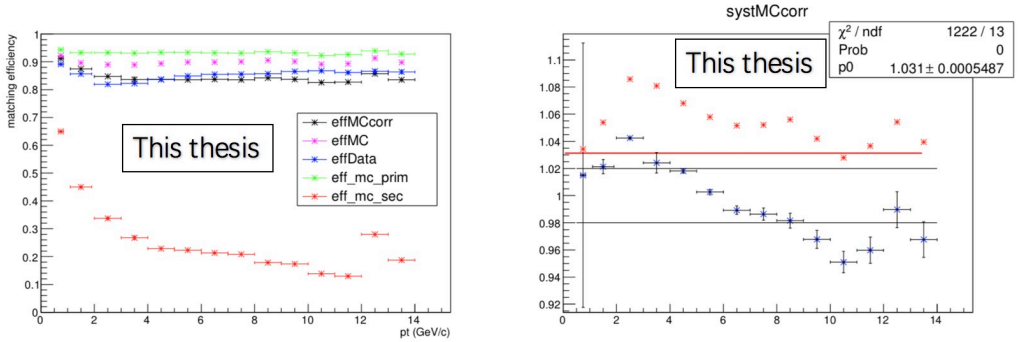

Figure 5.29: Left: Matching efficiency for data and for MC (before and after the correction) in different colours. Right: Systematic uncertainties due to the matching efficiency as a function of p_{t} for low IR. The systematics is shown for the MC corrected (blue) and the uncorrected MC (red).

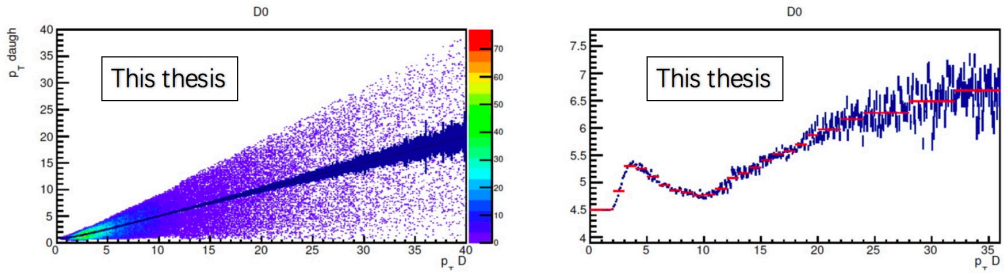

Figure 5.30: Left column: scatter plot of daughter's p_{T} versus D^0 p_{T}. Right column: final systematic uncertainties propagated at D-meson level after weighting for daughter's kinematics, as a function of p_{T}.

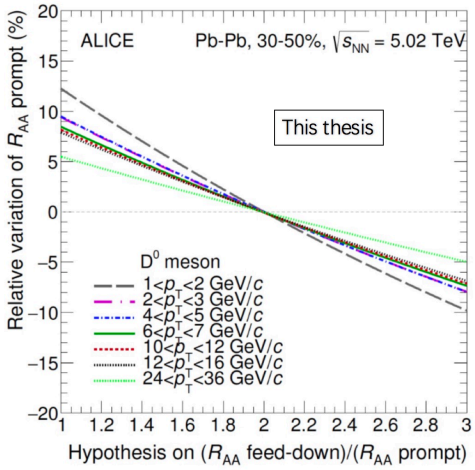

Figure 5.31: The relative variation of prompt D^0 yields is presented as a function of the hypothesis on $R_{\mathrm{AA}}^{\text{feed-down}}/R_{\mathrm{AA}}^{\text{prompt}}$ for 30-50% centrality class.

FONLL calculation was considered to be correlated in the Pb–Pb and pp measurements, while all the other sources of systematic uncertainties were treated as uncorrelated and added in quadrature.

5.4.8.1 Proton-proton reference

The reference p_{T}-differential cross section of prompt D^0-meson at mid-rapidity in pp collisions at $\sqrt{s}$ = 5.02 TeV was not available at the first Pb–Pb analysis. Instead, a scaling to $\sqrt{s}$ = 5.02 TeV is applied to the measurements at $\sqrt{s}$ = 7 TeV [137] based on the FONLL calculation [92]. Also, the results are extrapolated

to higher $p_{\rm T}$ intervals. The results can be written as:

$$\frac{{\rm d}\sigma}{{\rm d}p_{\rm T}}(5.02{\rm TeV}, p_{\rm T}^{1}, p_{\rm T}^{2}) = \frac{{\rm Fit}_{\rm intergral}({\rm data/FONLL}, p_{\rm T}^{3}, p_{\rm T}^{4})}{p_{\rm T}^{4} - p_{\rm T}^{3}} \times (\frac{{\rm d}\sigma}{{\rm d}p_{\rm T}}(5.02{\rm TeV}, p_{\rm T}^{1}, p_{\rm T}^{2}))^{\rm FONLL} \tag{5.4}$$

The procedure can be briefly described as: 1) compute the ratio between data and theoretical prediction considering the measurement statistical uncertainties, 2) doing the exercise for all the calculation parameters, 3) doing this by shifting up/down the data points by their systematic uncertainties. Then fitting the ratio between data and theoretical prediction. The uncertainties on the $p_{\rm T}$-dependent scaling factor from $\sqrt{s}$ =7 TeV to $\sqrt{s}$ =5.02 TeV are determined by varying the FONLL parameters (charm-quark mass, factorisation and renormalisation scales) as described in [138]. The uncertainties range from $^{+17}_{-4}$% for 1<$p_{\rm T}$<2 GeV/c to about ±3% for $p_{\rm T}$>10 GeV/c. As mentioned, at high $\rm D^0$-meson $p_{\rm T}$ (36<$p_{\rm T}$<50 GeV/c), the FONLL calculation at $\sqrt{s}$ = 5.02 TeV [92] is used as a reference by scaling the values to match the central value of the scaled data at lower $p_{\rm T}$. This procedure is described in Ref. [42]. As an example, the total systematic uncertainties on the pp reference with 36<$p_{\rm T}$<50 GeV/c is $^{+38}_{-28}$%.

5.4.8.2 Normalisation

The uncertainties on the $R_{\rm AA}$ normalisation are the quadratic sum of (i) the pp normalisation uncertainty (3.5%), (ii) the uncertainty on $\langle T_{\rm AA}\rangle$, which ranges from 1.9% to 3.4% depending on the centrality, and (iii) the variation of raw yield (< 0.1%, 2% and 3% for the 0–10%, 30–50% and 60–80% centrality classes, respectively) obtained when the centrality intervals are varied to account for the uncertainty on the fraction of the hadronic cross section used in the Glauber fit to determine the centrality [42]. The branching ratio uncertainty cancels out in the ratio.

The systematic uncertainties on the $p_{\rm T}$-differential spectra and $R_{\rm AA}$ in the two extreme centrality classes are listed in Table 5.8 for the lowest $p_{\rm T}$ interval accessible as well as for the intermediate range $7 < p_{\rm T} < 8$ GeV/c.

5.5 Results

The transverse-momentum distribution ${\rm d}N/{\rm d}p_{\rm T}$ of prompt $\rm D^0$-meson is shown in Fig. 5.32 for the 0–10%, 30–50% and 60–80% centrality classes. The vertical bars represent the statistical uncertainties and the empty boxes the systematic uncertainties. The uncertainty on the branching ratios is quoted separately.

Figure 5.33 shows the $p_{\rm T}$-dependent ratios of meson yields, $\rm D^+/D^0$, $\rm D^{*+}/D^0$, $\rm D_s^+/D^0$ and $\rm D_s^+/D^+$, in the 0–10%, 30–50% and 60–80% centrality classes in Pb–Pb collisions at $\sqrt{s_{\rm NN}}$ = 5.02 TeV [28], compared to the values measured in pp collisions at $\sqrt{s}$ =7 TeV [137]. The systematic uncertainties are propagated to the ratios, considering the contribution from the tracking efficiency as a fully correlated uncertainty among the four D-meson species. The beauty-hadron feed-down subtraction is considered as fully correlated among the three non-strange D-meson

	0–10% centrality class		60–80% centrality class	
$p_{\rm T}$ interval (GeV/c)	1–2	7–8	1–2	7–8
Syst. on dN/d$p_{\rm T}$ in Pb–Pb	$^{+21}_{-22}$%	$^{+16}_{-17}$%	22%	$^{+12}_{-13}$%
Yield extraction	15%	5%	10%	4.5%
Tracking efficiency	6%	7%	6%	7%
PID efficiency	0	0	0	0
Cut efficiency	10%	6%	10%	5%
MC $p_{\rm T}$ shape	8%	0	12%	0
Branching ratio	1.0%	1.0%	1.0%	1.0%
Feed-down subtraction	$^{+6.8}_{-7.3}$%	$^{+12.4}_{-12.8}$%	$^{+9.0}_{-9.7}$%	$^{+6.1}_{-7.2}$%
Centrality limit	<0.1%		3.0%	
Syst. on dN/d$p_{\rm T}$ in pp and $\sqrt{s}$-scaling of the pp ref.	$^{+8.8}_{-9.0}$%	$^{+8.4}_{-9.4}$%	$^{+8.8}_{-9.0}$%	$^{+8.4}_{-9.4}$%
Syst. on $R_{\rm AA}$	$^{+22}_{-27}$%	$^{+17}_{-16}$%	$^{+23}_{-28}$%	14%

Table 5.8: Relative systematic uncertainties on the dN/d$p_{\rm T}$ in Pb–Pb collisions, on the extrapolated dN/d$p_{\rm T}$ in pp collisions and on the $R_{\rm AA}$ in two centrality classes considered in the analysis for the lowest accessible $p_{\rm T}$ intervals and for the intermediate range $7 < p_{\rm T} < 8$ GeV/c .

species, while uncorrelated between $\rm D_s^+$ and non-strange D mesons. The $\rm D^+/D^0$ and $\rm D^{*+}/D^0$ ratios are compatible in Pb–Pb and pp collisions, indicating no significant modification of their relative abundances as a function of $p_{\rm T}$ and in centrality classes. The $\rm D_s^+/D^0$ and $\rm D_s^+/D^+$ ratios are measured at $\sqrt{s_{\rm NN}} = 5.02$ TeV with a precision better by a factor about two with respect to 2.76 TeV [42]. The values of these ratios are larger in Pb–Pb than in pp collisions, in all three centrality classes, however the measurements in the two systems are compatible within about one standard deviation of the combined uncertainties. At the same time, in Pb–Pb collisions, there is no evidence for centrality dependence within uncertainties, while theoretical calculation with pure-coalescence scenario [29] also expected negligible centrality-dependence as shown in Fig. 5.34.

Fig. 5.35 shows the prompt $\rm D^0$ in the 0–10%, 30–50% and 60–80% centrality classes. And the $R_{\rm AA}$ of prompt $\rm D^0$, $\rm D^+$ and $\rm D^{*+}$ mesons is shown in the left-hand panels of Fig. 5.36, from central (top) to peripheral (bottom) collisions. The nuclear modification factors of the three D-meson species are compatible within statistical uncertainties, which are obtained by propagating those on the Pb–Pb yields

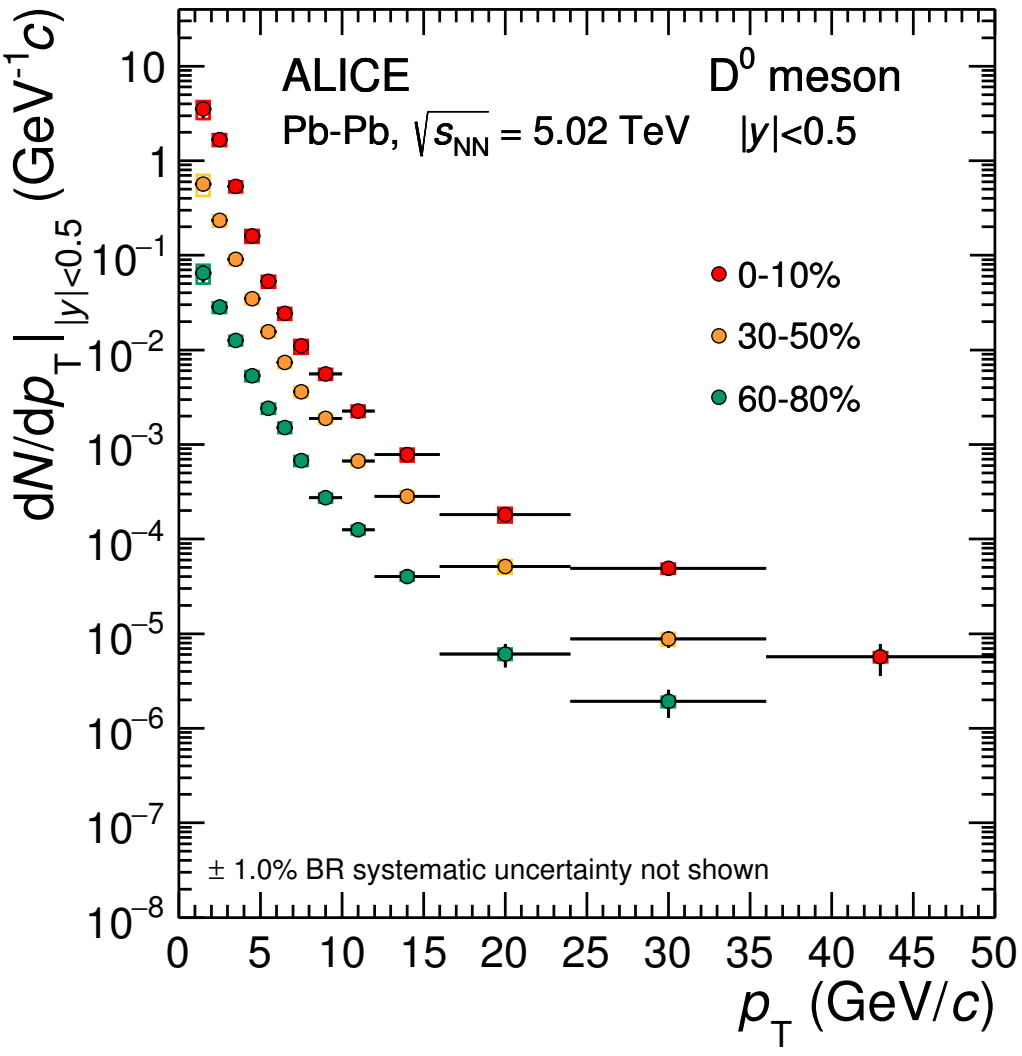

Figure 5.32: Transverse momentum distributions $\mathrm{N}/\mathrm{p}_{\mathrm{T}}$ of prompt D^0-meson in the 0–10%, 30–50% and 60–80% centrality classes in Pb–Pb collisions at $\sqrt{s_{\mathrm{NN}}} = 5.02$ TeV [28]. Statistical uncertainties (bars) and systematic uncertainties (boxes) are shown. The uncertainty on the branching ratios is quoted separately. Horizontal bars represent bin widths, symbols are placed at the centre of the bin.

and those of the pp reference. Their average was computed using the inverse of the quadratic sum of the relative statistical and uncorrelated systematic uncertainties as weights, in the p_{T} intervals where more than one D-meson species is available, (Fig. 5.36, right-hand panels). The systematic uncertainties were propagated through the averaging procedure, considering the contributions from the tracking efficiency, the beauty-hadron feed-down subtraction and the FONLL-based $\sqrt{s}$-scaling of the pp cross section from $\sqrt{s} = 7$ TeV to $\sqrt{s} = 5.02$ TeV as fully correlated uncer-

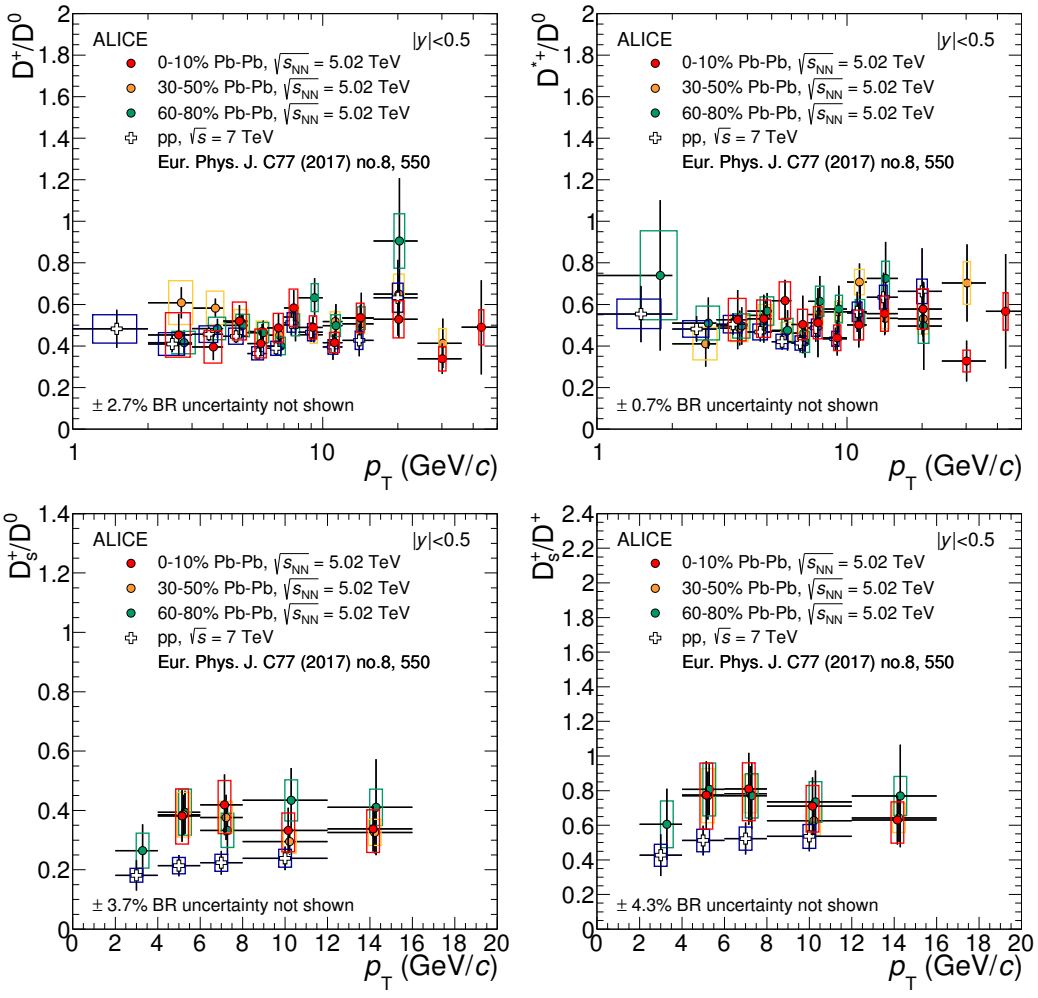

Figure 5.33: Ratio of prompt D-meson yields as a function of p_{T} [28]. Statistical (bars) and systematic (boxes) uncertainties are shown.

tainties among the three D-meson species. The average nuclear modification factors in the 0–10% and 30–50% centrality classes (top and middle right-hand panels of Fig. 5.36) show a suppression that is maximal at p_{T} = 6–10 GeV/c, where a reduction of the yields by a factor of about 5 and 2.5 with respect to the binary-scaled pp reference is observed in the two centrality classes, respectively. The suppression gets smaller with decreasing p_{T} for $p_{\mathrm{T}} < 6$ GeV/c, and R_{AA} is compatible with unity in the interval $1 < p_{\mathrm{T}} < 3$ GeV/c. The average R_{AA} in the 60–80% centrality class shows a suppression by about 20–30%, without a pronounced dependence on p_{T}.

The R_{AA} of prompt $\mathrm{D_s^+}$ mesons is shown in the right-hand panels of Fig. 5.36, where it is compared with the average R_{AA} of non-strange D mesons: the values are larger for $\mathrm{D_s^+}$ mesons, but the two measurements are compatible within one standard deviation of the combined uncertainties, as is the case for the ratios shown in Fig. 5.33. The average R_{AA} of prompt $\mathrm{D^0}$, $\mathrm{D^+}$ and $\mathrm{D^{*+}}$ in the 10% most cen-

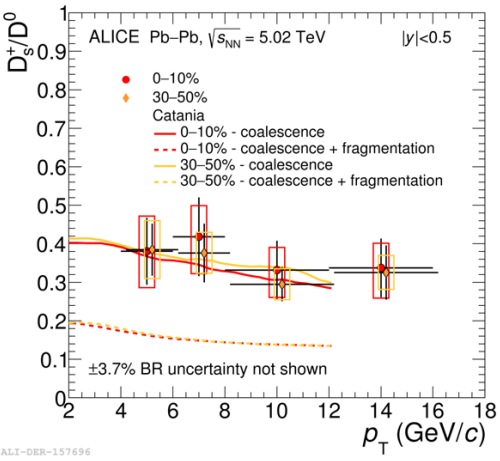

Figure 5.34: Ratio of prompt D_s^+/D^0 in $\sqrt{s_{NN}} = 5.02$ TeV Pb–Pb collisions at 0-10% and 30-50% centrality classes [28], compared with pure coalescence and coalescence plus fragmentation Monte-Carlo predictions [29].

tral collisions is compared with a measurement of prompt D^0 mesons by the CMS Collaboration [30] in the rapidity interval $|y| < 1$ in Fig. 5.37 (left panel): the measurements are compatible in the common p_T interval 2–50 GeV/c. In the right panel of Fig. 5.37, the nuclear modification factor of D mesons at $\sqrt{s_{NN}} = 5.02$ TeV in the 0–10% centrality class is compared with the same measurement at $\sqrt{s_{NN}} = 2.76$ TeV [42]. The measurement at $\sqrt{s_{NN}} = 5.02$ TeV have total uncertainties reduced by a factor of about two and extended p_T coverage from 36 to 50 GeV/c. The suppression is compatible within uncertainties at the two energies, as also observed for charged particles [32].

The close similarity of the R_{AA} measurements at the two energies was predicted by the Djordjevic model [31] (Fig. 5.37, right panel), and it results from the combination of a higher medium temperature at 5.02 TeV (estimated to be about 7% higher than at 2.76 TeV), which would decrease the R_{AA} by about 10%, with a harder p_T distribution of charm quarks at 5.02 TeV, which would increase the R_{AA} by about 5% if the medium temperature were the same as at 2.76 TeV.

As explained in Chapter. 1, the measurement of the R_{AA} of open-charm mesons is essential to understand in-medium parton energy loss, in particular its colour-charge and quark-mass dependence. In Fig. 5.38, the R_{AA} of prompt D mesons is compared with that of charged particles in the same p_T intervals, at the same energy and in the same centrality classes [32]. The ratio of their nuclear modification factors is displayed in the bottom panels, for the three centrality classes. The R_{AA} of D mesons and charged particles differ by more than $2\,\sigma$ of the combined statistical and systematic uncertainties in all the p_T intervals within $3<p_T<8$ GeV/c in central collisions. The difference is less than $2\,\sigma$ in this range for semi-central collisions, while the two R_{AA} are the same within $1\,\sigma$ for $p_T>10$ GeV/c in both central and semi-central collisions. In the 60–80% class the measurements are compatible in the

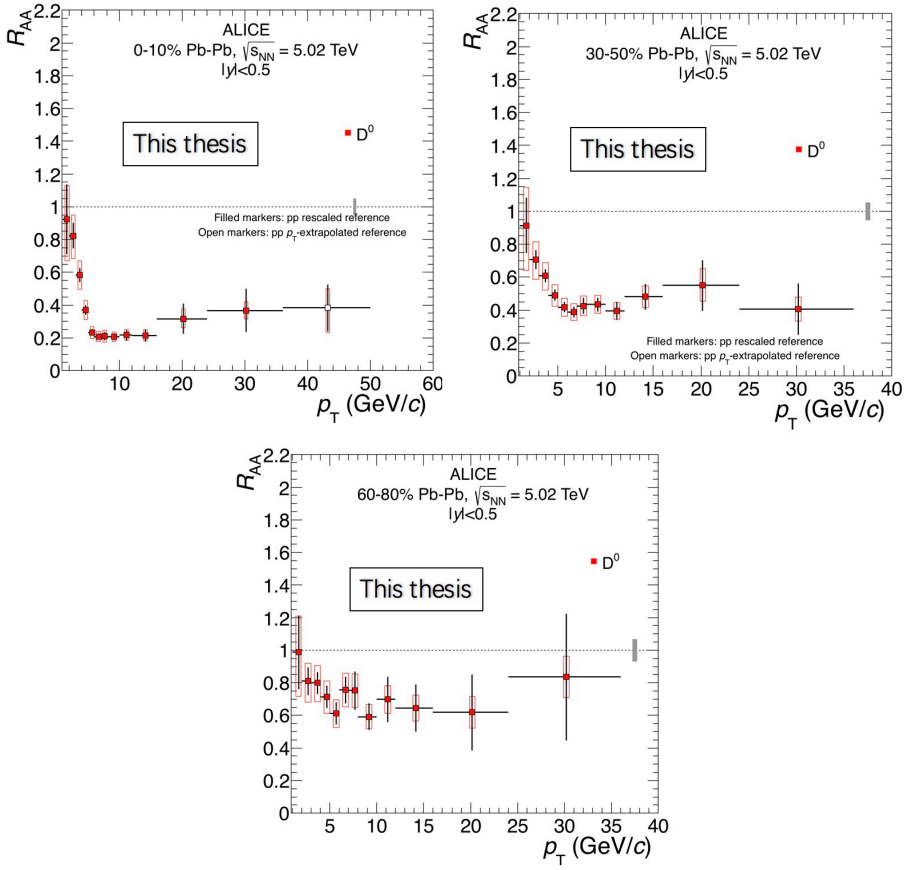

Figure 5.35: $R_{\rm AA}$ of prompt $\rm D^0$ for the 0–10%, 30–50% and 60–80% centrality classes [28]. Statistical (bars), systematic (empty boxes), and normalisation (shaded box around unity) uncertainties are shown. Filled markers are obtained with the pp rescaled reference, empty markers with the $p_{\rm T}$-rescaled reference.

common $p_{\rm T}$ interval. The interpretation of the difference observed for $p_{\rm T} < 8$ GeV/c in central and semi-central collisions is not straightforward, because several factors can play a role in defining the shape of the $R_{\rm AA}$.

In presence of a colour-charge and quark-mass dependent energy loss, the harder $p_{\rm T}$ distribution and the harder fragmentation function of charm quarks compared to those of light quarks and gluons should lead to similar values of D-meson and pion $R_{\rm AA}$ at high-$p_{\rm T}$ region, as discussed in [98]. Since the pions are the dominant contribution in the inclusive charged-particle yields, this statement is expected to be still valid for the comparison of the D-meson and the charged particle $R_{\rm AA}$. In addition, it should be considered that the yield of light-flavour hadrons could have a substantial contribution up to transverse momenta of about 2–3 GeV/c from soft production processes, such as the break-down of participant nucleons into quarks and gluons that subsequently hadronise. This component scales with the number of participants rather than the number of binary collisions. Finally, the effects of

radial flow and hadronisation via recombination, as well as initial-state effects, could affect D-meson and light-hadron yields differently at a given p_{T}.

The average R_{AA} of the three non-strange D-meson species in the three centrality classes are compared with theoretical models in Fig. 5.39. Models based on heavy-quark transport and models based on perturbative QCD calculations of high-p_{T} parton energy loss are shown in the left and in the right panels, respectively, details about the models have already been discussed in Chapter. 1. Transport models in the left panels include: BAMPS el. [33], POWLANG [38] and TAMU [40], in which the interactions are only described by collisional (i.e. elastic) processes; BAMPS el.+rad. [33], LBT [35], MC@sHQ+EPOS2 [36] and PHSD [37], in which also energy loss from medium-induced gluon radiation is considered, in addition to collisional process. In the right panels, the CUJET3.0 [34] and Djordjevic [31] models include both radiative and collisional energy loss processes, while the SCET [39] model implements medium-induced gluon radiation via modified splitting functions with finite quark masses. All models, with the exception of BAMPS and CUJET3.0, include a nuclear modification of the parton distribution functions. The LBT, MC@sHQ, PHSD, POWLANG and TAMU models include a contribution of hadronisation via quark recombination, in addition to independent fragmentation. Most of the models provide a fair description of the data in the region p_{T}<10 GeV/c in central collisions (except for BAMPS el., where the radiative term is missing), but many of them (LBT, PHSD, POWLANG and SCET) provide a worse description of non-central collisions. In the high-p_{T} region above 10 GeV/c only the BAMPS el.+rad., CUJET3.0, Djordjevic, MC@sHQ+EPOS2 and SCET models can describe the data in central collisions. The CUJET3.0 and Djordjevic models provide a fair description of the R_{AA} in all three centrality classes for $p_{\mathrm{T}} > 10$ GeV/c, where radiative energy loss is expected to be the dominant interaction mechanism, suggesting that the dependence of radiative energy loss on the path length in the hot and dense medium is well understood.

In Fig. 5.40, the non-strange and strange D-meson R_{AA} are compared with the models that provide both observables. An increase of the $\mathrm{D_s^+}$ R_{AA} is expected in the two models, PHSD and TAMU, in particular for $p_{\mathrm{T}} < 5$ GeV/c, with respect to non-strange D mesons. This increase is induced by hadronisation via quark recombination in the QGP, as well as by different interaction cross sections for non-strange D and for $\mathrm{D_s^+}$ in the hadronic phase of the system evolution. In the transverse momentum interval covered by the $\mathrm{D_s^+}$ measurement ($p_{\mathrm{T}} > 4$ GeV/c), the PHSD model predicts the effect to be very small, while the TAMU model predicts a sizeable difference of about 30% up to about 8 GeV/c, similar to the trend shown by the data.

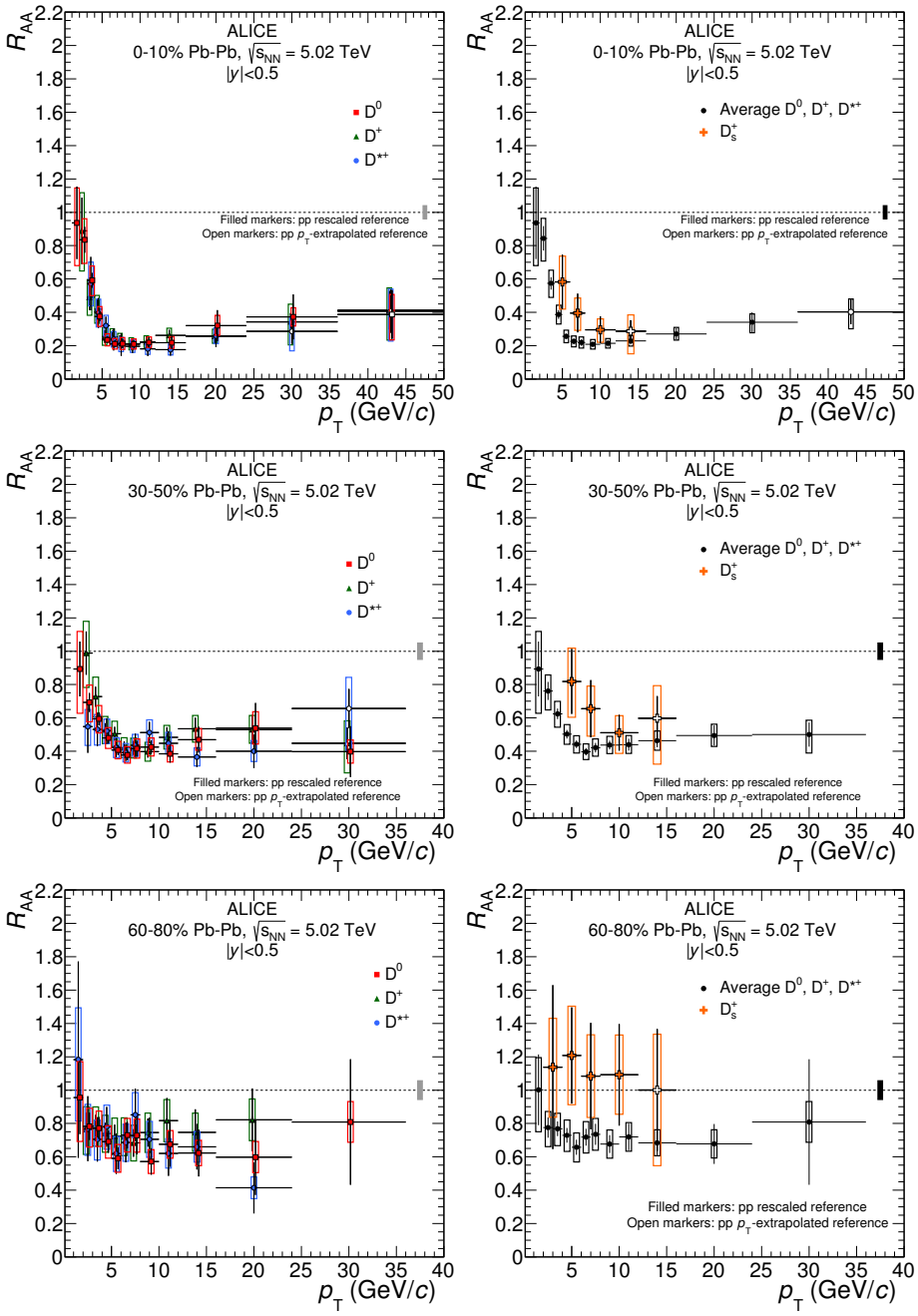

Figure 5.36: $R_{\rm AA}$ of prompt $\rm D^0$, $\rm D^+$ and $\rm D^{*+}$ mesons (left-hand panels) and of prompt $\rm D_s^+$ mesons compared with the average $R_{\rm AA}$ of the non-strange D-meson states available in each $p_{\rm T}$ interval (right-hand panels) for the 0–10%, 30–50% and 60–80% centrality classes [28]. Statistical (bars), systematic (empty boxes), and normalisation (shaded box around unity) uncertainties are shown. Filled markers are obtained with the pp rescaled reference, empty markers with the $p_{\rm T}$-rescaled reference.

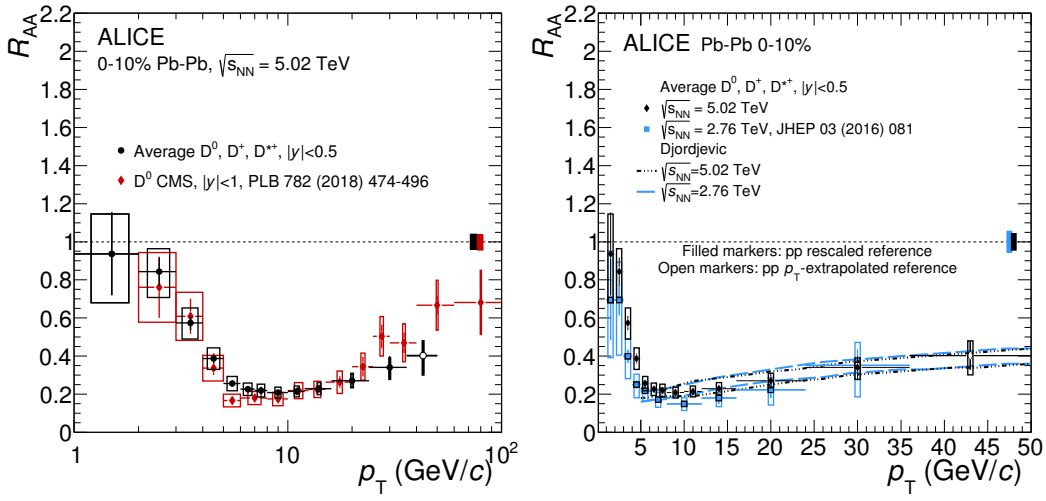

Figure 5.37: Left panel: average $R_{\rm AA}$ of prompt $\rm D^0$, $\rm D^+$ and $\rm D^{*+}$ mesons by ALICE compared to $R_{\rm AA}$ of prompt $\rm D^0$ mesons by CMS [30] in the 0–10% centrality class and at $\sqrt{s_{\rm NN}} = 5.02$ TeV. Statistical (bars), systematic (empty boxes), and normalisation (shaded box around unity) uncertainties are shown. Right panel: average $R_{\rm AA}$ of $\rm D^0$, $\rm D^+$ and $\rm D^{*+}$ mesons compared with the Djordjevic model [31] in the 0-10% centrality class at two collision energies. Statistical (bars), systematic (empty boxes), and normalisation (shaded box) uncertainties are shown.

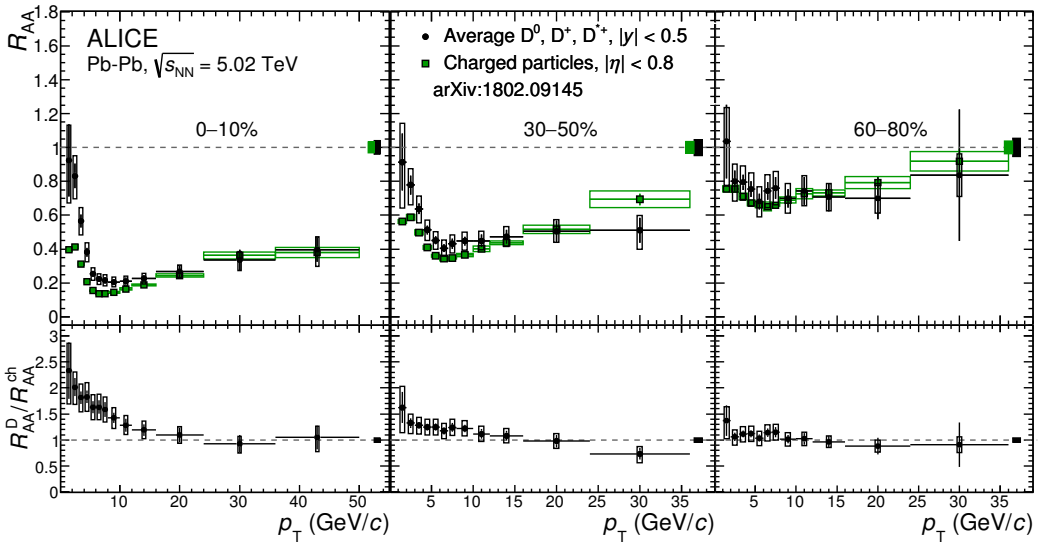

Figure 5.38: Average $R_{\rm AA}$ of prompt $\rm D^0$, $\rm D^+$ and $\rm D^{*+}$ mesons in the 0–10% (left), 30–50% (middle) and 60–80% (right) centrality classes at $\sqrt{s_{\rm NN}} = 5.02$ TeV compared to the $R_{\rm AA}$ of charged particles in the same centrality classes [32]. The ratios of the $R_{\rm AA}$ are shown in the bottom panels. Statistical (bars), systematic (empty boxes), and normalisation (shaded box around unity) uncertainties are shown.

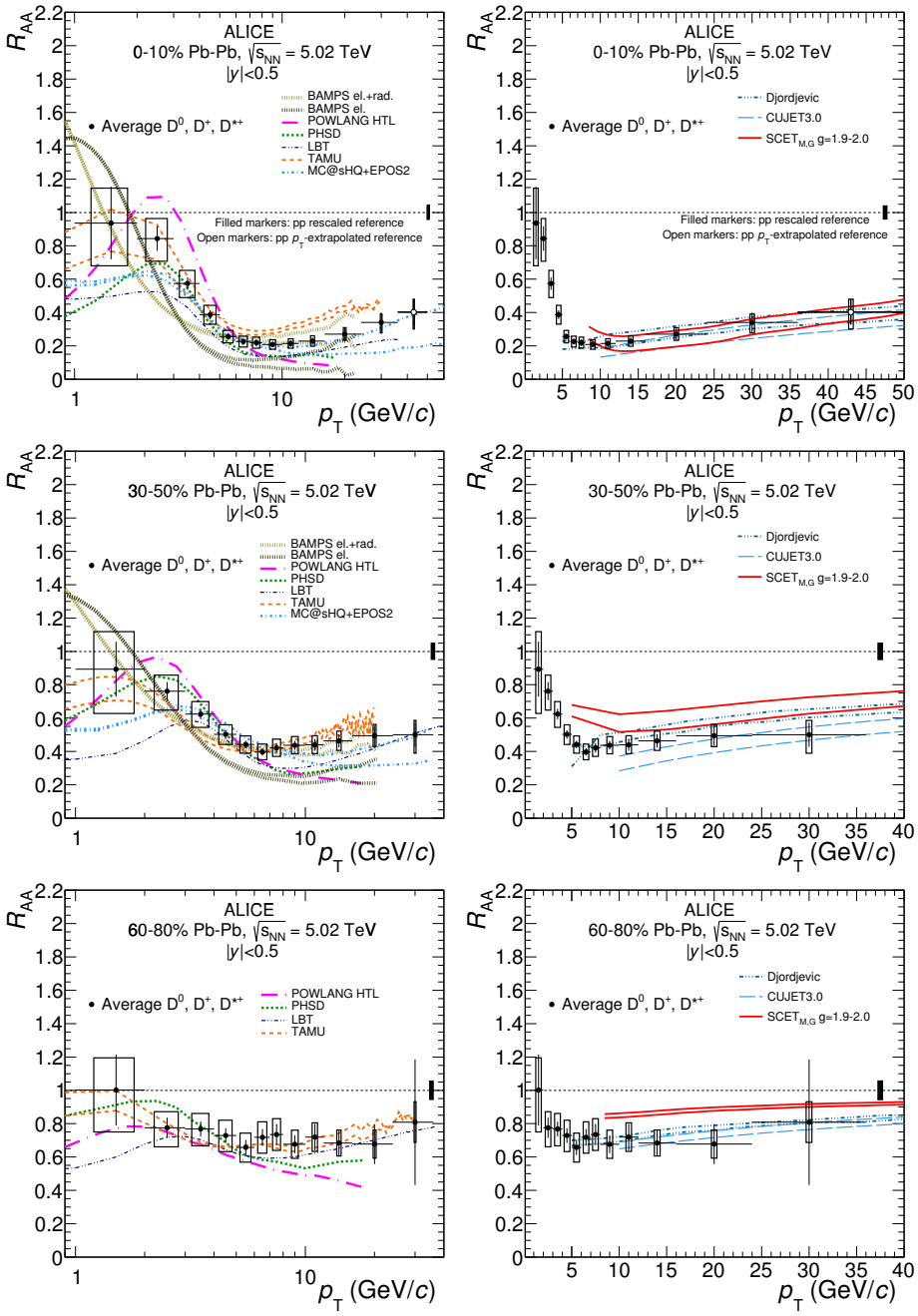

Figure 5.39: Average R_{AA} of D^0, D^+ and D^{*+} mesons compared with model calculations. The three rows refer to the 0–10%, 30–50% and 60–80% centrality classes. The left panels show models based on heavy-quark transport, while the right panels show models based on pQCD energy loss. Model nomenclature and references: BAMPS [33], CUJET3.0 [34], Djordjevic [31], LBT [35], MC@sHQ+EPOS2 [36], PHSD [37] POWLANG [38], SCET [39], TAMU [40]. Some of the models are presented with two lines with the same style and colour, which encompass the model uncertainty band.

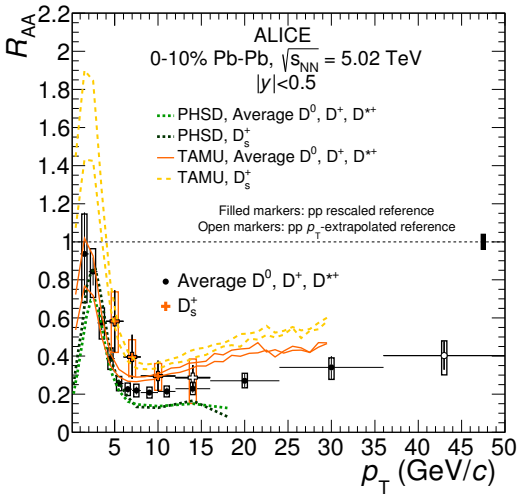

Figure 5.40: Average $R_{\rm AA}$ of $\rm D^0$, $\rm D^+$ and $\rm D^{*+}$ mesons and $R_{\rm AA}$ of $\rm D_s^+$ mesons in the 0–10% centrality class compared with the PHSD [37] and TAMU [40] model calculations.

The simultaneous comparison of $R_{\rm AA}$ and elliptic flow v_2 measurements at $\sqrt{s_{\rm NN}}$ = 5.02 TeV [41] with models can provide more stringent constraints to the implementation of the interaction and hadronisation processes for heavy quarks in the QGP. The comparison with models that compute both observables is shown in Fig. 5.41 for the $R_{\rm AA}$ and v_2, in the 0–10% and 30–50% centrality classes, respectively. The level of model-to-data consistency was quantified in terms of the reduced χ^2 in the $p_{\rm T}$ interval where the calculations are available. Values of reduced χ^2 for $R_{\rm AA}$ in the 0–10% and 30–50% centrality classes and for v_2 in the 30–50% centrality class are reported in Table 5.9. Note that the χ^2 values for the TAMU and MC@sHQ take into account the model uncertainties, in addition to the data uncertainties. The TAMU model yields large χ^2 values because it overestimates $R_{\rm AA}$ and underestimates v_2 at high $p_{\rm T}$, probably because it does not include radiative energy loss. The TAMU model overestimates $R_{\rm AA}$ and underestimates v_2 at high $p_{\rm T}$, probably because it does not include radiative energy loss. The BAMPS el. model overestimates the maximum flow while underestimating the $R_{\rm AA}$ value at high $p_{\rm T}$. The radiative energy loss contribution in BAMPS el.+rad. improves the description of $R_{\rm AA}$ but gives v_2 values lower than the data. The LBT, PHSD, POWLANG and MC@sHQ models provide instead a fair description of v_2, but cannot describe $R_{\rm AA}$ with a small χ^2 in both centrality classes. The MC@sHQ model describes the three data sets with $\chi^2/{\rm ndf} < 1$. Nevertheless, energy loss is overestimated at high $p_{\rm T}$ in the 0–10% centrality classes (but also in semi-central events) by PHSD, POWLANG and LBT, while at low $p_{\rm T}$ the measured $R_{\rm AA}$ is slightly higher than what predicted within LBT, PHSD and MC@sHQ.

χ^2/ndf	$R_{\rm AA}$ (0–10%)	$R_{\rm AA}$ (30–50%)	v_2 (30–50%)
BAMPS el.	3.3	3.8	1.9
BAMPS el.+rad.	1.2	0.5	6.7
LBT	1.4	1.7	0.8
MC@sHQ	0.4	0.8	0.5
PHSD	0.9	1.8	0.8
POWLANG	2.8	2.3	0.5
TAMU	1.5	0.6	4.1

Table 5.9: Reduced χ^2 values for $R_{\rm AA}$ in 0–10% and 30–50% centrality classes and v_2 in 30–50% centrality class.

5.6 Summary

In this Chapter, we have presented measurements of the $p_{\rm T}$-differential production yields of prompt $\rm D^0$ meson at central rapidity in Pb–Pb collisions in the three centrality classes 0–10%, 30–50% and 60–80% at a centre-of-mass energy per nucleon pair $\sqrt{s_{\rm NN}}$ = 5.02 TeV, as well as its nuclear modification factor $R_{\rm AA}$. The pp reference was obtained by scaling the recently-published measurements at 7 TeV [137] to $\sqrt{s}$ = 5.02 TeV.

The average $R_{\rm AA}$ of the three non-strange D-meson species ($\rm D^0$, $\rm D^+$ and $\rm D^{*+}$) shows minimum values of 0.2 and 0.4 in the centrality classes 0–10% and 30–50%, respectively, at $p_{\rm T}$ of 6–10 GeV/c. $R_{\rm AA}$ increases for $p_{\rm T}$ < 6 GeV/c, and it is compatible with unity at 1<$p_{\rm T}$<3 GeV/c. The average $R_{\rm AA}$ values are compatible with those measured at $\sqrt{s_{\rm NN}}$ =2.76 TeV and they have smaller uncertainties by a factor of about two, as well as extended $p_{\rm T}$ coverage up to 50 GeV/c in central collisions. The similarity of the $R_{\rm AA}$ values at the two energies was predicted by the Djordjevic model, and it results from the combination of a higher medium temperature at 5.02 TeV (estimated to be about 7% higher than at 2.76 TeV) with

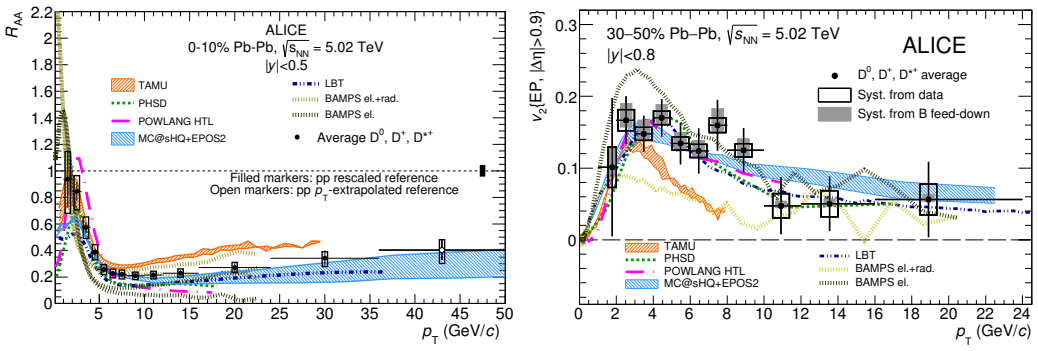

Figure 5.41: Average $R_{\rm AA}$ of $\rm D^0$, $\rm D^+$ and $\rm D^{*+}$ mesons in the 0–10% centrality class (left) and their average elliptic flow v_2 in the 30–50% centrality class (right) [41], compared with models that have predictions for both observables at low $p_{\rm T}$.

a harder p_{T} distribution of charm quarks at 5.02 TeV.

In central and semi-central collisions the average R_{AA} of non-strange D mesons is compatible with that of charged particles for $p_{\mathrm{T}} < 6$ GeV/c, while it is larger at lower p_{T}. The R_{AA} of $\mathrm{D_s^+}$ mesons have generally larger central values than those of the average of non-strange D mesons, but the two measurements are compatible within about one standard deviation of the combined uncertainties.

The R_{AA} of non-strange D mesons at high p_{T} (above 10 GeV/c) is fairly described in the three centrality classes by model calculations that include both radiative and collisional energy loss. This indicates that the centrality dependence of radiative energy loss, which is the dominant contribution at high p_{T}, is under good theoretical control. The R_{AA} in the transverse momentum region below 10 GeV/c is described by several transport model calculations in central collisions, but most models fail in describing the centrality dependence of R_{AA} and in describing simultaneously R_{AA} and the elliptic flow coefficient v_2. Therefore, the measurements provide significant constraints for the understanding of the interaction of charm quarks with the high-density QCD medium, especially at low and intermediate p_{T}, where the R_{AA} is the result of a more complex interplay among several effects.

Chapter 6

Towards a measurement of non-prompt D^0 using TMVA technique in p–Pb collisions at $\sqrt{s_{\mathrm{NN}}} = 5.02$ TeV

This chapter describes the non-prompt D^0 analysis in p–Pb collisions. A novel machine learning based method is used, aiming to separate the non-prompt and prompt D^0. In Sec. 6.1, the physics motivation of this non-prompt D^0 analysis will be described. A short introduction of Boosted Decision Tree (BDT) algorithm will be given in Sec. 6.2.1. The non-prompt D^0 selection strategy and correction procedure are described in Sec. 6.3 and Sec. 6.4, respectively. The results of non-prompt D^0 cross section in p–Pb collisions at $\sqrt{s_{\mathrm{NN}}} = 5.02$ TeV are shown in Sec. 6.5.

6.1 Introduction

At LHC energies, the inclusive D-meson yields not only originates from the decay of charm hadrons (prompt D mesons), but also from the decay of beauty hadrons (non-prompt D mesons). A measurement of the latter would be a indirect observable of beauty production. Experimentally, non-prompt and prompt D mesons can be distinguished according to the different decay topologies, such as the impact parameter. In ALICE, a data-driven method [42] has been employed to extract the non-prompt fraction $f_{\mathrm{non-prompt}}$ in the raw yield of D^0 mesons in p-Pb collisions. It exploits the different shapes of the distributions of the transverse-plane impact parameter to the primary vertex (d_0) of prompt and feed-down D mesons. Thus the non-prompt fraction can be estimated via an unbinned likelihood fit of the d_0 distribution. The fit function equation can be expressed as:

$$F(d_0) = S\cdot[f_{\mathrm{non-prompt}}F^{\mathrm{feed-down}}(d_0)+(1-f_{\mathrm{non-prompt}})F^{\mathrm{prompt}}(d_0)]+B\cdot F^{\mathrm{backgr}}(d_0), \tag{6.1}$$

where $F^{\mathrm{feed-down}}(d_0)$, $F^{\mathrm{prompt}}(d_0)$ and $F^{\mathrm{backgr}}(d_0)$ are the templates describing the impact parameter distributions of prompt D mesons, feed-down D mesons, and background, respectively. The template fit of the impact parameter for the three sources can be found on the left panel of Fig. 6.1 in p-Pb collisions [42]. The prompt fraction of D^0 can be estimated with the impact parameter fits found to be

compatible with the FONLL-based estimation within uncertainties, as shown in the right panel of Fig. 6.1.

A novel method based on TMVA technology is developed to obtain high fraction of non-prompt D^0. The TMVA approaching is widely used to reduce the combinatorial background for the yield extraction based on the different decay topology between signal and background. Nevertheless, TMVA can not only be used for two elements classification, but also the three elements classification. Thus it's suitable for this case, where we can treat the non-prompt D^0 as signal, prompt D^0 and combinatorial background as background.

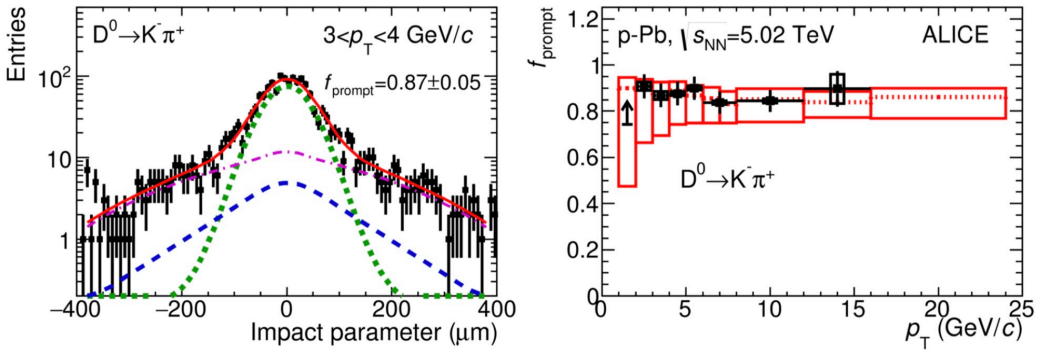

Figure 6.1: Left panel: the template fit of the impact parameter for $F^{\text{feed-down}}(d_0)$, $F^{\text{prompt}}(d_0)$ and $F^{\text{backgr}}(d_0)$. Right panel: the prompt fraction of D^0 as a function of p_{T} using the data-driven method and the FONLL-based approach [42].

6.2 TMVA technology

The goal of data analysis is to extract the best possible signal. For our HEP analysis, the task follows the procedure: 1.classification 2.parameter estimation 3.function fitting. Classification is the process of assigning objects or events to one of the possible discrete classes. Parameter estimation is the extraction of one or more parameters by fitting a model to data. By function fitting I mean the derivation of continuous functions of variables. While, in our traditional analysis, we often look at the parameter distribution of signal and background, and use a cut by "eye" to gain more signal and reduce more background. However, if the statistics are limited, and the S/B is low, the traditional cuts are not that sufficient. In this case, machine learning methods help to give the rank of each variable to help better understand the cuts which we used in traditional method.

The machine learning method has been widely used in particle physics to search for dark matter or particles beyond SM. To explain it in a simple way, in this method, if we can define enough kind of variables and give it to the machine, it can automatically distinguish the signal and background, and give a cut (not a continue cut) to maximize the significance. For ALICE analysis, we have used one of the

machine learning method (BDT) to extract the Λ_c^+ signal [139], which have a better significance compared to the traditional method, and the results are compatible with traditional rectangular cut method.

6.2.1 Boosted Decision Tree (BDT)

In the ROOT framework, there is a package called "TMVA" [140] which can be used to do many kinds analysis based on machine learning and deep learning methods. Here I take the BDT as an example.

6.2.1.1 Decision Tree

Decision trees (DT) employ sequential cuts as in the standard grid search to perform the classification (or regression) task, but with a critical difference. The flow chart of DT is shown in Fig. 6.2, at each step in the sequence, the best cut is searched for and used to split the data and this process is continued recursively on the resulting partitions until a given terminal criterion is satisfied. The DT algorithm starts at the so-called root node with the entire training data set containing signal and background events. At each iteration of the algorithm, and for each node, one finds the best cut for each variable and then the best cut overall. The data are split using the best cut thereby forming two branch nodes. One stops splitting when no further reduction in impurity is possible (or when the number of events is judged too small to proceed further).

The DT algorithm is applicable to discrimination of n-classes, even though what I have described is the binary decision tree method used in 2-class signal/background discrimination.

Decision trees are very popular because of the transparency of the procedure and interpretation. They also have some other advantages: (a) tolerance to missing variables in the training data and test data; (b) insensitivity to irrelevant variables since the best variable on which to cut is chosen at each split and therefore ineffective ones do not get used; (c) invariance to monotone transformation of variables which makes preprocessing of data unnecessary. However, decision trees also have serious limitations: (a) instability with respect to the training sample (a slightly different training sample can produce a dramatically different tree); (b) sub-optimal performance due to the piece-wise constant nature of the model, which means that the predictions are constant within each bin (region represented by a leaf) and discontinuous at its boundaries; (c) poor global generalization because the recursive splitting results in the use of fewer and fewer training data per bin and only a small fraction of the feature variables may be used to model the predictions for individual bins.

6.2.1.2 Boosting

Within the last few years a great improvement has been made. Starting with unweighted events and build a tree as above, If a training event is misclassified, i.e,

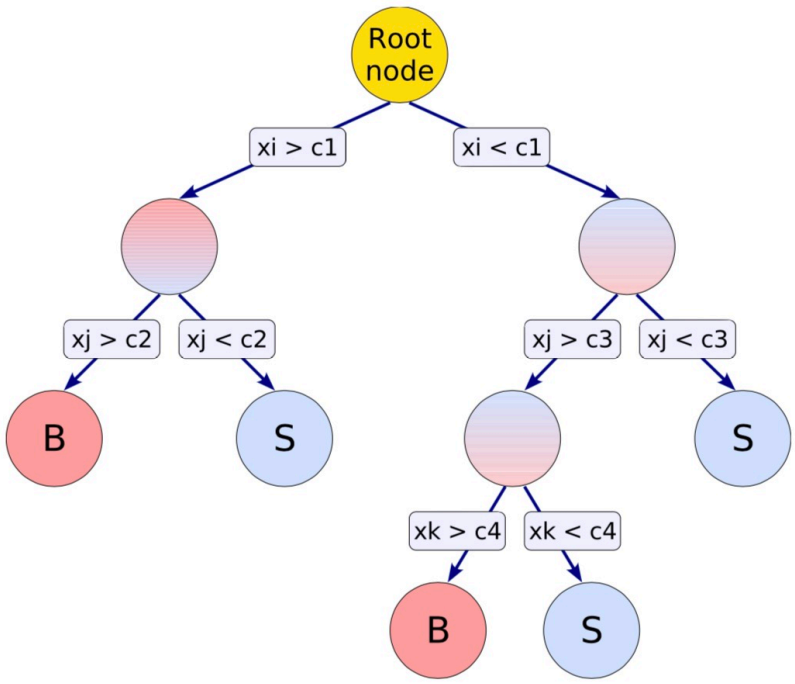

Figure 6.2: Schematic view of a decision tree

a signal event lands on a background leaf or a background event lands on a signal leaf, then the weight of that event is increased (boosted).

A second tree is built using the new weights, no longer equal. Again misclassified events have their weights boosted and the procedure is repeated. Typically, one may build 1000 or 2000 trees this way.

A score is now assigned to an event as follows. The event is followed through each tree in turn. If it lands on a signal leaf it is given a score of 1, and if it lands on a background leaf it is given a score of -1. The renormalized sum of all the scores, possibly weighted, is the final score of the event. High scores mean the event is most likely signal and low scores that it is most likely background. By choosing a particular value of the score on which to cut, one can select a desired fraction of the signal or a desired ratio of signal to background. High scores (BDT response) mean the selected sample is most lickly to be ea signal, low scores mean it seem to be a background.

6.3 Non-prompt D^0 Reconstruction

This work was based on the LHC run 2 data acquired by ALICE detector in 2016 with p–Pb collisions at centre-of-mass energy per nucleon-nucleon pair of $\sqrt{s_{\rm NN}}$ = 5.02 TeV, using the minimum-bias trigger according to the information of the

VZERO detector, the in-bunch collision pileup is removed. The number of events used for the analysis after reconstructed primary vertex cut (±10 cm) is 624M. The corresponding integrated luminosity is $L_{\rm int} \approx 292nb^{-1}$. The dedicated MC was generated using HIJING generator, with addition of D-meson signal decaying by the hadronic channel from PYTHIA6 requesting the $c\bar{c}$ pairs in 50% of the events and the $b\bar{b}$ pairs in the remaining half.

The strategy of non-prompt $\rm D^0$ reconstruction is similar with prompt $\rm D^0$ one which has been described in the previous chapter, thus the same procedure will not be discussed in details. The only difference comes from the topological selections which will of course lead to a difference for the reconstruction efficiency calculation.

6.3.1 Multivariate Selection

Before using BDT to optimize the rectangular topological selections, a pre-selection is applied, including the PID and very loose selection on the topological variables such as the minimum $p_{\rm T}$ of the daughter tracks and the DCA. the topological variables used for BDT training are the same as the ones used for prompt $\rm D^0$ which has been described in the previous chapter. The variable distributions of signal and background after pre-selection are showed in Fig. 6.3.

6.3.1.1 BDT training

The training stage is performed using one dataset to train the BDT, while another independent sample will be used for test and BDT efficiency calculation. This split is done to ensure a statistically independent evaluation of the BDT algorithm is performed with the test sample, as well as a statistically independent evaluation of the BDT cut efficiency. The training sample fully determines each stage of the BDT, and the BDT response for the training dataset is calculated. The test sample is then used to test the level of overtraining, which can occur when statistical fluctuations are interpreted as features of a variable. The BDT training is performed individually for each $p_{\rm T}$ bin, to optimize discrimination power of the BDT in each bin. Fig. 6.4 shows the BDT responses for training and test sample. It can be found that the training and test sample agree reasonably well.

The sidebands of the invariant mass distribution from data are taken as the combinatorial background, the sidebands are defined as $M_{\rm D^0} - 0.165 < M < M_{\rm D^0} - 0.065$ GeV/c^2 and $M_{\rm D^0} + 0.065 < M < M_{\rm D^0} + 0.165$ GeV/c^2. 2000 events of prompt and non-prompt $\rm D^0$ are randomly taken from the corresponding MC for each $p_{\rm T}$ bin, the other events are used for testing.

At the beginning, we tried to use non-prompt $\rm D^0$ as signal, prompt $\rm D^0$ and sidebands simultaneously as background for training. However, it was found that the fraction of non-prompt can only reach 40% even with an aggressive selection. Then, we attempted to scan the weight of prompt $\rm D^0$ and sidebands, and observed that, the higher weight of the prompt we use, the higher fraction of non-prompt we will obtain. Thus a two steps training model has been developed, the work flow can be found in Fig. 6.5: the first step treats the non-prompt $\rm D^0$ as signal and prompt

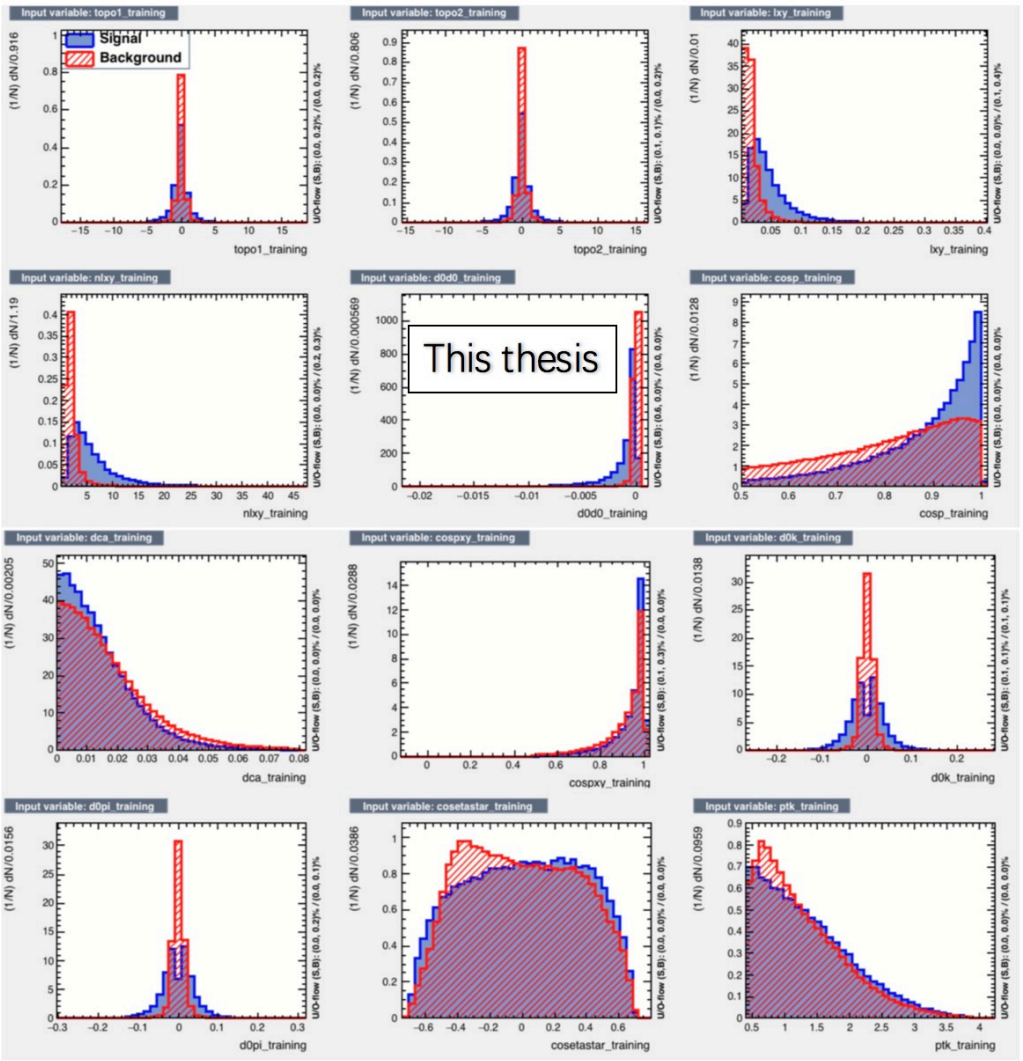

Figure 6.3: The topological variables distributions of signal and background non-prompt D^0 after pre-selection.

D^0 as background, and aims to separate these two sources. After a selection which guarantee a high fraction of non-prompt, we use filtered non-prompt D^0 as signal and combinatorial background as background to do the second step training, which will reduce the combinatorial background and improve the fit quality (significance).

A study is performed on the configuration options, only one varies at a time, to see if the performance can be improved. Finally, we Choose 500 trees in the forest maximized the signal efficiency, and the max. depth of the decision tree allows as 2 in both cases decreases the level of overtraining significantly, while also giving the best signal efficiency. And Minimum percentage of training events require in a leaf

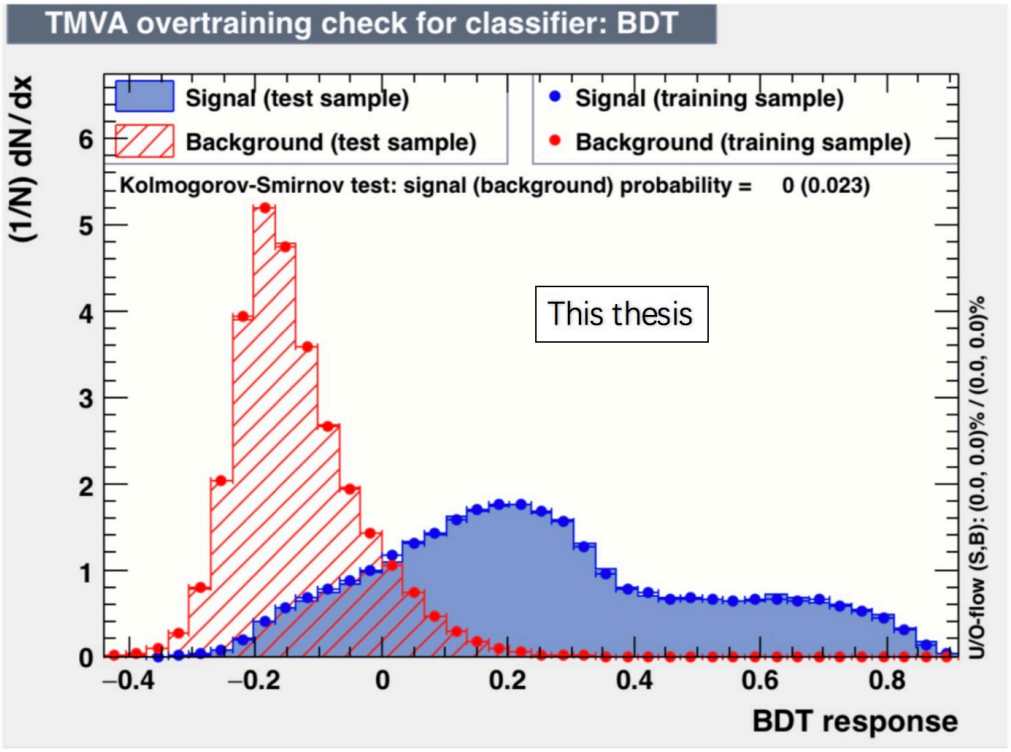

Figure 6.4: The BDT responses for training and test sample.

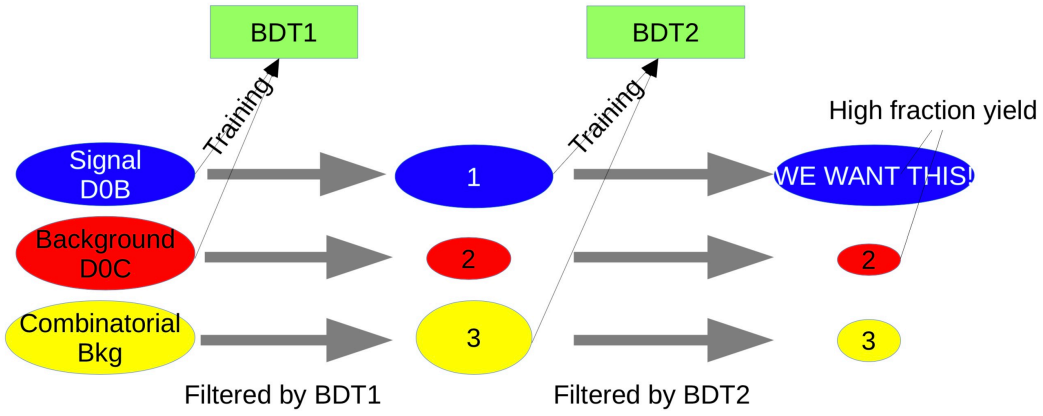

Figure 6.5: The work flow of two steps BDT training for non-prompt D^0.

node is 2.5%. The separation criteria is Gini Index, which defined by $p*(1-p)$. Since the splitting criterion is always a cut on a single variable, the training procedure selects the variable and cut value that optimizes the increase in the separation

index between the parent node and the sum of the indices of the two daughter nodes, weighted by their relative fraction of events. The cut values are optimized by scanning over the variable range with a granularity that is set via the option nCuts. the default value of nCuts is 20 which has a good compromise between computing time and step size. In order to optimal cut, given the training sample, the value is set to -1. Bagged Boost is also applied in order to avoid overtraining.

6.3.1.2 BDT application

The BDT weights obtained by training are applied to the datasets mentioned above. In order to simultaneously get high fraction of non-prompt and best fit significance, a study of BDT response cuts as a function of $f_{\mathrm{non-prompt}}$ and fit significance is performed in Fig. 6.6 left and right panels respectively. The $f_{\mathrm{non-prompt}}$ is calculated by Eq. 6.2. The fit significances are obtained by invariant mass of non-prompt D^0 candidates after different BDT selections. The final choice guarantees a very high non-prompt fraction (90%) and the best significance. Fig. 6.7 shows an example of candidates invariant mass at $4 < p_{\mathrm{T}} < 5$ GeV/c after each step BDT cuts. In the left panel, we have the significance around 24 after pre-selection cuts, the non-prompt fraction is around 5%. After first step of BDT selection, the fraction of non-prompt increase to around 60%, the significance reduces to 6. However, after second step of BDT selection aiming to reduce the combinatorial background, we achieve similar significance with pre-selection, but the non-prompt fraction stays around 60%.

$$f_{\mathrm{non-prompt}} = 1 - \left(\frac{\mathrm{d}^2\sigma}{\mathrm{d}y\,\mathrm{d}p_{\mathrm{T}}}\right)^{\mathrm{FONLL}}_{\mathrm{prompt}} \cdot \frac{(\mathrm{Acc}\times\varepsilon)_{\mathrm{prompt}} \cdot \Delta y\,\Delta p_{\mathrm{T}} \cdot \mathrm{BR} \cdot N_{\mathrm{evt}}}{N^{\mathrm{D^0\ raw}}/2}, \quad (6.2)$$

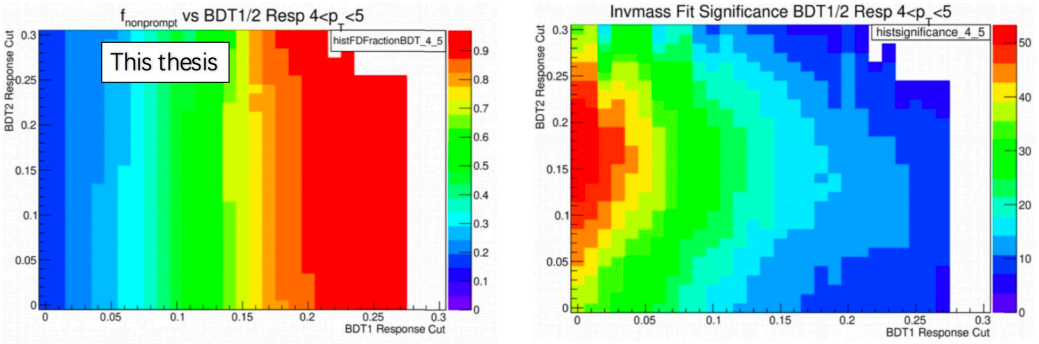

Figure 6.6: Left: BDT response 1 and 2 as a function of non-prompt fraction. Right: BDT response 1 and 2 as a function of fit significance.

Fig. 6.8 shows the impact parameter distributions after BDT selections from the total or sideband distributions (data), and prompt or non-prompt D^0 signal (MC). It can be found that, even after BDT selection, there are still large discrepancy

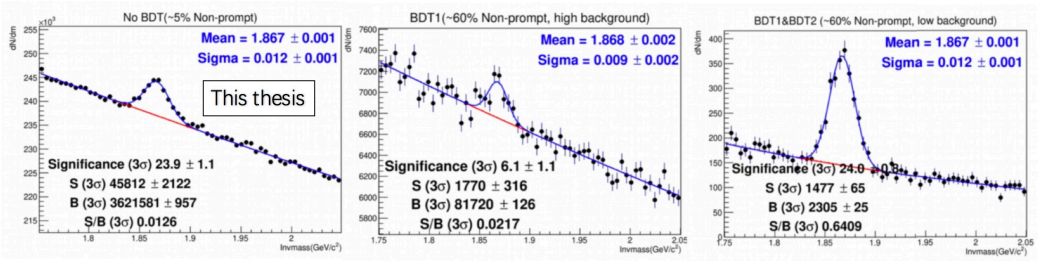

Figure 6.7: An example of candidates invariant mass at $4 < p_{\mathrm{T}} < 5$ GeV/c after each step BDT cuts, details described in the text.

between each source, which will allow us to calculate the $f_{\mathrm{non-prompt}}$ using data-driven method as described in Sec. 6.1.

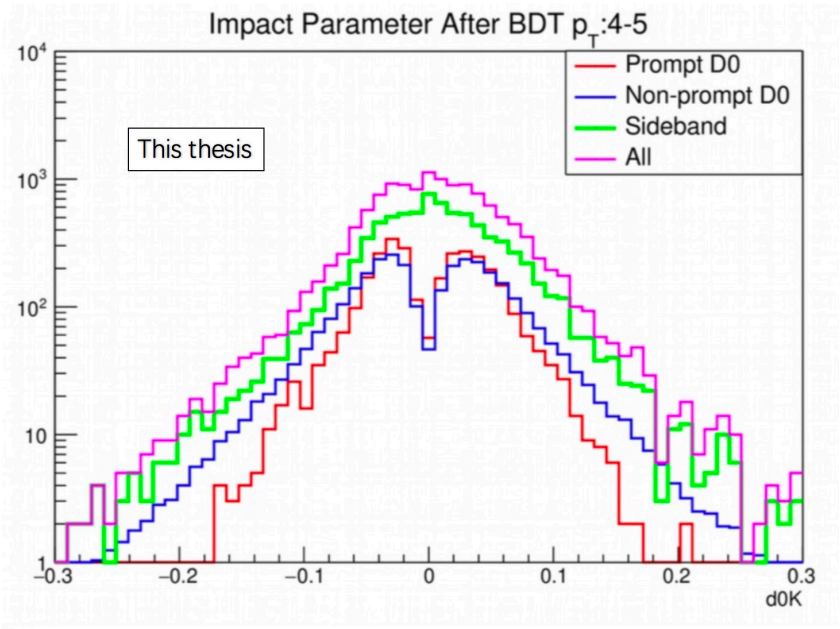

Figure 6.8: The impact parameter distributions after BDT selections from the total or sideband distributions (data), and prompt or non-prompt D^0 signal (MC).

6.3.2 Raw yield extraction

The raw yield of non-prompt D^0 can be extracted via invariant mass analysis after pre-selection and BDT cuts, as described in Sec. 5.2.5. Fig. 6.9 shows the invariant mass fit of non-prompt D^0 signal in 6 p_{T} bins in the range $3 < p_{\mathrm{T}} < 10$ GeV/c in p–Pb collisions at $\sqrt{s_{\mathrm{NN}}} = 5.02$ TeV. The reflection will be included after

further study. The information for number of signal S, number of background B, signal over background ratio S/B and significance can be found in each panel. In general, good quality of fit can be obtained in each p_{T} interval with the significances about 10. The $f_{\mathrm{non-prompt}}$ is around 90%.

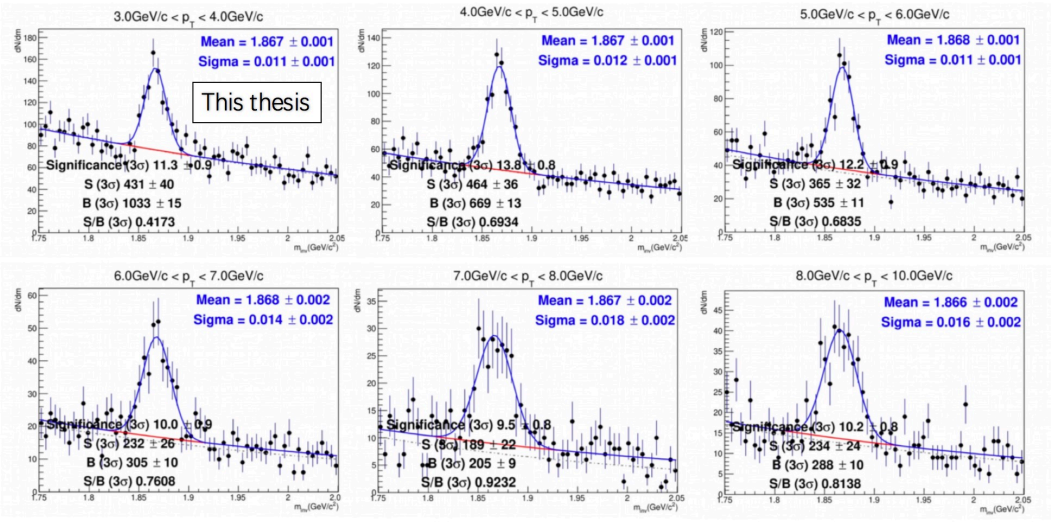

Figure 6.9: The invariant mass fit of non-prompt D^0 signal without reflection in 6 p_{T} bins in the range, $3 < p_{\mathrm{T}} < 10$ GeV/c in p–Pb collisions at $\sqrt{s_{\mathrm{NN}}} = 5.02$ TeV.

In order to illustrate the power of BDT, the BDT technique is also used for prompt D^0 analysis. The top panels of Fig. 6.10 6.11 show the invariant mass fit of prompt D^0 signal without reflection after BDT selections in 6 p_{T} bins in the range, $3 < p_{\mathrm{T}} < 10$ GeV/c in p–Pb collisions at $\sqrt{s_{\mathrm{NN}}} = 5.02$ TeV, compared with traditional rectangle cut method results (bottom panels). As we can find from the plots, the significance of BDT method is 20%-35% more than the traditional rectangular cuts method's one, which indicates that there is still room to improve the rectangular cuts, and BDT technique can be potentially used for D^0 yield extraction of flow or D^0 tagged-jet analysis, which are limited by the poor statistics.

6.4 Corrections

Similar with what has been discussed in Sec. 5.3, to calculate the non-prompt D^0 cross section, the correction includes selection efficiency and $f_{\mathrm{non-prompt}}$.

6.4.1 Selection Efficiency

The calculation of selection efficiency via BDT technique can be divided into two parts: the first part is pre-selection efficiency which follows the same procedure described in Sec. 5.3, the second part is the BDT selection efficiency which is calcu-

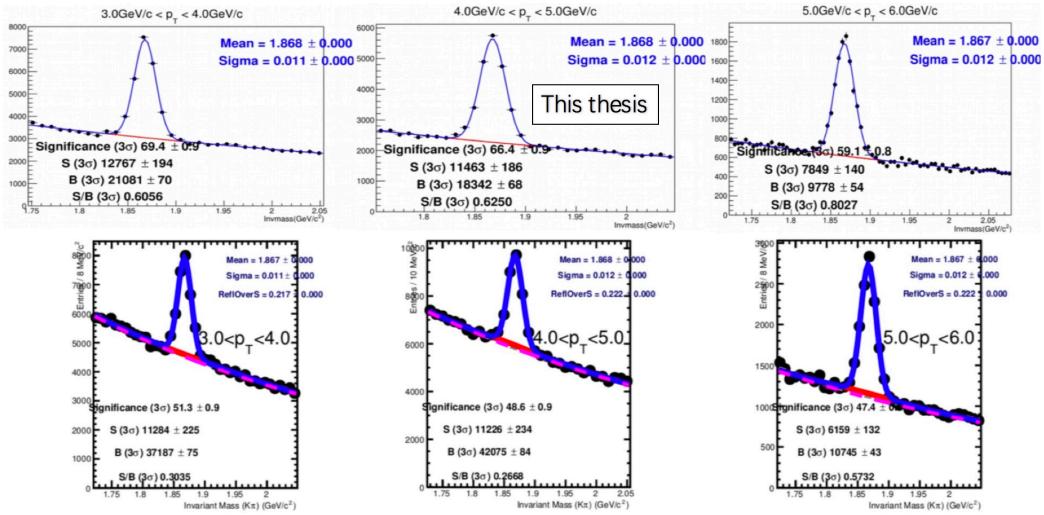

Figure 6.10: The invariant mass fit of prompt D^0 signal without reflection after BDT selections in 3 p_T bins in the range, $3 < p_T < 6$ GeV/c in p–Pb collisions at $\sqrt{s_{NN}} = 5.02$ TeV (top panels), compared with traditional rectangle cut method results (bottom panels).

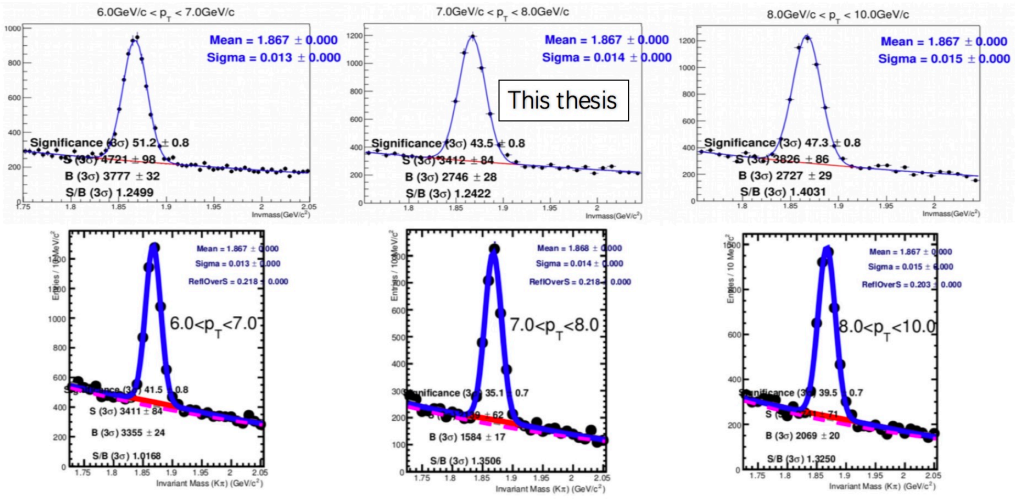

Figure 6.11: The invariant mass fit of prompt D^0 signal without reflection after BDT selections in 3 p_T bins in the range, $6 < p_T < 10$ GeV/c in p–Pb collisions at $\sqrt{s_{NN}} = 5.02$ TeV (top panels), compared with traditional rectangle cut method results (bottom panels).

lated by using the testing MC samples to avoid the bias from training samples. The left panel of Fig. 6.12 shows the pre-selection efficiency (acceptance*efficiency) of

prompt (red) and feed-down (blue) D^0 efficiency calculated by central (open circle, sample with SDD readout) and fast (solid circle, sample without SDD readout) MC samples, respectively. As we can find in the ratio, the efficiency from central sample is 3-5% larger than the fast one, the efficiency from fast is used for the final results currently. The right panel of Fig. 6.12 shows the BDT efficiency of prompt (red) and feed-down (blue) D^0 efficiency calculated by fast (solid circle) and fast+central (open circle) MC samples, respectively. Instead of calculating the two steps BDT efficiency individually, a overall BDT efficiency is obtained from the ratio between the number of signals before BDT selection and after the second step BDT selection in order to avoid the bias from statistical fluctuations during the middle step calculation.

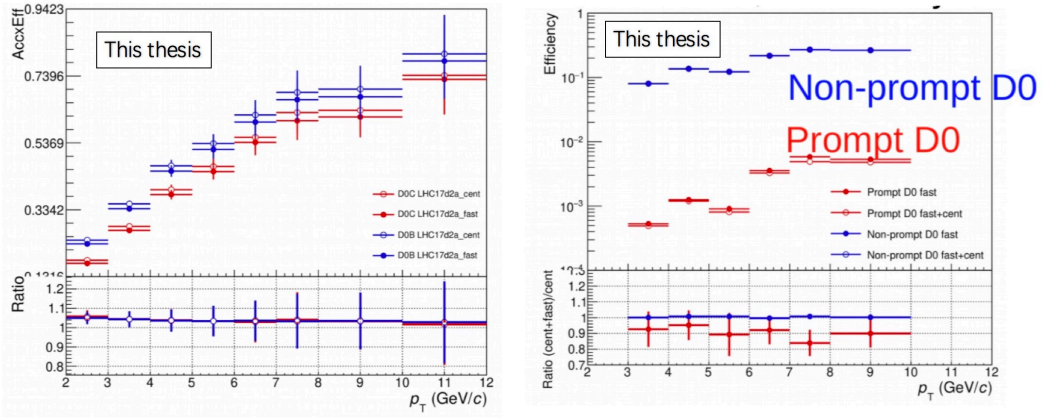

Figure 6.12: Left: the pre-selection efficiency (acceptance*efficiency) of prompt (red) and feed-down (blue) D^0 efficiency calculated by central (open circle) and fast (solid circle) MC samples, respectively. Right: BDT efficiency of prompt (red) and feed-down (blue) D^0 efficiency calculated by fast (solid circle) and fast+central (open circle) MC samples, respectively.

6.4.2 Correction for non-prompt D^0 fraction

The procedure of non-prompt D^0 fraction calculation is similar to what has been described in Sec. 5.3.2. First, the FONLL predictions based method is tried, the equation can be found in Eq. 6.2. To check the stability of this method, the final cross sections and corresponding $f_{\mathrm{non-prompt}}$ are calculated with different BDT cuts. The results are presented in Fig. 6.13. The numbers indicated in the plots are the BDT cuts used for the final cross section. One can find that as the BDT cut goes tighter, the $f_{\mathrm{non-prompt}}$ increases, and the values of cross section go down, nearly flat at high $f_{\mathrm{non-prompt}}$ fraction range. Due to the discrepancy between FONLL and data, when the $f_{\mathrm{non-prompt}}$ is not high, the corrections will lead bias or large uncertainties to the final cross section (only FONLL uncertainty is considered). In

this scenario, an improved method is developed which uses the prompt D^0 cross section obtained from data to replace the FONLL predictions. Fig. 6.14 shows the stability of cross sections with the new method, the cross section trend at low $f_{\mathrm{non-prompt}}$ disappears, although with different BDT selection, the results are quite stable if taking the statistical uncertainties into account. However, the trend is still there for the bin 3-4 GeV/c, which needs further investigation.

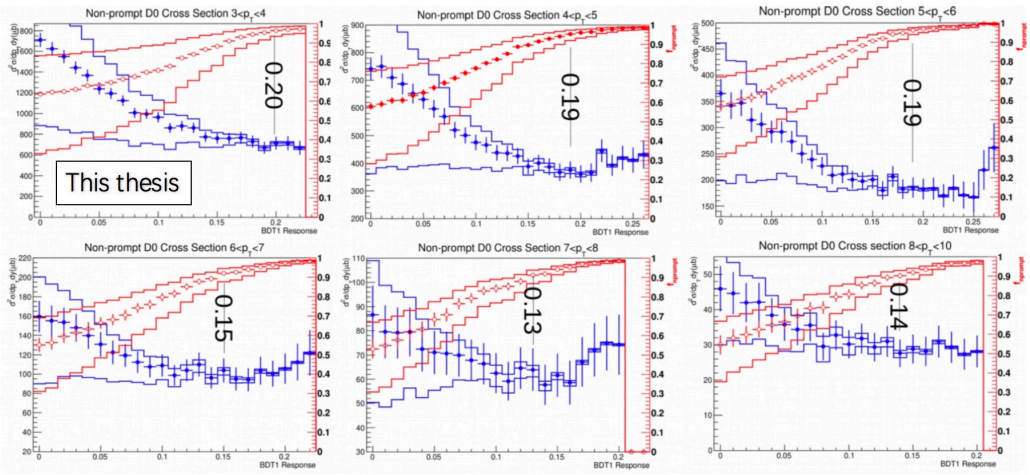

Figure 6.13: Non-prompt D^0 cross section (blue points) and $f_{\mathrm{non-prompt}}$ (red points) using FONLL predictions as a function of BDT cuts in 6 p_{T} bins in the range, $3 < p_{\mathrm{T}} < 10$ GeV/c in p–Pb collisions at $\sqrt{s_{\mathrm{NN}}} = 5.02$ TeV.

6.5 Results

The cross section of non-prompt D^0 can be expressed as:

$$\left.\frac{\mathrm{d}N^{\mathrm{D}^0}}{\mathrm{d}p_{\mathrm{T}}}\right|_{|y|<0.5} = \frac{1}{2}\frac{1}{\Delta y\,\Delta p_{\mathrm{T}}}\frac{\left. f_{\mathrm{non-prompt}}(p_{\mathrm{T}})\cdot N^{\mathrm{D}^0\ \mathrm{raw}}(p_{\mathrm{T}})\right|_{|y|<y_{\mathrm{fid}}}}{(\mathrm{Acc}\times\varepsilon_{pre}\times\varepsilon_{BDT})_{\mathrm{non-prompt}}(p_{\mathrm{T}})\cdot \mathrm{BR}\cdot N_{\mathrm{evt}}}\,. \quad (6.3)$$

The details have already been discussed in Sec. 5.3. Fig. 6.15 shows the non-prompt D^0 cross section obtained via BDT technique with data based approach (blue points) in 6 p_{T} bins in the range, $3 < p_{\mathrm{T}} < 10$ GeV/c in p–Pb collisions at $\sqrt{s_{\mathrm{NN}}} = 5.02$ TeV, compared with FONLL predictions (grey band). The data results are close to the upper band of FONLL predictions.

On the other hand, the prompt cross section can also be measured via BDT technique, the results is shown in Fig. 6.16, the data points are close to the upper band of FONLL predictions. Moreover, the result has better statistical precision with respective to the results obtained by traditional rectangular cut method.

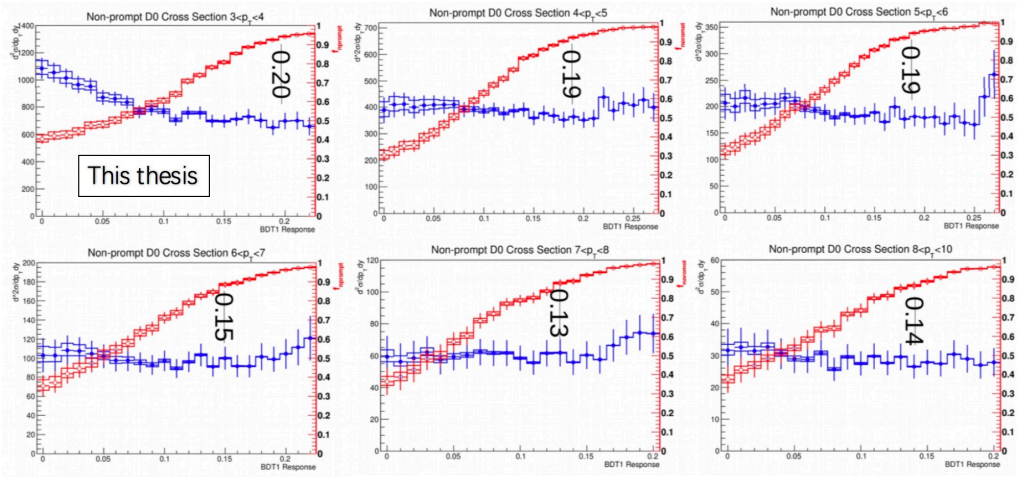

Figure 6.14: Non-prompt D^0 cross section (blue points) and $f_{\mathrm{non-prompt}}$ (red points) using the results from data as a function of BDT cuts in 6 p_{T} bins in the range, $3 < p_{\mathrm{T}} < 10$ GeV/c in p–Pb collisions at $\sqrt{s_{\mathrm{NN}}} = 5.02$ TeV.

6.6 Summary

In this chapter, we have presented the measurements of non-prompt D^0 cross section in p–Pb collisions at $\sqrt{s_{\mathrm{NN}}} = 5.02$ TeV via a novel machine learning based method, which can achieve very high fraction of non-prompt. The results is close to the upper band of FONLL predictions. At the same time, the prompt D^0 cross section can also be obtained via this method, which can achieve better significance compared with traditional rectangular cuts method, indicates that the traditional rectangular cuts method could still be improved. And the new technique can potentially be used to extract the raw yield for D^0 flow and D^0 tagged jet analysis, which is limited by the statistical fluctuations.

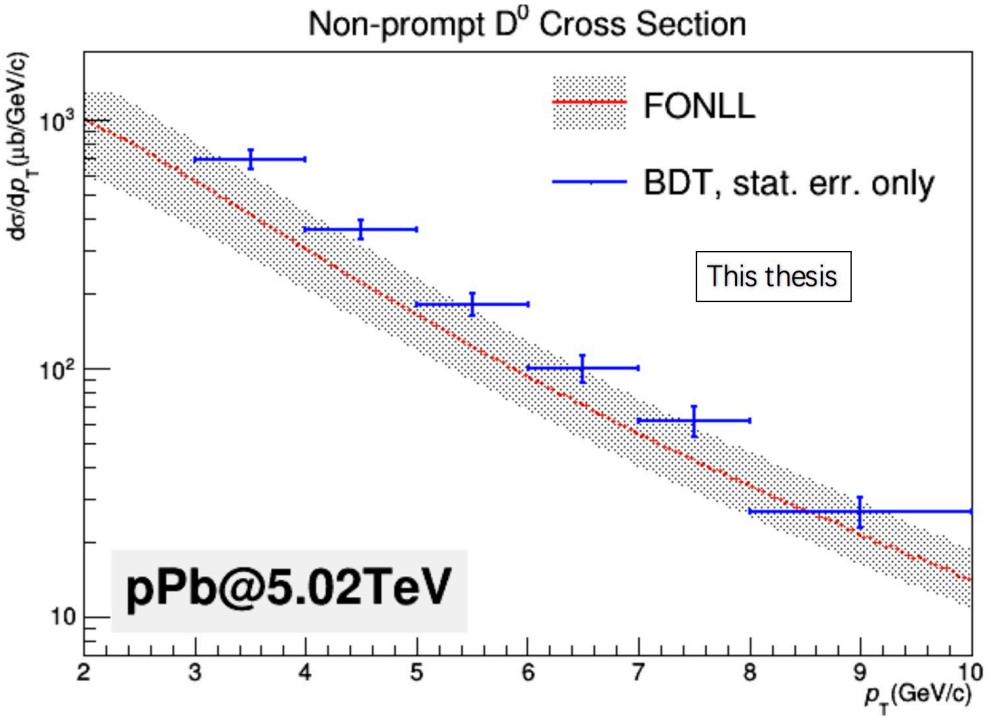

Figure 6.15: The non-prompt D^0 cross section obtained via BDT technique with data based approach (blue points) in 6 p_T bins in the range, $3 < p_T < 10$ GeV/c in p–Pb collisions at $\sqrt{s_{NN}} = 5.02$ TeV, compared with FONLL predictions (grey band).

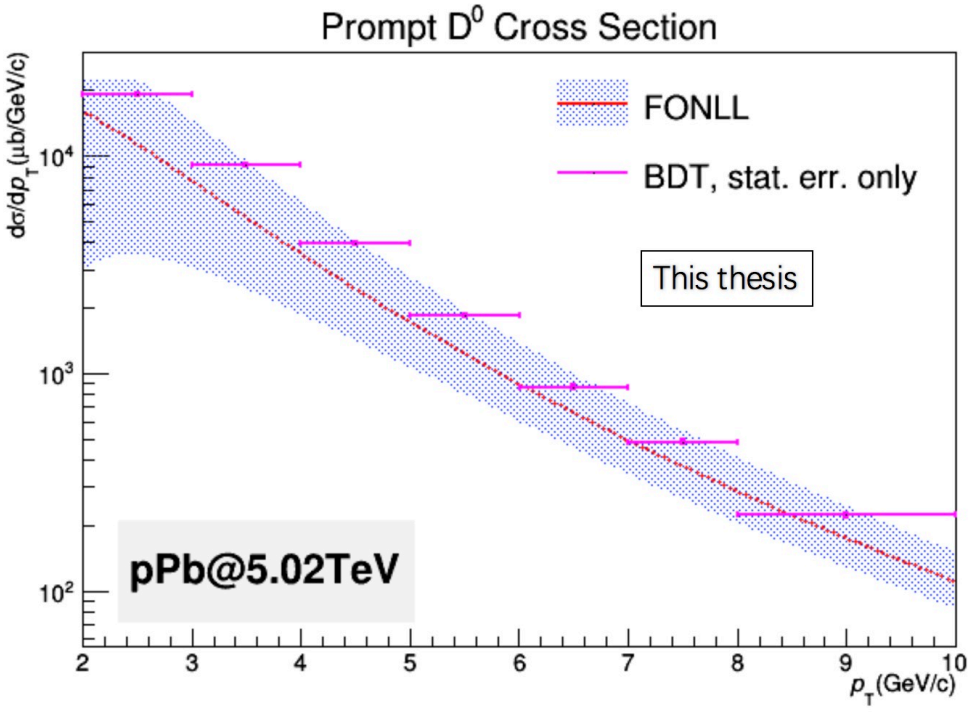

Figure 6.16: The prompt D^0 cross section obtained via BDT technique (pink points) in 6 p_T bins in the range, $3 < p_T < 10$ GeV/c in p–Pb collisions at $\sqrt{s_{NN}} = 5.02$ TeV, compared with FONLL predictions (grey band).

Conclusion and Outlooks

This thesis has presented the I_{AA} measurements with high p_{T} π^0 triggers in pp and central Pb–Pb collisions at $\sqrt{s_{\mathrm{NN}}} = 2.76$ TeV. On the Away side, the I_{AA} is strongly suppressed to around 0.6 with $p_{\mathrm{T}} > 3$ GeV/c, and increase as the momenta decrease, reaching about 5.2 at lowest p_{T}. On the near side, an enhancement of I_{AA} from 1.2 to 1.8 at lowest p_{T} is observed. Consulting the model predictions with the JEWEL and AMPT event generators, as well as a pQCD calculation. All the models can qualitatively describe the strong suppression on Away side at high p_{T}. Only AMPT can qualitatively predict the enhancement at low p_{T} on both Near and Away side. However, it's disfavored by data above 5 GeV/c, especially on the Near side. The coincidence of the away-side suppression at high p_{T} and the large enhancement at low p_{T} on the near and away side is suggestive of a common underlying mechanism, likely related to the energy lose by high momentum partons. The data hence provide a good testing ground to constrain model calculations which aim to fully describe jet-medium interactions.

The D^0 nuclear modification factor has been measured in 0-10%, 30-50% and 60-80% Pb–Pb collisions at $\sqrt{s_{\mathrm{NN}}} = 5.02$ TeV. The average non-strange D-mesons R_{AA} values are compatible with those measured at $\sqrt{s_{\mathrm{NN}}}$ =2.76 TeV and they have smaller uncertainties by a factor of about two, as well as extended p_{T} coverage up to 50 GeV/c in central collisions. The similarity of the R_{AA} values at the two energies was predicted by the Djordjevic model, and it results from the combination of a higher medium temperature at 5.02 TeV (estimated to be about 7% higher than at 2.76 TeV) with a harder p_{T} distribution of charm quarks at 5.02 TeV. In central and semi-central collisions the average R_{AA} of non-strange D mesons is compatible with that of charged particles for $p_{\mathrm{T}} < 6$ GeV/c, while it is larger at lower p_{T}. The R_{AA} of $\mathrm{D_s^+}$ mesons have generally larger central values than those of the average of non-strange D mesons, a hint of smaller suppression for $\mathrm{D_s^+}$ with respect to non-strange D mesons caused by coalescence in the strangeness enriched environment in QGP, but the two measurements are compatible within about one standard deviation of the combined uncertainties. The R_{AA} of non-strange D mesons at high p_{T} (above 10 GeV/c) is fairly described in the three centrality classes by model calculations that include both radiative and collisional energy loss. This indicates that the centrality dependence of radiative energy loss, which is the dominant contribution at high p_{T}, is under good theoretical control. The R_{AA} in the transverse momentum region below 10 GeV/c is described by several transport model calculations in central collisions, but most models fail in describing the centrality dependence of R_{AA} and in describing simultaneously R_{AA} and the elliptic flow coefficient v_2. Therefore, the measurements provide significant constraints for the understanding of the interaction of charm quarks with the high-density QCD medium, especially at low and intermediate p_{T}, where the R_{AA} is the result of a more complex interplay among

several effects.

The non-prompt D^0 cross section has been measured in p-Pb collisions at $\sqrt{s}_{NN}$ = 5.02 TeV, via BDT technique, which allows to extract very high fraction of non-prompt D^0 yields. The cross section is close to the upper band of FONLL predictions. Although this work is still not finalized, several potential technical problems need to be solved, but it provides a novel method to study the production of non-prompt D^0, and the preparation for the analysis in Pb–Pb, which can help us to investigate the beauty quark hadronisation in QGP.

ALICE has finished its Run 2 data taking at the beginning of December in 2018. 8.5 times more statistics in central collisions and 3.8 times in mid-central collision are acquired with respect to the 2015 data. The high statistic may make the non-prompt D^0 analysis possible in Pb–Pb collisions, it will also provide a better precision of prompt D^0 R_{AA} measurements, especially at low p_T, which can help us further understanding the centrality dependence of the energy loss. However, due to the current detector tracking resolution is not good enough, it's still hard to a precise prompt D^0 measurements in Pb–Pb collisions. Thanks to the upgrade of ALICE's Inner Tracking System, it will make a measurement of total charm cross section possible in Pb–Pb collisions during Run 3. On the other hand, a multivariable analysis approach has been applied to the analysis, which can aid in reducing the uncertainty in the measurement of prompt D^0 production. It's also possible to extend this approach to other physics signals. This technique could offer new insights of the observables which is limited by the uncertainties currently.

Bibliography

[1] "Standard Model," *Wikipedia* . https://en.wikipedia.org/wiki/Standard_Model. (Cited on pages ix, 3 and 5.)

[2] L. results on QCD thermodynamics, "Confinement of Quarks," *Nucl.Phys.* **A698** (2002) 199–208, arXiv:hep-ph/0103314. (Cited on pages ix and 6.)

[3] F. Karsch, "Lattice QCD at high temperature and density," *Lect.Notes Phys.* **583** (2002) 209–249, arXiv:hep-lat/0106019. (Cited on pages ix, 6 and 7.)

[4] **ALICE** Collaboration, J. Adam *et al.*, "Centrality dependence of the charged-particle multiplicity density at midrapidity in Pb–Pb collisions at $\sqrt{s_{\rm NN}}$ = 5.02 TeV," *Phys.Rev.Lett.* **116** (2016) no.22, 222302, arXiv:1512.06104 [nucl-ex]. (Cited on pages ix, 10 and 11.)

[5] M. Floris, "Hadron yields and the phase diagram of strongly interacting matter," *Nucl.Phys. A* **931** (2014) 103–112, arXiv:1408.6403 [nucl-ex]. (Cited on pages ix, 11 and 12.)

[6] J. C. S. Wheaton, "THERMUS: A Thermal model package for ROOT," *Comput.Phys.Commun.* **180** (2009) 84–106, arXiv:hep-ph/0407174. (Cited on pages ix, 11 and 12.)

[7] J. S. Peter Braun-Munzinger, Krzysztof Redlich, "Particle production in heavy ion collisions," *GSI-PREPRINT-2003-13* (2003) 109, arXiv:nucl-th/0304013 [nucl-ex]. (Cited on pages ix, 11 and 12.)

[8] V. P. Michal Petran, Jean Letessier and J. Rafelski, "Hadron production and quark-gluon plasma hadronization in Pb–Pb collisions at $\sqrt{s_{\rm NN}}$ = 2.76 TeV," *Phys.Rev.* **C88** (2013) no.3, 034907, arXiv:1303.2098 [hep-ph]. (Cited on pages ix, 11 and 12.)

[9] **ALICE** Collaboration, S. Acharya *et al.*, "Anisotropic flow of identified particles in Pb-Pb collisions at $\sqrt{s_{\rm NN}}$ = 5.02 TeV," *JHEP* **09** (2018) 006, arXiv:1805.04390 [nucl-ex]. (Cited on pages ix, 13 and 14.)

[10] S. J. Charles Gale *et al.*, "Event-by-event anisotropic flow in heavy-ion collisions from combined Yang-Mills and viscous fluid dynamics," *Phys.Rev.Lett.* **100** (2013) no.1, 012302, arXiv:1209.6330 [nucl-th]. (Cited on pages ix, 13 and 14.)

[11] **CMS** Collaboration, V. Khachatryan *et al.*, "Observation of Long-Range Near-Side Angular Correlations in Proton-Proton Collisions at the LHC," *JHEP* **1009** (2010) 091, arXiv:1009.4122 [nucl-ex]. (Cited on pages ix and 15.)

[12] **ALICE** Collaboration, J. Adam *et al.*, "Enhanced production of multi-strange hadrons in high-multiplicity proton-proton collisions," *Nature Phys.* **13** (2017) 535–539, arXiv:1606.07424 [nucl-ex]. (Cited on pages ix, 15 and 16.)

[13] N. Jacazio, "Production of identified charged hadrons in Pb?Pb collisions at $\sqrt{s_{\rm NN}}$ = 5.02 TeV ," *Nucl.Phys.* **A967** (2017) 421–424, arXiv:1704.06030 [nucl-ex]. (Cited on pages x, 17 and 18.)

[14] **PHENIX** Collaboration, G. Aad *et al.*, "Dihadron azimuthal correlations in Au+Au collisions at $\sqrt{s_{\rm NN}}$ = 200 GeV," *Phys.Rev.* **C78** (2008) 014901, arXiv:0801.4545 [nucl-ex]. (Cited on pages x, 18 and 19.)

[15] **ALICE** Collaboration, K. Aamodt *et al.*, "Particle-yield modification in jet-like azimuthal di-hadron correlations in Pb-Pb collisions at $\sqrt{s_{\rm NN}}$ = 2.76 TeV," *Phys.Rev.Lett.* **108** (2012) 092301, arXiv:1110.0121 [nucl-ex]. (Cited on pages x, 20 and 95.)

[16] **ALICE** Collaboration, B. B. Abelev *et al.*, "Centrality, rapidity and transverse momentum dependence of J/Ψ suppression in Pb–Pb collisions at $\sqrt{s_{\rm NN}}$ = 2.76 TeV ," *Phys.Lett.* **B734** (2014) 314–327, arXiv:1311.0214 [nucl-ex]. (Cited on pages x and 22.)

[17] **ALICE** Collaboration, J. Adam *et al.*, "J/Ψ suppression at forward rapidity in Pb–Pb collisions at $\sqrt{s_{\rm NN}}$ = 5.02 TeV ," *Phys.Lett.* **B766** (2017) 212–224, arXiv:1606.08197 [nucl-ex]. (Cited on pages x and 22.)

[18] **PHENIX** Collaboration, A. Adare *et al.*, "Centrality, rapidity and transverse momentum dependence of J/Ψ suppression in Pb–Pb collisions at $\sqrt{s_{\rm NN}}$ = 2.76 TeV ," *Phys. Rev.* **C84** (2011) 054912, arXiv:1103,6269 [nucl-ex]. (Cited on pages x and 22.)

[19] **ALICE** Collaboration, S. Acharya *et al.*, "Measurement of D-meson production at mid-rapidity in pp collisions at $\sqrt{s}$ = 7 TeV," *Eur.Phys.J.* **C77** (2017) no.8, 550, arXiv:1702.00766 [nucl-ex]. (Cited on pages x and 25.)

[20] **STAR** Collaboration, G. Xie, "Λ_c Production in Au+Au Collisions at $\sqrt{s_{NN}}$ = 200 GeV measured by the STAR experiment," *Nucl. Phys.* **A967** (2017) 928–931, arXiv:1704.04353 [nucl-ex]. (Cited on pages xi, 32 and 34.)

[21] **ALICE Collaboration** Collaboration, "Preliminary Physics Summary: Measurement of D^0, D^+, D^{*+} and D_s production in Pb-Pb collisions at $\sqrt{s}_{\rm NN}$ = 5.02 TeV,". https://cds.cern.ch/record/2265109. (Cited on pages xi and 35.)

[22] **ALICE** Collaboration, B. Abelev *et al.*, "Centrality determination of Pb-Pb collisions at $\sqrt{s_{NN}}$ = 2.76 TeV with ALICE," *Phys. Rev.* **C88** no. 4, (2013) 044909, arXiv:1301.4361 [nucl-ex]. (Cited on pages xi, 45 and 46.)

[23] **ALICE** Collaboration, B. B. Abelev *et al.*, "Performance of the ALICE Experiment at the CERN LHC," *Int. J. Mod. Phys.* **A29** (2014) 1430044, arXiv:1402.4476 [nucl-ex]. (Cited on pages xi, 40, 44 and 50.)

[24] **ALICE** Collaboration, J. Adam *et al.*, "Jet-like correlations with neutral pion triggers in pp and central Pb–Pb collisions at 2.76 TeV," *Phys. Lett.* **B763** (2016) 238–250, arXiv:1608.07201 [nucl-ex]. (Cited on pages xii, xv, 62, 94, 95 and 96.)

[25] K. C. Zapp, F. Krauss, and U. A. Wiedemann, "A perturbative framework for jet quenching," *JHEP* **03** (2013) 080, arXiv:1212.1599 [hep-ph]. (Cited on pages xv and 96.)

[26] G.-L. Ma and X.-N. Wang, "Jets, Mach cone, hot spots, ridges, harmonic flow, dihadron and γ-hadron correlation in high-energy heavy-ion collisions," *Phys. Rev. Lett.* **106** (2011) 162301, arXiv:1011.5249 [nucl-th]. (Cited on pages xv, 95, 96 and 97.)

[27] Z.-Q. Liu, H. Zhang, B.-W. Zhang, and E. Wang, "Quantifying jet transport properties via large p_T hadron production," *Eur. Phys. J.* **C76** no. 1, (2016) 20, arXiv:1506.02840 [nucl-th]. (Cited on pages xv, 96 and 97.)

[28] **ALICE** Collaboration, S. Acharya *et al.*, "Measurement of D^0, D^+, D^{*+} and D_s^+ production in Pb-Pb collisions at $\sqrt{s_{NN}} = 5.02$ TeV," *JHEP* **10** (2018) 174, arXiv:1804.09083 [nucl-ex]. (Cited on pages xvii, xviii, 130, 132, 133, 134, 135 and 137.)

[29] S. Plumari, V. Minissale, S. K. Das, G. Coci, and V. Greco, "Charmed Hadrons from Coalescence plus Fragmentation in relativistic nucleus-nucleus collisions at RHIC and LHC," *Eur. Phys. J.* **C78** no. 4, (2018) 348, arXiv:1712.00730 [hep-ph]. (Cited on pages xvii, 32, 131 and 134.)

[30] **CMS** Collaboration, A. M. Sirunyan *et al.*, "Nuclear modification factor of D^0 mesons in PbPb collisions at $\sqrt{\mathbf{s_{NN}}} = \mathbf{5.02} = 5.02$ TeV," arXiv:1708.04962 [nucl-ex]. (Cited on pages xviii, 134 and 138.)

[31] M. Djordjevic and M. Djordjevic, "Predictions of heavy-flavor suppression at 5.1 TeV Pb–Pb collisions at the CERN Large Hadron Collider," *Phys. Rev.* **C92** no. 2, (2015) 024918, arXiv:1505.04316 [nucl-th]. (Cited on pages xviii, 32, 114, 134, 136, 138 and 139.)

[32] **ALICE** Collaboration, S. Acharya *et al.*, "Transverse momentum spectra and nuclear modification factors of charged particles in pp, p-Pb and Pb-Pb collisions at the LHC," arXiv:1802.09145 [nucl-ex]. (Cited on pages xviii, 134 and 138.)

[33] J. Uphoff, O. Fochler, Z. Xu, and C. Greiner, "Elastic and radiative heavy quark interactions in ultra-relativistic heavy-ion collisions," *J. Phys.* **G42**

no. 11, (2015) 115106, arXiv:1408.2964 [hep-ph]. (Cited on pages xviii, 33, 136 and 139.)

[34] J. Xu, J. Liao, and M. Gyulassy, "Bridging Soft-Hard Transport Properties of Quark-Gluon Plasmas with CUJET3.0," *JHEP* **02** (2016) 169, arXiv:1508.00552 [hep-ph]. (Cited on pages xviii, 32, 136 and 139.)

[35] S. Cao, T. Luo, G.-Y. Qin, and X.-N. Wang, "Heavy and light flavor jet quenching at RHIC and LHC energies," *Phys. Lett.* **B777** (2018) 255–259, arXiv:1703.00822 [nucl-th]. (Cited on pages xviii, 34, 119, 136 and 139.)

[36] M. Nahrgang, J. Aichelin, P. B. Gossiaux, and K. Werner, "Influence of hadronic bound states above T_c on heavy-quark observables in Pb + Pb collisions at at the CERN Large Hadron Collider," *Phys. Rev.* **C89** no. 1, (2014) 014905, arXiv:1305.6544 [hep-ph]. (Cited on pages xviii, 33, 136 and 139.)

[37] T. Song, H. Berrehrah, D. Cabrera, W. Cassing, and E. Bratkovskaya, "Charm production in Pb + Pb collisions at energies available at the CERN Large Hadron Collider," *Phys. Rev.* **C93** no. 3, (2016) 034906, arXiv:1512.00891 [nucl-th]. (Cited on pages xviii, 34, 136, 139 and 140.)

[38] A. Beraudo, A. De Pace, M. Monteno, M. Nardi, and F. Prino, "Heavy flavors in heavy-ion collisions: quenching, flow and correlations," *Eur. Phys. J.* **C75** no. 3, (2015) 121, arXiv:1410.6082 [hep-ph]. (Cited on pages xviii, 34, 136 and 139.)

[39] Z.-B. Kang, F. Ringer, and I. Vitev, "Effective field theory approach to open heavy flavor production in heavy-ion collisions," *JHEP* **03** (2017) 146, arXiv:1610.02043 [hep-ph]. (Cited on pages xviii, 33, 136 and 139.)

[40] M. He, R. J. Fries, and R. Rapp, "Heavy Flavor at the Large Hadron Collider in a Strong Coupling Approach," *Phys. Lett.* **B735** (2014) 445–450, arXiv:1401.3817 [nucl-th]. (Cited on pages xviii, 35, 114, 136, 139 and 140.)

[41] **ALICE** Collaboration, S. Acharya *et al.*, "D-meson azimuthal anisotropy in mid-central Pb-Pb collisions at $\sqrt{s_{NN}} = \mathbf{5.02}$ TeV," *Phys. Rev. Lett.* **120** no. 10, (2018) 102301, arXiv:1707.01005 [nucl-ex]. (Cited on pages xviii, 140 and 141.)

[42] **ALICE** Collaboration, J. Adam *et al.*, "Transverse momentum dependence of D-meson production in Pb-Pb collisions at $\sqrt{s_{NN}} = 2.76$ TeV," *JHEP* **03** (2016) 081, arXiv:1509.06888 [nucl-ex]. (Cited on pages xix, 31, 112, 114, 130, 131, 134, 143 and 144.)

[43] S. L.Glashow, "Partial-symmetries of weak interactions," *Nucl. Phys.* **22** (1961) 579–588. https://doi.org/10.1016/0029-5582(61)90469-2. (Cited on page 3.)

[44] C. P. et al. (Particle Data Group), "The Review of Particle Physics," *Chin. Phys. C* **40** (2016) 100001. https://doi.org/10.1088/1674-1137/40/10/100001. (Cited on pages 3, 99 and 112.)

[45] G. S. et al., "Handbook of perturbative QCD," *PNAS* **102 (26)** (2005) 9099–9108. https://doi.org/10.1073/pnas.0503831102. (Cited on page 5.)

[46] D. J. Gross, "The discovery of asymptotic freedom and the emergence of QCD," *Rev. Mod. Phys.* **67** (1995) 157. https://journals.aps.org/rmp/abstract/10.1103/RevModPhys.67.157. (Cited on page 5.)

[47] D. J. Gross and F. Wilczek, "Ultraviolet Behavior of Nonabelian Gauge Theories," *Phys. Rev. Lett.* **30** (1973) 1343. https://journals.aps.org/prl/issues/30/26. (Cited on page 5.)

[48] H. D. Politzer, "Reliable Perturbative Results for Strong Interactions?," *Phys. Rev. Lett.* **30** (1973) 1346. https://doi.org/10.1103/PhysRevLett.30.1346. (Cited on page 5.)

[49] K. G. Wilson, "Confinement of Quarks," *Phys. Rev.* **D10** (1974) 2445–2459. (Cited on page 6.)

[50] O. Kaczmarek *et al.*, "Phase boundary for the chiral transition in (2+1) -flavor QCD at small values of the chemical potential," *Phys.Rev.* **D83** (2011) 014504, arXiv:1011.3130. (Cited on page 7.)

[51] E. V. Shuryak, "Quantum Chromodynamics and the Theory of Superdense Matter," *Phys.Rept.* **61** (1980) 71–158. (Cited on page 8.)

[52] S. J. S. Michael L. Miller, Klaus Reygers and P. Steinberg), "Glauber modeling in high energy nuclear collisions," *Ann.Rev.Nucl.Part.Sci.* **57** (2007) 205–243, arXiv:nucl-ex/0701025. (Cited on page 8.)

[53] J. Bjorken, "Highly Relativistic Nucleus-Nucleus Collisions: The Central Rapidity Region," *Phys.Rev.* **D27** (1983) 140–151. (Cited on page 10.)

[54] **ALICE** Collaboration, J. Adam *et al.*, "Measurement of transverse energy at midrapidity in Pb–Pb collisions at $\sqrt{s_{\rm NN}} = 2.76$ TeV," *Phys.Rev.*. **C94** (2016) no.3, 034903, arXiv:1603.04775 [nucl-ex]. (Cited on page 11.)

[55] S. P. Yinghua Pan, "Hadron yields and the phase diagram of strongly interacting matter," arXiv:1210.1577 [nucl-th]. (Cited on page 12.)

[56] R. S. Ulrich Heinz, "Collective flow and viscosity in relativistic heavy-ion collisions," arXiv:1301.2826 [nucl-th]. (Cited on page 12.)

[57] S. A. V. Denes Molnar, "Elliptic flow at large transverse momenta from quark coalescence," *Phys.Rev.Lett.* **91** (2003) 092301, arXiv:nucl-th/0302014. (Cited on page 13.)

[58] D. A. Teaney, "Viscous Hydrodynamics and the Quark Gluon Plasma," arXiv:arXiv:0905.2433 [nucl-th]. (Cited on page 13.)

[59] **ATLAS** Collaboration, G. Aad *et al.*, "Observation of Associated Near-Side and Away-Side Long-Range Correlations in $\sqrt{s_{\rm NN}} = 5.02$ TeV Proton-Lead Collisions with the ATLAS Detector," *Phys.Rev.Lett.* **110** (2013) no.18, 182302, arXiv:1212.5198 [nucl-ex]. (Cited on page 15.)

[60] B. S. Kevin Dusling, Wei Li, "Novel collective phenomena in high-energy proton-proton and proton-nucleus collisions," *Int.J.Mod.Phys.* **E25** (2016) no.01, 1630002, arXiv:1509.07939 [nucl-ex]. (Cited on page 15.)

[61] **NA57** Collaboration, L. Sandor *et al.*, "Results on hyperon production from the NA57 experiment," *Acta Phys.Hung.* **A22** (2005) 113–120, arXiv:nucl-ex/0404030. (Cited on page 15.)

[62] **ALICE** Collaboration, B. Abelev *et al.*, "Multiplicity Dependence of Pion, Kaon, Proton and Lambda Production in p–Pb Collisions at $\sqrt{s_{\rm NN}} = 5.02$ TeV ," *Phys.Lett.* **B728** (2014) 25–38, arXiv:1307.6796 [nucl-ex]. (Cited on page 15.)

[63] D. T. J. Casalderrey-Solana, E.V. Shuryak, "Hydrodynamic flow from fast particles," arXiv:hep-ph/0602183. (Cited on page 20.)

[64] X.-N. W. V. Koch, A. Majumder, "Cerenkov radiation from jets in heavy-ion collisions," *Phys.Rev.Lett.* **96** (2006) 172302, arXiv:nucl-th/0507063 [nucl-th]. (Cited on page 20.)

[65] I. Vitev, "Large angle hadron correlations from medium-induced gluon radiation," *Phys.Lett.* **B630** (2005) 78–84, arXiv:hep-ph/0501255. (Cited on page 20.)

[66] **PHENIX** Collaboration, A. Adare, "Trends in Yield and Azimuthal Shape Modification in Dihadron Correlations in Relativistic Heavy Ion Collisions," *Phys.Rev.Lett.* **104** (2010) 252301, arXiv:1002.1077 [nucl-ex]. (Cited on pages 20 and 95.)

[67] U. A. W. Nestor Armesto, Carlos A. Salgado, "Measuring the collective flow with jets," *Phys.Rev.Lett.* **93** (2004) 242301, arXiv:hep-ph/0405301. (Cited on page 20.)

[68] S. A. Voloshin, "Transverse radial expansion in nuclear collisions and two particle correlations," *Phys.Lett.* **B632** (2006) 490–494, arXiv:nucl-th/0312065. (Cited on page 20.)

[69] G. R. B. Alver, "Collision geometry fluctuations and triangular flow in heavy-ion collisions," *Phys.Rev.* **C81** (2010) 054905, arXiv:1003.0194 [nucl-th]. (Cited on page 20.)

[70] **ATLAS** Collaboration, G. Aad *et al.*, "Observation of a Centrality-Dependent Dijet Asymmetry in Lead-Lead Collisions at $\sqrt{s_{\rm NN}} = 2.77$ TeV with the ATLAS Detector at the LHC," *Phys.Rev.Lett.* **105** (2010) 252303, arXiv:1011.6182 [nucl-ex]. (Cited on page 21.)

[71] H. S. T. Matsui, "J/Ψ Suppression by Quark-Gluon Plasma Formation," *Phys.Lett.* **B178** (1986) 416–422. (Cited on page 21.)

[72] **NA50** Collaboration, M. Abreu *et al.*, "Evidence for deconfinement of quarks and gluons from the J / psi suppression pattern measured in Pb + Pb collisions at the CERN SPS," *Phys.Lett.* **B477** (2000) 28–36. (Cited on page 21.)

[73] S.-X. L. Fu-Ming Liu, "Quark-gluon plasma formation time and direct photons from heavy ion collisions," *Phys.Rev.* **C89** (2014) no.3, 034906, arXiv:1212.6587 [nucl-th]. (Cited on page 23.)

[74] D. E. S. John C. Collins and G. F. Sterman, "Factorization of Hard Processes in QCD," *Adv.Ser.Direct.High Energy Phys.* **5** (1989) 1–91, arXiv:hep-ph/0409313. (Cited on page 23.)

[75] I. S. B.A. Kniehl, G. Kramer and H. Spiesberger, "Reconciling open charm production at the Fermilab Tevatron with QCD," *Phys.Rev.Lett.* **96** (2006) 012001, arXiv:hep-ph/0508129. (Cited on page 24.)

[76] M. G. Matteo Cacciari and P. Nason, "The P(T) spectrum in heavy flavor hadro production ," *JHEP* **9805** (1998) 007, arXiv:hep-ph/9803400. (Cited on pages 24 and 111.)

[77] N. H. Matteo Cacciari, Stefano Frixione, "Theoretical predictions for charm and bottom production at the LHC," *JHEP* **1210** (2012) 137, arXiv:1205.6344. (Cited on pages 24 and 111.)

[78] I. S. B.A. Kniehl, G. Kramer and H. Spiesberger, "Inclusive Charmed-Meson Production at the CERN LHC," *Eur.Phys.J.* **C72** (2012) 2082, arXiv:1202.0439. (Cited on page 24.)

[79] **ALICE** Collaboration, S. Acharya *et al.*, "$\Lambda_{\rm c}^{+}$ production in pp collisions at $\sqrt{s} = 7$ TeV and in p–Pb collisions at $\sqrt{s_{\rm NN}} = 5.02$ TeV," *JHEP* **1804** (2018) 108, arXiv:1712.09581 [nucl-ex]. (Cited on page 24.)

[80] G. R. Stefano Frixione, Paolo Nason, "A Positive-weight next-to-leading-order Monte Carlo for heavy flavour hadroproduction," *JHEP* **0709** (2007) 126, arXiv:0707.3088. (Cited on page 24.)

[81] N. Fischer and T. Sjöstrand, "Thermodynamical String Fragmentation," *JHEP* **1701** (2017) 140, arXiv:1610.09818. (Cited on page 25.)

[82] **ALICE** Collaboration, C. W. Fabjan *et al.*, "ALICE: Physics performance report, volume II," *J. Phys.* **G32** (2006) 1295–2040. (Cited on page 27.)

[83] H. P. Kari J. Eskola, Petja Paakkinen and C. A. Salgado, "EPPS16: Nuclear parton distributions with LHC data," *Eur.Phys.J.* **C77** (2017) no.3, 163, arXiv:1612.05741 [nucl-ph]. (Cited on page 27.)

[84] H. P. Kari J. Eskola and C. A. Salgado, "EPS09: A New Generation of NLO and LO Nuclear Parton Distribution Functions," *JHEP* **0904** (2009) 065, arXiv:0902.4154 [nucl-ph]. (Cited on page 27.)

[85] P. Z. Daniel de Florian, Rodolfo Sassot and M. Stratmann, "Global Analysis of Nuclear Parton Distributions," *Phys.Rev.* **D85** (2012) 074028, arXiv:1112.6324 [nucl-ph]. (Cited on page 27.)

[86] **ALICE** Collaboration, S. Acharya *et al.*, "Production of muons from heavy-flavour hadron decays in p-Pb collisions at $\sqrt{s_{\rm NN}} = \mathbf{5.02}$ TeV," *Phys. Lett.* **B770** (2017) 459–472, arXiv:1702.01479 [nucl-ex]. (Cited on page 28.)

[87] M. L. Mangano, P. Nason, and G. Ridolfi, "Heavy quark correlations in hadron collisions at next-to-leading order," *Nucl. Phys.* **B373** (1992) 295–345. (Cited on page 28.)

[88] R. Sharma, I. Vitev, and B.-W. Zhang, "Light-cone wave function approach to open heavy flavor dynamics in QCD matter," *Phys. Rev.* **C80** (2009) 054902, arXiv:0904.0032 [hep-ph]. (Cited on page 28.)

[89] Z.-B. Kang, I. Vitev, E. Wang, H. Xing, and C. Zhang, "Multiple scattering effects on heavy meson production in p+A collisions at backward rapidity," *Phys. Lett.* **B740** (2015) 23–29, arXiv:1409.2494 [hep-ph]. (Cited on page 28.)

[90] **ALICE Collaboration** Collaboration, "Preliminary Physics Summary: Measurement of prompt D^0, D^+, D^{*+} and D_s^+ production in p-Pb collisions at $\sqrt{s_{\rm NN}} = 5.02$ TeV,". https://cds.cern.ch/record/2272160. (Cited on page 28.)

[91] H. Fujii and K. Watanabe, "Nuclear modification of forward D production in pPb collisions at the LHC," arXiv:1706.06728 [hep-ph]. (Cited on page 28.)

[92] M. Cacciari, S. Frixione, N. Houdeau, M. L. Mangano, P. Nason, and G. Ridolfi, "Theoretical predictions for charm and bottom production at the LHC," *JHEP* **10** (2012) 137, arXiv:1205.6344 [hep-ph]. (Cited on pages 28, 129 and 130.)

[93] Y. Xu, S. Cao, G.-Y. Qin, W. Ke, M. Nahrgang, J. Auvinen, and S. A. Bass, "Heavy-flavor dynamics in relativistic p-Pb collisions at $\sqrt{S_{NN}} = 5.02$ TeV," *Nucl. Part. Phys. Proc.* **276-278** (2016) 225–228, arXiv:1510.07520 [nucl-th]. (Cited on page 29.)

[94] A. Beraudo, A. De Pace, M. Monteno, M. Nardi, and F. Prino, "Heavy-flavour production in high-energy d-Au and p-Pb collisions," *JHEP* **03** (2016) 123, arXiv:1512.05186 [hep-ph]. (Cited on page 29.)

[95] S. Cao, G.-Y. Qin, and S. A. Bass, "Model and parameter dependence of heavy quark energy loss in a hot and dense medium," *J. Phys.* **G40** (2013) 085103, arXiv:1205.2396 [nucl-th]. (Cited on page 30.)

[96] R. Baier, Y. L. Dokshitzer, A. H. Mueller, S. Peigne, and D. Schiff, "Radiative energy loss of high-energy quarks and gluons in a finite volume quark - gluon plasma," *Nucl. Phys.* **B483** (1997) 291–320, arXiv:hep-ph/9607355 [hep-ph]. (Cited on page 31.)

[97] Y. L. Dokshitzer and D. E. Kharzeev, "Heavy quark colorimetry of QCD matter," *Phys. Lett.* **B519** (2001) 199–206, arXiv:hep-ph/0106202 [hep-ph]. (Cited on page 31.)

[98] M. Djordjevic, "Heavy flavor puzzle at LHC: a serendipitous interplay of jet suppression and fragmentation," *Phys. Rev. Lett.* **112** no. 4, (2014) 042302, arXiv:1307.4702 [nucl-th]. (Cited on pages 31 and 135.)

[99] R. J. Fries, V. Greco, and P. Sorensen, "Coalescence Models For Hadron Formation From Quark Gluon Plasma," *Ann. Rev. Nucl. Part. Sci.* **58** (2008) 177–205, arXiv:0807.4939 [nucl-th]. (Cited on page 31.)

[100] E. V. Shuryak and I. Zahed, "Towards a theory of binary bound states in the quark gluon plasma," *Phys. Rev.* **D70** (2004) 054507, arXiv:hep-ph/0403127 [hep-ph]. (Cited on page 32.)

[101] Y. Oh, C. M. Ko, S. H. Lee, and S. Yasui, "Heavy baryon/meson ratios in relativistic heavy ion collisions," *Phys. Rev.* **C79** (2009) 044905, arXiv:0901.1382 [nucl-th]. (Cited on page 32.)

[102] S. Ghosh, S. K. Das, V. Greco, S. Sarkar, and J.-e. Alam, "Diffusion of Λ_c in hot hadronic medium and its impact on Λ_c/D ratio," *Phys. Rev.* **D90** no. 5, (2014) 054018, arXiv:1407.5069 [nucl-th]. (Cited on page 32.)

[103] S. K. Das, J. M. Torres-Rincon, L. Tolos, V. Minissale, F. Scardina, and V. Greco, "Propagation of heavy baryons in heavy-ion collisions," *Phys. Rev.* **D94** no. 11, (2016) 114039, arXiv:1604.05666 [nucl-th]. (Cited on page 32.)

[104] L. Evans and P. Bryant, "LHC Machine," *JINST* **3** (2008) S08001. (Cited on page 39.)

[105] **ALICE** Collaboration, K. Aamodt *et al.*, "The ALICE experiment at the CERN LHC," *JINST* **3** (2008) S08002. (Cited on page 40.)

[106] **ALICE EMCal** Collaboration, J. Allen *et al.*, "Performance of prototypes for the ALICE electromagnetic calorimeter," *Nucl. Instrum. Meth.* **A615** (2010) 6–13, arXiv:0912.2005 [physics.ins-det]. (Cited on pages 45 and 56.)

[107] **ALICE** Collaboration, B. Abelev *et al.*, "Anisotropic flow of charged hadrons, pions and (anti-)protons measured at high transverse momentum in Pb-Pb collisions at $\sqrt{s_{NN}}$=2.76 TeV," *Phys. Lett.* **B719** (2013) 18–28, arXiv:1205.5761 [nucl-ex]. (Cited on page 70.)

[108] **ALICE** Collaboration, K. Aamodt *et al.*, "Harmonic decomposition of two-particle angular correlations in Pb-Pb collisions at $\sqrt{s_{NN}} = 2.76$ TeV," *Phys. Lett.* **B708** (2012) 249–264, arXiv:1109.2501 [nucl-ex]. (Cited on page 70.)

[109] **ALICE** Collaboration, B. B. Abelev *et al.*, "Energy Dependence of the Transverse Momentum Distributions of Charged Particles in pp Collisions Measured by ALICE," *Eur. Phys. J.* **C73** no. 12, (2013) 2662, arXiv:1307.1093 [nucl-ex]. (Cited on page 83.)

[110] **ALICE** Collaboration, B. Abelev *et al.*, "Centrality Dependence of Charged Particle Production at Large Transverse Momentum in Pb–Pb Collisions at $\sqrt{s_{\rm NN}} = 2.76$ TeV," *Phys. Lett.* **B720** (2013) 52–62, arXiv:1208.2711 [hep-ex]. (Cited on page 83.)

[111] A. Peshier, "The QCD collisional energy loss revised," *Phys. Rev. Lett.* **97** (2006) 212301, arXiv:hep-ph/0605294 [hep-ph]. (Cited on page 95.)

[112] X.-N. Wang, M. Gyulassy, and M. Plumer, "The LPM effect in QCD and radiative energy loss in a quark gluon plasma," *Phys. Rev.* **D51** (1995) 3436–3446, arXiv:hep-ph/9408344 [hep-ph]. (Cited on page 95.)

[113] M. Gyulassy and X.-n. Wang, "Multiple collisions and induced gluon Bremsstrahlung in QCD," *Nucl. Phys.* **B420** (1994) 583–614, arXiv:nucl-th/9306003 [nucl-th]. (Cited on page 95.)

[114] M. Gyulassy and M. Plumer, "Jet Quenching in Dense Matter," *Phys. Lett.* **B243** (1990) 432–438. (Cited on page 95.)

[115] X.-N. Wang and M. Gyulassy, "Gluon shadowing and jet quenching in A + A collisions at s**(1/2) = 200-GeV," *Phys. Rev. Lett.* **68** (1992) 1480–1483. (Cited on page 95.)

[116] B. Z. Kopeliovich, J. Nemchik, A. Schafer, and A. V. Tarasov, "Cronin effect in hadron production off nuclei," *Phys. Rev. Lett.* **88** (2002) 232303, arXiv:hep-ph/0201010 [hep-ph]. (Cited on page 95.)

[117] I. Vitev, "Large angle hadron correlations from medium-induced gluon radiation," *Phys. Lett.* **B630** (2005) 78–84, arXiv:hep-ph/0501255 [hep-ph]. (Cited on page 95.)

[118] **ATLAS** Collaboration, G. Aad *et al.*, "Measurement of inclusive jet charged-particle fragmentation functions in Pb+Pb collisions at $\sqrt{s_{NN}} = 2.76$ TeV with the ATLAS detector," *Phys. Lett.* **B739** (2014) 320–342, arXiv:1406.2979 [hep-ex]. (Cited on page 96.)

[119] **CMS** Collaboration, S. Chatrchyan *et al.*, "Measurement of jet fragmentation in PbPb and pp collisions at $\sqrt{s_{NN}} = 2.76$ TeV," *Phys. Rev.* **C90** no. 2, (2014) 024908, arXiv:1406.0932 [nucl-ex]. (Cited on page 96.)

[120] **JET** Collaboration, K. M. Burke *et al.*, "Extracting the jet transport coefficient from jet quenching in high-energy heavy-ion collisions," *Phys. Rev.* **C90** no. 1, (2014) 014909, arXiv:1312.5003 [nucl-th]. (Cited on page 97.)

[121] Z.-W. Lin, C. M. Ko, B.-A. Li, B. Zhang, and S. Pal, "A Multi-phase transport model for relativistic heavy ion collisions," *Phys. Rev.* **C72** (2005) 064901, arXiv:nucl-th/0411110 [nucl-th]. (Cited on page 97.)

[122] J. Xu and C. M. Ko, "Pb-Pb collisions at $\sqrt{s_{NN}} = 2.76$ TeV in a multiphase transport model," *Phys. Rev.* **C83** (2011) 034904, arXiv:1101.2231 [nucl-th]. (Cited on page 97.)

[123] S. Pal and M. Bleicher, "Suppression of high p_T hadrons in Pb + Pb collisions at LHC," *Phys. Lett.* **B709** (2012) 82–86, arXiv:1201.2546 [nucl-th]. (Cited on page 97.)

[124] T. Sjostrand, S. Mrenna, and P. Z. Skands, "PYTHIA 6.4 Physics and Manual," *JHEP* **0605** (2006) 026, arXiv:hep-ph/0603175 [hep-ph]. (Cited on page 108.)

[125] P. Z. Skands, "The Perugia Tunes," *FERMILAB-CONF-09-113-T* (2009) 284–297, arXiv:0905.3418 [hep-ph]. (Cited on page 108.)

[126] X.-N. Wang and M. Gyulassy, "HIJING: A Monte Carlo model for multiple jet production in p p, p A and A A collisions," *Phys.Rev.* **D44** (1991) 3501–3516. (Cited on page 108.)

[127] J. Uphoff, O. Fochler, Z. Xu, and C. Greiner, "Elliptic Flow and Energy Loss of Heavy Quarks in Ultra-Relativistic heavy Ion Collisions," *Phys.Rev.* **C84** (2011) 024908, arXiv:1104.2295 [hep-ph]. (Cited on pages 111 and 120.)

[128] O. Fochler, J. Uphoff, Z. Xu, and C. Greiner, "Jet quenching and elliptic flow at RHIC and LHC within a pQCD-based partonic transport model," *J.Phys.* **G38** (2011) 124152, arXiv:1107.0130 [hep-ph]. (Cited on page 111.)

[129] J. Uphoff, O. Fochler, Z. Xu, and C. Greiner, "Open Heavy Flavor in Pb+Pb Collisions at $\sqrt{s} = 2.76$ TeV within a Transport Model," *Phys.Lett.* **B717** (2012) 430–435, arXiv:1205.4945 [hep-ph]. (Cited on page 111.)

[130] **ALICE** Collaboration, B. Abelev *et al.*, "Measurement of charm production at central rapidity in proton-proton collisions at $\sqrt{s} = 7$ TeV," *JHEP* **1201** (2012) 128, arXiv:1111.1553 [hep-ex]. (Cited on pages 112 and 127.)

[131] **ALICE** Collaboration, J. Adam *et al.*, "Centrality dependence of high-p_T D meson suppression in Pb-Pb collisions at $\sqrt{s_{NN}} = 2.76$ TeV," *JHEP* **11** (2015) 205, arXiv:1506.06604 [nucl-ex]. (Cited on page 114.)

[132] **CMS** Collaboration, V. Khachatryan *et al.*, "Suppression and azimuthal anisotropy of prompt and nonprompt J/ψ production in PbPb collisions at $\sqrt{s_{NN}} = 2.76$ TeV," *Eur. Phys. J. C* **77** (2017) 252, arXiv:1610.00613 [nucl-ex]. (Cited on page 114.)

[133] **Particle Data Group** Collaboration, C. Patrignani *et al.*, "Review of Particle Physics," *Chin. Phys.* **C40** no. 10, (2016) 100001. (Cited on page 114.)

[134] **ALICE** Collaboration, B. Abelev *et al.*, "Suppression of high transverse momentum D mesons in central Pb-Pb collisions at $\sqrt{s_{NN}} = 2.76$ TeV," *JHEP* **1209** (2012) 112, arXiv:1203.2160 [nucl-ex]. (Cited on page 114.)

[135] **ALICE** Collaboration, J. Adam *et al.*, "Measurement of D_s^+ production and nuclear modification factor in Pb-Pb collisions at $\sqrt{s_{NN}} = 2.76$ TeV," *JHEP* **03** (2016) 082, arXiv:1509.07287 [nucl-ex]. (Cited on page 114.)

[136] R. Barlow, "Systematic errors: Facts and fictions," in *Advanced Statistical Techniques in Particle Physics. Proceedings, Conference, Durham, UK, March 18-22, 2002*, pp. 134–144. 2002. arXiv:hep-ex/0207026 [hep-ex]. http://www.ippp.dur.ac.uk/Workshops/02/statistics/proceedings/barlow.pdf. (Cited on page 116.)

[137] **ALICE** Collaboration, S. Acharya *et al.*, "Measurement of D-meson production at mid-rapidity in pp collisions at $\sqrt{s} = 7$ TeV," arXiv:1702.00766 [hep-ex]. (Cited on pages 129, 130 and 141.)

[138] R. Averbeck, N. Bastid, Z. C. del Valle, P. Crochet, A. Dainese, and X. Zhang, "Reference Heavy Flavour Cross Sections in pp Collisions at $\sqrt{s} = 2.76$ TeV, using a pQCD-Driven $\sqrt{s}$-Scaling of ALICE Measurements at $\sqrt{s} = 7$ TeV," arXiv:1107.3243 [hep-ph]. (Cited on page 130.)

[139] **ALICE** Collaboration, S. Acharya *et al.*, "Λ_c^+ production in pp collisions at $\sqrt{s} = 7$ TeV and in p-Pb collisions at $\sqrt{s_{NN}} = 5.02$ TeV," *JHEP* **04** (2018) 108, arXiv:1712.09581 [nucl-ex]. (Cited on page 145.)

[140] A. Hocker *et al.*, "TMVA - Toolkit for Multivariate Data Analysis," arXiv:physics/0703039 [physics.data-an]. (Cited on page 145.)

Publication List

1. Acharya, S $\cdots$ Xinye, Peng $\cdots$ (ALICE Collaboration), **Measurement of D^0, D^+, D^{*+} and D_s^+ production in Pb-Pb collisions at $\sqrt{s_{NN}} = 5.02$ TeV**, *JHEP 10 (2018) 174, (main analyzer, paper committee).*

2. Adam, J $\cdots$ Xinye, Peng $\cdots$ (ALICE Collaboration), **Jet-like correlations with neutral pion triggers in pp and central Pb–Pb collisions at 2.76 TeV**, *Phys. Lett. B763 (2016) 238-250, (main analyzer, paper committee).*

3. Xinye, Peng for ALICE Collaboration, **Non-strange and strange D-meson and charm-baryon production in heavy-ion collisions measured with ALICE at the LHC**, *Accepted By Nuclear Physics A, arXiv:1807.07286.*

4. Xinye, Peng for ALICE Collaboration, **π^0-hadron correlations in pp and Pb–Pb collisions and π^0 elliptic flow in Pb–Pb collisions measured at the ALICE experiment**, *Nucl.Part.Phys.Proc. 289-290 (2017) 346-349.*

5. Acharya, S $\cdots$ Xinye, Peng $\cdots$ (ALICE Collaboration), **D-meson azimuthal anisotropy in mid-central Pb–Pb collisions at $\sqrt{s_{NN}} = 5.02$ TeV**, *Phys. Rev. Lett. 120 no. 10, (2018) 102301, (important contribution).*

As Member of ALICE

I have more than 80 additional publications as member of ALICE until December 2018.

Other contributions in ALICE

During my PhD, I did the service work as train operator in GA group, and participated in ITS QA checks from 2016 to 2018. I participated the ALICE Run 2 data taking and SPD operation. At the same time, I took the duty of Analysis Review Committee for "D^0-tagged jet in pp, p–Pb and Pb–Pb collisions at 5.02 TeV", and participated in the discussion and code framework development in D2H working group.

Selected presentations list

1. Xinye, Peng (for the ALICE Collaboration), **Non-strange and strange D-meson and charm-baryon production in heavy-ion collisions measured with ALICE at the LHC**, *Quark Matter 2018, Venice, Italy, May, 2018.*

2. Xinye, Peng (for the ALICE Collaboration), **π^0-hadron correlations in pp and Pb–Pb collisions and π^0 elliptic flow in Pb–Pb collisions measured at the ALICE experiment**, *Hard Probes 2016, Wuhan, China, September, 2016.*

3. Xinye, Peng (for the ALICE Collaboration), **Neutral pion-hadron correlations in pp and Pb–Pb collisions measured at the ALICE experiment**, *EPS-HEP 2017, Venice, Italy, July, 2017.*

4. Xinye, Peng (for the ALICE Collaboration), **D^0-meson production and elliptic flow measurements in Pb–Pb collisions at $\sqrt{s_{NN}} = 5.02$ TeV with ALICE (poster)**, *LHCP 2017, Shanghai, China, May, 2017.*

5. Xinye, Peng (for the ALICE Collaboration), **π^0-hadron correlations in pp and Pb–Pb collisions with EMCal in ALICE**, *CLHCP 2015, Hefei, China, December, 2015.*

6. Xinye, Peng (for the ALICE Collaboration), **D^0-meson production measurements in Pb–Pb collisions at $\sqrt{s_{NN}} = 5.02$ TeV with ALICE**, *CLHCP 2017, Nanjing, China, December, 2017.*

7. Xinye, Peng (for the ALICE Collaboration), **Non-strange and strange D-meson and charm-baryon production in heavy-ion collisions measured with ALICE at the LHC**, *CLHCP 2018, Wuhan, China, December, 2018.*

Acknowledgments

There are many persons that I would like to thank for various reasons.

First, I would like to thank my supervisor Andrea Dainese at Padova University in Italy and, Daicui Zhou at Central China Normal University, Wuhan in China who gave me the opportunity to work alternately in Italy and China, in the ALICE Collaboration on very exciting topics during PhD thesis. Their support, guidance and availability deserve my deepest gratitude. Their experience and personal qualities have been of great influence for me both on professional and personal aspects. I really enjoyed the two years staying in Italy, and hope to go on to cooperate with Padova Group in the future. In addition, I'd like to thanks to Constantin Loizides who gave me a lot of help for my first analysis, I really learnt so much from him not only on physics but also on how to do things well.

I am also grateful to others in Padova Group, especially Federico Antinori, Rosario Turrisi, Andrea Rossi Andrea Festanti, Cristina Terrevoli, Mattia Faggin for the discussions and helps. And the people in D2H group, Alessandro Grelli, Francesco Prino, Elena Bruna, Pietro Antonioli, Zaida, Jaime, Jeremy, Fabrizio, Anastasia, Grazia, Cristina Bedda, Syaefudin, Andrea Alici. Also other people from GA group, Friederike Bock, Ana, Yuri, Klaus, Thomas. And other senior people from ALICE, You Zhou, Rachid, Marco, Andreas, Elena Botta, Marie.

Many thanks to the faculties on wuhan group, Prof. Yin Zhongbao, Prof. Zhang Xiaoming, Prof. Mao Yaxian, Prof. Pei Hua and Prof. Paolo Bartalini. And the people from IOPP, Prof. Wang Xinnian, Prof. Xu Nu, Prof. Cai Xu, Prof. Liu Feng, Prof. Zhang Benwei, Prof. Xie Yuehong, Prof. Hou Defu, Prof. Zhang Hanzhong, Prof. Zhou Daimei, Prof. Liu Fuming, Prof. Wu Yuanfang, et al.

It's also my please to thank all the members from ALICE wuhan group (including the ones already left): Zhu Xiangrong, Li Shuang, Zhang Haitao, Zhan Yang, Dang Ruina, Wang Mengliang, Zhu Jianhui, Zhu Hongsheng, Zhang Zuman, Zhang Yonghong, Ren Xiaowen, Zhua Ya, Li Xinlong, Xu Ran, Chang Wan, Ding Yanchuan, Fan Feng, Cui Pengyao, Cai Mengke, Tang Siyu, Zhang Biao, Zhou Yingjie, Hou Yongzhen, Zhang Wenjing, Qiao Qi, Guo Wenda, Ceng Shuxin, Yuan Qi, Jiang Xiuxiu, Dang Yuxing, Tan Yalei, Cheng Tiantian, Liu Donghai, Wang Ruiqin and so on.

Finally, last but not least in my thoughts, I want to express my heartfelt gratitude to my parents and girlfriend, for their understanding and encouragement in

these years.

All my apologies for the people I may have forgotten.

Xinye Peng

January 3, 2019

Wuhan